Nano-Structuring of Micro-Alloyed Steels via Nano-Precipitate Formation

Samuel James Clark

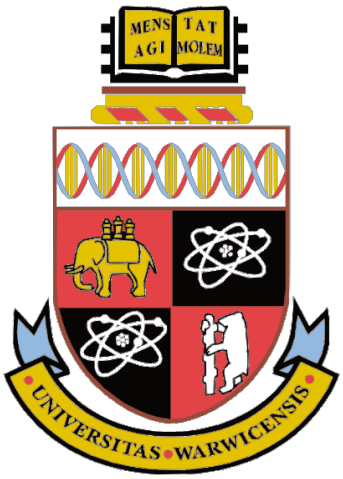

A thesis submitted in partial fulfilment of the requirements for the degree of

Doctor of Philosophy in Engineering

University of Warwick, WMG, January 2019

Declaration of Originality

This thesis is submitted to the University of Warwick in support of my application for the degree of Doctor of Philosophy. It has been composed by myself and has not been submitted in any previous application for any degree.
The work presented (including data gathered and data analysis) was carried out by the author except in the case outlined below:

The work Chapter 4 *Investigating nano-precipitation in a V-containing HSLA steel using small angle neutron scattering* was carried out in collaboration with Dr. Yiqiang Wang and Prof. Peter Lee of the University of Manchester, Prof. Graham McCartney of the University of Nottingham and Dr. Richard Heenan and Dr. Diego Alba Venero of the ISIS Neutron Source. In this work I contributed significantly throughout the process having co-authored the successful beam-time proposal, provided the samples, prepared and performed the experiments with Dr. Yiqiang Wang and made significant contributions to the final interpretation and analysis.

The Hot-Stage EBSD microscopy scans and TEM in Chapter 5 *Analysis of the extent of interphase precipitation in V-HSLA steels through in-situ characterization of the γ/α transformation* were co-performed with Dr. Vit Janik. The study design and all data post-processing, analysis and interpretation was performed by myself.

The work in Chapter 7 *Phase-Field Model Investigations of the Role of Elastic Strain Energy During the Growth Interphase Precipitates* was carried out in collaboration with Dr. Alireza Rahnama of the University of Warwick. Dr. Rahnama co-developed and ran the phase field simulations. In this work I

designed the study, co-developed the phase field model, its analysis and interpretation.

Parts of this thesis have been published by the author in the following journal articles:

- **S. Clark**, V. Janik, Y. Lan, S. Sridhar, Interphase Precipitation – An Interfacial Segregation Model, ISIJ Int. 57 (2017) 524–532. doi:10.2355/isijinternational.ISIJINT-2016-544.
- **S.J. Clark**, V. Janik, R.A. Rijkenberg, S. Sridhar, Analysis of the extent of interphase precipitation in V-HSLA steels through in-situ characterization of the γ/α transformation, Mater. Charact. 115 (2016) 83–89. doi:10.1016/j.matchar.2016.03.021.
- **S. Clark**, Y. Lan, V. Janik, R.A. Rijkenberg, S. Sridhar, In-Situ Characterisation of Austenite/Ferrite Transformation Kinetics and Modelling of Interphase Precipitation Inter-Sheet Spacing in V Microalloyed HSLA Steels, Mater. Sci. Forum. 879 (2017) 356–362. doi:10.4028/www.scientific.net/MSF.879.356.
- Y.Q. Wang, **S. Clark**, V. Janik, R.K. Heenan, D. Alba Venero, K. Yan, et al., Investigating nano-precipitation in a V-containing HSLA steel using small angle neutron scattering, Acta Mater. 145 (2018) 84–96.
- A. Rahnama, **S. Clark**, V. Janik, S. Sridhar, A phase-field model for interphase precipitation in V-micro-alloyed structural steels, Comput. Mater. Sci. 137 (2017) 257–265. doi:10.1007/s11661-001-0249-9.
- A. Rahnama, **S. Clark**, V. Janik, S. Sridhar, A phase-field model investigating the role of elastic strain energy during the growth of closely spaced neighbouring interphase precipitates, Comput. Mater. Sci. 142 (2018) 437–443. doi:10.1016/j.commatsci.2017.09.053.

Abstract

This Thesis presents work undertaken in order to develop the fundamental understanding of nano interphase precipitation in steels.

Small angle neutron scattering (SANS) was employed to characterize the precipitates and their size distributions in an Fe-0.047C-0.2V-1.6Mn (in wt.%) alloy isothermally transformed at $700\ °C$ up to $600\ min$. Analysis suggested the major axis diameter increased from $18\ nm$ after $3\ min$ to $35\ nm$ after $600\ min$. The precipitate volume fraction correspondingly increased from 0.009 to 0.022 over the same period and number density fell from 2×10^{21} to $5 \times 10^{20}\ m^{-3}$.

In-situ Electron Dispersive Backscatter Diffraction (EBSD) and High Temperature Laser Confocal Microscopy (HT-CSLM) were applied to elucidate the influence of $\gamma \rightarrow \alpha$ transformation upon the extent of interphase precipitation. Analysis of the γ/α orientation relationship during cooling at 2 and $10\ °Cs^{-1}$ suggests the proportion of ferrite likely to hold interphase precipitation varies little with cooling rate. At cooling rates in excess of $20\ Ks^{-1}$, interphase precipitation is increasingly suppressed due to the Widmanstätten $\gamma \rightarrow \alpha$ transformation.

An analytical model is presented which suggests the inter-sheet spacing of interphase precipitates is controlled by a complex interplay between the interfacial energy and interfacial segregation. It is shown that the general trend of refining inter-sheet spacing with growing ferrite half-thickness can be well predicted.

The multi-phase field method, is used to investigate the pairing of interphase precipitates in micro-alloyed steels. Where only the interfacial energy is considered it is shown that this energy can lead to a neck between two

neighbouring precipitates. When both strain and interfacial energies act on the system, the bridge between the particles becomes stabilized.

A procedure for the 'layman' to optimise interphase precipitation in any given alloy is proposed. For the Fe-0.047C-0.2V-0.18Si-1.6Mn (in wt.%) alloy considered in this study specific recommendations of processing parameters are given.

Acknowledgements

I would like to thank my supervisors Prof. Sridhar Seetharaman and Dr. Vit Janik for all the help and guidance they provided throughout my studies. I would particularly like to thank Prof. Sridhar Seetharaman whose enormous knowledge and love of fundamental science has both inspired me and provided for endless debates and discussions. To Vit Janik not only for sharing his technical microscopy skills but also through our shared love of craft beer.

I would also like to thank the people that have collaborated with me in this study especially to Dr. Yiqiang Wang and Prof. Peter Lee whom I have worked with since the very beginning of this work. I would like to thank Prof. Graham McCartney both for the valuable insights and rigour he brought to my work but also the support advice about academic life he has given me in completing my Thesis and onwards into an academic career. To Tata Steel who contributed to the funding of this work and provided the materials and in particular to Dr. Yongjun Lan and my industrial supervisor Dr. Arjan Rijkenberg. I would also like to thank Dr. Alireza Rahnama whose immense knowledge of phase field modelling was invaluable for this work.

I would like to thank parents and grandparents who have given me endless support. To my brother Adam and my friends and colleagues Tazdin and Kateryna who have been the best company throughout. And finally, to my partner Delia Moldovan who tolerated me unconditionally during the final writing of this Thesis.

Preamble

Table of Contents

Table of Figures

Nomenclature

Symbol	Description	Chapters
$\Delta\rho_{mag}$	Magnetic component of the neutron scattering contrast	4
$\Delta\rho_{nuc}$	Nuclear component of the neutron scattering contrast	4
$\Delta\sigma_{pp}$	Yield strength contribution due to precipitates	2,4
$\alpha_{\alpha\beta}$	Grain boundary energy between different phases α and β.	7
$\gamma_{\alpha\beta}$	Interface width between different phases α and β	7
ϵ^{ij}	Total strain in directions i and j	7
ϵ_{α}^{*ij}	Eigenstrain in each respective phase	7
ϵ_{α}^{ij}	Total phase strain in directions i and j for phase α	7
$\bar{\eta}$	Scaled dilatational strain parameter	7
θ_1	The angle between the lowest mobility orientation of the γ/α interphase boundary and the γ grain boundary	2
θ_2	and the angle between lowest mobility orientation of the γ/c interphase boundary and the mobility orientation γ/α	2
$\mu_{\alpha\beta}$	Interfacial mobility matrix	7
$\vec{\mu}$	Chemical potential vector	7
ρ_0	Density	7
ρ_m	Magnetic scattering length density	4
ρ_p	Nuclear scattering length density	4
ρ_{Total}	Total dislocation density	2
$\sigma_c^{\gamma\alpha}$	Interfacial energy of the more coherent broad	2

	face of a pillbox nucleus	
$\sigma_i^{\gamma\alpha}$	Interfacial energy of the more incoherent riser of a pillbox nucleus	2
$\sigma^{\gamma\gamma}$	Interfacial energy of the austenite grain boundary	2
ϕ_i	Solute concentration	2
ϕ_α	Density of each respective phase	7
$\Delta\sigma_{Diss}$	Yield strength contribution due to dislocations	2
$\Delta\sigma_{GB}$	Yield strength contribution due to grain boundaries	2
$\Delta\sigma_{SS}$	Yield strength contribution due solid solution strengthening	2
$\Delta\rho$	Difference in the scattering length densities of the particle and the matrix	4
$\Delta\theta$	Misorientation from a defined orientation relationship	2,5
α	Phase i.e. austenite, ferrite or carbide precipitate	7
δ	Half interphase boundary thickness	6
η	Dilatational strain due to compositional change	7
θ	Angle between the normal to terrace plane and the broad face of a platelet precipitate	2
θ	Rotation angle about the axis $\hat{r}$	5
λ	Inter-sheet spacing of interphase precipitates	2,6
ν	Poisson's ratio	2
ρ	Rodrigues-Frank parameterization	5
σ	Dispersion parameter of the equatorial radii in model fitting	4
σ	Interfacial energy of the γ/α interphase boundary	2,6,7

φ	Angle between the normal to terrace plane and the slip plane in ferrite	2
ϕ	Angle between the scattering vector and the magnetic field	4
ω	Inter-particle spacing	2
A_C	Atomic mass of carbon	6
a_{crit}	Critical height of a successfully nucleated α super-ledge	2,6
A_{Fe}	Atomic mass of iron	6
A_M	Atomic mass of the carbide forming element M in an MC carbide	6
a	Precipitate radius of the large semi-axis	2,4
b	Average polar radii of ellipsoidal precipitates	4
b	Burgers vector	2,4
$\overrightarrow{c^0}_{\alpha\beta}$	Quas`i-equilibrium concentration	7
c_0	Stress free composition	7
C_1	Hall-Petch strengthening coefficient	2
C_2	Empirical constant for the Bailey-Hirsch relationship	2
C_3	Constant related to the geometry of the ledge nucleation mechanism	2
C_i	Solid solution strengthening coefficient for element i	2
C_α^{ijkl}	Hooke's matrix for each respective phase	7
$\vec{c}$	Component concentration	7
c	Half thickness of the plate or oblate spheroid	2
$\vec{\vec{D}}$	Diffusion matrix	7
D_C^γ	Diffusion coefficient of carbon in γ	6
D_i^α	Diffusion coefficient of element i in α	6

$D_i^{\alpha\alpha}$	Diffusion coefficient of element i in an α/α grain boundary	6
D_i^{γ}	Diffusion coefficient of element i in γ	6
$D_i^{\gamma\gamma}$	Diffusion coefficient of element i in an γ/γ grain boundary	6
D_i	Effective γ/α interphase boundary diffusion coefficient for element i	6
$\bar{d}$	Dimensionless spacing	7
d	Grain size in microns	2
ΔE_i	Half chemical potential difference of element i over the γ/α interphase boundary	6
E_i^0	Binding energy of the solute element i to the γ/α interphase boundary	6
f^{ch}	Chemical free energy density	7
f^{el}	Elastic energy density	7
f^{gb}	Grain boundary energy density	7
f_v	Volume fraction of precipitates	4
F	Total free energy	7
$F(q,r)$	The form factor for the particles of size and q the scattering vector	4
ΔG_{Diss}^{Total}	Total dissipation of Gibbs energy in the γ/α interphase boundary	6
ΔG_m^{diff}	Dissipation of Gibbs Energy due to the diffusion of substitutional alloying elements in the interphase boundary	6
ΔG_m^{frict}	Dissipation of Gibbs Energy in the interphase due to intrinsic interphase mobility	6
$\Delta G_m^{\gamma\to\alpha}$	Molar driving force for the $\gamma \to \alpha$ transformation	2,6
ΔG_v^{el}	Elastic strain energy associated with the nuclei	2

	formation	
G	Shear modulus	2,4
h_α	Factor dependent on the elastic properties of each individual phase	7
h	Precipitate aspect ratio	2
$I_{\alpha\gamma}$	Generalized curvature	7
I	SANS scattering intensity	4
i	Alloying element i.e. Mn, Si, V, ect….	6
J	Empirical constant for Orowan relationship	2
$\vec{\vec{k}}_{\alpha\beta}$	Generalized partition coefficient	7
K_{MC}	Solubility product for an MC carbide in γ	6
L_0	Half prior γ grain size	6
L	Average inter-particle spacing on the slip plane	2
L	Diffusion length of carbon ahead of the γ/α interphase boundary	6
$\vec{\vec{M}}$	Chemical mobility matrix	7
M_0	Pre-exponential γ/α interphase boundary mobility factor	6
M_m^{int}	Intrinsic γ/α interphase boundary mobility	6
M	Taylor factor	2
n_a	Number of precipitates per unit area pinning a boundary	2
n	Total number of alloying elements in the alloy	6
$N(r)dr$	The number density of particles with size between r and $r+dr$	4
P_z	Zener pinning force	2
P	Solute drag force	6
Q	Integrated small angle scattering	4
R_{g1}	Guinier radius	4

R_{g2}	Radius of gyration	4
R_{max}	Pseudo-Guinier radius	4
r_v	Equivalent volumetric radius of a precipitate	2
$\hat{r}$	Rotation axis	5
$\bar{r}$	Dimensionless radius	7
R	Disc radius	4
r	Precipitate radius	2,4
R	Universal gas constant	6
$R(q)$	Ratio between the nuclear and magnetic scattering intensities	4
S	Half α grain thickness	6
$\bar{t}$	Dimensionless time	7
T	Disc thickness	4
T	Absolute temperature	6
t	Time	6
$u_i^{\alpha 0}$	Chemical potential of element i with a mole fraction of X_i^{α} in α	6
$u_i^{\alpha\gamma}$	Chemical potential of element i on the α side of the γ/α interphase boundary	6
$u_i^{\gamma 0}$	Chemical potential of element i with a mole fraction of X_i^{γ} in γ	6
$u_i^{\gamma\alpha}$	Chemical potential of element i on the γ side of the γ/α interphase boundary	6
V_m	Molar volume of iron	2,6,7
v	Interface velocity	6
$V(r)$	The volume of a particle of size r	4
$w_{\alpha\beta}$	Dimensionless repulsive potential function between different phases α and β	7

X_C^0	Bulk carbon mole fraction	6
X_C^m	Mole fraction of carbon in the center of the γ grain	6
$X_C^{\alpha\gamma}$	Mole fraction of carbon on the α side of the γ/α interphase boundary	6
$X_C^{\gamma\alpha}$	Mole fraction of carbon on the γ side of the γ/α interphase boundary	6
X_i^0	Bulk mole fraction of alloying element i	6
X_i^α	Mole fraction of element i in forming α	6
$X_i^{\alpha\gamma}$	Mole fraction of element i on the α side of the γ/α interphase boundary	6
X_i^γ	Mole fraction of element i in forming γ	6
$X_i^{\gamma\alpha}$	Mole fraction of element i on the γ side of the γ/α interphase boundary	6
$X_i(x)$	Mole fraction of element i in the interphase with respect to distance from the center of the interphase boundary x	6
X_M^0	Bulk mole fraction of the carbide forming element M in an MC carbide	6
$X_M^{\gamma\alpha}$	Mole fraction of the carbide forming element M in an MC carbide on the γ side of the γ/α interphase boundary	6
x	Outer cut-off radius of the precipitate	2
X	Carbon consumption parameter	6
x	Distance from γ/α interphase boundary center	6
y	C/M ratio in an MC carbide precipitate	6

Abbreviations

AHSS – Advanced High Strength Steel

ACV – Alloy Contrast Variation Method

APT – Atom Probe Tomography

DP – Dual Phase Steel

EBSD – Energy Dispersive Backscatter Diffraction

FIB – Focussed Ion Beam

HSLA – High Strength Low Alloy Steel

HT-CSLM - High Temperature Laser Confocal Microscopy

IP - Interphase Precipitation

IPC – Curved Interphase Precipitation

IPF – Fibrous Interphase Precipitation

IPP – Planar Interphase Precipitation

KS-OR - Kurdjumov-Sachs Orientation Relationship

NW-OR – Nishiyama-Wasserman Orientation Relationship

OECD - Economic Co-Operation and Development

OR – Orientation Relationship

SAS – Small Angle Scattering

SANS – Small Angle Neutron Scattering

SAXS – Small Angle X-ray Scattering

SEM – Scanning Electron Microscopy

TEM – Transmission Electron Microscopy

TRIP – Transformation Induced Plasticity

XPF – Extra Process Formability

1. Introduction

1.1. General Introduction

Steel is often stated to be the 'gold standard' against which structural materials are compared [1]. Table 1.1-1 shows that the global annual production of steel is only second in tonnage to concrete. Steel production and use, however, dwarfs that of other metals, for example, aluminium. H.K.D.H. Bhadeshia and R.W.K. Honeycombe stated that *"One reason for the overwhelming dominance of steel is the endless variety of microstructures and properties that can be generated by solid-state transformation and processing*" [1].

Table 1.1-1 Useful numbers for key materials (taken from Allwood et al. [2])

Material	Global Annual Production (Mt)	Energy Intensity (GJ/t)	Carbon Intensity (tCO_2/t)
Cement	2,800	5	1
Steel	**1,400**	**35**	**3**
Plastic	230	80	3
Paper	390	20	1
Aluminium	70	170	10

Steel is essential to virtually all industrial sectors: automotive, construction, mechanical engineering, shipbuilding, household appliances, and consumer electronics. Figure 1.1-1 shows a breakdown of the steel product catalogue. Steel usage in construction dominates over all other sectors combined, however, the sector where the full variety of microstructures and properties are used is transport. Based on 2008 data transport applications which are composed of cars, light trucks, heavy trucks and ships accounted for 12% of all steel usage.

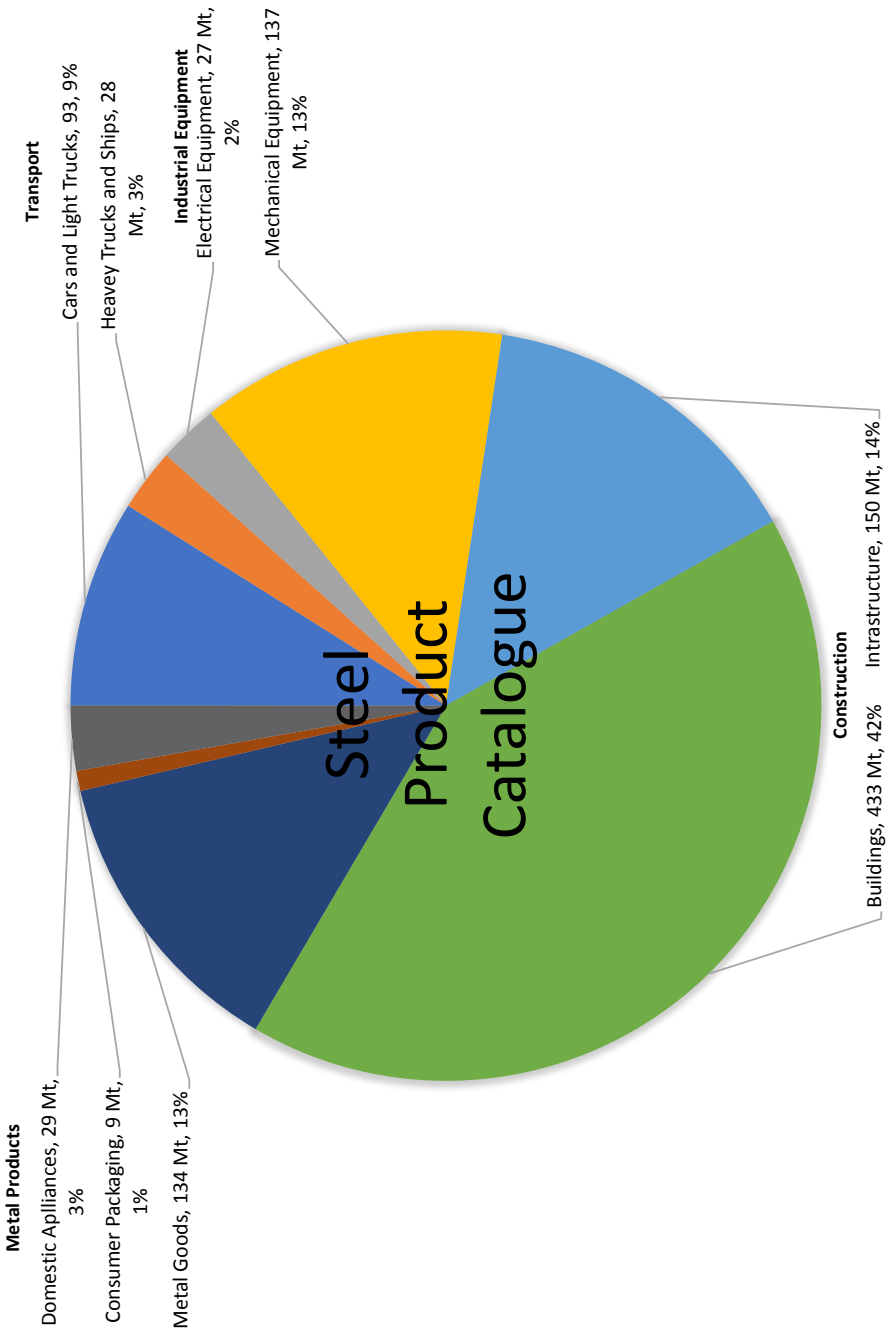

Figure 1.1-1 The steel product catalogue based on 2008 data published in Allwood et al. [2]

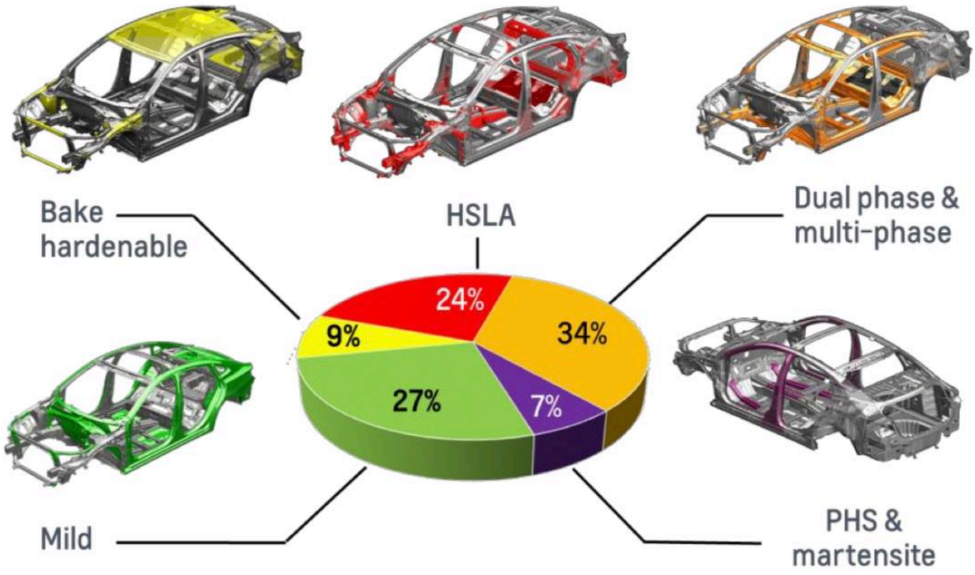

Figure 1.1-2 Steel usage by grade in a modern family automobile (GM Chevrolet Malibu 2016 taken from Swartzell [3])

According to 2016 Worldsteel Association figures [4], on average, 900 kg of steel is used per vehicle. Of this 34% is used in the body structure, 23% is in the drive train and 12% is in the suspension system. There are also smaller contributions found in the wheels, tyres, fuel tank, steering and braking systems. Figure 1.1-2 shows the percentage of different automotive steel grades within a modern family automobile body structure.

Increasingly stringent environmental regulations, however, are a powerful driver for manufacturers within the automotive industry to strive for lightweight solutions for automotive body and chassis applications. Current European Union legislation for passenger automobiles stipulates the reduction of CO_2 emissions by 18% and 40% by 2015 and 2021 respectively, compared to a baseline in 2007 [5]. This must be achieved without compromising passenger safety. The leading consultancy McKinsey & Company suggested that requirement of increasingly lightweight solutions would lead the automotive industry to follow the path of the aviation industry and adopt the widespread use of composite materials such

as carbon fibre [6]. It was suggested, the use of a one-piece carbon fibre car fender instead of a four-piece metal part would unlock the potential for a 30% percent weight reduction and a 60 percent reduction tooling cost. Over the past 20 years, the steel industry has responded to this challenge [7–9] by developing Advanced High Strength Steels (AHSS), both in their hot-rolled as well as cold-rolled and annealed product offerings.

Full life cycle assessments are required in order for automotive manufacturers to determine the optimal material for constructing assemblies such as the body-in-white. Mayyas *et al.* [10], performed an extensive study the results of which are shown in Figure 1.1-3. Comparing the different material options aluminium and magnesium intensive body in white are found to result in the lowest energy consumption over the entire life of the vehicle (200,000 miles). However, if the lifetime decreased to around 50,000 miles, the baseline steel and Advanced High Strength Steel (AHSS) result in the greatest savings in energy and CO2 emissions.

a

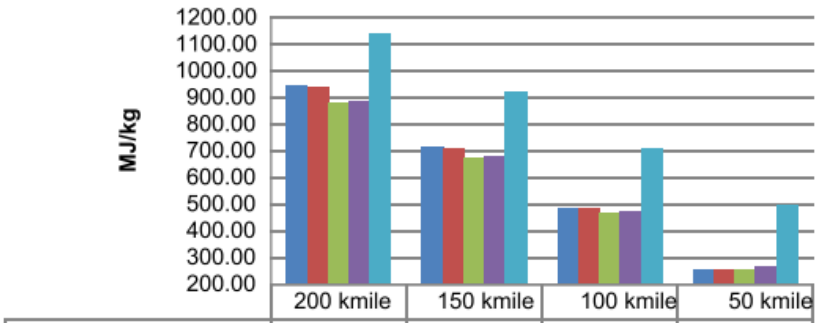

	200 kmile	150 kmile	100 kmile	50 kmile
Baseline BIW	945.35	715.84	486.32	256.80
AHSS BIW	937.40	710.02	482.63	255.25
Al-intensive BIW	881.78	673.39	465.00	256.62
Mg-intensive BIW	886.29	679.39	472.50	265.60
Composite intensive BIW	1137.88	924.49	711.11	497.73

b

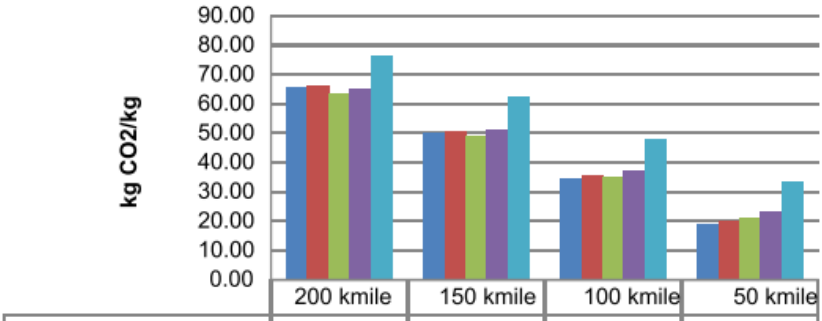

	200 kmile	150 kmile	100 kmile	50 kmile
Baseline BIW	65.68	50.15	34.62	19.09
AHSS BIW	66.09	50.71	35.32	19.94
Al-intensive BIW	63.18	49.08	34.98	20.88
Mg-intensive BIW	65.27	51.27	37.27	23.28
Composite intensive BIW	76.55	62.11	47.68	33.24

Figure 1.1-3 (a) Total life cycle energy analysis values for different BIW options (different estimated lifetimes); (b) Total life cycle CO2 emission analysis values for different BIW option (different estimated lifetimes) (taken from Mayyas et al. [10]).

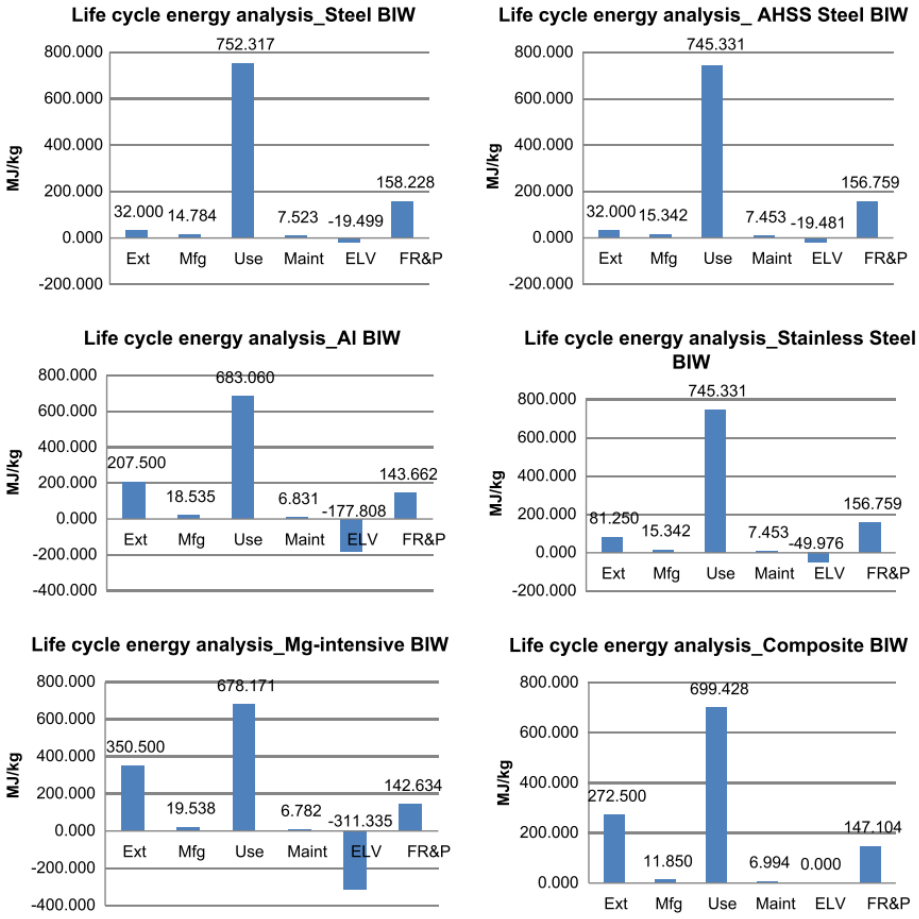

Figure 1.1-4 (a) Total life cycle energy analysis values for different BIW options (different estimated lifetimes); (b) Total life cycle CO2 emission analysis values for different BIW option (different estimated lifetimes) (taken from Mayyas et al. [10]).

Despite the apparent availability of more favourable materials considering the full lifespan of the vehicle steels retain a dominant position in the market to date. The reason for this can be understood through considering the embodied energy which is defined as 'the energy associated with the production of a good or service' [11]. Considering just the material extraction and production phase energy (Ext) and manufacturing phase energy in Figure 1.1-4 it is evident that the embodied energy associated with the production of the vehicle is significantly lower in the cases of the baseline steel case and the AHSS. Considering that one of the principal areas of competition between automotive manufacturers is the

price of their product the lower embodied energy/cost in steel use remains attractive despite the potential savings to the owner or multiple owners of the vehicle over its entire lifespan. This is a finding supported by a review of 43 life cycle analyses performed by Kim and Wallington [12] which concluded that replacing conventional materials such as; steel and iron with lighter alternatives e.g. aluminium, magnesium, and composites the energy consumption and greenhouse gas emissions during vehicle use are decreased. However, the use of such lightweight materials increases energy consumption and greenhouse gas emissions during vehicle production.

Typically, AHSS steels rely upon complex multi-phase microstructures as shown in Figure 1.1-5, which result in excellent strength and formability. However, these steels are compromised by insufficient stretch-flange formability. Increased formability is highly desirable for automotive manufacturers reducing manufacturing costs and complexity. For example, typical dual-phase, DP and transformation-induced-plasticity, TRIP or TRIP-assisted steels have low yield ratios, which makes them unfavourable for roll-forming applications.

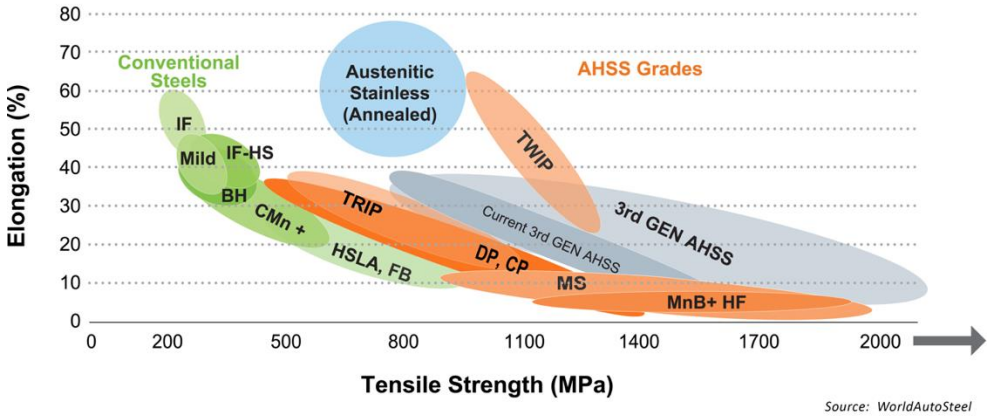

Figure 1.1-5 A strength-ductility diagram illustrating an overview of current AHSS grades (taken from World Auto Steel [13]).

In response to the relatively low stretch-flange formability of conventional AHSS grades and to offer attractive alternatives for roll-forming applications in the

strength region typically dominated by AHSS, an expansion of the present cold-rolled and annealed High Strength Low Alloy (HSLA) product offering is considered. HSLA steels with a single-phase ferritic microstructure and corresponding high yield ratio offer an attractive and promising solution. The extension of the current cold-rolled HSLA steel range by introducing the cold-rolled high-formability XPF, eXtra Processing Formability, product range within Tata Steel (Figure 1.1-6). The XPF grades of steels offer further advantages over conventional AHSS grades through minimising the use of costly alloying elements.

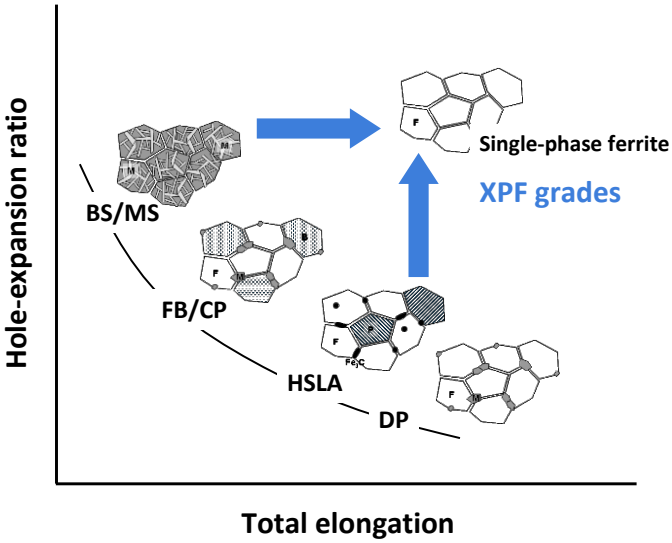

Figure 1.1-6 A schematic diagram showing hole expansion ratio against elongation, illustrating the benefit of single-phase XPF over multi-phase AHSS hot-rolled steels (taken from Rijkenberg et al. [5]).

The principal purpose of this study was to further develop the fundamental understanding required for bridging the gap for development of cost-effective novel hot-rolled and cold-rolled annealed high-strength steels. High-strength yet formable steels, known as nano-steels have been produced which exploit the formation of nano-sized carbide precipitates in regular arrays through the mechanism of interphase precipitation (IP) [14]. The phenomena, whilst having been studied extensively for over 50 years, remains to be comprehensively

understood. It is, therefore, likely that there remains significant untapped potential for further exploitation for novel optimal nano-steels.

The formation of interphase carbides is well established to be directly coupled to the formation of ferrite, α, during the decomposition of austenite, γ. The coupled nature of the process of interphase precipitation renders it difficult to study fundamentally as it is impossible to isolate variables relating to the micro-scale growth kinetics of α, the nano-scale morphology kinetics of the γ/α interphase boundary and the nucleation of carbides at the interphase boundary. This fundamentally limits what can be elucidated through traditional *a posteriori* characterisation techniques. In this work, powerful high-resolution, *in-situ* characterisation will be coupled with traditional *a posteriori* characterisation along with advanced bulk characterisation of the nano-scale features to partially resolve this difficulty by exploring the coupled and transient nature of the interphase precipitation processes.

The results of this characterization work are critical as they are a prerequisite for the development of modelling approaches with predictive capability of precipitation strengthening and in designing suitable thermomechanical processing schedules for optimal material production. To this extent, this study endeavours to develop new models for the prediction of the evolution of inter-sheet-spacing and nature of interphase carbides and in multi-component industrially applicable alloys that are validated for the first time by application of novel *in-situ* or *quasi-in-situ* characterisation techniques such as HT-CLSM, SANS and HT-EBSD.

This thesis forms part of a project related to efforts within Tata Steel R&D to pursue new product concepts in the area of a new range of hot-rolled and annealed HSLA with increased tensile strength. These new grades will rely on

precipitation hardening and will require alternative exploitation of precipitation hardening than conventional HSLA.

1.2. Thesis Structure

This thesis is divided into 9 chapters as described below:

1) The general introduction as given above.
2) A comprehensive literature review concerning the principal strengthening mechanisms in steels is presented. The current understanding of the strengthening potential and underlying fundamental mechanisms behind the phenomenon of interphase precipitation in ferrous alloys is identified. Gaps in the literature and unanswered questions are identified where further work is required.
3) A chapter outlining the objectives and hypothesis of this thesis based upon the unanswered questioned proposed in the literature review.

These introductory chapters are followed by 4 self-contained chapters which each individually contain a concise introduction, experimental methods and model proposition (where appropriate), results and discussion and finally concluding remarks.

4) An investigation of the Interphase precipitation (IP) of nanoscale carbides in a vanadium-containing high-strength low-alloy steel. Small angle neutron scattering (SANS) and transmission electron microscopy (TEM) were employed to characterize the precipitates and their size distributions. Model-independent analysis of the nuclear SANS signal and model fitting calculations, using oblate spheroid and disc-shapes.
5) An investigation utilizing *in-situ* characterization techniques has been applied to elucidate the influence of $\gamma \rightarrow \alpha$ transformation upon the extent of interphase precipitation in a low-carbon, vanadium-HSLA steel. Electron Back-scattered diffraction analyses of the γ/α orientation relationship with continuous cooling at 2 and $10\ Ks^{-1}$.
6) An analytical model is proposed which predicts the evolution of inter-sheet spacing of *MC* carbides during the $\gamma \rightarrow \alpha$+*MC* transformation. It is

suggested the evolution of inter-sheet spacing can be explained considering the interfacial segregation and the corresponding dissipation of Gibbs energy inside the moving interphase boundary.

7) A multi-phase field model is developed to investigate the effects of transformation strain on the transformation kinetics, thermodynamic stability and pairing of interphase precipitates in micro-alloyed steels.
8) An overarching discussion linking the findings of the previous chapters and a series of 'layman's' recommendations for how to optimise interphase precipitation.
9) A summary of the principal conclusions determined throughout the course of this thesis and suggestions for further work.

2. Literature Review

The development of new hot-rolled high-strength formable steels offering innovative light-weight solutions to reduce vehicle weight is crucial for automotive designers to improve fuel economy without compromising safety, performance or manufacturability. This focus extends to the chassis system, where hot-rolled Advanced High Strength Steels (AHSS) with increased strength and improved stretch-flange formability over conventional High Strength Low Alloy (HSLA) steels are increasingly used. However, the advent of ever more demanding light-weight chassis designs requires that any intrinsic loss in stiffness due to down-gauging with higher strength steels is compensated with increased structural stiffness derived from geometrical optimization [15]. This challenge requires hot-rolled high-strength steels offering an unsurpassed freedom in design derived from a balance between stretch-ability and stretch-flange formability that is superior to that of highly alloyed AHSS typically used for chassis applications [16].

The principal purpose of this study is to develop the fundamental understanding required for bridging the gap for development of cost-effective novel hot-rolled and cold-rolled annealed high-strength steels. In the following section, a comprehensive review of the literature is undertaken to establish the *state-of-the-art* of the current understanding and to identify gaps inhibiting the development of new advanced high-strength steel products. This review shall outline the principle strengthening mechanism's in steels identifying the mechanisms most appropriate for exploitation.

2.1. Strengthening Mechanisms in Steels

2.1.1. Solid Solution Strengthening

The addition of given concentrations ϕ_i of individual additional alloying elements in solid solution can induce strengthening of a microstructure through several mechanisms as reviewed by Gladman [17]. It is typically found that the solid solution strengthening due to substitutional atoms bound to dislocations, contribute to the yield strength, $\Delta\sigma_{SS}$, as the sum of contributions of n individual components and thus correlate linearly with the concentrations, ϕ_i. The total magnitude $\Delta\sigma_{SS}$ as a result of several alloying elements within a given system can therefore be determined by their linear algebraic summation as shown in Equation (2.1-1)

$$\Delta\sigma_{SS} = \sum_{i=0}^{i=n} \phi_i C_i$$

(2.1-1)

Experimental evaluations of solid solution strengthening coefficients C_i of ferritic α iron have been undertaken in studies such as Pickering [18]. Gladman [17] compiled the results of several studies, the compilation of solid solution strengthening coefficients are shown in Table 2.1-1.

Table 2.1-1 Solid solution strengthening coefficients per wt.% and at.% for α iron (taken from Gladman [17])

	(C,N)	**P**	**Sn**	**Si**	**Cu**	**Mn**	**Mo**	**Ni**	**Cr**
$C_i/wt\%[MPa]$	4620-5544	678	123	83	39	31-32	11	0	-31
$C_i/at\%[MPa]$	990-1188	384	262	42	44	31-32	18	0	-29

2.1.2. Grain Boundary Strengthening – The Hall-Petch Relationship

The collaborative studies of Hall [19] and Petch [20] elucidated the effect of grain size upon the strengthening of a matrix yielding the relationship known as the Hall-Petch equation (2.1-2).

$$\Delta\sigma_{GB} = C_1 d^{-\frac{1}{2}}$$

(2.1-2)

Where C_1 is a constant and d is the grain size in microns. Several studies have experimentally evaluated C_1 in α iron with an average value similar to the theoretical evaluation of Dingley and McLean [21], $C_1 = 219\ MPa\ \mu m^{-\frac{1}{2}}$. While steel chemistry does not appear explicitly in equation 2.1-2, the grain size is influenced by chemistry due to recrystallization temperature, grain boundary mobility etc.

2.1.3. Dislocation Strengthening- The Bailey Hirsch Relationship

Dislocation strengthening is caused, essentially by the entanglement and reduced mobility caused by increasing dislocation density. Bailey and Hirsch [22] derived the following relationship for the strengthening contribution attributed to dislocations:

$$\Delta\sigma_{Diss} = C_2 M G b \rho_{Total}^{\frac{1}{2}}$$

(2.1-3)

Where M is the Taylor factor ($M = 2.75$ in α iron [23]), C_2 is a constant ($C_2 = 0.38$ in α iron [23]), G is the shear modulus ($G = 80.3\ GPa$ in α iron [17]) b is the magnitude of the Burgers vector ($b = 0.248\ nm$ in α iron [17]) and ρ_{Total} is the total dislocation density ($10^{12} \leq \rho_{Total} \leq 10^{14}$ dependent on level

of hot deformation [24]). While steel chemistry does not explicitly appear in Equation 2.1-3, the grain boundary mobility may be affected by stacking fault energy which is compositionally dependent.

2.1.4. Precipitation Strengthening - The Orowan and Ashby-Orowan Relationships

Precipitation strengthening is caused by 2nd phase particles that inhibit the movement of dislocations. In steels precipitation strengthening is often achieved by the addition of small quantities of strong carbo-nitride forming micro-alloying elements such as V, Nb or Ti [17] however, in steels for particularly high temperature applications oxide particles may be used [25]. Matrix strengthening precipitates may adopt many morphologies dependent upon their location within the microstructure and vary in morphology as they grow. Table 2.1-2 shows a selection of the diverse range of morphologies for precipitates of which Ti is a major constituent that have been reported in ferritic steels.

Table 2.1-2 Selection of the diverse reported morphologies precipitates in Ti-alloyed ferritic steels

Reference	Size Range nm	Morphology	Location	Composition
Charleux *et al.* [26]	200 - 2000	Square or polyhedral	random	TiN
Charleux *et al.* [26]	7 - 12	Spherical	grain or subgrain boundaries	Nb + Ti (Nb/TiC)
Charleux *et al.* [26]	Length 3 – 6 Diameter 0.7 – 0.9	Needlelike	on dislocations in grains with high dislocation density	Nb + Ti (Nb/TiC)
Charleux *et al.* [26]	3 - 5	Spherical	in grains with low dislocation density	Nb + Ti (Nb/TiC)
Wei *et al.* [27]	Thickness > 20 Diameter > 60	Disc	Random in grains	TiC
Wei *et al.* [27]	Thickness < 20	Platelet	Random in grains	TiC

	Diameter < 60			
Yen *et al.* [28]	Diameter 15 - 25	Disc	Periodic rows (interphase precipitates) in grains	TiC
Yen *et al.* [28]	Diameter < 15	Platelet	Periodic rows (interphase precipitates) in grains	TiC
Yen *et al.* [29]	Length 4.5 – 6 Aspect ratio 0.9 – 1.2	Platelet	Periodic rows (interphase precipitates) in grains	(Ti,Mo)C

The relationship between precipitation and its associated strengthening component $\Delta\sigma_{pp}$ was proposed by Orowan [30], where L is the average inter-particle spacing on the slip plane. J is a correction coefficient which has been evaluated using computational studies of dislocation ensemble movement through random arrays of obstacles, Kocks [31] suggested $J = 0.84$ whereas Foreman and Makin [32] suggested a value of 0.81.

$$\Delta\sigma_{pp} = \frac{JMGb}{L}$$

(2.1-4)

Ashby [33] later improved Orowan's initial proposition in order to account for the surface-to-surface inter-particle spacing rather than the centre-to-centre considered by Orowan. Where ν is the Poisson's ratio of the matrix phase ($\nu = 0.2888$ [34]) and x is the outer cut-off radius of the precipitate. Ardell [35] showed that in the case of spherical precipitates $x = \frac{\pi}{4}r$ where r is the radius of the precipitate.

$$\Delta\sigma_{pp} = \frac{JMGb}{2\pi(1-\nu)L}\ln\left(\frac{x}{b}\right)$$

(2.1-5)

It has been stated that experimentally observed precipitation strengthening in micro-alloyed steels have shown excellent correlation with the predictions of the Ashby–Orowan relationship (2.1-5) [36].

2.1.5. Relative importance of Individual Strengthening Contributions

In the latest generations of advanced steels [14,37–39] exploiting nano interphase precipitation, alloyed with combinations of Ti, Mo, and V, exhibit yield strengths from $500\,MPa$ to $1\,GPa$ [40]. These yield strengths can be achieved through precipitate core-shell nano-precipitate structures which inhibits particle coarsening, thus enhancing the material's strength [41]. An indication of the relative contribution of precipitation strengthening to the other strengthening mechanisms in a modern 'nano steel' is shown in Figure 2.1-1.

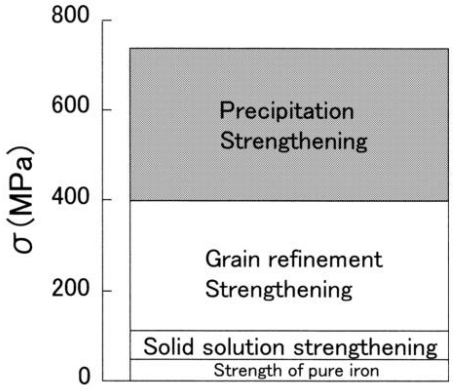

Figure 2.1-1 Increased importance of precipitation strengthening in new, innovative 'nano-steels' (taken from Funakawa et al. [42])

In the literature there has been some controversy as to how individual strengthening mechanisms should be summed. Gladman [17] in 'The Physical Metallurgy of Microalloyed Steels' suggested the use to the linear algebraic sum of the individual strengthening mechanisms. Foreman and Malkin [43] however, suggested that the Pythagorean sum of the strengthening mechanisms due to

dislocation interactions with a combination of strong and weak obstacles should be used as per the flowing equation:

$$\sigma = \sigma_0 + \Delta\sigma_{SS} + \Delta\sigma_{GB} + \sqrt{\Delta\sigma_{Diss}{}^2 + \Delta\sigma_{pp}{}^2}$$

(2.1-6)

Where, σ is the yield strength and σ_0 is the friction stress. Both the aforementioned approaches have been used recently in the literature with the linear algebraic sum being used by Kamikawa *et al.* [44] and the Pythagorean sum being used by Charleaux *et al.* [26], Yen *et al* [29], Chen *et al.* [45] and a more recent study by Kamikawa *et al.* [46].

2.2. Experimental Observations on Interphase Precipitation

In steels alloyed with a strong carbide forming element M, where (M= Nb, Ti, V, Cr Mo etc.) a phenomenon known as interphase precipitation (IP) can be observed under suitable processing conditions. V alloyed steels are often selected as an interphase precipitate because the solubility product of VC in austenite is much larger than that of TiC or NbC [17]. The earliest investigations of the phenomenon of interphase precipitation appear in 1964 in the studies by Mannerkoski [47] and Relander [48]. This was followed by a series of pioneering investigations over 20 years by Honeycombe and co-workers [49–59] and since then it has become widely accepted that in IP rows of carbide precipitates form at the moving interphase boundary between austenite γ and ferrite α [60].

Two in-depth reviews have been published on the topic of interphase precipitation by Honeycombe [60] as the R. F. Mehl Medallist at the 1976 Institute of Metals Lecture The Metallurgical Society of AIME and again at the 29th Hatfield Memorial Lecture in 1980 [61]. In addition, several noteworthy introductory sections have provided additional updated reviews of the topic such as Abara [62], Li and Todd [63], Smith and Dunn [64] and Yen et al. [29].

Smith and Dunne [64] reviewed the morphologies of interphase precipitate distributions in steels in 1988, identifying the following 5 categories:

1) *Planar rows of discrete precipitates (IPP)* – Davenport and Honeycombe [52], investigated planar interphase precipitation where precipitates form in distinct planar arrays, as shown in Figure 2.2-1 (a). Upon each respective plane of interphase precipitates the particles are randomly distributed, as shown in Figure 2.2-1 (a) (b-c).
2) *Curved rows of coarse discrete precipitates (IPC-irregular)* – Campbell and Honeycombe [54] observed coarse and irregularly spaced curved arrays of interphase precipitates.

3) *Curved rows of fine discrete precipitates (IPC-regular)* – In contrast to the above, curved arrays of interphase precipitates have also been observed by Ricks and Howell [65,66] to be fine and regular.
4) *Random (IPR)* – Smith and Dunne [64] identified that in each of the above under the condition where the inter-sheet spacing of interphase precipitates is roughly equal to the inter-particle spacing on the plane of precipitates the precipitates would appear, at least locally, to be randomly distributed.
5) *Fibrous (IPF)* – Berry and Honeycombe [50] in highly alloyed steels (Fe-4wt%Mo-0.2wt%C). The fibrous morphology occurred with an inter-sheet spacing of $30 - 50\ [nm]$, an order of magnitude finer than a pearlitic microstructure within the same temperature range.

In addition, this literature review has identified an additional interphase precipitate distribution morphology:

6) *Coupled Interphase and pearlite precipitation (IP-pearlite)* – Dunlop *et al.* [67] investigated the occurrence of interphase precipitation in between pearlite lamellae in a (Fe-0.45wt%C-1wt%Mn-0.01wt%V).

As identified in Section 2.1.5 to achieve optimal strengthening in steels via precipitation strengthening precipitates must be as numerous and as fine as possible. Therefore, in the industrial perspective the two most significant interphase precipitate distribution morphologies are, planar interphase precipitation 1) (*IPP*) and 2) regular finely spaced curved arrays of interphase precipitates (*IPC-regular*).

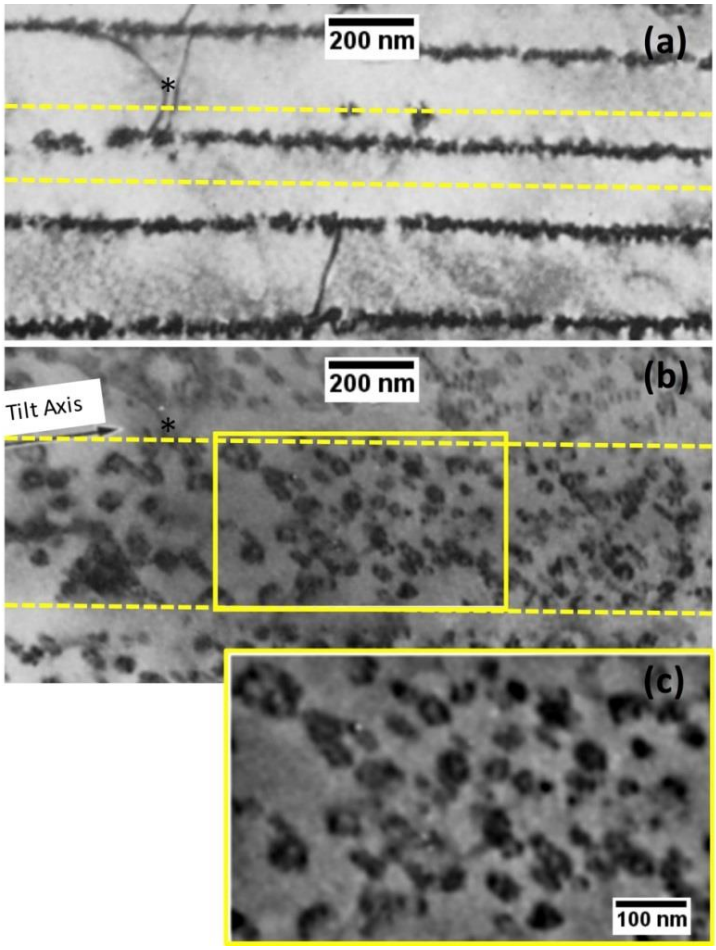

Figure 2.2-1 Typical interphase precipitation a) inter-sheet spacing, b) rows rotated such that individual precipitates on a row can be resolved and c) an expanded subsection of b) after Davenport and Honeycombe [52]

2.2.1. Strengthening Potential of Interphase Precipitation

The matrix strengthening contribution due to Interphase Precipitation IP has in many previous studies been predicted using the Ashby-Orowan Equation (2.1-5), achieving, in many circumstances a good agreement between predicted and measured strengthening values [42,44,46,68,69]. It should be noted that the Ashby-Orowan Equation (2.1-5) strictly considers the distribution of precipitates to be random. In the case of interphase precipitation, the precipitates are neither randomly arranged nor completely regular array. Batte and Honeycombe [53] explored the influence of the non-random nature of the IP dispersions and derived several equations for the effective inter-particle spacing L. Batte and

Honeycombe [53] found that even with their modification of the Ashby-Orowan equation for interphase precipitation the predicted strengthening potential considerably over-predicted that of measured yield strengths. Yen *et al.* [29] and Chen *et al.* [45] have recently used effective inter-particle spacing L derived by Batte and Honeycombe [53], achieving a good correspondence between measured and predicted strengthening.

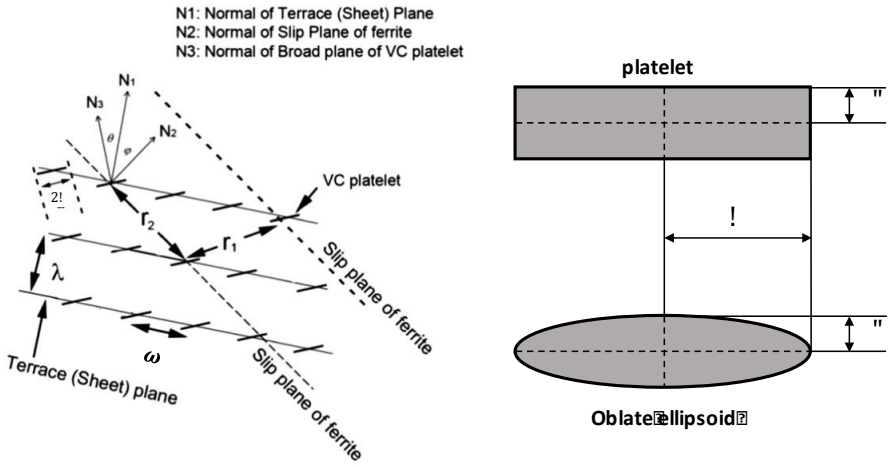

Figure 2.2-2 A schematic diagram showing the orientations of the sheet plane, the slip plane in the ferrite matrix, and the broad planes of carbides (adapted from Chen et al.[45])

Although Batte and Honeycombe [53] considered plate-shaped precipitates, due to the similarity of plates and oblate spheroids this analysis should be approximately valid for the latter morphology. In both cases the aspect ratio h can be defined by the following equation:

$$h = \frac{c}{a}$$

(2.2-1)

where a is the radius of the large semi-axis and c is the half thickness of the plate or oblate spheroid. The effective inter-particle distance can be expressed as:

$$L = \sqrt{r_1 r_2}$$

(2.2-2)

Where r_1 is the average inter-particle spacing along the intersection between the slip plane of ferrite and the IP sheet plane. r_2 is the average value of the precipitate spacing along the ferrite slip plane. r_1 and r_2 can be computed from the following equations using the parameters described in Figure 2.2-2.

$$r_1 = \frac{\omega^2}{2a} + \frac{\pi a}{2} - \frac{ah}{\sin(\theta)}, \qquad r_2 = \frac{\lambda - 2a\sin(\theta)}{\sin(\varphi)}$$

(2.2-3)

In a bcc crystal structure, the slip surface may in fact be a series of segments of the $(1,1,0)$, $(1,1,2)$, and the $(1,2,3)$ planes rather than a unique plane considered in (2.2-3). However, Batte and Honeycombe [53] resolved since the geometric constructions are similar in the cases of all three planes the simplification in (2.2-3) minimally influences the results obtained.

Yen *et al.* who considered (Ti,Mo)C platelet precipitates, reported $\frac{1}{\sin(\varphi)} = 3$ and $\frac{1}{\sin(\theta)} = 1.73$. Batte and Honeycombe [53] who considered VC platelet precipitates reported $\frac{1}{\sin(\varphi)} = 3.72$ when $h = 0.2 \rightarrow \frac{1}{\sin(\theta)} = 3.5$ and when $h = 0.1 \rightarrow \frac{1}{\sin(\theta)} = 5.3$ respectively. In the case where $h \rightarrow 1$ the term $\frac{1}{\sin(\varphi)}$ becomes unity. Although there is a paucity of available data a tentative relationship between precipitate aspect ratio and $\frac{1}{\sin(\theta)}$ can be plotted as shown in Figure 2.2-3 considering a y-intercept at unity.

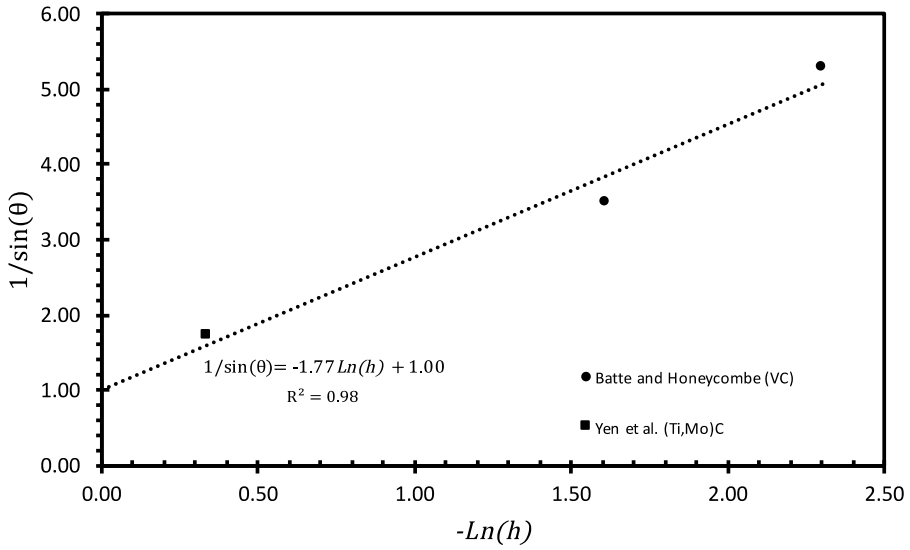

Figure 2.2-3 Relationship between precipitate aspect ratio h and $\frac{1}{sin(\theta)}$

Yen *et al.* [29] and Chen *et al.* [45] both substituted into equation (2.2-2) into the simple Orowan Equation (2.1-4). However, Ahmadi et al. [70] proposed in the case of non-spherical precipitates in FCC the outer cut-off radius x in the Ashby-Orowan equation (2.1-5) can be approximated by the Ardell equivalent radius [35] of a spherical precipitate with the same volume i.e.:

$$x = \frac{\pi}{4} r_v, \quad {r_v}^3 = a^2 c = a^3 h \ (Ellipsoid), \quad {r_v}^3 = \frac{3}{2} a^2 c = \frac{3}{2} a^3 h \ (\text{platelet})$$

(2.2-4)

2.2.2. Factors Influencing Interphase Precipitate Dispersions

1) Transformation temperature

Numerous studies such as [40,49–59,71–74] have elucidated that generally the lower the $\gamma \rightarrow \alpha$ transformation temperature the finer the inter-sheet spacing of interphase precipitates, λ. Relatively few studies have reported the spacing, ω, between particles on rows of interphase precipitates and only Yen *et al.* [29] has reported a unified data set of the inter-sheet/particle/particle dimensions, the results of which are shown in Figure 2.2-4 for a steel alloyed with Ti and Mo.

One can be critical of the postulated trend in Figure 2.2-4 (b) which shows the relationship between the inter-carbide spacing on a given IP sheet plane and the $\gamma \rightarrow \alpha$ transformation temperature. There is a large spread in the experimental data which was sparsely obtained from limited sample of 3 individual grains at each temperature interval. It could be argued that the data would be more justifiably stated as showing a mean inter-carbide spacing of $\approx 40\,nm$ with spacings being observed as small as $\approx 20\,nm$ and as high as $\approx 80\,nm$ over $620\,℃$ to $720\,℃$ temperature range. It should also be noted that these results suggest that IP are less densely packed on each IP sheet plane than the characteristic rows themselves in the perpendicular plane are spaced.

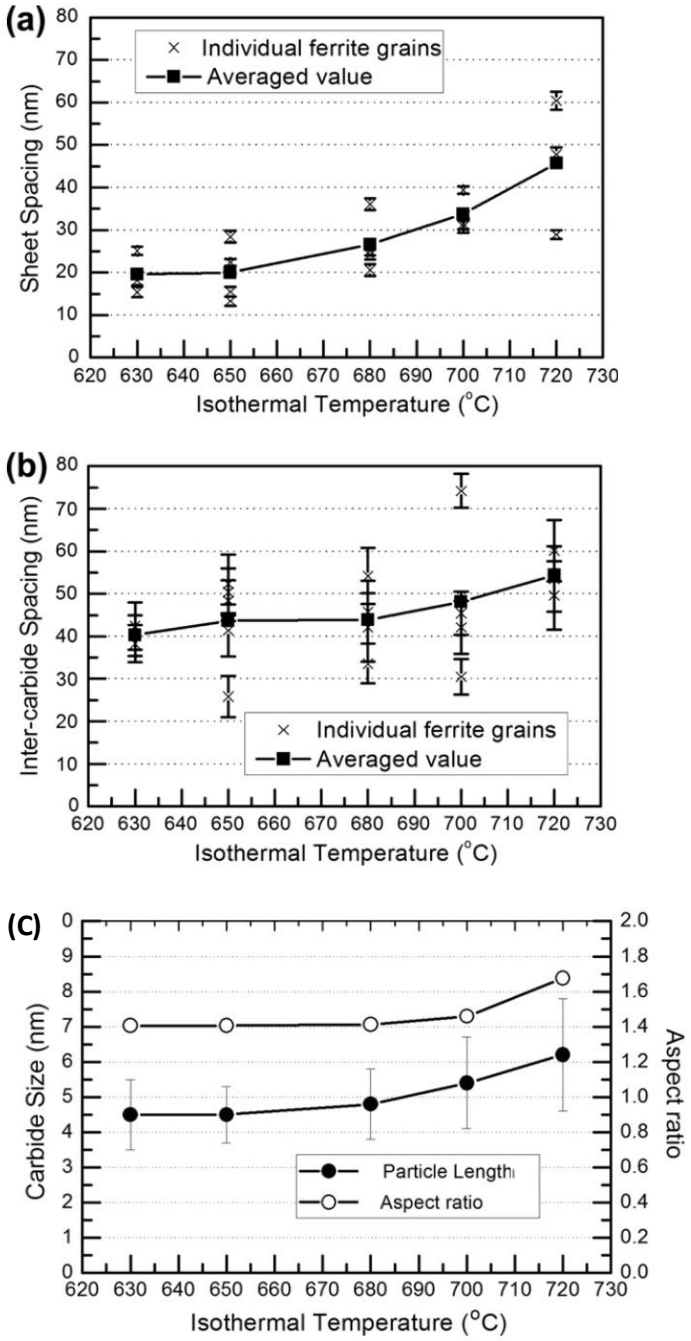

Figure 2.2-4 The variation of (a) inter-sheet spacing and (b) inter-carbide (inter-particle) spacing and (c) the carbide diameter and aspect ratio as a function of isothermal holding temperature (adapted from Yen et al. [29])

2) α growth rate

Gray and Yeo [75] showed that the inter-sheet spacing decreases with the progression of the austenite to ferrite transformation during continuous cooling.

This decreasing inter-sheet spacing, however, is the combined effect of ferrite growth rate and transformation temperature. Sakuma and Honeycomb [51] reported that the inter-sheet spacing was increased when Mn was added to a Nb micro-alloyed steel to slow down the austenite to ferrite transformation. Recent experimental studies have elucidated the periodicity of interphase precipitates; Murakami *et al.*[72] found that the inter-sheet spacing decreases as the interface velocity reduces during an isothermal transformation at 675 ℃.

As the diffusional controlled growth of allotriomorphic ferrite exhibits a parabolic growth rate, with the transformation becoming increasingly sluggish as the necessary diffusion distance of carbon increases, it follows that the inter-sheet spacing should refine as $\gamma \rightarrow \alpha$ transformation progresses. However, there has been very little experimental validation for this. A single study can be found in the literature where the inter-sheet spacing was characterised as a function of distance transformed from the prior austenite grain boundary (centre of ferrite) [72]. Figure 2.2-5 summarises the findings of Murakami *et al.*[72] who showed from a very limited sample, at a single transformation temperature and in a single alloy that the inter-sheet spacing of interphase carbides can refine. Okamoto *et al.* [71] conversely showed that in a Nb-micro-alloyed steel that the inter-sheet spacing as a function of distance from an arbitrary row varied very little. Taken together it appears the relationship between $\gamma \rightarrow \alpha$ transformation kinetics and inter-sheet spacing is complex and likely depends upon the alloy composition and thermal history.

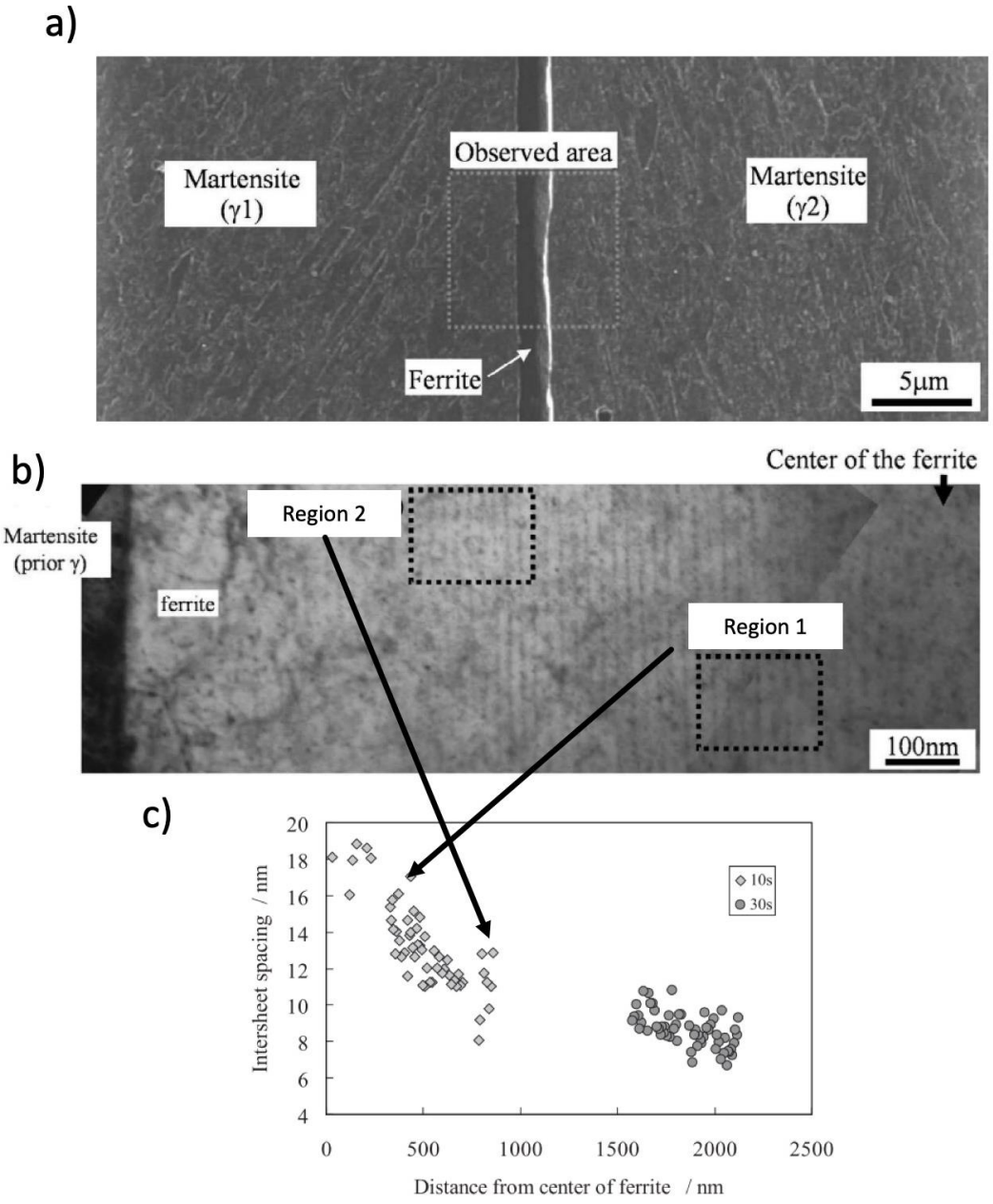

Figure 2.2-5 Experimental evidence for the refinement of inter-sheet spacing as the $\gamma \rightarrow \alpha$ transformation progresses (after Murakami et al. [72]).

3) *Carbide/matrix orientation relationship*

Baker and Nutting (BN) [76] established that V_4C_3 forms in supersaturated α as semi-coherent discs obeying a strict orientation relationship $(001)_\alpha \parallel (001)_{MC}, [110]_\alpha \parallel [010]_{MC}$ which has three variants. This orientation

relationship has since been found to hold for nearly all MC B1 (NaCl)-type carbides and nitrides precipitated in ferrite [77]. In the context of interphase precipitation, Davenport and Honeycombe [52] reported that vanadium carbide only obeys one of the three possible variants, the variant selected is the variant which enables the habit planes of all three planes to be parallel, this minimises the energy barrier for nucleation. Batte and Honeycombe [53] and recent studies by Okamoto *et al.* [71] and Yen *et al.* [29] have claimed that there are several preferred sheet planes for planar interphase precipitation rather than solely $[110]_{\alpha}$.

Recently, Yen *et al.* [29,78] have suggested that in the case of TiC precipitates (a previous study had found a similar effect in the cases of TiN and CrN [79]), whilst the precipitates are small they exhibit the BN orientation relationship, at the later stages of precipitate growth and during coarsening the precipitate matrix orientation relationship evolves from the BN orientation relationship towards the Nishiyama-Wasserman (NW) orientation relationship ($(0\ 1\ 1)_{\alpha} \parallel (1\ 1\ 1)_{MC}$, $[1\ 0\ 0]_{\alpha} \parallel [1\ \bar{1}\ 0]_{MC}$) [80,81]. This result is however in contradiction to other high-resolution transmission electron microscopy (TEM) studies where it has been found even in the case of large sized TiC particles an exact BN orientation relationship is observed with the ferrite matrix [27]. TiC precipitates formed in austenite before the transformation to ferrite have a cube-on-cube OR with austenite [82] upon transformation of austenite to ferrite the orientation relationship between the carbide and the ferrite would be dictated by the orientation relationship between the austenite and ferrite [83] which could explain an observed NW orientation relationship. Yen *et al.* [28] argued that this was not the case as only 2 variants of the NW orientation relationship were observed i.e. those which are closest related to the BN orientation relationship. Several recent atom probe tomography APT studies have suggested a coexistence between interphase precipitates and nano-clusters which have the

same crystal structure as the matrix which remains even after prolonged periods of ageing [84–86].

4) The effects of orientation γ/α orientation relationship

Obara *et al.* [62] using a procedure based on the classical experiment by Smith [87] where a partially transformed sample is deformed at room temperature then recrystallized at a transformation temperature. The procedure renders the γ/α interphase boundaries incoherent and disordered. Comparing undeformed and deformed samples Obara *et al.* [62] were able to draw the following conclusion in "the presence of at least some areas of partially coherent γ/α interphase boundary is a prerequisite for the nucleation of carbides at these boundaries in either the interphase boundary or the fibrous eutectoid structure configurations." The relative lack of interphase precipitation after the decomposition of deformed austenite compared to a undeformed control case was recently confirmed by Chih-Yuan *et al.* [88].

Recently Furuhara and co-workers [74,89,90] have investigated the influence of γ/α interphase boundary orientation relationship upon interphase precipitate dispersions. Partially transformed samples were created allowing the prior γ orientation to be reconstructed from the martensite formed on quenching. Figure 2.2-6 (a-d) shows a series of 3D atom probe tomography reconstructions depicting the influence of increasing γ/α misorientation $\Delta\theta$ from an ideal Kurdjumov-Sachs orientation relationship. Figure 2.2-6 (e) shows that a $\Delta\theta$ of $5°$ is required for defined sheets of interphase precipitation to be observed. The highly variable nature of interphase precipitation within a microstructure is supported by the heterogeneous hardness measurements for individual ferrite grains measured by Chih-Yuan *et al.* [73,91].

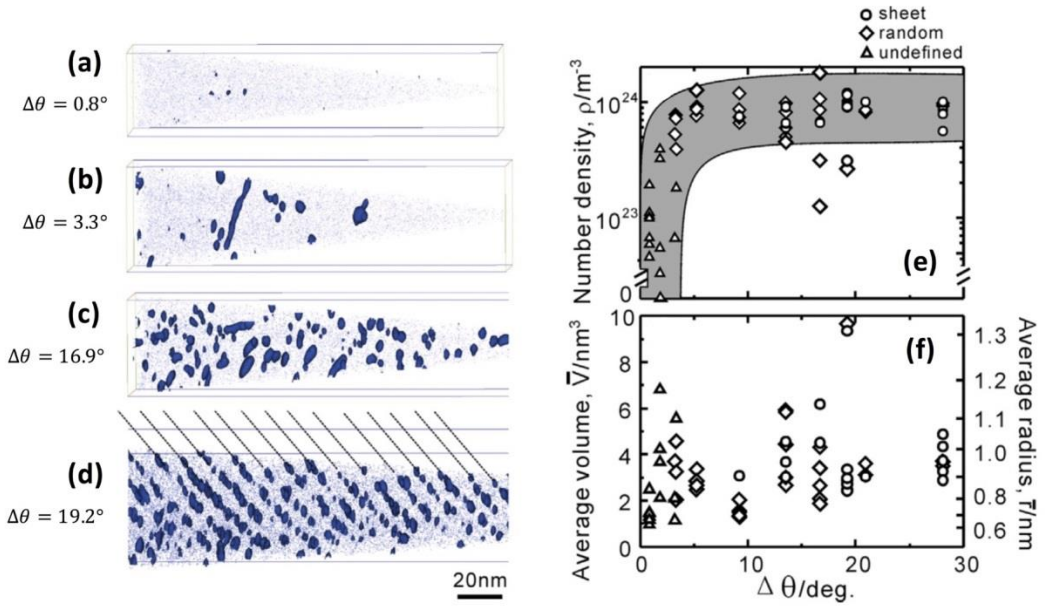

Figure 2.2-6 Role of γ/α orientation relationship upon the dispersion of interphase precipitates (adapted from Zhang et al. [90])

5) Solute Accumulation

Zhang *et al.* [92] recently, using field emission – electron probe microanalysis (FE-EPMA) investigated the solute profiles within the region of the prior of γ/α interphase boundary in partially transformed samples where the γ phase has decomposed to displacive martensite during quenching. It was found at γ/α interphase boundaries with a non-K-S orientation relationship $\Delta\theta > 5°$, which their previous studies had suggested was necessary for the occurrence of interphase precipitation, substitutional solute elements accumulated at the interphase boundary (Figure 2.2-7). It was suggested that the accumulation of solute elements at the γ/α interphase boundary provides the necessary supersaturation for the successful precipitation of a carbide precipitate.

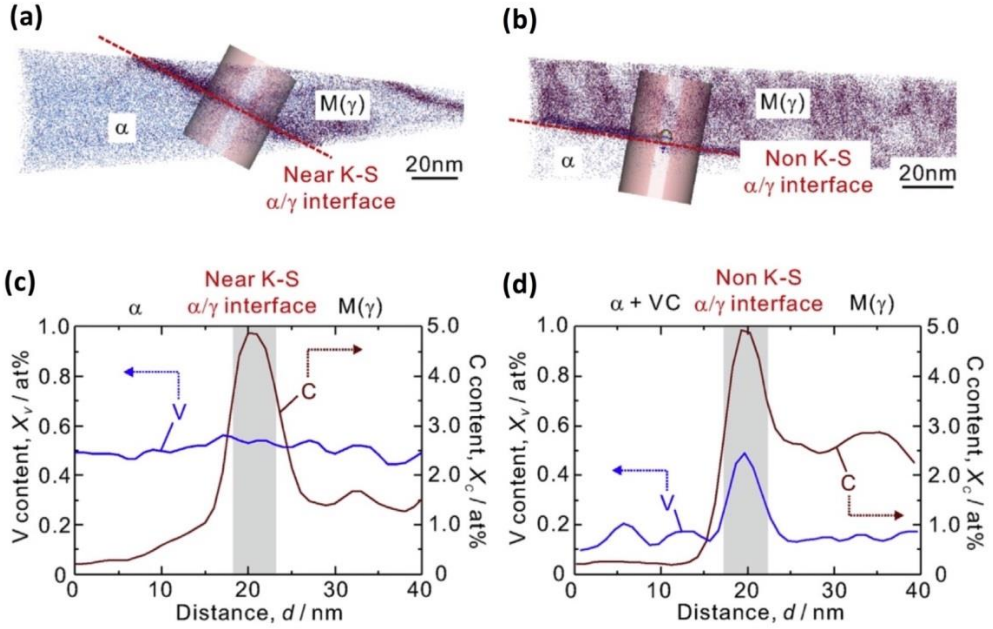

Figure 2.2-7 3D elemental profiles of a) an γ/α interphase boundary with a near K-S orientation relationship b) an γ/α interphase boundary with a non-K-S orientation relationship $\Delta\theta > 5°$ c-d) corresponding 2D plots of the cylindrical areas marked in a-b) respectively (taken from Zhang et al. [92]).

6) Mo additions

Several recent studies have suggested in steels alloyed with both Ti and Mo [41,44,84,86,93], Mo is present in the early stages of carbide precipitation, this is principally due the lattice mismatch with the ferritic matrix being decreased by the partial replacement of Ti with Mo and significant sub-stoichiometry in terms of C [94], the effect of this being the interfacial energy between the precipitate and the matrix reduces and subsequently the energetic barrier for nucleation. Furthermore, as Mo is not thermodynamically favoured in TiC therefore it partitions steadily to the surface of the precipitates. This partitioning leads to a greater free energy reduction than that associated with true coarsening dramatically slowing the rate of coarsening. It should also be noted that the first-principles calculations by Jang *et al.* [94] would suggest that the same mechanism would not be possible in the case of steels alloyed with a combination of V and Mo as the lattice parameter mismatch with ferrite would

not be reduced by the presence of Mo regardless of the degree of C sub-stoichiometry.

2.2.3. Mechanisms for Interphase Precipitation

Li and Todd [63] identified that 6 mechanisms had been proposed for the phenomenon of interphase precipitation in 1988. These 6 mechanisms can be assigned to 2 categories: 1) mechanisms which require stationary portions of γ/α interphase boundary typically exhibiting a low energy orientation relationship between the γ and α. 2) mechanisms which enable precipitation at non-stationary γ/α interphase boundaries, typically high-energy, incoherent boundaries (the nature of different γ/α interphase boundaries is reviewed in Section 2.2.5). Of the mechanisms and models proposed since 1988 they all can be assigned to one of the following 6 mechanisms:

1) The Ledge Mechanism

Aaronson forwarded the "theory of precipitate morphology", which proposed that semi-coherent precipitates in general grow via a ledge mechanism [95] since this theory's publication ledges and ledge-like features have been widely observed during the austenite to ferrite ($\gamma \rightarrow \alpha$) phase transformations in steels. Observations have been made *in-situ* using hot-stage TEM observation, such as that by Onink *et al*. [96]. However despite this, relatively little is definitively known about their formation and progression [97–101]. This is in part attributable to the significant experimental difficulty in observing *in-situ* transformations with sufficient resolution both spatially and temporally [101].

A growth ledge on a semi-coherent γ/α interphase boundary consists of a disordered, mobile riser and a comparatively coherent and immobile tread [97]. Smith [102] suggested, an allotriomorph growing into two neighbouring parent grains should only exhibit a defined orientation relationship (OR) with one parent matrix grain. This would suggest that a ledge mechanism should only be

observed on one side of the growing allotriomorph whereas on the other side the allotriomorph has been suggested to grow via the movement of a random high angle disordered γ/α interphase boundary. During the ($\gamma \rightarrow \alpha$) phase transformation the two orientation relationships frequently detected are the Kurdjumov-Sachs (KS) [103], or the Nishiyama-Wasserman (NW) [80,81] OR.

Davenport and Honeycombe [52], observed planar interphase precipitation (IPP) to be associated with $\gamma \rightarrow \alpha$ decomposition via a ledge mechanism. The stationary low energy treads $\left((110)_\alpha \parallel (111)_\gamma\right)$ of the ledged α terrace were observed to be marked by the presence of interphase carbide precipitates, which are considered to offer a greater likelihood of successful precipitate nucleation than either ledge risers or planar disordered interphase boundaries [104]. Honeycombe [60] suggested the $(110)_\alpha$ habit plane of the precipitates is the variant which is most closely parallel to the γ/α interphase boundary in order to minimise the interfacial energy. Since these observations, ledge terraces during interphase precipitation have been recorded on many occasions [29,54,66].

Diffusional growth ledges in Fe-C alloys are thought to form at either: junctions between grain boundary allotriomorphs and secondary side-plates (boundaries) or via a mechanism where the volume change distorts the path of the boundary, creating a ledge [105]. The direct nucleation of growth ledges at boundaries, 2D nucleation, is considered to be the simplest mechanism for ledge formation [106].

A 2D model for the heterogeneous nucleation of diffusional super-ledges was forwarded by Bhadeshia [107]. As super-ledge was defined by Laird and Aaronson [108] as the agglomerations of multiple unit ledges one or a few atomic planes in height [109]. Bhadeshia proposed Equation (2.2-5), which states that the critical height a_{crit} for the successful nucleation of an α super-ledge upon an γ/α interphase boundary (which is assumed to be equal to the

inter-sheet spacing, λ, in the case of interphase precipitation), is controlled by the interfacial energy of the facet plane of the ledged interphase boundary, σ, and the driving force for the transformation, $\Delta G_m^{\gamma \to \alpha}$:

$$\lambda = a_{crit} = \frac{\sigma V_m}{\Delta G_m^{\gamma \to \alpha}}$$

(2.2-5)

were, V_m is the molar volume. Although as proposed, this approach [107] was able to predict the trend of refining inter-sheet spacing with reducing temperature excellently, there was still a separation between the expected and predicted curves.

Todd and co-workers [63,110,111] developed and then revised a model of interphase precipitation based on the concept of a combined α and carbide pseudo-phase. Under the assumption that the overall kinetics of a ledged interphase boundary is well approximated by that of a planar disordered boundary the authors propose a similar diffusional growth equation to that originally proposed by Zener [112]. Liu [113] criticised this model on the basis of its many perceived unrealistic simplifying assumptions, and for the fact that the model considered the transformation mode to incorporate the full partitioning of substitutional solute elements. Liu [113] commented that this would only be expected if the γ/α interphase boundary was moving particularly slowly.

2) The Bowing Mechanism

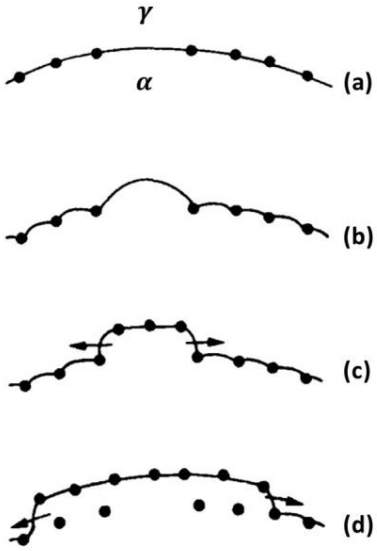

Figure 2.2-8 The bowing and quasi-ledge mechanisms (adapted from Ricks and Howell [66])

The Bowing mechanism was proposed by Heikkinen [114] in response to frequent observations that interphase precipitate carbide rows are frequently curved. The bowing mechanism is shown in Figure 2.2-8 (a-b) where, the γ/α interphase boundary is pinned and bows between the precipitates, the boundary then advances until sufficient solute is accumulated in the vicinity of the boundary for the successful nucleation of carbides [63]. Curved arrays of precipitates are not thought to be possible where the interphase boundaries progress by the lateral motion of ledges perpendicular to the overall growth direction of the γ/α interphase boundary when the boundary obeys a low energy orientation relationship. Ricks and Howell [65] developed a mathematical model to predict the inter-sheet spacing of interphase carbide precipitates under the bowing mechanism proposing Equation (2.2-6) which described the formation of a hemispherical cusp upon forming a high-energy γ/α interphase boundary pinned by a row of carbide precipitates. Equation (2.2-6) describes the minimum height of the hemispherical cap which both Ricks and Howell [65] in the case of the bowing mechanism and Bhadeshia [107] in the case of super-

ledges was assumed to be equal to the inter-sheet spacing of interphase carbide precipitates λ.

$$\lambda = a_{crit} = \frac{2\sigma V_m}{\Delta G_m^{\gamma \to \alpha}}$$

(2.2-6)

It should be noted that Equation (2.2-6) only differs from Bhadesia's equation for super-ledges by the addition of the 2 in the numerator. Ricks and Howell [65] noted that the predicted inter-sheet spacing nearly always exceeds the measured inter-sheet spacing in the Fe-1V-0.2C $wt\%$ and to a lesser extent the Fe-10Cr-0.2C $wt\%$ systems, concluding that for the majority of interphase precipitate distributions the dominating mechanism must be ledge or ledge-like.

In an aside, beyond the context of interphase precipitation, a model for a coherent pillbox nuclei was proposed by Lange III *et al.* [115], Equation (2.2-7), in order to explain observed α nucleation rates. $\sigma_i^{\gamma\alpha}$, $\sigma_c^{\gamma\alpha}$ and $\sigma^{\gamma\gamma}$ are the interfacial energies of the more incoherent riser, more coherent broad face of a pillbox nucleus and the interfacial energy of the austenite grain boundary, respectively.

$$\lambda = a_{crit} = \frac{2\left(\sigma_i^{\gamma\alpha} + \sigma_c^{\gamma\alpha} - \sigma^{\gamma\gamma}\right)}{\Delta G_v^{\gamma \to \alpha} - \Delta G_v^{el}}$$

(2.2-7)

Neglecting the elastic strain energy associated with the nuclei $\Delta G_v^{el}$and considering the pillbox nuclei to be equally applicable in the case it is semi-coherent and incoherent with respect to the parent γ upon the γ/α interphase boundary therefore, $\left(\sigma_i^{\gamma\alpha} + \sigma_c^{\gamma\alpha} - \sigma^{\gamma\gamma}\right)$ can be replaced with just σ, Equation (2.2-7) becomes analogous to Equation (2.2-6). This suggests a ledge which has nucleated at a junction according to Bhadeshia's Equation (2.2-5).

Liu [113] proposed a model for interphase precipitation based on the concept of an advancing incoherent high-energy γ/α interphase boundary. The model evaluates the cyclical balance between the pinning force and the driving force acting upon the γ/α interphase boundary. The boundary is initially 1) considered to be mobile, at a series of time steps the balance between the driving force and the pinning force is evaluated until the condition is met such that the pinning force exceeds the driving force and the boundary is considered pinned. 2) The precipitates at the γ/α interphase boundary consume carbon increasing the driving force for α growth, the cycle then repeats.

3) The Quasi-Ledge Mechanism

Ricks and Howell [66] in response to the shortcomings of the bowing mechanism, for which they found the minimum inter-sheet spacing were significantly larger than that of that of fine *IPC-regular* (although in broad agreement of precipitate populations in the *IPC-irregular* regimen) [65] proposed the quasi-ledge mechanism. The quasi-ledge mechanism Figure 2.2-9 (b) is analogous to that of the ledge mechanism Figure 2.2-9 (a) except that the fact that the interphase boundary in the case of the quasi-ledge mechanism is a high-energy disordered interphase boundary. Ricks and Howell [65] proposed that the source of quasi-ledges could originate from the bowing mechanism, Figure 2.2-8 (c-d). In the presence of copious precipitation, the bowing mechanism is interrupted, the γ/α interphase boundary pinned by precipitates and the only allowed motion of the γ/α interphase boundary is lateral. This necessarily stipulates that the precipitation of interphase carbide precipitates must occur either just ahead of the γ/α or at least on the γ side of the interphase boundary. The quasi-ledge mechanism has been recently developed by Chen *et al.* [45,116], who proposed an analytical model for the mechanism. Through the fitting of the pre-exponentials for the nucleation rates of ferrite ledges and carbide precipitates

the model was found to be able to predict the clear majority of experimentally measured inter-sheet spacing.

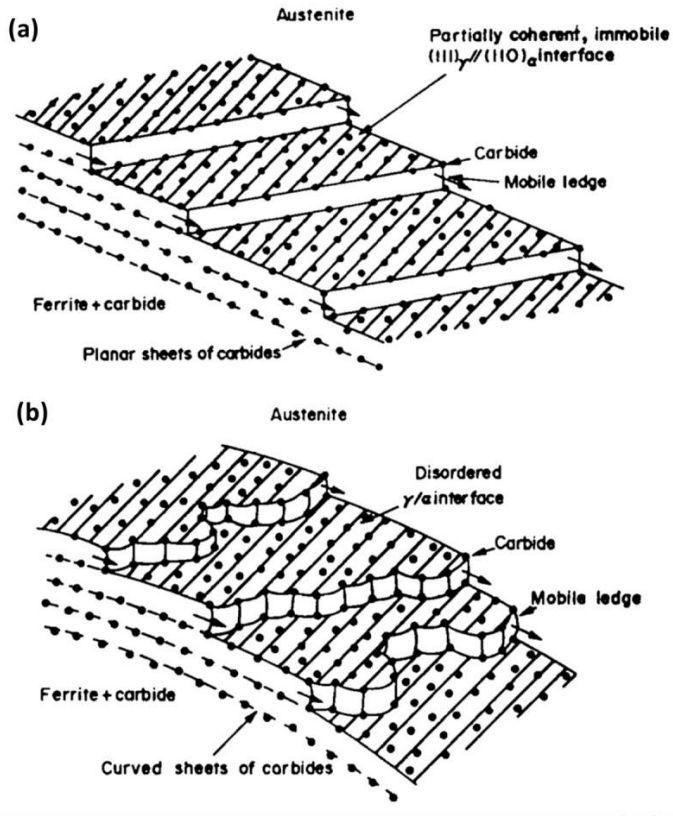

Figure 2.2-9 a) The ledge mechanism b) quasi-ledge mechanism (taken from Ricks and Howell [66])

The quasi-ledge mechanism as proposed by Ricks and Howell [65] requires the γ/α interphase boundary to be temporarily pinned by the precipitation of carbide precipitates. The maximum Zener pinning force [117] can be estimated using an equation proposed by Gladman [118] for grain boundary pinning, Equation (2.2-8).

$$P_z = \pi r \sigma n_a$$

(2.2-8)

Where n_a is the number of precipitates per unit area fraction of precipitates and r is their radius. Considering the interfacial energy of the γ/α interphase boundary to have an upper bound of $0.8\,Jm^{-2}$ (assumed similar to a disordered austenite grain boundary) for a high-energy disordered interphase boundary, a reasonable estimate of $r = 1\,nm$ and inter-particle spacing to be $\omega = 40\,nm$ [29]. The number of precipitates per unit area of γ/α interphase boundary can be calculated using following equation:

$$n_a = \frac{\omega^2 - 2\omega + 1}{\omega^2}$$

(2.2-9)

which, can be reasonably approximated by $n_a \approx \frac{1}{\omega^2}$ when ω is suitably small. Multiplying Equation (2.2-8) by the molar volume of the system, in this case, taken to be approximately equal to that of the α phase alone gives the pinning force acting per mole of the boundary.

$$P_z = \pi r \sigma n_a V_m = \pi \times 1 \times 10^{-9} \times 0.8 \times 2.50 \times 10^{14} \times 7.11 \times 10^{-6}$$
$$= 23.34\,Jmol^{-1}$$

(2.2-10)

Considering the interphase precipitation shown in Figure 2.2-1 (c) of which the precipitates have a radius of approximately $5\,nm$, a number density per unit area of approximately $2.50 \times 10^{14}\,m^{-2}$ and the molar volume of the system being $V_m = 7.11 \times 10^{-6}\,m^3$ the Zener pinning force would be $23.34\,Jmol^{-1}$ (Eqn. (2.2-10)). Furthermore, in the densely-packed population of interphase precipitates in alloys containing both Ti and Mo the spacing between interphase precipitates within a row was $\omega = 40\,nm$, substituting this into Equation (2.2-9) yields $n_a = 6.25 \times 10^{14}\,m^{-2}$ and in turn a maximal Zener pinning force of $55.84\,Jmol^{-1}$ when considering the precipitates to be as large as $5\,nm$ in radius. This should be regarded as being the upper bound of the pinning forces to be

expected as the precipitates may have grown considerably once encased in α matrix after the γ/α interphase boundary has progressed. Using a similar approach, for a specific steel grade, Murakami *et al.* predicted that the Zener pinning force would be $6\,Jmol^{-1}$[72]. Therefore, it would not be expected that the presence of interphase boundary particles would inhibit the movement of the γ/α interphase boundary except at very small undercooling where the chemical driving force is exceptionally small. In analogy to the pinning of grain growth, Ashby noted that the effective pressure on the advancing γ/α interphase boundary is typically in the range of $10^7 - 10^{11} Nm^{-2}$ which is 10^4 times greater than that which would be expected for grain growth where Zener pinning is pertinent [119].

Aaronson *et al.* [104] explored the nucleation of precipitates on planar disordered γ/α interphase boundaries using classical nucleation theory, they found that for interstitial systems, for example, Fe-C nucleation of cementite precipitates at moving interphase boundaries should not be possible. It is additionally found that planar disordered γ/α interphase boundaries are not preferred nucleation sites in Fe-C-X systems [60]. This led Aaronson *et al* [104] to state that their analysis of cementite precipitation at planar disordered γ/α interphase boundaries is in fact applicable also broadly to Fe-C-X alloys.

Considering Aaronson's calculations suggest that it is both unlikely that a dispersion of interphase precipitates could pin an γ/α interphase boundary and that the nucleation of interphase boundary carbides on mobile portions of the interphase boundary are unlikely, alternative mechanisms must be sought in order to explain the observations of curved arrays of interphase precipitates.

4) Eutectoid Decomposition Mechanism

Obara *et al.* [62] proposed a thermodynamically based eutectoid decomposition model, shown in Figure 2.2-10, which although was unable to predict inter-sheet

spacing was able to differentiate between the different morphologies of interphase precipitate dispersions. θ_1 and θ_2 relate to the angle between the lowest mobility orientation of the γ/α interphase boundary and the γ grain boundary and the angle between lowest mobility orientation of the γ/c interphase boundary and the mobility orientation γ/α, respectively.

When:

a) θ_1 and θ_2 are small a planar interphase precipitate morphology develops analogous to the ledge mechanism.
b) As θ_1 becomes larger the quasi-ledge and the bowing mechanisms become dominant.
c) With further increasing θ_1 and additionally θ_2 the fibrous mechanism becomes dominant.

Finally, when $\theta_1 = \theta_2$ the growth of α and c becomes cooperative and a pearlitic morphology becomes dominant.

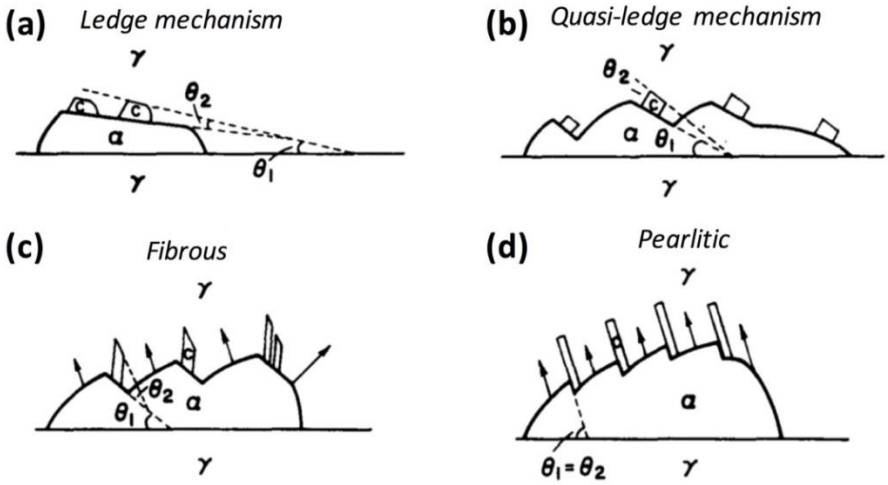

Figure 2.2-10 Schematic drawings of carbide nucleation at facets on γ/α boundaries as a function of increasing values of θ_1 and θ_2 (adapted from Obara et al. [62])

5) Solute Depletion Mechanism

Roberts [120] proposed the solute depletion model which was later developed by Lagneborg and Zajac [121]. They proposed an adaption of the quasi-ledge model where the height of the ledge was controlled by the boundary diffusion of the carbide forming element along the disordered riser of the quasi-ledge. The inter-sheet spacing is computed considering the transformation to be analogous to Cahn's model for a pearlitic transformation [122]. Okamoto and Ågren [123] built upon the model of Lagneborg and Zajac [121]. Whilst using Cahn's model for a pearlitic transformation [122] they incorporated an assessment of the solute drag at the γ/α interphase boundary ledge riser according to the model of Odqvist *et al*. [124,125]. The plausibility of this mechanism can be questioned as it requires the γ/α interphase boundary tread to be pinned by interphase carbide precipitates which have nucleated below the thread on the α side of the γ/α interphase boundary.

Rios [126,127] also considered a solute depletion model however, in contrast to the cases above where the diffusion coefficient used was required to be that of an enhanced boundary diffusion coefficient, a matrix α diffusion coefficient was used. This however required the introduction of additional assumptions.

6) Solute Drag Nucleation Mechanism

Edmonds [128] proposed that the accumulation of substitutional solutes at the γ/α interphase boundary through a solute drag effect would enhance the supersaturation locally at the boundary and facilitate carbide nucleation. Murakami *et al.* [72] recently, developed a coupled solute drag-nucleation model, a planar disordered interphase considering the accumulation of substitutional solute elements at the γ/α interphase boundary through solute drag. The model coupled the computation of the solute drag with classical nucleation theory at interphase boundaries similar to that developed by Aaronson *et al.* [104]. However, the binding energy of V to the γ/α interphase

boundary required to fit this model to experimental data was $30.11\ kJ.mol^{-1}$ which is in the order of 4 times greater than the binding energy suggested by the *ab initio* calculations of Jin *et al.* [129].

2.2.4. Experimental Observations of Ledges during Interphase Precipitation and the Relationship Between Ledge Spacing and Inter-sheet Spacing

The earliest investigations of the phenomenon of interphase precipitation appear in 1964 in the studies by Mannerkoski [47] and Relander [48]. 5 Years later in 1969 Mannerkoski [130] published the first convincing micrograph (Figure 2.2-11 I) of the formation of interphase precipitates on the stationary treads of a terrace of laterally moving ledges. Mannerkoski's [130] micrograph clearly shows that the inter-sheet spacing of interphase precipitates is consistently equal to the height of the ledge riser. Soon after Mannerkoski, Davenport and Honeycombe [52] also showed convincing evidence (Figure 2.2-11 II) showing both the association of interphase precipitation with the progression of the $\gamma \rightarrow \alpha$ phase transformation via lateral ledges and again the equivalence between ledge height and inter-sheet spacing.

In 1974 Campbell and Honeycombe published a series of micrographs (Figure 2.2-11 III a-c) showing the association of interphase precipitation with the progression of the $\gamma \rightarrow \alpha$ phase transformation via lateral ledges. However, in (Figure 2.2-11 III c) it is clear that in some cases the ledge spacing varies dramatically, in some cases interphase precipitates are formed in banded microstructures with large areas devoid of interphase precipitates between. This finding is however consistent with the "theory of diffusional super-ledges" by Bhadeshia [107] who proposed a model for the minimum height a diffusional super-ledge could take, whilst suggesting a super-ledge could exhibit a height equal to several multiplications of this minimum ledge height. These

observations were followed by further observations of the association of interphase precipitation with the progression of the $\gamma \rightarrow \alpha$ phase transformation via lateral ledges by Rios [126] (Figure 2.2-11 IV) and; Khalid and Edmonds [131] (Figure 2.2-11 V). One can be critical of the aforementioned experimental observations as they are all associated with model alloys with large amounts of interstitial carbon and substitutional alloying elements. This would lead to the $\gamma \rightarrow \alpha$ transformation to be sluggish, which has the advantage that partially transformed specimens can be easily produced but does not confirm that interphase precipitation occurs via the same mechanism as in alloys where the $\gamma \rightarrow \alpha$ transformation would be significantly faster.

More recently Yen *et al.* [29] published a TEM micrograph of the association of interphase precipitation with the progression of the $\gamma \rightarrow \alpha$ phase transformation via lateral ledges in a low C and low substitutional, industrial, micro-alloyed steel (Figure 2.2-11 VI). However, although 2 large ledges are clearly visible it is hard to distinguish the relationship between ledge height and inter-sheet spacing from Yen's micrograph as the inter-sheet spacing is very fine. To the best of the authors knowledge the most recent observation of the association of interphase precipitation with the progression of the $\gamma \rightarrow \alpha$ phase transformation via lateral ledges was described by Chen *et al.* in 2014.

Based on the not insignificant accumulation of experimental observations across a range of alloys temperatures and research groups the author believes there is strong evidence for the association of interphase precipitation with the progression of the $\gamma \rightarrow \alpha$ phase transformation via lateral ledges. Based on studies using model alloys it has been shown that the ledge height and the inter-sheet spacing is usually equal however there has been no systematic study to prove this. It is suggested that this is due to this being experimentally challenging.

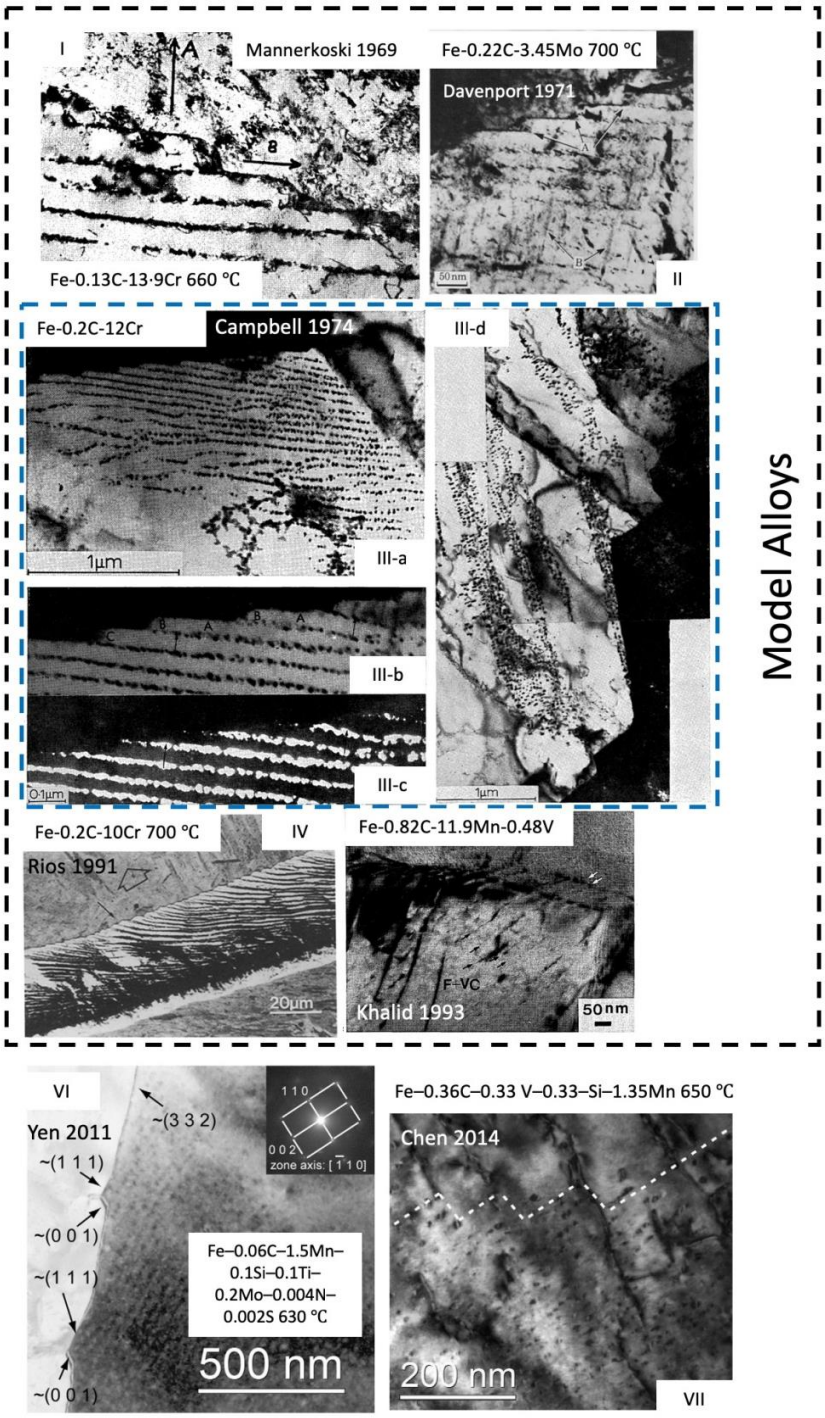

Figure 2.2-11 Summary of the experimental evidence for the association of interphase precipitates with the progression of the γ → α via a ledge mechanism. TEM micrographs after, I) Mannerkoski [130], II) Davenport and Honeycombe [52]*, III a-c) Campbell and Honeycombe* [54]*, IV) Rios [126], V) Khalid and Edmonds [131], VI) Yen et al. [29] and VII) Chen et al. [45].*

In contrast to the large body of evidence regarding the association of interphase precipitation with the progression of the $\gamma \rightarrow \alpha$ phase transformation via lateral ledges there are very few experimental studies where the inter-carbide spacing of interphase precipitates is measured. As mentioned in Section 2.2.2 Yen *et al.* [29] determined the inter-carbide spacing from an extremely modest sample of 3 individual grains at each temperature interval. It was noted that the data showed a large degree of dispersion and it was argued the data would be more justifiably stated as showing a mean inter-carbide spacing of $\approx 40\ nm$ with spacings being observed as small as $\approx 20\ nm$ and as high as $\approx 80\ nm$ over $620\ ℃$ to $720\ ℃$ temperature range. To the best of the authors knowledge the only other convincing measurement of the inter-carbide spacing was performed by Davenport and Honeycombe [52] from a single micrograph shown in Figure 2.2-1. It is concluded that there is a significant deficiency in the literature regarding the inter-carbide spacing which should be addressed with future studies.

2.2.5. Generality of γ→α Phase Transformation via Growth ledges in steels

Edmonds and Honeycombe [132], observed using photoemission electron microscopy, faceted and possibly ledged interphase boundaries irrelevant of γ/α OR, with considerable variation in step heights even in the context of polygonal allotriomorphic α. This led Honeycombe [60] to conclude that the 'migration of truly curved high-energy ferrite/austenite boundaries is rare and likely only to occur at higher transformation temperatures'.

More recently, Yen *et al* [29] proposed a classification scheme of ledged γ/α interphase boundaries, shown in Figure 2.2-12:

a) *Type A*- a semi-coherent γ/α interphase boundary. In steels, such interphase boundaries typically exhibit either the Kurdjumov-Sachs (KS)

[103] or the Nishiyama-Wasserman (NW) [80,81] orientation relationships (OR).

b) *Type B* - a disordered interphase boundary [133,134]. An interphase boundary exhibiting an irrational orientation relationship between γ and α, the atomic matching of the interface can be manifested in the form of densely packed atomic-scale ledges [33,35]. This type of interphase boundary can be curved, with both high interfacial energy and high mobility, moving through the quasi-random-jump process during phase transformation [10], wherein atoms may cross all parts of the interface.

c) *Type C1* - the incoherent interface can form ledges or facets (tens to hundreds of nanometres in height or more) due to the intrinsic bi-crystallography at the nucleation stage or during the growth stage [33]. Although the incoherent interface is associated with a random orientation, its nanostructure can be regarded as similar to the nanostructure of a semi-coherent interface, consisting of high-energy ledge structures with relatively low-energy terrace planes. Interphases of this type may appear macroscopically curved on such a length scale they would be indistinguishable from the type B interphase boundary.

d) Type C2 - during the phase transformation, the uneven incoherent interface can become macroscopically flat by gradually reducing the interfacial energy; i.e. type C2 interface, as shown in Figure 2.2-12 (d). Unlike the type B interface, type C1 and type C2 interfaces can possibly grow by the ledge mechanism: the step planes run over the terrace planes, which are less mobile, through lateral growth. In general, it can be concluded [33] that the migration of incoherent interfaces can be concerned with so-called continuous quasi-random jumping of atoms from γ to α or a ledge mechanism depending on the nature and length scale of the interface structure.

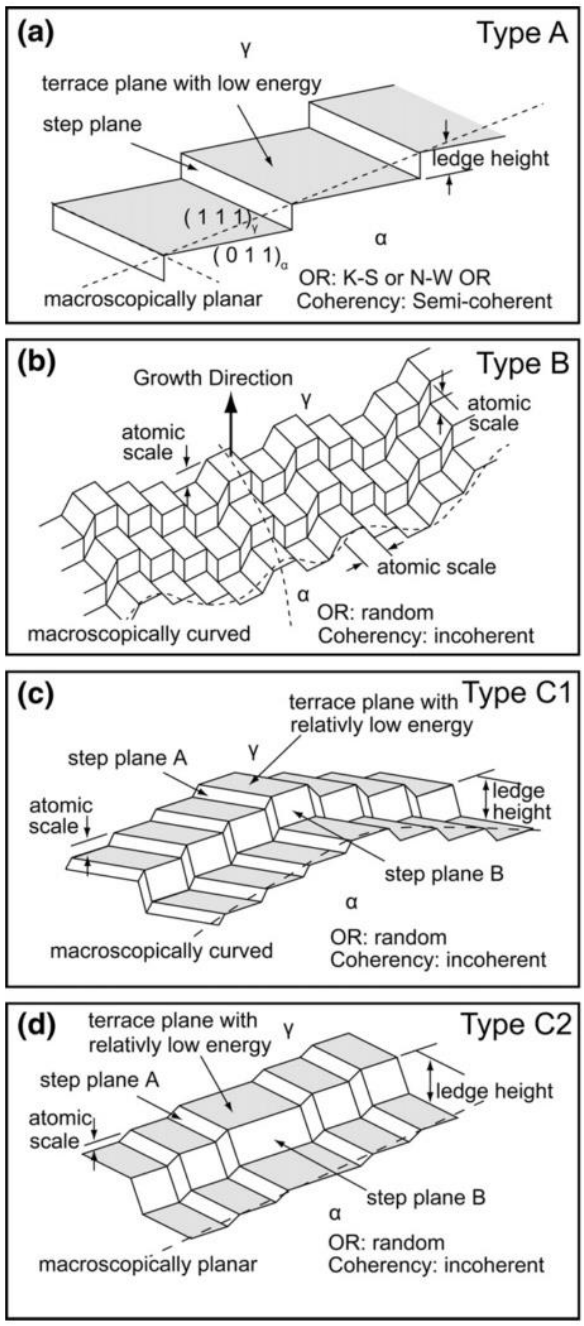

Figure 2.2-12 Classification scheme of ledged γ/α interphase boundaries (taken from Yen et al. [29])

The generality of transformations via a ledge mechanism has been proposed, in particular by Cahn [135] who stated that 'the mechanism of the motion of an interface in a crystalline material depends on the driving force rather than on the crystallographic nature of the interface. At sufficiently large driving forces, the

interface can move uniformly'. However, at 'sharp interfaces the necessary driving force is so large that it may be difficult to achieve'. More recently the incoherency view has received renewed attention, Massalski *et al.*[134] reviewed the experimental and theoretical nature of interphase boundaries concluding that an incoherent boundary may be facetted on various length scales. For the purposes of this study, it will be assumed that all the γ/α interphase boundaries regardless of crystallographic OR exhibit growth ledges.

Yen *et al.* [29], clearly showed a ledged terrace on what would be conventionally seen as a high-energy incoherent γ/α interphase boundary (fig. 3(B) in [29]). The likelihood of this finding was previously discussed by Furuhara and Aaronson [136] in light of experimental results in the Ti-Cr system (precipitation of a HCP phase in a BCC matrix) [137,138], which suggested the presence of growth ledges on the side of the allotriomorph regardless of the orientation relationship with the parent matrix grain. This result was confirmed by Furuhara and Maki for precipitation of BCC in an FCC matrix for a Ni-Cr alloy [139]. Furuhara and Aaronson [136] proposed Figure 2.2-13 which shows that an arrangement of ledges, small structural ledges and larger super-ledges can, in fact, explain a curved array of interphase precipitates. The interphase boundary morphology proposed by Furuhara and Aaronson [136] is very similar to types C1 and C2 proposed by Yen *et al*. [29] in Figure 2.2-12.

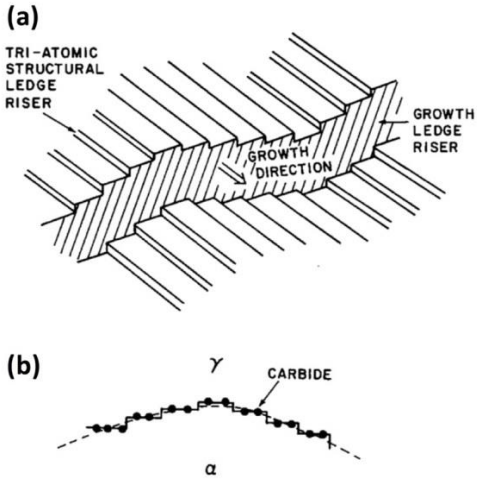

Figure 2.2-13 Curved arrays of interphase precipitates via a ledge mechanism (taken from Furuhara and Aaronson [136])

It is suggested in light of Equations (2.2-5), (2.2-6) and (2.2-7) interphase precipitation attributable to either the ledge, bowing mechanisms and presumably the intermediate quasi-ledge mechanism all can be determined by the following equation (2.2-11):

$$\lambda = a_{crit} = \frac{C_3 \sigma V_m}{\Delta G_m^{\gamma \to \alpha}}$$

(2.2-11)

which states that the minimum spacing between rows of interphase precipitates is controlled by the interfacial energy of the facet plane of the ledged interphase boundary, σ, the driving force for the transformation, $\Delta G_m^{\gamma \to \alpha}$. C_3 is a constant that can be varied according to the geometry of the mechanism. When the constant C_3 is equal to 1 Equation (2.2-11) is analogous to the theory of diffusional super ledges proposed by Bhadeshia [107]. When C_3 is equal to 2 Equation (2.2-11) is analogous to the model for the bowing mechanism proposed by Ricks and Howell [65]. Similarly when C_3 is equal to 2 Equation (2.2-11) is also analogous to the pillbox model proposed by Lange III [115].

Figure 2.2-14 shows the predicted and measured inter-sheet spacing (for dispersions of interphase precipitates reported in studies; a) Balliger and Honeycombe [57], b) Okamoto et al. [71], c) Yen et al. [29] and d) Chen et al. [45]) λ using Equation (2.2-11) with two values for a $C_3\sigma$. A combination of ($C_3 = 1,\ \sigma = 0.2\,Jm^{-2}$ is analogous to the model proposed by Bhadeshia [107] considering a semi-coherent γ/α interphase boundary and a combination of $(C_3 = 2, \sigma = 0.8\,Jm^{-2})$[72] is analogous to the model proposed by Ricks and Howell [65] considering an incoherent high energy γ/α interphase boundary). As can be seen, the clear majority of the experimental spread of inter-sheet spacing, λ, can lie between the predicted upper and lower bounds for interphase precipitation. In each case the Widmanstätten start temperature range, W_S, bainite start temperature, B_s, and the predicated TTT C-curves for diffusional transformation (DIFFT) and shear transformation (SHEART) have been plotted using Program MAP_STEEL_MUCG83 [140]. Whilst the nucleation of Widmanstätten α is expected in the majority of cases the $\gamma \rightarrow \alpha$ transformation associated with interphase precipitation is expected to be diffusional due to the diffusional transformation (DIFFT) C-curve being at a shorter incubation time than the shear transformation (SHEART) transformation.

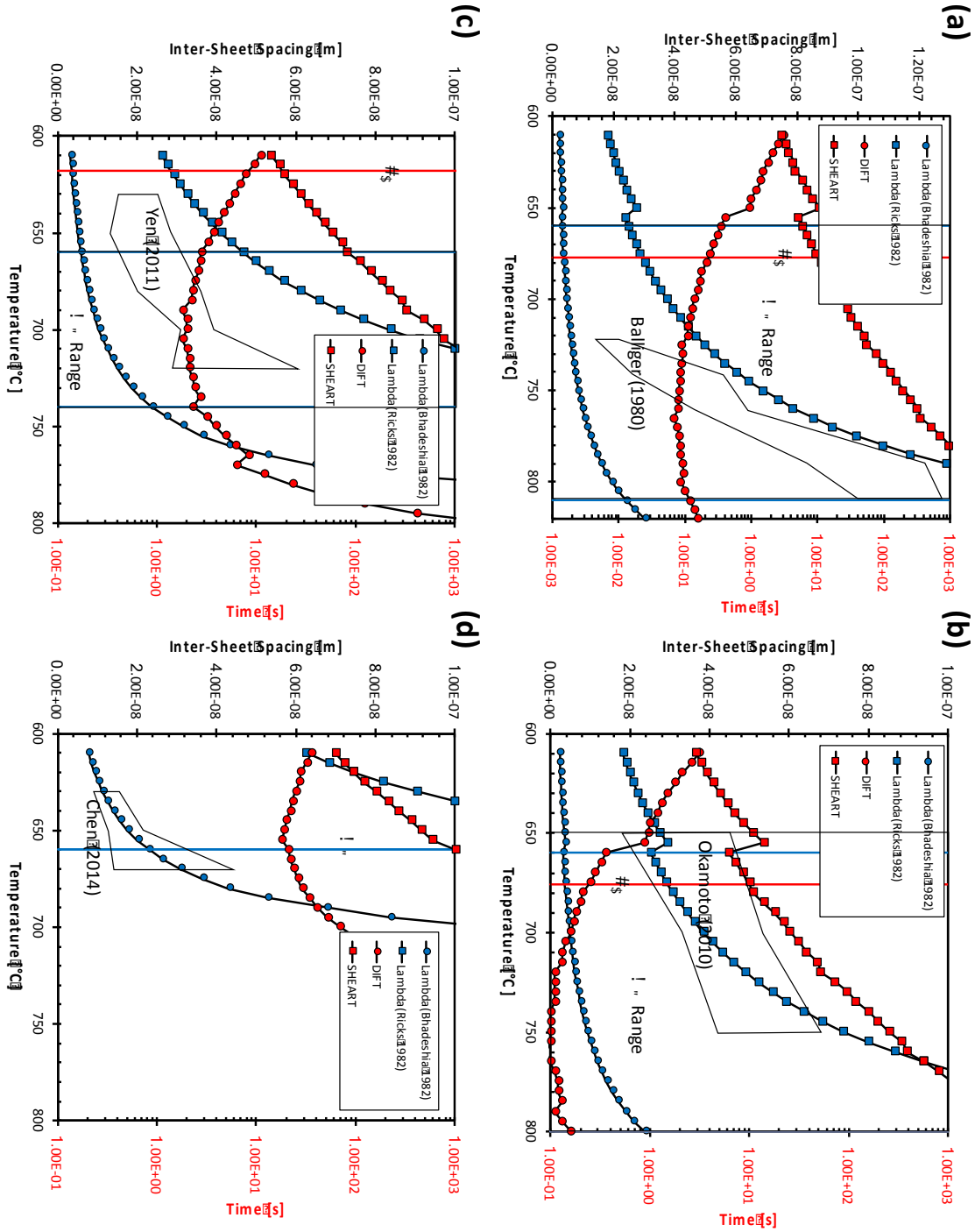

Figure 2.2-14 Predicted and measured inter-sheet spacing (for dispersions of interphase precipitates reported in studies a) Balliger and Honeycombe [57]*, b) Okamoto et al. [71], c) Yen et al. [29] and d) Chen et al. [45]) λ using Equation (2.2-11) with two values for $C_3\sigma$ ($C_3\sigma = 0.2\,Jm^{-2}$ analogous to the model proposed by Bhadeshia [107] considering a semi-coherent γ/α interphase boundary and $C_3\sigma = 1.6\,Jm^{-2}$ analogous to the model proposed by Ricks and*

Howell [65] considering an incoherent high energy γ/α interphase boundary). In each case the Widmanstätten start temperature range W_S, bainite start temperature B_s and the predicated TTT C-curves for diffusional (DIFFT) and dispalcive shear (SHEART) transformations using Program MAP_STEEL_MUCG83 [140].

2.2.6. Interphase Precipitation During Continuous Cooling

Thus far this review has only documented the study of interphase precipitation during isothermal transformations. However, industrially most transformations occur during continuous cooling. Edmonds published one of the first systematic studies of interphase precipitation during continuous cooling in 1973 [141]. This study is particularly useful as it uses exactly the same alloy used by Batte and Honeycombe [53] who explored isothermal transformations. This facilitates the direct comparison between the two thermal histories. Edmonds [141] found that the inter-sheet spacing of interphase precipitates decreases as cooling rate decreases just as Batte and Honeycombe found with decreasing isothermal transformation temperature. The mechanical strength of the alloy was found to increase with increasing cooling rate but a ductile-brittle transition occurs at cooling rates in excess of 20 °C min^{-1}. These findings have been supported by later studies such as that by Dunlop *et al.* [67].

Recently there has been a resurgence of academic interest in understanding interphase precipitation during continuous cooling with studies by Chen *et al.* [142], Bu *et al.* [143,144] and Chen *et al.* [88]. This interest has coincided with and focused predominantly upon the study of the effect of Mo alloying in Ti and Nb carbide precipitates as outlined in Section 2.2.2.

2.2.7. Coarsening of Interphase Precipitates

Carbide particles can coarsen during cooling or high-temperature in-service operations, degrading the strength of the materials significantly. It is therefore of significant importance that the coarsening behaviour of interphase precipitates is well understood. The work which specifically studied the coarsening of interphase precipitates was conducted by Dunlop and Honeycombe in 1975 [145] on VC and TiC precipitates aged up to 15 hours (0.25, 1, 4.5 and 15 hours). At each time interval between 400-500 precipitates were measured using TEM in order to characterise the precipitate population. Dunlop and Honeycombe [145] reported the coarsening of interphase precipitates was consistent with pipe diffusion along dislocations rather than bulk matrix diffusion. This finding was later supported by the follow up study performed by Balliger and Honeycombe, who studied the coarsening of V(C,N) interphase precipitates [57] and who used a larger sample size of 750-2000 precipitates to characterize each heat treatment.

More recently, the coarsening of interphase precipitates has been the subject of fervent academic activity. This was due to the report of a mechanism through which the coarsening of interphase precipitates could be effectively retarded through the addition of molybdenum (Mo), as previously described in Section 2.2.2. Funakawa and Seto [146], and later work conducted by Chen *et al.* [142], Jang *et al.* [94,147] and Kamikawa *et al.* [44,46] have found that steels with Mo additions showed mechanical properties were retained longer during high-temperature ageing. However, all the aforementioned studies compared the coarsening of interphase precipitation in Ti-containing (~0.2wt%) and Ti-Mo-containing (~0.1wt%Ti and ~0.2wt%Mo) low carbon steels with a fixed basic composition ~0.04%C, 1.5%Mn, 0.2%Si in wt.%. It can be observed that in these studies, the atomic ratio of Ti:C and (Ti+Mo):C were designed to be ~1:1.

The most well-known mechanism for this effect was reported by Jang *et al.* [94], who used first principles calculations to propose that the Mo only participates during the early stages of precipitation and becomes passive due to the energetic disadvantage during the subsequent growth and coarsening stages. The coarsening of precipitates is mainly controlled by diffusion of Ti atoms, therefore, the replacement of Ti by Mo reduces the Ti concentration in the ferrite matrix, which decelerates the coarsening of (Ti, Mo)C precipitates. However, later Jang *et al.* [148], used CALPHAD and diffusion simulations to show that the coarsening rate of TiC in Fe-Ti-C steels (fixed 0.04wt%C) can be significantly retarded by decreasing the Ti/C ratio which calls into question some of the previous attributions this effect to the role of Mo.

However, both the effect of Ti/C ratio and Mo on the interphase precipitation have not been well examined quantitatively, which leaves a question to the automotive industry whether it is necessary to add Mo into Ti-containing steels. This is due to the widely used techniques of transmission electron microscopy (TEM) and atom probe tomography (APT) which have a limited capability to analyse statistically significant numbers of precipitates. The size difference of precipiates between Ti and Ti-Mo alloys presented in the literature are typically in the range of 1.6 nm to 10 nm. It is thus difficult to statistically and accurately investigate the role of Mo on precipitate size, volume fraction and chemical composition which are key information to uncover the precipitation kinetics and hardening behaviour.

2.2.8. Interactions between Precipitates on interphase Precipitate Planes

Chamisa [149] recently observed using TEM that in some circumstances disc-shaped interphase precipitates appear to join at the tips and form pairs of connected precipitates as shown in Figure 2.2-15. The reason for the paucity of TEM observations of connected precipitates is that unless the planes of

interphase carbides are suitably spread it is impossible to tilt a specimen such that an individual plane can be imaged [52]. It should be noted that the micrograph presented by Chamisa is not tilted to reveal individual precipitates on an IP sheet plane therefore, a critical appraisal would suggest that the 'paired' precipitates may actually be spaced though the thickness of the TEM sample. Re-examination of Figure 2.2-1 adapted from Davenport and Honeycombe [52], which is tilted such that individual precipitates can be resolved on the sheet plane does however suggest that individual carbide precipitates located on planar rows of interphase precipitates often interact with one another. To the best of the author's knowledge, the mechanisms for this interaction between neighbouring interphase precipitates has yet to be elucidated.

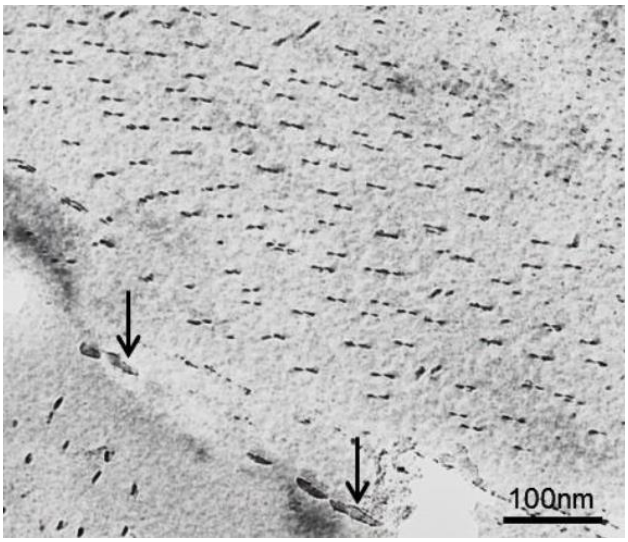

Figure 2.2-15 Interactions (Pairing) of neighbouring IP (grain boundary carbides shown by the arrows) (taken from Chamisa [149])

2.2.9. Characterization of populations of interphase precipitates

In Section 2.2.6. it was found that many of the previous studies of interphase precipitation in micro-alloyed steels has utilised the characterisation technique TEM and more recently APT. However, both TEM and APT have a limited capability to analyse statistically significant numbers of precipitates.

Furthermore, in many cases, the raw number of precipitates analysed is unreported and therefore it can be challenging to come to a critical assessment of the reliability of the work performed. For example, Yen *et al.* [29] using high-resolution TEM reported the size of interphase precipitates in steel based upon the measurement of just 15 and 25 precipitates in each condition. However, more statistically representative studies are reported in the literature. Dunlop and Honeycombe [145] studied the coarsening of VC and TiC precipitates aged up to 15 hours (0.25, 1, 4.5 and 15 hours). At each time interval between 400-500 precipitates were measured using TEM in order to characterise the precipitate population. Balliger and Honeycombe [57], who again studied the coarsening of V(C,N) interphase precipitates used a larger sample size of 750-2000 precipitates to characterise each heat treatment. Zhang *et al.* [74] measured just under 4100 precipitates in a vanadium micro-alloyed steel using APT.

An alternative, bulk characterisation too is small angle scattering (SAS) techniques based on neutrons or X-rays as being potentially suitable for acquiring bulk-scale, statistically sound data on fine-scale IP precipitates of the MX type in HSLA steels. Small angle neutron scattering (SANS) is generally preferred, as neutrons can penetrate a far greater thickness of material than X-rays. By comparison to the aforementioned studies using TEM and APT, in the SANS measurements to be reported in Chapter 4 a number density in the order of $10^{21}\ m^{-3}$ was determined from a sample of thickness $1\ mm$ and a beam of diameter $8\ mm$. This would indicate that the number of precipitates measured would be in the order of $\frac{\pi\times\left(8\times10^{-3}\right)^2\times10^{21}}{4} = 5.03\times10^{13}$, this represents a sample size of 10 orders of magnitude more than measured by conventional methods.

If the large probed volume is considered the principle advantage of SANS in relation to TEM and APT it can also be seen as one of its disadvantages. In most

situations, a microstructure of a steel and especially a precipitate population are intrinsically inhomogeneous. For example, in this Thesis, the phenomenon of interphase precipitation is studied in Section 2.2.2. The principal factors which influence the process of interphase precipitation were reviewed. It was revealed that the γ/α orientation relationship was an especially important factor with grains where the γ/α orientation relationship obeyed a low-energy orientation relationship being found unlikely to exhibit interphase precipitation. In a ferritic steel, there will be a proportion of ferritic grains which formed obeying a low-energy orientation relationship and a proportion which did not. This suggests that the dispersion of interphase precipitates will be intrinsically inhomogeneous within a bulk sample. In this work (Chapter 5) it was found that $\approx 30\%$ of ferrite transformed with a γ/α orientation relationship likely to result in interphase precipitation. However, it is possible to exploit partially transformed then quenched samples, as at short transformation times the carbide precipitation is likely to be dominated by interphase precipitation as the kinetics of random precipitation in super-saturated ferrite is slow in comparison to interphase precipitation kinetics. This strategy is made possible particularly in V-alloyed steels because V is much more soluble in austenite than other microalloying elements such as Nb and Ti [17] therefore, there is little precipitation of VC in the austenite prior to decomposition to ferrite. Whereas in the case of TEM and APT specific regions can be sampled which do exhibit interphase precipitation a SAS technique such as SANS will sample the whole beam interaction volume regardless of whether there are interphase precipitates or not. However, a critical assessment would suggest that the direct corollary of this statement is that prior research using TEM have had a systematic selection bias for the regions of the microstructure where interphase precipitation is observed and their findings less representative of the bulk material.

In comparison to the imaging methods, there are several other notable drawbacks of a SAS characterisation approach. Wagner *et al.* [150] in an

extensive review of second phase precipitation reviewed the techniques for characterising populations of precipitates. It was stated that the analysis of scattering curves is not trivial. The compositional and morphological characteristics are often required *a priori* in order to perform such analysis reliably. In many cases, this necessitates the use of imaging methods such as TEM and APT. It is important to recognise that the complicating factors involved in SAS analysis demand that multiple characterisation tools be used in conjunction with one another. Fratzl [151] who also produced a review on the use of SAS in materials science identified that due to the relatively simple sample preparation and that the method is usually non-destructive, in contrast to TEM and APT the possibility of in-situ, time-resolved studies is enabled.

Over the past twenty years, there has been a growing interest in the use of SANS use to measure the size, size distribution and volume fraction of nanoscale precipitates in various types of steel. In the specific context of interphase precipitation, the following studies have been reported. Yasuhara *et al.* [152] reported the evaluation of the number density and average precipitate dimensions in a (0.045C–1.8Mn–0.2Ti–0.004N, wt%) alloy. It should be noted that this is a very similar alloy to the NANOHITEN [38] alloy which provoked a resurgence of interest in the study of interphase precipitation. The precipitate dimensions reported by Yasuhara *et al.* [152] suggest that the diameter of the disc-shaped TiC precipitates assumed in the SANS analysis significantly exceed even the upper bound of the measurements using TEM.

Dorin *et al.* [153] and most recently, from the same research group, Dhara *et al.* [154] have explored the precipitation kinetics and clustering in micro-alloyed steels using a combination of TEM, APT and SANS. The SANS analysis procedure adopted by Dorin *et al.* [153] assumed that the precipitates were spherical and there was no direct comparison of the precipitate dimensions measured using SANS and APT. Dhara *et al.* [154] who studied a similar composition to that of

NANOHITEN [38] compared the precipitate dimensions measured by all three techniques. In this case, the average precipitate radius measured using SANS was reported to be similar to the measurements made using TEM but significantly smaller than that measured using APT. In this case, again the SANS analysis assumed that the precipitates had a spherical morphology.

Oba *et al.* [155] presented an innovative study of the precipitation kinetics in a vanadium mico-alloyed medium carbon steel using both small angle X-ray scattering (SAXS) and SANS in a technique known as the alloy contrast variation method (ACV). The combination of the two techniques allowed Oba *et al.* [155] to determine that the precipitates were stoichiometric vanadium carbide (VC) when isothermally transformed above $675\,℃$, and as $VC_{0.9}$ below this temperature. In this case, the SANS analysis assumed that the morphology of the precipitates had a spherical morphology when the isothermally transformed below $675\,℃$ and a disc morphology when transformed above. This was justified using *a priori* characterisation using TEM.

Wiskel *et al.* [156] studied NbC precipitation kinetics in a range of X-70 and X-80 pipeline steel variants after rolling and coiling operations. Although, Wiskel *et al.* [156] state that they believe the quantity of interphase precipitation to be minimal as most of the precipitates are strain induced and form in the austenite phase, it seems likely from knowledge of similarly alloyed steels with similar heat treatments that there is a potential that interphase precipitation was present. Wiskel *et al.* [156] presented, in a single case, a comparison between the size distribution of precipitates measured using SANS and TEM (the number of precipitates measured was unreported). In this single presented case, there appeared to be a strong correlation between the two results.

In summary of the above SANS studies, it can be concluded that the average precipitate dimensions measured using SANS compare resonably well with those

measured using other techniques, such as TEM and APT. SANS offers the possibility of bulk characterisation with the results being derived from the scattering associated with many orders of magnitude more precipitates than are typically imaged using TEM or reconstructed using APT. However, it must be noted that the analysis of SANS scattering curves is not trivial. The compositional, morphological characteristics are often required *a priori* in order to perform such analysis reliably. In many of the prior studies which utilised SANS a questionable assumption that the precipitates were spherical was adopted.

2.3. Unanswered Questions

1) It is well established that interphase precipitation is not present throughout a microstructure. It has been suggested that only interphases with a certain degree of misorientation from an ideal orientation relationship exhibit interphase precipitation. The question of what proportion of a microstructure is likely to exhibit interphase precipitation, as a result of this, and whether this quantitatively aligns with a proportion of interfaces with a certain deviation from an ideal γ/α orientation relationship has yet to be answered.
2) Measurements of interphase precipitates have been conducted on infinitesimally small volumes of a sample containing 1 or 2 matrix grains and limited numbers of precipitates, either electro-polished TEM foils, FIB lift-out lamellae or tapered tips for atom probe tomography. No bulk characterization techniques have been exploited in the context of interphase precipitation. Only through characterising a statistically significant number of precipitates can questions be elucidated such as coarsening kinetics. Critical quantitative data, representative of a bulk sample, on inter-particle and inter-sheet spacing, are therefore not available.
3) Although several models have been proposed for predicting interphase precipitation parameters none are able to replicate all the current experimental findings i.e.; refining inter-sheet spacing with slowing interphase boundary velocity, interphase precipitation being associated with relatively incoherent interphase boundaries. The reasons for these shortcomings and therefore the understanding of the mechanism of interphase precipitation remain yet to be elucidated. A new or revised model should be developed which can at least qualitatively predict the aforementioned experimentally observed trends.
4) It was identified that the growth of carbide precipitates on ledge terrace treads has received little academic attention. It has been suggested with

limited evidence that precipitates may interact with one-another to ‘pair', however, no physical mechanism has been suggested for these microstructural evolutions.

3. Objectives and Hypotheses

3.1. Research Aims and Objectives

3.1.1. Specific Objectives

This work aims to fulfil the following specific objectives:

1) The prevalence of interphase precipitation within an overall microstructure has yet to be established. The likelihood of interphase precipitation is known to be related to the degree of misorientation from an ideal low-energy orientation between the γ and α. This work aims to address the shortcoming in the literature regarding the prevalence of interphase precipitation in a microstructure through exploiting advanced *in-situ* characterisation techniques such as HT-EBSD. Therefore, I aim to utilize HT-EBSD to enable the evaluation of the γ/α orientation relationship to be performed on a much larger scale through determining the spatially resolved orientations of γ grains which are not preserved to room temperature for *a posteriori* characterisation.

2) To experimentally determine the dispersion, dimensions and the coarsening kinetics of populations of interphase precipitates through bulk characterization, this study endeavours to address the paucity of statistically representative datasets of interphase precipitate populations through utilizing SANS. The results of this objective will elucidate the mechanisms at play when populations of interphase precipitates grow and coarsen. The results of which will be used to guide industrial material processing. The results will also be used for validation of newly developed predictive models.
3) This work endeavours to derive a new microstructural model capable of explaining all the known phenomena regarding the evolution of inter-sheet spacing and transformation kinetics.

4) This work aims to produce a new microstructural model, utilizing phase field approach, elucidating the interactions between neighbouring, growing precipitates.
5) Based on the findings of the specific objectives above, this work will offer a suggested pathway for optimal industrial exploitation of interphase precipitation for the manufacture of hot-rolled high-strength steels. Furthermore, this work will suggest industrial pathways of how interphase precipitation can be optimally suppressed so the potential for precipitation can be retained to be exploited during the annealing of a cold-rolled coil.

3.2. Research Hypotheses

The work was carried out based on a series of research questions, to which I designed a set of parametric tests to answer. These investigations and the resulting answers are treated in the subsequent results and discussion chapters that follow.

1) It is hypothesized that the nucleation of interphase precipitates plays little role in the determination of ferrite growth ledge height and that interphase precipitates merely mark the prior growth ledge height in alloys where a strong carbide forming element is present.
2) It is hypothesized that the observed refinements in inter-sheet spacing during the initial stages of the $\gamma \rightarrow \alpha + MC$ transformation can be explained by the transition in α growth mode from parequilibrium to negligible partitioning local equilibrium.
3) The precipitation of carbides will consume sufficient carbon at the γ/α interphase boundary, therefore, the amount of carbon redistributed into the remaining γ is reduced. It is hypothesised that this will significantly accelerate the growth kinetics of the $\gamma \rightarrow \alpha$ phase transformation.
4) The elastic strain associated with interphase precipitate growth and the minimisation of interfacial energy is hypothesised to play a critical role in the growth of individual interphase precipitates and the interactions between neighbouring interphase precipitates, explaining the complex, compound morphologies, particularly necking behaviour of interphase carbide precipitates.

4. Investigating nano-precipitation in a V-containing HSLA steel using small angle neutron scattering

This work was published in: Wang, Y. Q. *et al.* Investigating nano-precipitation in a V-containing HSLA steel using small angle neutron scattering. *Acta Mater.* **145,** 84–96 (2018).

This chapter fulfills the Specific Objective *"To experimentally determine the dispersion, dimensions and the coarsening kinetics of populations of interphase precipitates through bulk characterization, this study endeavours to address the paucity of statistically representative datasets of interphase precipitate populations through utilizing SANS. The results of this objective will elucidate the mechanisms at play when populations of interphase precipitates grow and coarsen. The results of which will be used to guide industrial material processing. The results will also be used for validation of newly developed predictive models."*

This chapter also explores the hypothesis *"The precipitation of carbides will consume sufficient carbon at the γ/α interphase boundary, therefore, the amount of carbon redistributed into the remaining γ is reduced. It is hypothesised that this will significantly accelerate the growth kinetics of the $\gamma \rightarrow \alpha$ phase transformation".* It was found in a low carbon HSLA steel that that after $3\ mins$ of isothermal transformation the phase fraction of VC interphase precipitates was 0.009 which is well below the thermodynamic equilibrium value of 0.030 determined by the CALPHAD method. It was also shown that the VC precipitates

were significantly sub-stoichiometric in terms of C (VC_x where x is less than 1). Taken in combination these two findings indicate that in the case of the low carbon HSLA transformed at $700\,℃$ a small quantity of C is consumed by precipitation at the interphase boundary which is in contradiction to the aforementioned hypothesis.

4.1. Chapter Summary

Interphase precipitation (IP) of nanoscale carbides in a vanadium-containing high-strength low-alloy steel has been investigated. Small angle neutron scattering (SANS) and TEM were employed to characterize the precipitates and their size distributions in Fe-0.047C-0.2V-1.6Mn (in wt.%) alloy samples which had been austenitised, isothermally transformed at $700\,°C$ for between 3 and $600\,min$ and water quenched. TEM confirms that, following heat treatment, rows of vanadium-containing nanoscale interphase precipitates were present. Model-independent analysis of the nuclear SANS signal and model fitting calculations, using oblate spheroid and disc-shapes, were performed. The major axis diameter increased from $18\,nm$ after $3\,min$ to $35\,nm$ after $600\,min$. Precipitate volume fraction increased from 0.009 to 0.022 over the same period and number density fell from 2×10^{21} to $5 \times 10^{20}\,m^{-3}$. A limited number of measurements of precipitate maximum diameters from TEM images showed the mean value increased from $8\,nm$ after $5\,min$ to $28\,nm$ after $600\,min$ which is in reasonable agreement with the SANS data.

4.2. Introduction

The majority prior studies of interphase precipitation have used TEM to characterise the precipitates [44–46,69,147,153]. More recently APT [41,74,84,86,90,92,157] has been employed to directly measure the

composition, morphology, and size of individual precipitates. However, obtaining reliable statistical data on particle size distributions, chemical composition, morphology and volume fractions following IP is a particular challenge as IP typically occurs inhomogeneously [60,74,90]. TEM and APT both have a limited capability to analyse statistically significant numbers of precipitates efficiently which limits our ability to predict mechanical properties via models of precipitate - dislocation interactions. The lack of representative data on precipitates from significant volumes of bulk material, including factors such as size and spacing, also restricts the development of new and improved models of interphase precipitation. Improved, statistically significant, data on the size and distribution of interphase precipitates from bulk samples are thus needed.

Small angle scattering techniques based on neutrons or X-rays are potentially suitable for acquiring bulk-scale, statistically sound data on fine-scale IP precipitates of the MX type in HSLA steels. Small angle neutron scattering (SANS) is generally preferred and over the past twenty years, there has been a growing interest in its use to measure the size, size distribution and volume fraction of nanoscale precipitates in various types of steel. This has included studies at room temperature on strip cast low carbon steels [153,158,159] maraging and martensitic steels [160,161]. Ti and Nb-containing micro-alloyed steels [152,162–164], Nb-containing pipeline steels [156] and NbC precipitation in the austenite phase [165]. Oba *et al.* [166] investigated IP using a combination of Small Angle X-Ray Scattering (SAXS) and SANS in a medium carbon vanadium micro-alloyed steel. Quantitative data on IP in low-carbon, V- micro-alloyed steels have not apparently been reported.

The overall purpose of the present work was to use SANS to quantitatively analyze the size and volume fraction of IP precipitates and to investigate the changes occurring during isothermal transformation. A steel of composition Fe-0.047C-0.2V-1.6Mn (in wt.%) was selected for the present investigation because

V is the most soluble of the micro-alloying elements in austenite (γ) at high temperature and it does not readily precipitate in the γ-phase during cooling making it a very suitable addition for the formation of IP precipitates. In the present study, the precipitate characteristics were measured from both the magnetic and the nuclear scattering signals and correlated the measurements with electron microscope observations and micro-hardness data. The results will aid modelling of precipitation strengthening and in the selection of suitable thermomechanical processing schedules for controlled IP. The SANS methodology developed is proposed to be extendable to a wider range of ferromagnetic alloys.

4.3. Materials and methods

4.3.1. Materials

Table 4.3-1 Chemical composition of vanadium micro-alloyed steel in weight percent $[wt\%]$ *and atomic percent* $[at\%]$*.*

	C	Mn	Si	Al	P	S	V	N (ppm)	Fe
wt%	0.047	1.60	0.18	0.043	0.013	0.005	0.20	50	Bal.
at%	0.22	1.62	0.36	0.009	0.023	0.009	0.22	200	Bal.

A V-containing, micro-alloyed low-carbon steel provided by Tata Steel Europe was employed. The composition of the alloy, as determined by chemical analysis, is given in Table 4.3-1. The alloy was prepared by vacuum induction melting and cast into ingots with dimensions of $350 \times 105 \times 100\ mm^3$. These ingots were forged at approximately 1250 ℃ to a final thickness of $35\ mm$ (i.e. a reduction of $65\ \%$) and air cooled. To ensure that the thermomechanical processing was relevant to that employed in industrial operations, the additional $2-3\ day$ homogenization stage at high temperature used in some prior studies on other

alloys, was not applied. Six samples (with dimensions of $30 \times 10 \times 6\,mm^3$) were machined from the forgings and austenitized in a salt bath at 1150 ℃ for $5\,min$. One of the samples was water quenched directly from 1150 ℃. The remaining samples were transferred directly to another salt bath and held at 700 ℃ for periods in the range $3\,min$ to $600\,min$ and water quenched (see Supplementary Data 10.1). Approximately $0.5\,min$ was removed from the surfaces prior to SANS analysis or further sample preparation for microscopy.

4.3.2. Materials characterization

Samples were sectioned and metallographically prepared by the normal methods. Scanning electron microscopy (SEM) was conducted using an FEI Quanta 650 FEG-SEM operated at a voltage of $20\,kV$. Specimens were given a final polish with a colloidal silica suspension (OPS) and etched with 2% Nital.

For examination in the transmission electron microscope (TEM), samples were prepared by mechanical grinding/polishing to 50 µm thickness and then twin-jet electro-polished in a solution of 10 vol.% $HClO_4$ mixed with $90\,vol.\%$ CH_3COOH at approximately -15 ℃. TEM observations were performed using a JEOL 2100 scanning TEM operating at $200\,kV$ equipped with $80\,mm^2$ silicon drift EDS detector (SDD) Oxford Instruments X-Max; aperture size $5\,nm$ was used for STEM-EDS acquisition. Additionally, to examine in more detail the sample heat-treated for $600\,min$, a FEG-TEM FEI Talos F200X operating at $200\,kV$ with four integrated Super-X SDD EDS detectors at a detection angle of 0.9 srad was used for high-resolution imaging and elemental mapping of vanadium. In this case, a modified focused ion beam (FIB) lift-out method was used to prepare foils $\sim 120\,nm$ in thickness. The modified FIB preparation procedure involved an initial standard sample lift-out preparation with $25\,kV$ Ga-ions followed by a final low energy Ga-ion milling at $500\,V$ and at an angle of $12°$ on both sides of the TEM foil sample [167]. This was designed to minimise the level of ion-

induced damage due to surface re-deposition, amorphisation and implantation and to allow accurate observation of nano-scale features.

The average precipitate diameters in the samples aged for $5\,min$ and for $600\,min$ were measured from bright field TEM images and STEM-EDS maps by exporting them to ImageJ software [168]. Assuming that all precipitates have either oblate spheroid or disc-shaped morphologies an individual particle diameter was calculated as being equal to the calibrated diameter of the major axis (long axis) on the image plane. For each ageing condition, a minimum of 160 precipitates, both random and interphase, were analysed from a total of 20 TEM images.

The micro-hardness (Hv) of isothermally transformed samples was measured using a Wilson VH3100 micro-hardness tester with a load of $0.1\ kgf$. In partially transformed samples, indents were placed only within the ferrite grains. The mean value of 25 measurements from 25 individual grains is reported and the error is given as one standard deviation.

4.3.3. SANS experimental method

Small angle neutron scattering (SANS) experiments were performed on the SANS2d beamline at the ISIS Pulsed Neutron Source, UK [169]. A schematic of the experimental setup is shown in Figure 4.3-1. Small angle scattering arises from nanoscale precipitates embedded in the ferritic matrix (as shown in Figure 4.3-1 (a) and (b)) as well as larger-scale structural features. A magnetic field of $1.5\ T$ was applied in a horizontal direction parallel to the sample surface (i.e. perpendicular to the neutron beam) sufficient to saturate the α-Fe matrix and suppress multiple scattering. Polychromatic neutrons ($\lambda_N = 1.7\ to\ 16.5$ Å) were used but only wavelengths in the range of $4.7 - \ 16.5$ Å were selected for data analysis in order to avoid multi-Bragg diffraction [170–172]. Samples of approximately $10 \times 10 \times \sim 1\ mm^3$ were polished to $1\ \mu m$ diamond surface

finish and exposed for $60\,min$ to a neutron beam of $8\,mm$ diameter. The detector configuration gave a small angle scattering vector (q) range of $0.004 - 0.3\,\text{Å}^{-1}$, where $q = 4\pi \sin\left(\frac{\theta}{\lambda_N}\right)$ and the scattering angle is 2θ. Absolute SANS intensities were obtained using standard procedures through the use of a polymeric calibration standard [173]. Nuclear and "nuclear plus magnetic" scattering cross-sections were obtained by partial azimuthal averaging in $30°$ sectors around the transmitted beam as shown in Figure 4.3-1(c) leading to one-dimensional plots of scattering intensity, I, versus q (Figure 4.3-1(d)). (Further details in Supplementary Data 10.2).

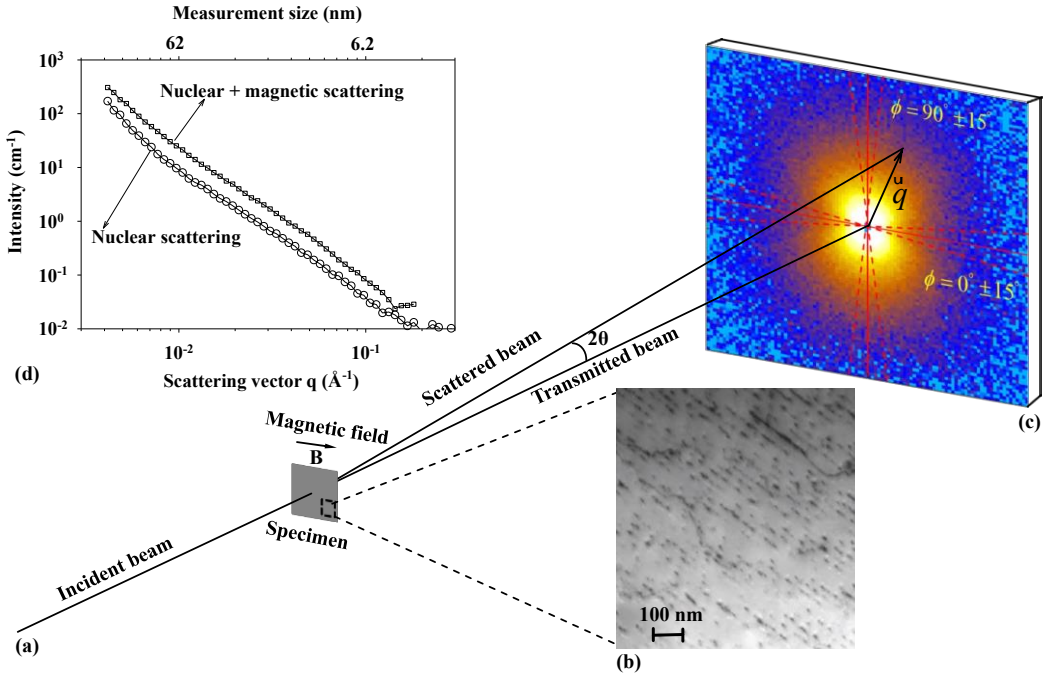

Figure 4.3-1 Experimental configuration used in the current SANS measurements. (a) An incident neutron beam transmitted through a specimen containing (b) nano-sized precipitates embedded in a ferritic matrix. (c) The resultant SANS two-dimensional pattern in the presence of a horizontal magnetic field. (d) The one-dimensional plot of the 'nuclear+magnetic' and nuclear scattering intensities.

4.3.4. SANS data reduction and analysis method

If the precipitates are assumed to be non-interacting particles then the SANS scattering intensity, I, of the particle dispersion is given by

$$I(q) = (\Delta\rho)^2 \int_0^\infty N(r)V(r)^2F(q,r)^2\,dr$$

(4.3-1)

where $\Delta\rho$ is the difference in the scattering length densities of the particle and the matrix, $N(r)dr$ is the number density of particles with size between r and $r + dr$, $V(r)$ is the volume of a particle of size r and $F(q,r)$ is the form factor for the particles and q is the scattering vector [172,174,175].

Neutron scattering contrast has both a magnetic, $\Delta\rho_{mag}$, and a nuclear, $\Delta\rho_{nuc}$, contribution. In a field that magnetizes the matrix to saturation, $I(q)$ depends on the angle ϕ between the scattering vector and the magnetic field. Thus $\Delta\rho$ in Equation. (4.3-1) can be written as

$$(\Delta\rho)^2 = (\Delta\rho_{nuc})^2 + \left(\Delta\rho_{mag}\right)^2 sin^2\phi$$

(4.3-2)

Figure 4.3-1 (c) shows an example of a two-dimensional detector image arising from this effect. The nuclear scattering intensity is measured along $\phi = 0°$ and the sum of nuclear and magnetic scattering along $\phi = 90°$. To produce one-dimensional scattering profiles (Figure 4.3-1 (d)) azimuthal data integration from $-15° < \phi < 15°$ was employed to determine nuclear scattering and between $75° < \phi < 105°$ to find nuclear plus magnetic scattering.

When the matrix is magnetized to saturation, and the chemical size of the precipitates is the same as their magnetic size, the ratio $R(q)$ depends on their chemical composition through the dependence of $\Delta\rho_{nuc}$ on precipitate chemistry.

$$R(q) = \frac{I_{mag}(q)}{I_{nuc}(q)} = \left(\frac{\Delta\rho_{mag}}{\Delta\rho_{nuc}}\right)^2$$

(4.3-3)

If all precipitates have the same composition then $R(q)$ is constant. However, $R(q)$ will vary if either there is more than one type of precipitate present of differing size or the precipitate composition is size dependent [162].

The model-independent analysis presented in this work (assuming disc-shaped IP precipitates) of the particles is based on the Guinier, Kratky and Porod representations of the absolute scattering intensity data and follows standard methods [174–176].

A radius of gyration, R_{g1}, is calculated from the Guinier plot (which takes the form of $\ln(I)$ *vs* q^2) using a self-consistent method with $1 < R_{g1} < 2$. It should be noted that in principle this is only strictly valid for single no-interacting particles [172].

For a distribution of monodispersed thin discs of thickness, T, and radius, R, the relationship between T, R and R_{g1} is given by [176]:

$$R_{g1}^2 = \frac{T^2}{12} + \frac{R^2}{2}$$

(4.3-4)

A second Guinier plot of $\ln[q^2(I)]$ vs q^2 is known to give a radius of gyration, R_{g2}, that is related to the thickness, T, of a disc.

$$R_{g2} = \left(\frac{T^2}{12}\right)^{1/2}$$

(4.3-5)

However, for polydisperse distributions, there is not a simple relationship between R_{g1}, R_{g2} and mean particle dimensions as discussed in detail by Deschamps and De Geuser [174].

In the Kratky plot, Iq^2 is plotted versus q and a characteristic particle size, R_{max}, (the "pseudo Guinier radius",) can be determined from the maximum, q_{max}, in the plot [174].

$$R_{max} = \frac{\sqrt{3}}{q_{max}}$$

(4.3-6)

Equation (4.3-6) also gives an estimate of the Guinier radius. The validity of this expression has been shown to be true over wide range of dispersion [174].

The volume fraction of precipitate, f_v, in a dilute incompressible two-phase system is also obtained from the Kratky plot. The integrated small angle scattering, Q, (i.e. the Porod invariant) is given by

$$Q = \int_0^\infty I(q)q^2 dq = 2\pi^2(\rho_p - \rho_m)^2 f_v(1 - f_v)$$

(4.3-7)

where ρ_p and ρ_m are the scattering length densities (either nuclear or magnetic) of precipitate and matrix respectively. The q-range for integration was extrapolated to 10^{-5} Å^{-1} for low q and 10 Å^{-1} for high q with the Guinier equation and the Porod law respectively as recommended in reference [172]. Thus f_v can be found using the data in Supplementary Note 10.3. Deschamps and

De Guesser reviewed the accuracy of the predictions using Equation (4.3-7) [177]. Strictly Equation (4.3-7) is only valid for the homogeneous two-phase model with phases separated by a sharp interface. It should also be noted that the precise measurement of precipitate volume fraction requires the measurement of the integrated intensity from 0 to infinity which is experimentally impractical. This necessitates the use of extrapolations at either end of the q-range which often use simple rules that are themselves only valid when the precipitate population is monodisperse. Finally, the evaluation of the precipitate volume fraction is dependent upon the composition of the precipitate. However, in this work the SANS was undertaken using a saturating magnetic field, which allows the interrogation of the magnetic and nuclear scattering. The ratio between these two signals depends on the compositions of the matrix and precipitate and thus the composition of the precipitate can be approximated using the assumptions documented in Supplementary Note 10.3.

A model fitting analysis was also carried out based on physical understanding from the model-independent analysis and using the SasView software program [178]. Two kinds of form factor fitting functions were investigated based on precipitates being assumed to be either disc or an oblate ellipsoid of revolution shape (i.e. an oblate spheroid).
In the case of a disc, the form factor is given by

$$F_{disc}(q,R,T) = \frac{2J_1\big(qRsin(\alpha)\big)}{qRsin(\alpha)}\frac{sin\big(qTcos(\alpha)\big)}{qTcos(\alpha)}$$

(4.3-8)

where α is the angle between the axis of the thin disc, q the scattering vector, T the thickness of the disc and R is the radius. J_1 is a first order Bessel function.

For the ellipsoidal shape, the form factor becomes

$$F_{ellipsoid}(q, a, b) = 3\frac{sin[qr(a,b,\alpha)] - cos[qr(a,b,\alpha)]}{(qR)^3}$$

(4.3-9)

where,

$$r(a, b, \alpha) = (asin^2\alpha + bcos^2\alpha)^{0.5}$$

(4.3-10)

α is the angle between the axis of the ellipsoid and q, where b and a are the radii along and perpendicular to the rotation axis of the ellipsoid respectively; b is referred to as the polar axis and a is the equatorial axis.

4.4. Results and Discussion

4.4.1. Microstructural characterization

The SEM image of Figure 4.4-1 (a) shows the microstructure of the water quenched alloy which is seen to consist of acicular units, irregularly shaped laths and fine-scale precipitates. These features indicate the formation of an auto-tempered martensite and lower bainite. Figure 4.4-1 (b)-(f) show the microstructure of samples transformed at 700 ℃ followed by water quenching. Regions of bainite, which formed from untransformed austenite that was present at the time of quenching, are evident in Figure 4.4-1 (b)-(d). However, bainite is not visible in the samples transformed for $300\,min$ and $600\,min$ (Figure 4.4-1 (e) and (f)), indicating that transformation from austenite was complete prior to $300\,min$ of isothermal holding. In the SEM image of Figure 4.4-1 (f), IP precipitates are visible within the ferrite grains. These precipitates can be resolved in the SEM because they have coarsened as a result of the long holding time at 700 ℃.

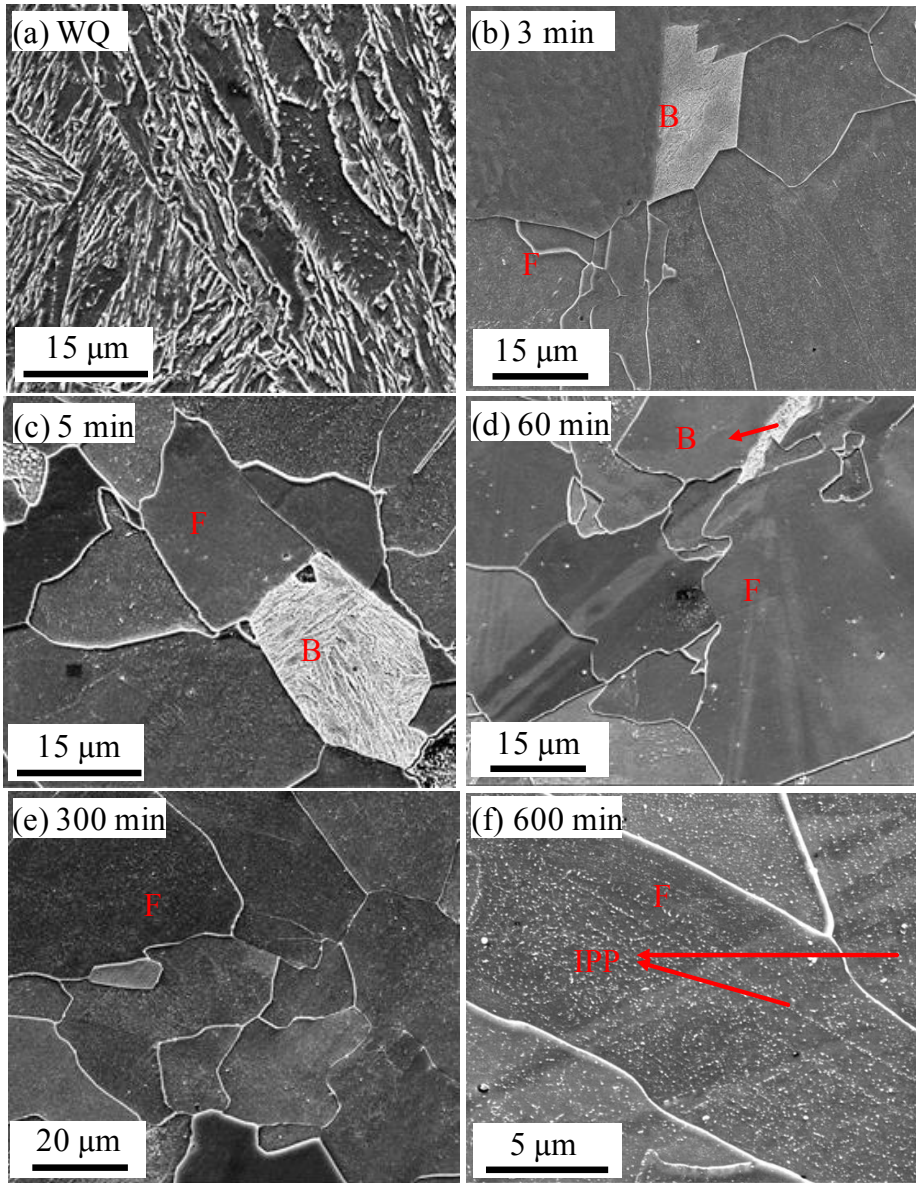

Figure 4.4-1 SEM images of the samples isothermally transformed at $700\ ^{\circ}C$ *for various times and water quenched. (a) directly water quenched; (b) – (d) isothermally transformed for* 3, 5 *and* $60\ min$ *respectively showing ferrite grains (F) and regions of bainite (B) (transformed* γ*). (e) and (f)* 300 *and* $600\ min$ *isothermal transformation times respectively. Coarsened interphase precipitates visible in (f).*

Bright field TEM images of the samples transformed at $700\ ^{\circ}C$ for $5\ min$ and $600\ min$ respectively are shown in Figure 4.4-2 (a) and (b). For both

transformation times, planar rows of carbide precipitates are observed which indicate that they have most probably been formed by interphase precipitation.

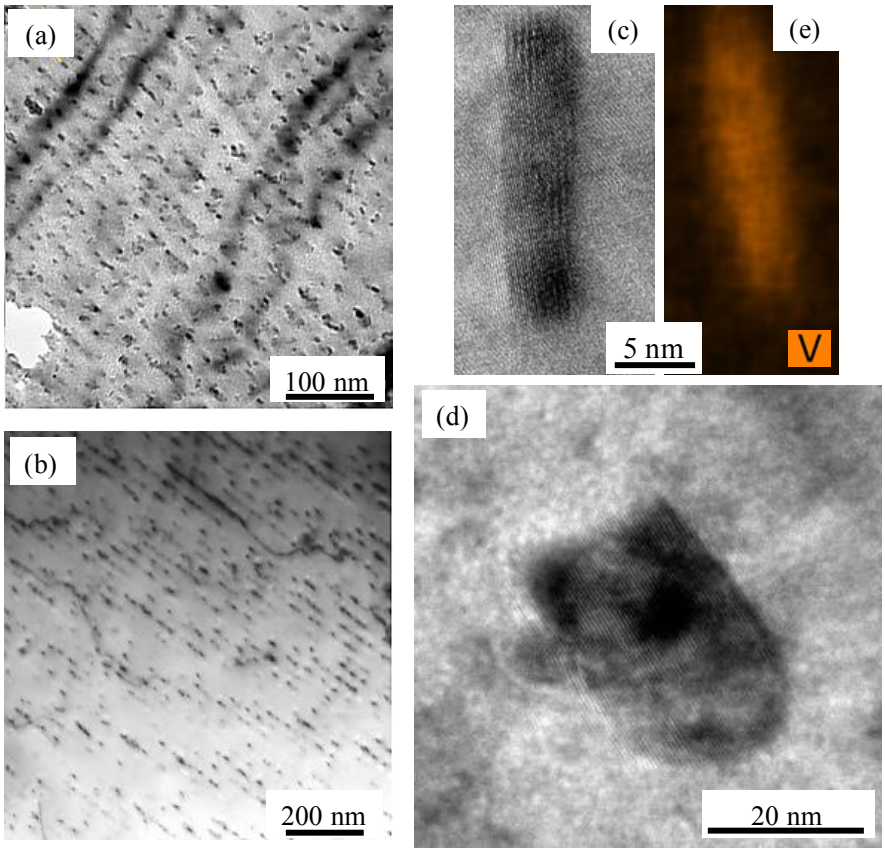

Figure 4.4-2 Bright field TEM images of periodic interphase precipitation taken from the samples isothermally transformed at $700\,℃$ *for (a)* $5\,min$ *and (b)* $600\,min$*. (c-d) High-resolution TEM lattice image from the sample held for* $600\,min$*, (d) elucidating the disc nature of the precipitates and (e) EDX map for vanadium.*

The morphology of the precipitates cannot be fully determined from these two images but is consistent with either a rod or disc-shape. Previous work has reported that IP precipitated vanadium carbides are not spherical but mostly elongated along the $(001)_{VC}$ plane to give an oblate spheroid (i.e. disc-shaped) morphology. This occurs because the $(001)_{VC}$ plane is a habit plane of VC and parallel to (001) plane in the ferrite [46,69]. Therefore, in this study, it was

assumed that the vanadium carbides also exhibit such a morphology. Figure 4.4-2 (c) and (d) show representative high-resolution TEM lattice images of the carbide precipitates in the sample held for $600\ min$ with an indexed diffraction pattern from the matrix in Figure 4.4-2 (d). The long axis diameter of the precipitates are around $21\ nm$ to $28\ nm$. The corresponding EDX map (Figure 4.4-2 (e)) confirms the precipitates are V-rich.

Precipitate size measurements, performed as described in Section 4.3.2 on TEM images and EDX maps, give a mean value for the long axis carbide diameter. After 5 min ageing, this was found to be $7.8 \pm 3.6\ nm$ and after $600\ min$ ageing, it was $27.8 \pm 8.0\ nm$ (where the errors correspond to the standard deviation in the data). The long axis measurement is consistent with the HR-TEM lattice image and the change in long axis diameter with ageing time indicates a significant coarsening effect.

4.4.2. Interpretation of small angle neutron scattering measurements

One-dimensional plots of intensity versus scattering vector extracted from the SANS data for the water quenched and isothermally transformed (3, 60 and $300\ [min]$) alloys are shown in Figure 4.4-3 (a)-(d) respectively. In the water quenched sample, only the nuclear signal closely follows a q^{-4} variation (i.e. the Porod Law) over the entire q-range until the background level is reached at $q > 0.1\ \text{Å}^{-1}$. This shows that the principal contribution to nuclear scattering is from the interface between scattering particles and the matrix where the particles are large-scale features typically $> \frac{2\pi}{q_{min}}$ (approx. $150\ nm$). These will typically be alloying element carbides, nitrides or sulphides formed during steel manufacture. The iron carbides present in the bainitic regions of the quenched alloy (Figure 4.4-1 (a)) make negligible contribution to the nuclear scattering pattern because of their small contrast factor (See Supplementary Data 10.3). If nanoscale VC precipitates had formed they would contribute strongly to the

nuclear signal due to their large contrast factor and so the q^{-4} behaviour of the nuclear signal indicates that there is no detectable nanoscale VC present following austenitization and quenching. However, the magnetic scattering signal deviates significantly from a q^{-4} behaviour over the range $0.004 < q < 0.05\ \text{Å}^{-1}$ because magnetic scattering is significant from iron carbide precipitates (they are not ferromagnetic and behave as magnetic "holes" in the matrix).

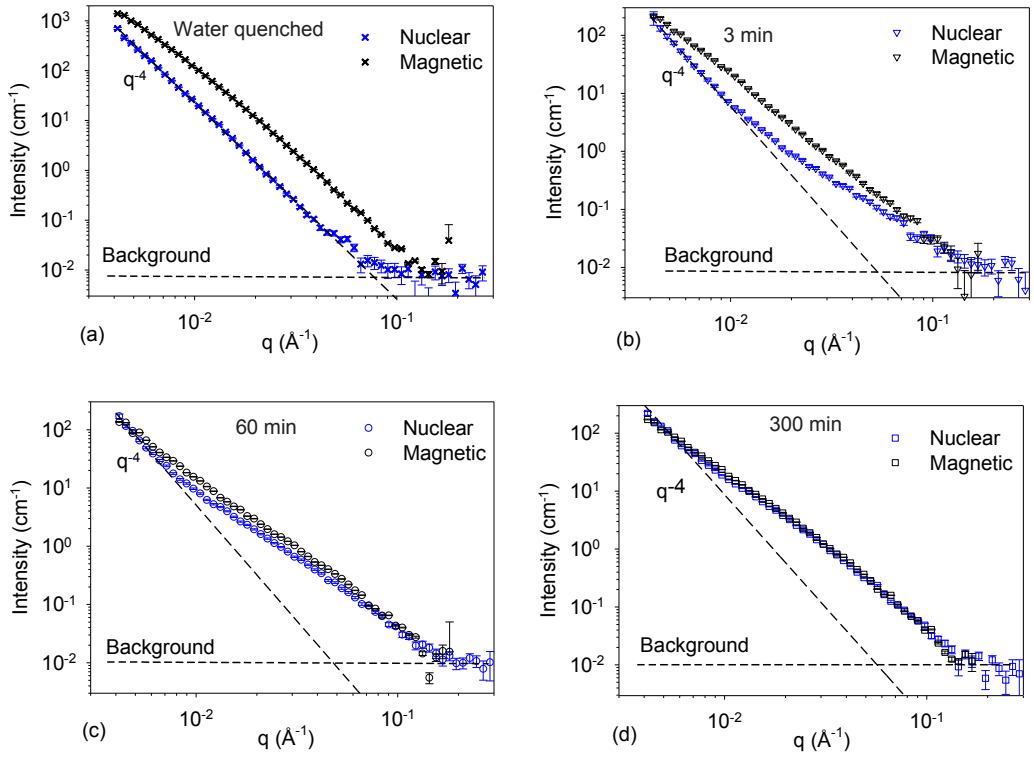

Figure 4.4-3 One-dimensional SANS patterns of intensity versus scattering vector obtained from the following samples: (a) water-quenched and (b) to (d) isothermally transformed. Transformation times of: (b) $3\ min$, (c) 60 min, (d) $300\ min$. In (a)-(c) there is a clear difference between nuclear and magnetic signals. In (d) they are virtually identical. The line of slope -4 is shown for reference on the log-log plot.

The SANS results obtained from the isothermally transformed samples which were water quenched following transformation times of 3, 60, and $300\ min$ are also shown in Figure 4.4-3. In Figure 4.4-3 (b) both magnetic and nuclear scattering intensities deviate from a q^{-4} Porod-type behaviour. In the case of the nuclear signal, the deviation at $q{\sim}0.01\ \text{Å}^{-1}$ arises from the formation of nanoscale ($d \leq 50\ nm$) VC precipitates, formed during the isothermal hold as seen in the TEM images of Figure 4.4-2. The magnetic signal shows a different behavior to the nuclear one due to the presence of residual islands of transformed austenite (i.e. bainite) (Figure 4.4-1 (b)-2(d)) which contain iron carbides. The magnetic signal thus has contributions from both the nanoscale VC and the somewhat larger iron carbide phases giving rise to a deviation from q^{-4} behavior at lower values of the scattering vector q (larger values of particle size). Figure 4.4-3 (c) shows similar features to Figure 4.4-3 (b) but the difference between nuclear and magnetic signals is diminished due to the reduced fraction of bainite in the microstructure following $60\ min$ transformation followed by quenching, giving a reduced quantity of iron carbide compared to the shorter ageing time. The magnitude of the nuclear signal is evidently increased as a result of a greater phase fraction of VC and the signal covers a larger range of scattering vector, q. Following $60\ min$ transformation, the nuclear and magnetic signals are similar, consistent with the very small volume fraction of bainite seen in Figure 4.4-1 (d). In Figure 4.4-3 (d), the nuclear and magnetic signals have a similar magnitude over the entire q-range following $300\ min$ transformation. Two factors contribute to this. First, the nuclear and magnetic contrast factors of VC are similar (Supplementary Data 10.3). Secondly, isothermal transformation of austenite to ferrite was complete following a $300\ min$ hold and hence there was no additional scattering contribution from iron carbides. Thus, the large overall scattering signal above the Porod background is due to the nanoscale VC precipitates as seen in the TEM images of Figure 4.4-2. The 1-D pattern for the sample transformed for $600\ min$ is not shown but it has very similar features to Figure 4.4-3 (d).

Figure 4.4-4 shows the ratio of magnetic to nuclear scattering ($R(q)$ versus q, Equation (4.3-3)) for the water quenched and isothermally transformed samples. For the water quenched sample, the plot has a maximum value of 10.5 at $q{\sim}0.04$ Å. This implies the magnetic scattering signal was raised by iron carbide particles ranging in size from 15 to 150 nm. The dependence of $R(q)$ on q decreased significantly with increasing transformation time and the maximum value of $R(q)$ shifted to smaller q values indicating an increase in the size of the iron carbides in the bainite formed on quenching as well as the formation of a second type of precipitate with a much lower $R(q)$ value, presumably the vanadium carbide precipitates.

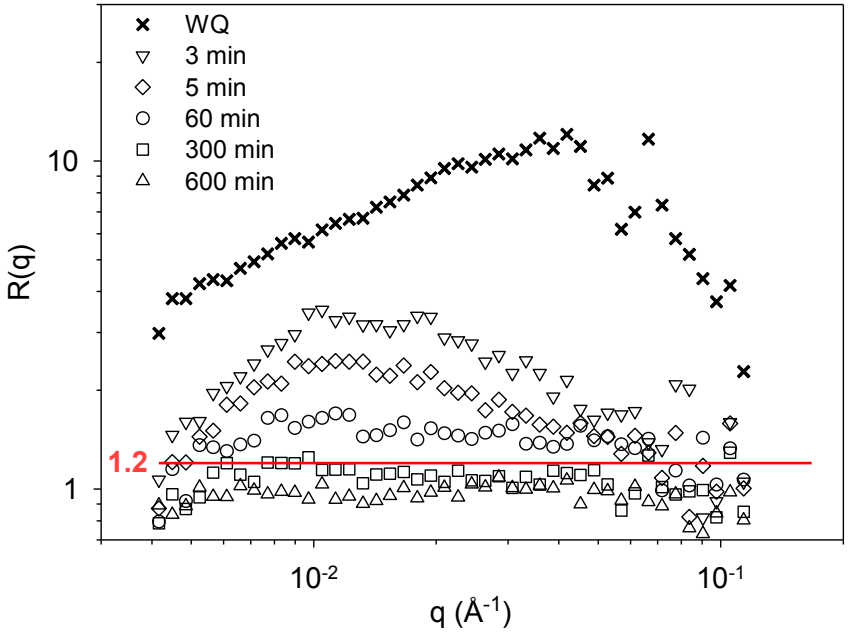

Figure 4.4-4 Plot of $R(q)$ versus scattering vector calculated from the scattering curves in Fig. 4 for the water-quenched alloy and for the samples isothermally transformed for the times shown. $R(q)$ is the ratio of magnetic to nuclear scattering intensity (equation 3). The theoretical value for VC is shown by the horizontal line.

Table 4.4-1 Calculated precipitate characteristics determined from model-independent analysis of SANS data for samples isothermally transformed for different times. R_{g1}, R_{g2}, R_{max}, and f_v are defined in section 3. $R(q)$ is the ratio of magnetic to nuclear scattering intensity

Transformation time (min)	R_{g1} (nm)	R_{g2} (nm)	R_{max} (nm)	Mean R(q)	f_v (mean R(q))	f_v (constant $\Delta\rho_{nuc}$)
3	6.9	0.8	4.4	-	-	0.009
5	8.3	0.9	5.2	-	-	0.013
60	10.6	1.0	6.8	-	-	0.018
300	13.0	1.7	9.8	1.09	0.021	0.024
600	15.5	2.3	12.6	0.98	0.022	0.028

The austenite to ferrite transformation was completed in the samples transformed for 300 and $600\,min$ and the corresponding values of $R(q)$ are almost independent of q and close to 1. This is consistent with the formation of a single V-containing carbide, the composition of which is independent of size. However, the mean value decreases slightly with transformation time (*Table 4.4-1*), which could be due to the mean carbide composition changing with time.

4.4.3. Determination of precipitate characteristics and the effect of transformation time

Further analysis of the changing VC volume fraction, size and size distribution during isothermal transformation is based on the 1-D nuclear data shown in Figure 4.4-3, with the removal of (i) the effect of Porod Law scattering (large particles) and (ii) the incoherent background [172]. Figure 4.4-5 (a) shows the intensity, I, versus scattering vector, q, the Kratky representation (Iq^2 versus q) is shown in Figure 4.4-5 (b), Figure 4.4-5 (c) is the first Guinier representation ($\ln(I)$ versus q^2) and Figure 4.4-5(d) is the second Guinier representation ($\ln(\mathrm{q^2I})$ *vs* $\mathrm{q^2}$).

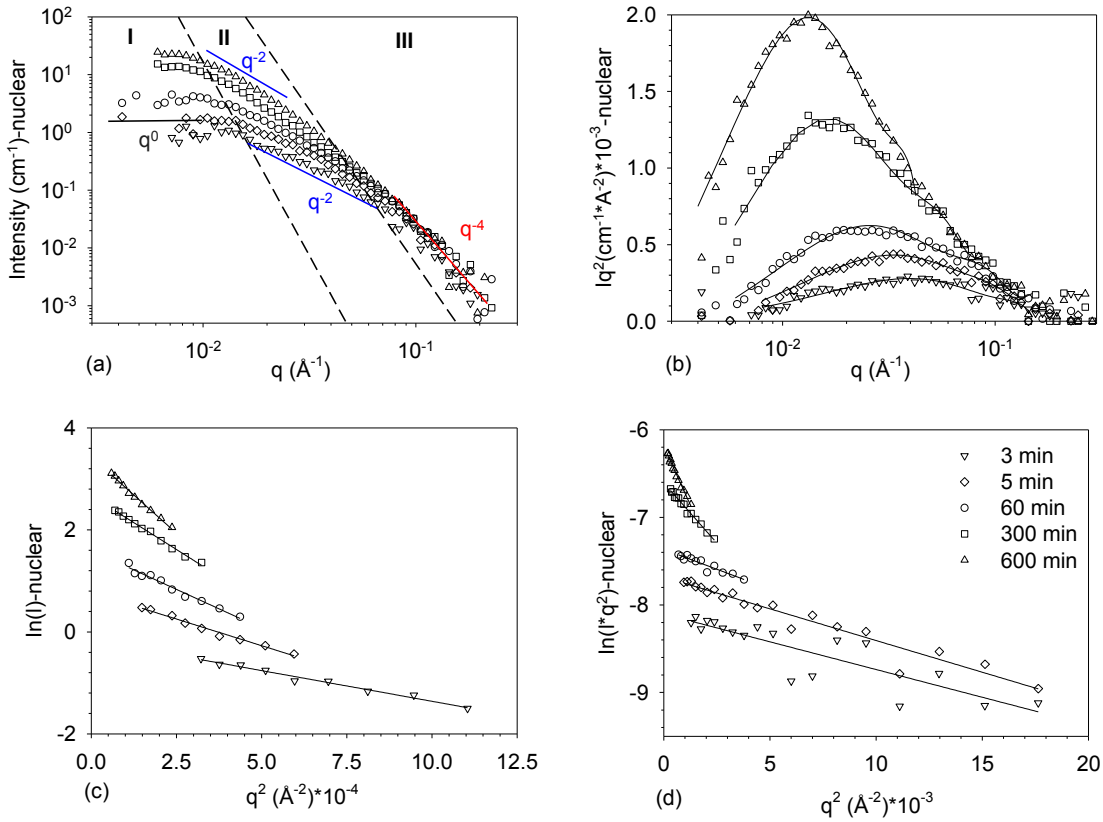

Figure 4.4-5 SANS nuclear scattering data from the samples isothermally transformed at $700\,℃$ *following subtraction of Porod Law behaviour and incoherent scattering background. Transformation times shown by the symbols on the plots. (a) Plots of* I *versus* q*; (b) the corresponding* Iq^2 *versus* q *Kratky plots; (c) the first Guinier plot of* $ln(I)$ *versus* q^2*; (d) the second Guinier plot of* $ln(q^2 I)$ *versus* q^2*.*

i. Principal features of the I(q) versus q plots

It is clear from Figure 4.4-5 (a) that the I versus q^n power law exponents depend on the q range. At low q (region I) and high q (region III) ranges, the exponent is found to have values of 0 and -4 respectively. The exponent zero corresponds to the Guinier regime which probes real space regions of size q^{-1}; ie regions >> precipitate sizes [179]. The exponent -4 relates to the Porod regime which probes the interfaces between the precipitate and the matrix. The scattering

intensity is related to the precipitate surface area per unit volume. The intermediate q region (II) follows an exponent of approximately -2 as indicated in Figure 4.4-5 (a). In this regime, the slope is related to the shape of the precipitate and q^{-2} indicates that the precipitates are thin discs or oblate spheroids [177] and so this slope is consistent with the precipitate morphology observed in the TEM images (Figure 4.4-2).

ii. Precipitate size and precipitate volume fraction calculated from Kratky plot

The Kratky plots of Iq^2 versus q (where I is the nuclear intensity) for samples transformed for different times are shown in Figure 4.4-5 (b). These plots provide a visual indication of volume fraction and size of the VC precipitates. The precipitate volume fraction is calculated from the area under the Kratky plot (Equation (4.3-7)) whilst, q_{max} (Equation(4.3-6)) provides an estimate of the particle size which is termed the pseudo-Guinier radius, $R_{max.}$ Numerical curve fitting was used to find q_{max} and R_{max} values. The values obtained for volume fraction, $f_{v,}$ and R_{max} are listed in *Table 4.4-1* and it is evident that both of these increase with transformation time. The different sets of values for f_v arise from the different assumptions made in applying Equation (4.3-7). In one case, it was assumed that the precipitate had the stoichiometric VC composition giving a constant nuclear contrast factor in the calculation of f_v. In the other case, a mean $R(q)$ value (taken from Figure 4.4-4) was used to calculate the nuclear contrast factor on the assumption of a constant magnetic contrast factor (see Supplementary Note 10.3). It was only possible to perform mean $R(q)$ estimates for the fully transformed samples i.e. the 300 and $600\,min$ transformation times. Only these times were used as the $\gamma \rightarrow \alpha$ transformation is completed and therefore there is no residual austenite that can decompose forming iron carbides on quenching. The values obtained from the constant nuclear contrast calculation probably represent an upper-bound value for f_v.

Considering now the interpretation of the pseudo-Guinier radius R_{max} it is shown in reference [174] that the relationship between R_{max} and the mean particle radius depends on both the value of the dispersion parameter and also on the aspect ratio of the precipitate. Despite this limitation, the increase in R_{max} with transformation time shown in *Table 4.4-1* suggests a marked coarsening behaviour of the precipitate population with the transformation time when held at 700 ℃.

iii. Precipitate size calculated from Guinier plot

Plots of the Guinier equations used to derive $R_{g1}(\ln(I)\ vs\ q^2)$ and $R_{g2}(\ln(I)\ vs\ q^2)$ from the gradients are displayed in Figure 4.4-5 (c) and (d) respectively and values of R_{g1} and R_{g2} are listed in *Table 4.4-1*. In both cases, self-consistent methods were applied for the boundaries of the linear gradient fitting [174]. Clearly, these parameters increase with transformation time, which correlates with the change in R_{max} and indicate a progressive increase in precipitate dimensions.

Table 4.4-2 Average precipitate dimensions determined from analysis of SANS data for samples isothermally transformed for different times. R and T are the average radius and thickness of precipitate discs determined from the Guinier measurements of R_{g1}, R_{g2}. a and b are average equatorial and polar radii respectively from model fitting with an oblate spheroid. ($2b$ is polar diameter for direct comparison with T). σ is the dispersion parameter of a in model fitting.

Transformation time (min)	**Calculated from Guinier measurements**		**Oblate spheroid model fitting (σ =0.2)**	
	R (nm)	**T (nm)**	**a (nm)**	**2b (nm)**
3	9.8	2.8	9.1	2.7
5	11.6	3.0	10.4	2.8
60	14.9	3.3	11.5	3.3
300	18.2	5.7	14.8	4.8
600	21.7	8.0	17.5	6.2

The limitations of the classical Guinier approach in calculating average particle dimensions for polydisperse systems are well documented [174]. Nonetheless, estimates of disc radius, R, and thickness, T, of the assumed disc-shaped VC precipitates based on the Guinier approach can give valuable size data, recognizing that they represent particle ensemble information, and are given in Table 4.4-2 as calculated using Equations (4.3-4) and (4.3-5). These show that both radius and thickness increase significantly and the aspect ratio of the particles is seen to be around $3-4$ and changes little with transformation time. The Guinier radii after $5\ min$ and $600\ min$ ageing time of $11.6\ nm$ and $21.7\ nm$ respectively are larger than the mean TEM radius values of 3.9 and $13.9\ nm$ respectively. It is evident that both techniques measure significant coarsening at 700 ℃.

iv. Precipitate size calculated from shape dependent model fitting

Thus far each of the model independent SAS analysis methods have implicitly assumed a monodisperse particle size distribution although, in each the extracted precipitate characteristics are known, as discussed, to be reasonably strong estimates of the true values. Deschamps and De Gueser [174] showed that when analysing SAS data where the sample contains ellipsoid-shaped particles the model independent analysis methods above are almost not affected for aspect ratios in the range 0.5–2. However, for larger aspect ratios, which is apparent in this study, differences occur, and the Guinier radius should be quoted with caution. In such cases, Deschamps and De Gueser [174] stated that a full model fitting should be undertaken [174]. In order to refine the real-space precipitate size characterization in this study and remove the assumption of monodipersity model fitting was undertaken using the SasView software program [178]. At this point it should be noted that the process of model fitting requires *a priori* knowledge of the shape, size of the precipitates. For each of these parameters the estimates provided by the model independent analyses above are used.

This analysis employed two different precipitate shape models namely a disc shape (radius, R_c, and thickness, T_c, as given in Equation (4.3-8)) and an ellipsoid of revolution (polar axis, b, and equatorial axis, a, as given in equation (4.3-9)). An ellipsoid of revolution is also referred to as an oblate spheroid and this term will be used hereafter. The disc model was considered in order to be consistent with the Guinier analysis presented in the previous section whilst the oblate spheroid shape was chosen as this shape has been one that has been assumed in previous work on the IP of VC studied by TEM e.g. in reference [69]. In both cases, the precipitates were assumed to have a lognormal size dispersion of the major axis (i.e. R_c for the disc and the equatorial axis, a, for the oblate spheroid). The magnitude of the dispersion was expressed in terms of the dispersion parameter, σ, which is the standard deviation of the lognormal

distribution. The ratio between disc thickness and spheroid polar radius (i.e. the aspect ratio) was assumed to have a zero-dispersion parameter.

The calculated 1-D nuclear scattering profiles were then sequentially fitted to the experimental 1-D scattering curves using, as fixed parameters, the precipitate volume fractions, obtained from Equation (4.3-7), and the contrast between precipitates and ferrite matrix calculated from $R(q)$ (*Table 4.4-1*). The starting estimates in the model for the disc mean radius and half-thickness (major and minor axes respectively in the case of the oblate spheroid) were the R and T values found from the Guinier analysis which assumed the precipitates to be monodisperse. The goodness of fit between experimental and calculated 1-D scattering profiles was determined using the well known chi-squared quantity for all computations. The effect of altering the dispersion parameter in the range 0 to 0.5 was explored and it was found that consistently better fitting was obtained with values of σ in the range 0.1 to 0.3 than for larger values of σ. The Supplementary Data 10.4 provides a summary of the calculations for both shapes and for different dispersion values.

It should be noted, both the disc and oblate spheroid models give acceptable fitting results with very little difference between them for all ageing times, the results (mean equatorial radius of particles, a, and mean polar radius, b) given by the oblate spheroid model for the mid-point polydispersity value, $\sigma = 0.2$ are reported here (there was little difference in goodness of fit for σ in the range 0.1 to 0.3) and the reader is referred to the Supplementary Data 10.4 for the extended calculations.

Figure 4.4-6 shows representative full model fitting plots using the oblate spheroid model with $\sigma = 0.2$. There is clearly good agreement over the full q-range for all the transformation times. The mean values of particle dimensions obtained from the model calculations are listed in Table 3 (where the dispersion

parameter has been taken to be 0.2) along with the values of R and T determined from the Guinier measurements of Figure 4.4-5 (c) and (d). It is evident that there is generally reasonable agreement between R and a although some larger discrepancies do arise in thickness values at the longest ageing time where the Guinier analysis gives somewhat greater values.

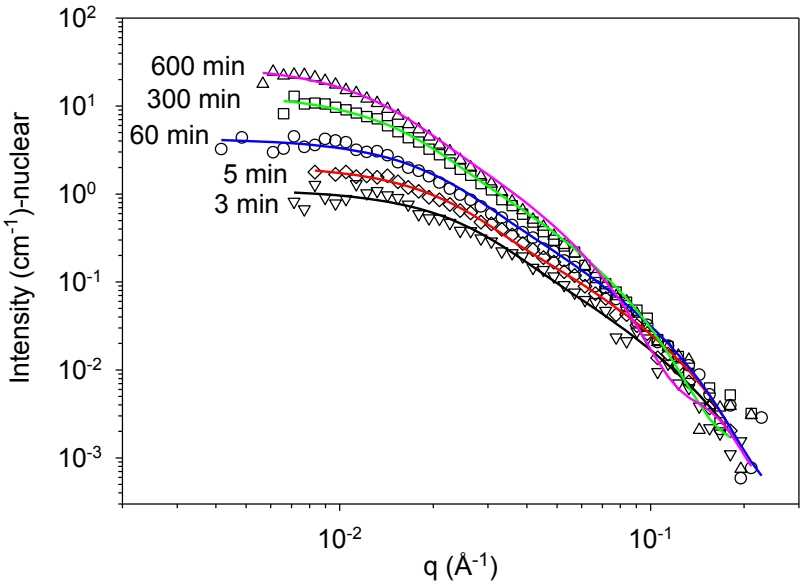

Figure 4.4-6 Experimental SANS nuclear scattering data plotted as I versus q from samples transformed for the times shown (symbols) along with model fitted data (solid lines) using an oblate spheroid model with dispersion parameters of 0 and 0.2 for the polar and equatorial radii respectively.

The data listed in Table 4.4-2 for the Guinier measurements and the oblate spheroid model fitting are plotted in Figure 4.4-7 and the error bars on the model fitting data points correspond to uncertainties generated from the calculations. Overall, there is seen to be good agreement between particle radius and thickness from the Guinier method calculations and from the model fitting.

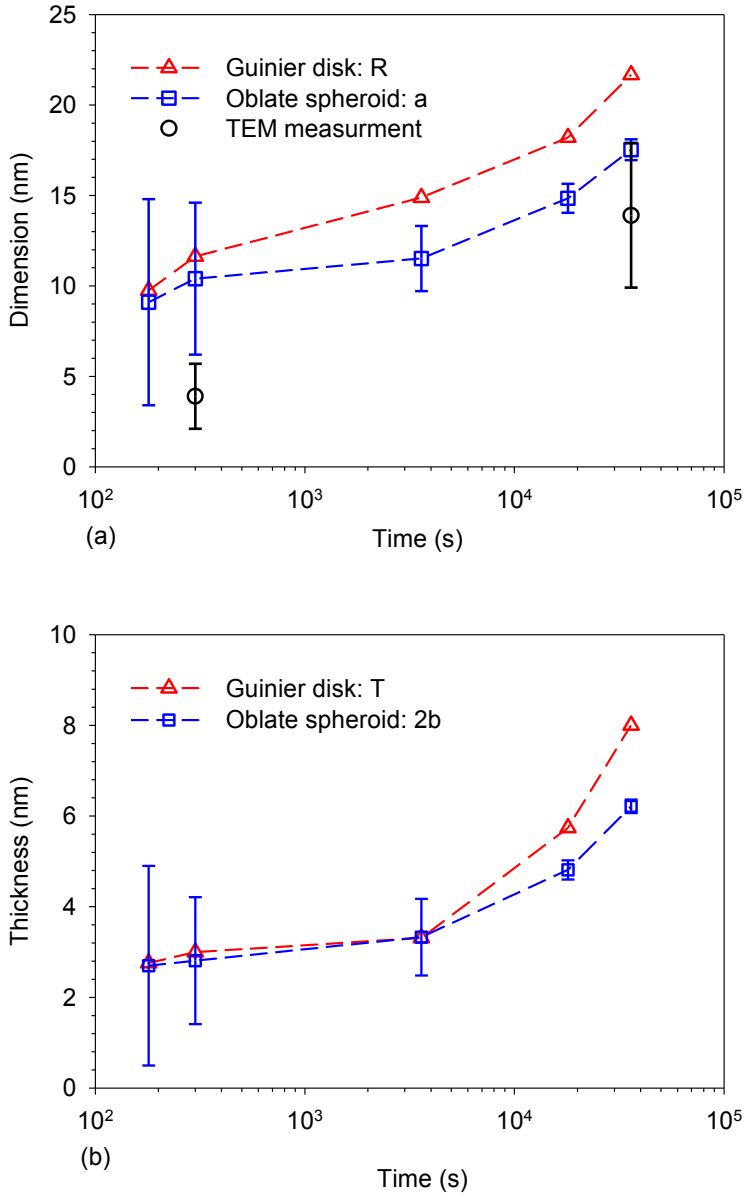

Figure 4.4-7 Graphs to show the effect of isothermal holding time, t on particle dimensions obtained from Guinier analysis and model fitting. Data are shown for R (radius) and T (thickness) calculated from Guinier plots and a and $2b$ from oblate spheroid model fitting. (a) is a plot of R and a (oblate spheroid major axis) versus time; (b) is a plot of T and $2b$ (b= oblate spheroid minor axis) versus time. TEM measurements are radii calculated from major axis diameters (size distribution shown in Supplementary Note 10.5).

4.5. Further Discussion

This section, considers, first, the evidence from the SANS data regarding the composition of the vanadium-containing precipitates and secondly the effect of the particle size and volume fraction on the strengthening contribution of IP to the ferrite phase.

4.5.1. Effects of transformation time on composition of MX precipitates

Information on the chemical composition of the precipitates (more generally written as MX where M=V, Fe and X=C, N) can be gained from the ratio $R(q)$ of those samples in which the γ has fully transformed to α and there is no residual martensite or bainite in the microstructure following quenching, i.e. 300 and $600\ min$ transformation times. The mean $R(q)$ decreases from 1.09 to 0.98 (*Table 4.4-1*) suggesting a change in composition of the MX phase. For stoichiometric VC, the value of $R(q)$ from the contrast factors in Supplementary Data 10.3 is 1.23. The contrast factor for VN is larger than for VC so the substitution of N into the MX phase in place of C cannot provide an explanation for the difference.

Thermodynamically it is feasible for Fe to substitute for V. Using Thermo-Calc and the TCFE7 database the full equilibrium calculation predicts $0.08\ mol\%Fe$ at 700 ℃. However, Fe substitution decreases the nuclear contrast factor, increases $R(q)$ and is not a consistent explanation. An alternative to be considered is that the carbide phase is sub-stoichiometric with respect to carbon. This would lead to a higher nuclear contrast factor and hence a reduction in $R(q)$ in line with the experimental measurements.

Assuming a composition $VC_{0.90}$ gives a theoretical $R(q)$ of ~ 1.1 which is close to the experimental value for the $300\ min$ sample. This value is within the range of

possible compositions reported by Baker [77] and several researchers have measured a similar sub-stoichiometry. For example, Oba *et al.* [166] found that in a medium carbon steel the value of x $(x < 1)$ in VC_x is dependent on the transformation temperature whilst Zhang *et al.* [92] used APT to shows that x is about 0.81 in Fe-0.1C-0.4V alloy isothermally transformed at $690\,℃$ for 48 hours. Furthermore, Ishiguro and Sato [180] used electron energy loss spectroscopy (EELS) to identify non-stoichiometric MC_x in ultra-low carbon micro-alloyed steels with x in the range 0.82 to 0.91. Overall, a sub-stoichiometric vanadium carbide seems a possible explanation for the present $R(q)$ measurements.

4.5.2. Effect of transformation time on precipitate size and volume fraction

The SANS data clearly demonstrate that changes in size and volume fraction (f_v) of IP precipitates in a low carbon micro-alloyed steel during isothermal ageing at $700\,℃$ can be quantified.

There is a steady increase in f_v with transformation time which continues after the γ to α transformation is complete (*Table 4.4-1* and Figure 4.5-1 (a)) which suggests growth of the carbide from supersaturated ferrite (α). Depending on the assumptions about the scattering length densities, the volume percent after $600\,min$ is in the range 0.022 to 0.028. This is consistent with the equilibrium volume fraction of 0.030 calculated using Thermo-Calc and the TCFE7 database.

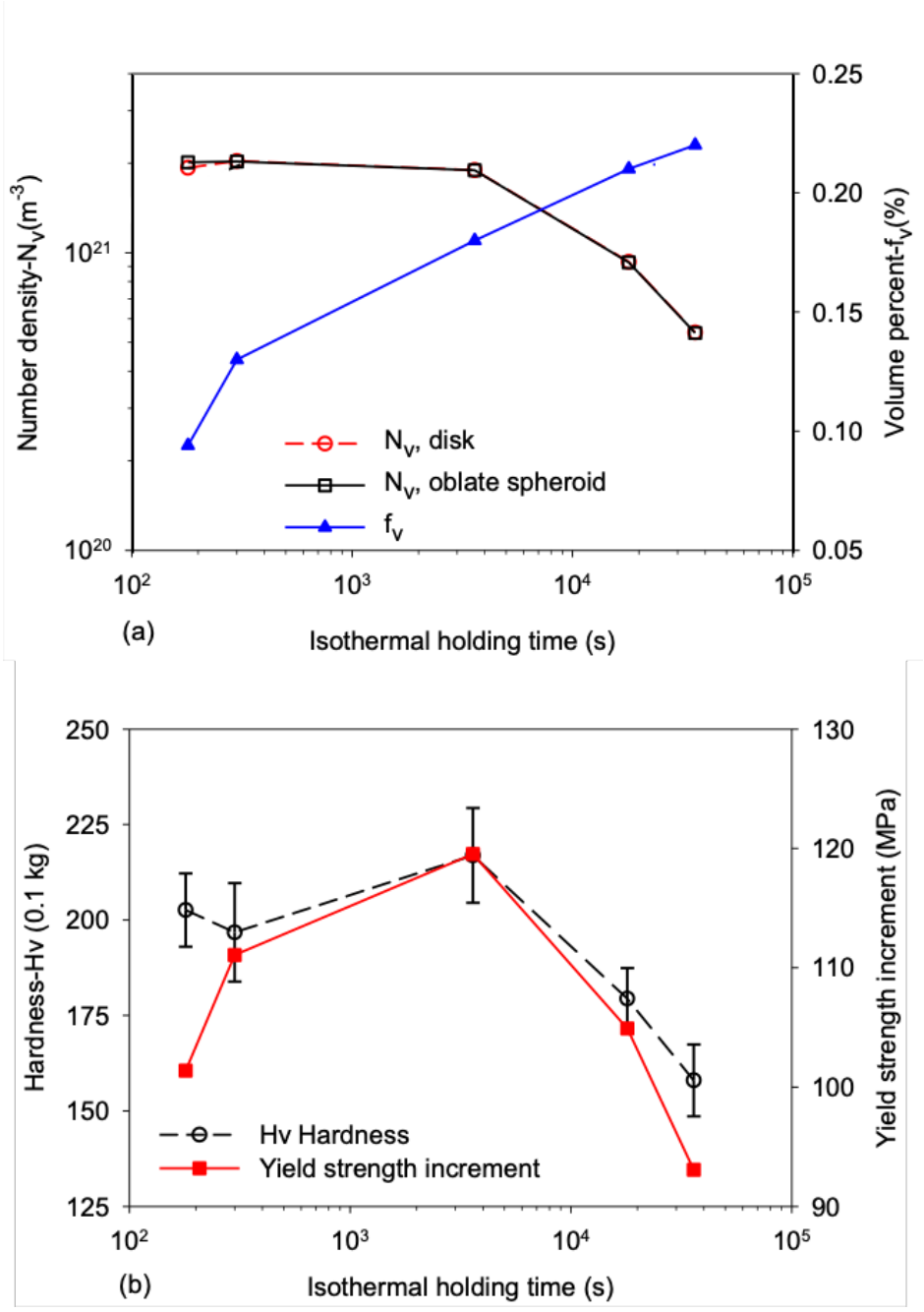

Figure 4.5-1 Effect of isothermal holding time, t, on precipitate number density (left-hand axis) and volume fraction (right-hand axis) determined from SANS data. (b) Effect of isothermal holding time, t, on measured micro-hardness, Hv, (left-hand axis) and calculated yield strength increment (right-hand axis). Error bars in Hv correspond to one standard deviation from the mean.

In the present work, it is clear that precipitate dimensions, as represented by Guinier and pseudo-Guinier radii both increase with ageing time at 700 ℃. Real space particle dimensions cannot be derived from the above model-independent parameters analytically for polydisperse precipitate distributions [172,174,177] However, from model fitting, both an oblate spheroid and disc model are found to give good fits to the data and to be in very reasonable agreement with disc radius and thickness from the Guinier analysis. In Figure 4.4-7, dimensions from Guinier analysis are compared with the oblate spheroid dimensions from model fitting. When the SANS results are compared with the somewhat limited TEM values, the observations of an increase in radius with ageing time agree, as seen in Figure 4.4-7 (a) but the TEM values are seen to be consistently smaller than those obtained from SANS. However, it is not surprising that there is a discrepancy since the SANS measurements include orders of magnitude more measurements than the TEM and the SANS measurements will include random and grain boundary precipitates as well as the characteristic aligned rows and sheets of interphase precipitation. Therefore, SANS will tend to measure a larger precipitate size than the TEM method and the latter may well be biased to the IP precipitates with a row and sheet morphology.

The measured increase in precipitate radius and thickness with ageing time is consistent with the increasing volume fraction that is measured and is attributed to carbide growth from supersaturated ferrite. To examine whether precipitates also undergo Ostwald ripening (coarsening) the number density, N_v, was calculated based on the mean precipitate volume at each transformation time and the variation of N_v with time is also shown on Figure 4.5-1 (a). Coarsening (decreasing N_v) is significant when ageing times exceed $60\ min$ $(3600\ s)$ which correlates approximately with the completion of the γ to α transformation (i.e. the cessation of nucleation of new carbides by interphase precipitation). N_v is insensitive to whether disc or oblate ellipsoid shapes are considered.

Comparison of the present number density data with values reported by Zhang, Kamikawa and co-workers [46,74,92] on V-containing micro-alloy steels is not straightforward due to differences in alloy composition and transformation temperatures and the fact that either TEM or 3DAP were used to arrive at number density values. Zhang *et al.* [92] used 3DAP and found mean number densities of the order of $5 \times 10^{22}\ m^{-3}$ for a $0.2\ wt\%V$ steel transformed for $1\ min$ at 690 ℃. Zhang *et al.* [92] also show that the number densities of VC increases approximately 14 times when increasing the V content from $0.2\ wt\%$ to $0.43\ wt\%$. Kamikawa *et al.* [46] used TEM and measured inter-particle spacing in the range of $44\ nm$ to $78\ nm$ in $0.288\ wt\%V$ steels which had been transformed at 690 ℃ for $5\ mins$ to $300\ min$ at 690 ℃. This leads to number densities of $1.2 \times 10^{22}\ m^{-3}$ to $1.2 \times 10^{21}\ m^{-3}$ which (linearly scaled to the present V content of $0.2\ wt\%$ according to Zhang et. al.'s study [92]) are from $2.2 \times 10^{21}\ m^{-3}$ to $4 \times 10^{20}\ m^{-3}$ which agree well with the current SANS studies (Figure 4.5-1 (a)).

4.5.3. Precipitation strengthening

The strengthening mechanism of IP precipitates and their contribution to the strengthening of ferrite was initially studied by Batte and Honecombe [53]. Subsequent work has shown that the strengthening contribution depends on sheet spacing, particle spacing and particle mean radius [45]. Recently, Kamikawa *et al.* [44] indicated that the Ashby-Orowan model gave a better fit to IP precipitation strengthening than the Orowan equation [33], eqn. 11 below.

$$\Delta\sigma_{pp} = \frac{0.538 G b f_v^{0.5}}{2R} ln\left(\frac{R}{b}\right)$$

(4.5-1)

$\Delta\sigma_{pp}$ is the increase in yield strength, G is the shear modulus, b is the Burgers vector, f_v is the carbide volume fraction and R is the mean carbide radius.

The values of $\Delta\sigma_{pp}$ for the various ageing times are plotted alongside the micro-hardness data in Figure 4.5-1 (b) and are seen to follow the same trend except at very short times. This is possibly associated with the loss of coherency of the growing precipitates with the ferritic matrix [36]. Micro-hardness measurements reveal little difference in hardness between the samples aged for 3 and $5\ min$. The sample aged for $60\ min$ has a hardness which is slightly above those aged for 3 and $5\ min$ but there is a clear and significant decrease in hardness for the longer holding times, suggesting a marked reduction in the resistance to dislocation movement. The decreasing yield strength increment beyond $60\ min$ ($3600\ s$) which is calculated from Equation (4.5-1) demonstrates that the decrease in ferrite hardness after $60\ min$ is directly influenced by the increasing particle radius which outweighs the increasing volume fraction of carbide precipitate. In a recent study, Chen *et al.* [45] measured the IP contribution to ferrite strengthening (in an alloy with 50% more V than in the present material) as 170 to $220\ MPa$ for somewhat lower transformation temperatures. This suggests the values from the simple Ashby-Orowan equation used here are on the low side and that an improved model would require direct microstructural data on sheet spacing and particle spacing that is not available from SANS.

4.6. Conclusions

Small angle neutron scattering (SANS) was employed to quantify interphase precipitation in samples of a V-containing, low-C micro-alloyed steel which were isothermally transformed at $700\ °C$ for various times followed by water quenching. It is shown to be important to extract both nuclear and magnetic scattering signals so that nanoscale micro-alloyed carbide precipitates in partially transformed samples can be quantified. Results have been correlated with a microstructural investigation using scanning electron and transmission electron microscopy (TEM).

I. TEM observations confirmed the presence of fine-scale carbide precipitates, rich in V, which exhibited the well-known interphase precipitate morphology of aligned rows and sheets. Precipitates appeared to be either disc or oblate ellipsoid shaped with the mean radius of the major axis increasing from ~ 4 to $\sim 14\ nm$ as the ageing time increased from 5 to $600\ min$.

II. Analysis of the nuclear SANS data clearly reveals the presence of the nanoscale precipitates in the isothermally transformed and quenched samples. From Kratky plots, it is clear that the precipitate size and volume fraction both increase with transformation time. The latter increased from around 0.009 to a value in the range 0.022 to 0.028 with ageing time.

III. Using simple model-independent Guinier analysis of the 1-D nuclear SANS plots, particle radii (R) and thickness values (T) were calculated. The radii increase with transformation time from ~ 10 to $\sim 22\ nm$. The Guinier analysis was also used to show that the disc-shaped precipitates have an aspect ratio of ~ 3. These values agree well with a model fitting analysis based on an oblate spheroid shape which showed an increased in the radius of the major axis from 9 to $18\ nm$. The precipitate number density decreases from a peak of $2 \times 10^{21}\ m^{-3}$ to $5 \times 10^{20}\ m^{-3}$ over the course of the isothermal transformation time when an oblate ellipsoid model is employed for precipitate morphology.

IV. The micro-hardness values of ferrite grains were measured and found to decrease from 215 to $150\ Hv$ as the transformation time increased. They correlate well with the yield strength increments in the range 120 to $90\ MPa$ calculated for different transformation times by using the mean carbide radius in the Ashby-Orowan model.

5. Analysis of the extent of interphase precipitation in V-HSLA steels through *in-situ* characterization of the γ/α transformation

This work was published in: Clark, S. J., Janik, V., Rijkenberg, R. A. & Sridhar, S. Analysis of the extent of interphase precipitation in V-HSLA steels through in-situ characterization of the γ/α transformation. *Mater. Charact.* **115,** 83–89 (2016).

This chapter fulfills the Specific Objective, *'The prevalence of interphase precipitation within an overall microstructure has yet to be established. The likelihood of interphase precipitation is known to be related to the degree of misorientation from an ideal low-energy orientation between the γ and α. This work aims to address the shortcoming in the literature regarding the prevalence of interphase precipitation in a microstructure through exploiting advanced in-situ characterisation techniques such as HT-EBSD. Therefore, I aim to utilize HT-EBSD to enable the evaluation of the γ/α orientation relationship to be performed on a much larger scale through determining the spatially resolved orientations of γ* grains *which are not preserved to room temperature for a posteriori characterisation.'*

5.1. Chapter Summary

In-situ characterization techniques have been applied to elucidate the influence

of $\gamma \rightarrow \alpha$ transformation upon the extent of interphase precipitation in a low-carbon, vanadium-HSLA steel. Electron Back-scattered diffraction analyses of the γ/α orientation relationship with continuous cooling at 2 and 10 $°Cs^{-1}$ suggest that the proportion of ferrite likely to hold interphase precipitation varies little with cooling rate. However, TEM analyses show that the interphase precipitation refines with increasing cooling rate in this cooling range. With cooling rates in excess of 20 $°Cs^{-1}$, interphase precipitation is increasingly suppressed due to the increasingly diffusional-displacive nature of the Widmanstätten $\gamma \rightarrow \alpha$ transformation that is activated. The present study illustrates that the extent and dimensions of interphase precipitation can be controlled through controlled cooling.

5.2. Introduction

Interphase precipitation has recently re-gained substantial interest as its optimized exploitation leading to densely packed ordered arrays of precipitates contributes significantly to matrix strengthening through the Orowan mechanism [45]. Interphase precipitation can both occur on semi-coherent and incoherent γ/α interfaces [72,74,89,90] and its morphology can be both planar and curved [66], depending on the curved or faceted nature of the migrating incoherent interphase boundaries [134].

Okamoto [71] suggested that interphase precipitation in Niobium micro-alloyed steels was not associated with the $(110)_\alpha$ plane, rather that interphase precipitation could be found to be associated with many varying interfaces and can have different orientations within one single ferrite grain. Yen [29] found through the use of careful TEM analysis of isothermally transformed Ti-Mo low carbon steel that the sheet planes of interphase-precipitated carbides are oriented close to any one of the $(211)_\alpha$, $(111)_\alpha$, and $(210)_\alpha$ planes rather than that of the commonly asserted $(110)_\alpha$. A corollary of this finding is that the interphase precipitation mechanism is connected with the development of

incoherent γ/α interfaces. Furthermore, Furuhara and co-workers [72,74,89,90] have shown through analysis of partially transformed samples and the reconstruction of the γ/α orientation relationship from quenched martensite, that the number density of interphase precipitates initially increases rapidly as the orientation angle between parent γ and α deviates $\Delta\theta$ increasingly from the ideal Kurdjumov-Sachs orientation relationship (KS-OR).

The number density of interphase precipitates then stabilizes with $\Delta\theta$ greater than $5°$ [90]. Apart from KS-OR, the Nishiyama-Wassermann Orientation Relationship (NW-OR) provides an additional rational low-energy γ/α OR with partially coherent boundaries hindering α growth [181].

This chapter, using a suite of advanced *in-situ* characterization techniques, aims to elucidate the OR at the γ/α interphase and its influence upon interphase precipitation for a near stoichiometric V-based alloy. Specifically, the validate the following hypotheses is integrated:

- Interphase precipitation is promoted by ferrite growth with a greater degree of incoherency of the γ/α interphase (deviation from the semi-coherent KS and NW OR's).
- The extent of interphase precipitation is influenced by cooling rate and the morphology of the resulting γ/α formation.

5.3. Experimental Methods

5.3.1. Chemistry and pre-treating of the as-received steel

The experimental material was provided by Tata Steel in the form of forged blocks with the following composition: 0.046 C, 1.60 Mn, 0.18 Si, 0.45 Al, 0.2 V, 0.005 N $wt.\%$. Samples for thermal treatment and simultaneous characterization using *in-situ* EBSD were sectioned from the forged blocks, producing $6 \times 32\,mm$ sized strips with $250\,\mu m$ thickness from which $3\,mm$ diameter discs were punched using a Gatan Model 623. The samples were subsequently thinned to $120\,\mu m$ using a Buhler MiniMet 1000 Polisher Grinder

with Precision Thinning Attachment on a $15\ \mu m$ diamond-grinding disc. Further polishing was achieved using reinforced tape on a 2500 grit paper and final near-mirror polishing using a $1\ \mu m$ diamond polishing compound.

The steel samples were heat-treated using a High-Temperature Confocal Laser Scanning Microscope (HT-CLSM), Yonekura MFG, VL2000DX-SVF17SP, with a super-pure Ar atmosphere achieved using an Agilent indicating O_2 trap in order to prevent excessive oxidation. The samples were heated at a rate of $5\ ℃s^{-1}$ to $1200\ ℃$ and held for $120\ s$ in order to dissolve any V(C, N) precipitates in the as-received material. The samples were then rapidly quenched at a cooling rate of $30\ ℃s^{-1}$ to room temperature through rapid exchange of the Ar atmosphere with He.

5.3.2. *In-Situ* HT-CLSM heat treatment and characterization

The samples were further heat-treated and imaged *in-situ* using High-Temperature Confocal Laser Scanning Microscopy (HT-CLSM). The heat-treatments used in these experiments were as follows: heating at $5\ ℃s^{-1}$ to $900\ ℃$ followed by an isothermal hold for $180\ s$ then continuously cooled at rates of 2, 5, 10 and $20\ ℃s^{-1}$ to room temperature. Stacks of HT-CLSM micrographs were collected at a rate of 15 frames per second using 25 times magnification. These stacks were subsequently analyzed, the characteristic transformation temperatures were determined using ImageJ digital image analysis software [168].

Additional, samples for micro-hardness analysis were prepared in the form of cuboids with dimensions 5 by 5 by $0.5\ mm$ and mirror polished using standard metallographic techniques. The samples were heat treated using HT-CLSM adopting corresponding thermal cycles to those used for the $3\ mm$ diameter discs. After the thermal treatment was finished the samples were etched using 2% Nital solution, revealing the ferritic grain boundaries and allowing micro-hardness measurements to be taken from the interior of 8 polygonal ferritic

grains for each condition. The Vickers micro-hardness measurements were performed using a Buehler Tukon 1102 micro-hardness tester employing $0.01\ kg$ load for a dwell time of $10\ s$. Further Vickers hardness measurements were undertaken in order to characterize the bulk microstructure in the form of line scans of 20 indents evenly distributed diagonally across the surface of the sample using the same Tukon 1102 micro-hardness tester employing $0.5\ kg$ load for a dwell time of $10\ s$.

5.3.3. *In-situ* EBSD heat treatment and characterization

In-situ High-Temperature Electron Backscatter Diffraction (HT-EBSD) Analysis was performed using a Gatan Murano hot stage Model 525 to characterize both the austenitic grain structure at 900 ℃ after heating at 5 ℃s^{-1} as well as the ferritic grain structure after continuous cooling at 2 and 10 ℃s^{-1} to 600 ℃. This was undertaken inside the chamber of Secondary Electron Microscope Carl Zeiss Gemini, equipped with Electron Back Scattered Diffraction camera Nordlys EBSD by Oxford Instruments. Samples for HT-EBSD were taken directly from the HT-CLSM after undergoing the thermal cycle as described above with aim to dissolve all preexisting V(C, N) precipitates. No further re-polishing or etching of the post-CLSM samples was necessary since sufficient surface quality was maintained after the HT-CLSM, leading to ab EBSD indexing quality above 95%. EBSD data sets were acquired using a $25\ kV$ accelerating voltage, a $240\ \mu m$ aperture size, and a $0.5\ \mu m$ step size. Analyses of the EBSD data-sets were done with HKL Chanel 5 post-processing software, with the (.ctf) files exported for further analysis using the MTEX texture analysis toolbox, MTEX-4.0.23 http://mtex-toolbox.github.io , for MATLAB, R20014b.

5.3.4. *In-situ* EBSD data post-processing

Following continuous cooling from 900 ℃ to 600 ℃ at 2 ℃s^{-1} and 10 ℃s^{-1} the EBSD maps corresponding with the start (austenitic) and final (ferritic) temperatures were aligned using oxides or MnS inclusions visible in both

mapped areas as small non-indexing regions common to both the austenitic and ferritic EBSD scans.

The aligned γ/α EBSD maps were further post-processed in order to spatially quantify the OR between parent γ and daughter α. Subsequently, the spatial distribution of $\Delta\theta$ is calculated, which is the difference between the measured OR and that of the closest fitting KS or NW OR variant. $\Delta\theta$ was determined using the Rodrigues-Frank parameterization as shown in Equation (5.3-1); Rodrigues-Frank parameterization was chosen as it provides an intuitive way of evaluating misorientation [182], where, $\hat{\mathrm{r}}$ is an axis and θ is the rotation angle.

$$\rho = \hat{r}\tan\left(\frac{\theta}{2}\right) \quad \hat{r} = [r_1, r_2, r_3]$$

(5.3-1)

Each of the 24 variants of the KS-OR and the 12 variants of the NW-OR were expressed as Rodrigues-Frank vectors using the orientation transformation matrices described in References [183] and [184] respectively, and calculated according to the relations described in Reference [185].

For the entire population of γ grains within the sampled area of $120 \times 80\ \mu m$, the misorientation $\theta_{measured}$ between the mean orientation of each γ grain and the individual orientation of α-indexed pixels within its γ grain boundary was computed.

$$\Delta\theta = min.\left|\theta_{OR\ i}^{Variant\ j} - \theta_{Measured}\right|$$

(5.3-2)

Next, the $\Delta\theta$ between $\theta_{measured}$ and every variant of KS-OR and NW-OR was determined by calculating the minimum absolute difference between the two

θorientations. The closest matching OR, i, where, (i=1=K-S, 2=N-W, and 3=None Detected), and OR variant, j, where, (j=1:24 for K-S and 1:12 for N-W) for each α EBSD measurement was selected according to Equation (5.3-2). The fitting of an OR was deemed to be inappropriate if $\theta \leq 5°$.

5.4. Results and Discussion

5.4.1. *In-situ* EBSD characterization of the low-energy OR's during γ/α transformation

Figure 5.4-1shows for two different cooling rates (i.e., A, 2 and B, 10 °Cs^{-1}), the distribution and magnitude of $\Delta\theta$ mapped for regions where either the KS or NW OR were fitted for continuous cooling at 2 and 10 °Cs^{-1}, respectively.

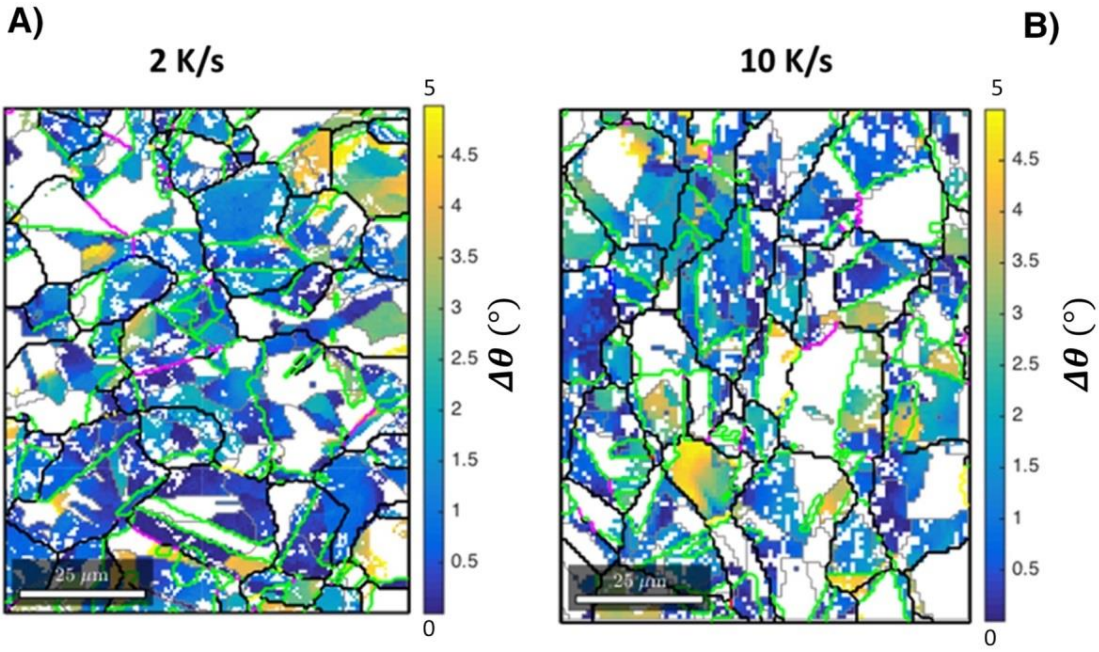

Figure 5.4-1 A) and B) Overlapping EBSD micrographs of initial austenite and resulting ferritic microstructure acquired in-situ and processed with MTEX texture toolbox; cooling rates 2 °Cs^{-1} *A), and* 10 °Cs^{-1} *B). Color-coding for the austenitic grain boundaries: black = random grain boundaries, green = coincidence site lattice (CLS) boundaries* $\Sigma 3$*, blue = CLS* $\Sigma 5$*, red = CLS* $\Sigma 7$*, magenta = CLS* $\Sigma 9$ *and yellow = CLS* $\Sigma 11$*. Distribution of the Ferrite orientation exhibiting a minimum* $\Delta\theta$

of less than $5°$ with regard to a low-energy orientation relationship with the original austenitic matrix.

Figure 5.4-2 A and 2B show the surface area fractions for which the minimum $\Delta\theta$ is less than 5° with regard to the KS-OR, NW-OR, and regions where $\Delta\theta$ is larger than $5°$ and where no KS-OR or NW-OR was detected. A close match (i.e., $\Delta\theta < 5°$) with the KS-OR was found for 47% and 49% of the mapped area at 2 and $10\ °Cs^{-1}$, respectively. For the NW-OR, this was considerably lower, with fractions of 21% and 18% of the mapped area at 2 and $10\ °Cs^{-1}$, respectively. The remaining area has a value of $\Delta\theta$ which is greater than $5°$, showing no close fit with either the K-S or N-W orientation relationship. The distributions of $\Delta\theta$ at cooling rates of 2 and $10\ °Cs^{-1}$ are shown in the histograms in Figure 5.4-3.

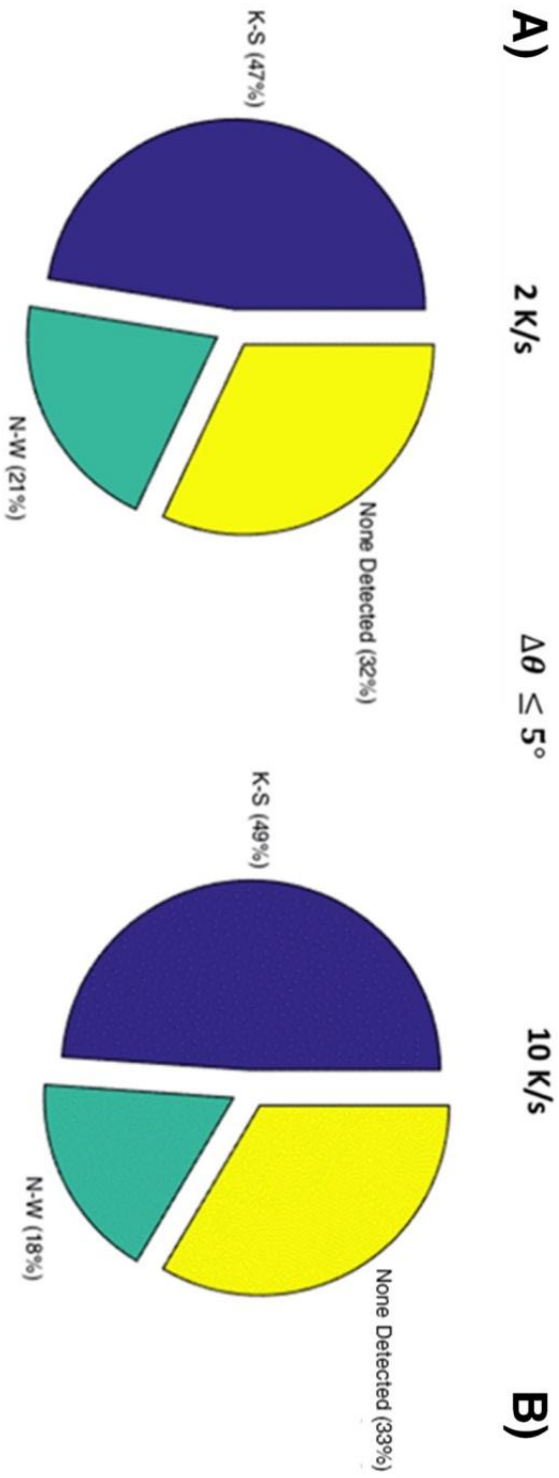

Figure 5.4-2 A) and B) show the surface fraction of the Ferrite EBSD mapped region exhibiting α minimum Δθ below 5° *with regard to γ/α low-energy K-S and*

N-W orientation relationships as well as the surface fraction with $\Delta\theta$ higher than $5°$ (labeled as "None Detected") with the K-S and N-W orientation relationships.

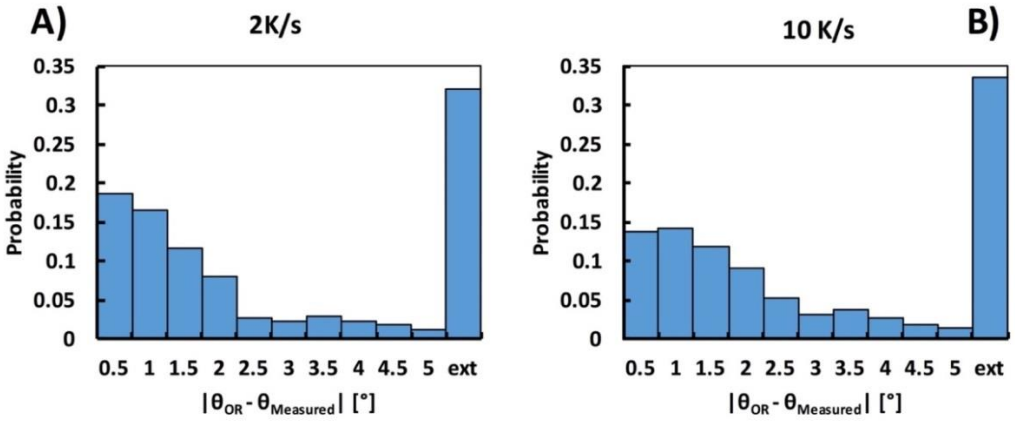

Figure 5.4-3 A) and B) show the corresponding normalized probability histograms displaying the distribution of $\Delta\theta$, for values less than 5^o after continuous cooling at 2 and $10\ ℃s^{-1}$ respectively.

5.4.2. *In-situ* HT-CLSM characterization of γ/α transformation

In order to further elucidate the transformation kinetics, samples were imaged using *in-situ* using HT-CLSM. These samples were first heat treated by reheating to $1200\ ℃$ for full precipitate dissolution, followed by rapid cooling at $30\ ℃s^{-1}$ to room temperature to refine the microstructure. Next, the samples were reheated to $900\ ℃$ and subjected to four different continuous cooling rates from the austenitic region to room temperature, i.e., 20, 10, 5 and $2\ ℃s^{-1}$. This allowed the assessment of the characteristic transformation start temperatures to be deduced through direct observation of the γ/α interface nature. The regions where Widmanstätten ferrite formation is observed during continuous cooling have been marked with yellow arrows in specific micrographs in Figure 5.4-4. The regions of Widmanstätten ferrite are distinguished by the rapid transformation kinetics and the 'jagged' interphase morphology, in contrast to that of the interphases of allotriomorphic ferrite.

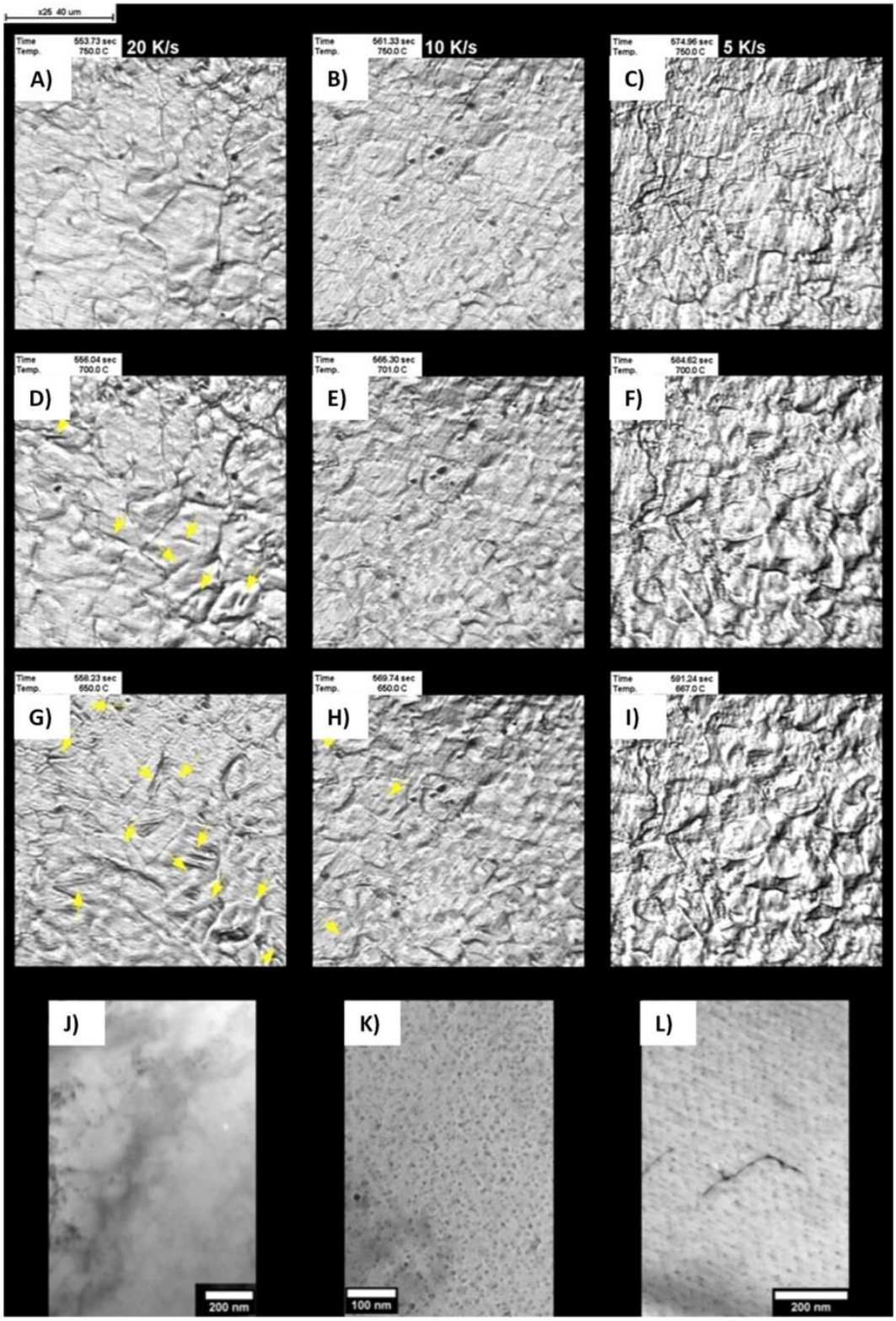

Figure 5.4-4 Montage of HT-CLSM micrographs and typical TEM micrographs of the precipitates observed within each foil after continuous cooling at 20, 10 *and*

$5\ ℃s^{-1}$, respectively. Full transformation video included as supplementary material.

Reheating the supersaturated ferritic matrix to $900\ ℃$ and continuously cooling at $20\ ℃s^{-1}$ (Figure 5.4-4 A, D, G) led to pro-eutectoid allotriomorphic ferrite nucleating at $759\ ℃$, followed by the nucleation of displacive ferrite, i.e., primarily Widmanstätten ferrite, at $495\ ℃$, marked with yellow arrows. With continuous cooling rates of 10 (Figure 5.4-4 B,E,H) and $5\ ℃s^{-1}$ (Figure 5.4-4 C,F,I) austenite decomposes to almost purely pro-eutectoid allotriomorphic ferrite at a start temperature of 762 and $768\ ℃$, respectively, regions where Widmanstätten ferrite nucleates has once again been highlighted with yellow arrows.

Figure 5.4-4 J to Figure 5.4-4 L show bright field TEM micrographs of regions where interphase precipitation is observed after continuous cooling from $900\ ℃$ at 20, 10 and $5\ ℃s^{-1}$, respectively, to room temperature. Four TEM samples were prepared for each condition. As the mean ferritic grain size in each case was less than $15\ \mu m$ there were many regions of clearly identifiable ferrite grains within the thin transparent rim of each TEM sample. The micrographs presented were typical of the many regions observed. The TEM micrographs show that the increasing cooling rate from 5 to $10\ ℃s^{-1}$ refines interphase precipitation. However, a further increase in the cooling rate to $20\ ℃s^{-1}$ results in a microstructure that is devoid of precipitates. Random precipitates are not observed due to the insufficient time for such precipitates to nucleate and grow.

Figure 5.4-5 A) shows a Continuous Cooling Transformation (CCT) of measured allotriomorphic and Widmanstätten ferrite start temperatures for the bulk 5 by 5 by $0.5\ mm$ block samples plotted along with the predicted Widmanstätten start temperature range generated by MAP program MUCG83 [140]. It is shown that

the experimentally observed start temperatures, determined by carefully analysing the first regions to transform within the imaged surface area, lie within the range of start temperatures predicted by MUCG83 for this composition. In addition, Figure 5A shows the results bulk HV(0.50) measurements and targeted HV(0.010) micro-hardness of the allotriomorphic regions. Figure 5.4-5 (B-D) shows the corresponding optical micrographs obtained after continuous cooling from $900\,℃$ at the marked cooling rates. As 20 HV(0.50) measurements were made and the indents covered many grains incorporating both the allotriomorphic and Widmanstätten ferrite, it is shown that generally with increasing cooling rate the measured micro-hardness increases with the cooling rate. However, with the targeted use of HV(0.010) indents it was possible to generate indents which lay within the allotriomorphic or polygonal ferritic grains. Whilst the measured Vickers hardness increases with increasing cooling rate, in general, the Vickers hardness increases more profoundly between the cooling rates of 5 and $10\,℃s^{-1}$. The Vickers hardness of the allotriomorphic regions in the $20\,℃s^{-1}$ condition appears to have plateaued and remained at a similar level to that which is measured in the $10\,℃s^{-1}$ condition. This step change in hardness appears to correspond to the refinement of the interphase precipitation observed in Figure 5.4-4 (K) and (L) at the same cooling rates.

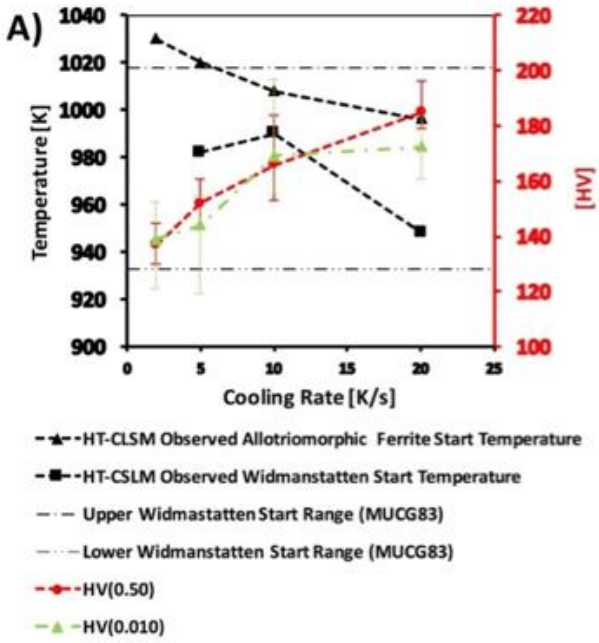

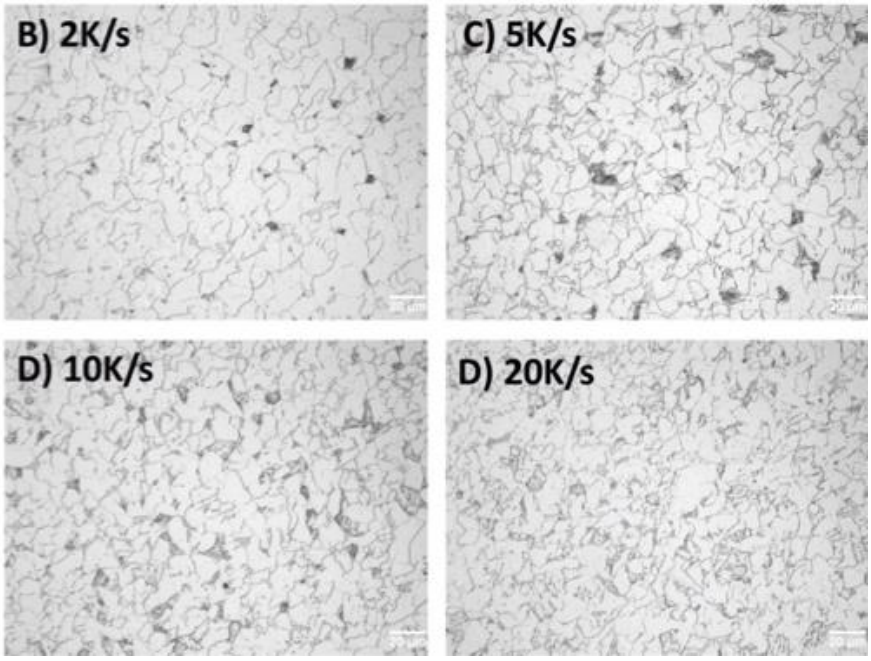

Figure 5.4-5 A) shows the measured allotriomorphic and Widmanstätten ferrite start temperatures for the bulk block samples plotted with the predicted Widmanstätten start temperature range obtained using the MAP program MUCG83, bulk HV(0.50) measurements and targeted HV(0.010) micro-hardness of the allotriomorphic regions. B-D) show optical micrographs after continuous cooling from 900 ℃ *at the marked cooling rates.*

However, as the targeted micro-hardness measurements plateau between the cooling rates of $10\ ℃s^{-1}$ and $20\ ℃s^{-1}$ whereas, no interphase precipitates are observed in Figure 5.4-4 (J). This suggests that in the polygonal allotriomorphic ferrite regions measured after cooling at $20\ ℃s^{-1}$ there is a similar number density of interphase carbides as in the polygonal allotriomorphic regions after continuous cooling at a rate of $10\ ℃s^{-1}$. These regions have not been observed in the TEM (Figure 5.4-4 J) as there is a comparatively low volume fraction of Allotriomorphic ferrite compared to that of Widmanstätten ferrite.

The kinetics of Widmanstätten ferrite have been investigated *in-situ* previously [186–188] and it has been shown that the free surface of a cross-section has an influence upon the kinetics of Widmanstätten ferrite growth. The average growth rate of Widmanstätten plates measured *in-situ* for free-surface samples is estimated to be one order of magnitude greater than that measured for the bulk. One explanation for this difference in average growth rate is that in case of a free surface the growth kinetics are close to para-equilibrium, whereas for the bulk local partitioning equilibrium is believed to be negligible [188]. Another aspect that may play a role is that the Widmanstätten ferrite start temperature is also influenced by the presence of a free surface. It has been found that for martensitic transformations the free surface allows martensitic transformations to occur at a higher temperature than in bulk material. The reason for this is the fact that a free surface compared to bulk facilitates the shape deformation, i.e., volume expansion, accompanying the transformation from austenite to martensite [189].

With greater cooling rates or lower transformation temperatures, the mobility of interfaces with a random orientation relationship with the parent austenite decreases, whereas the mobility of that of the coherent interface increases and becomes dominant [1]. The nucleation of Widmanstätten ferrite also becomes

increasingly significant [190], in particular since the growth rate of Widmanstätten ferrite is much greater than that of spherical allotriomorphic ferrite [191]. In addition, the plate shape of Widmanstätten allows solutes to partition to the sides of the growing plate rather than pile up ahead of the plate as is the case with allotriomorphic ferrite [192]. In the case of Widmanstätten ferrite, it is conceivable that this partitioning of the solute to the side of growing plates prevents the formation of interphase precipitates.

Conventionally, it is thought that an allotriomorphic ferrite grain nucleates and grows at an austenite grain boundary with a coherent, low-energy OR with one of the surrounding austenite grains. However, this allotriomorphic ferrite grains will have a different OR with the other neighbouring austenite grain, or grain in case of a triple point. This means that an allotriomorphic ferrite grain will maintain a semi-coherent γ/α interphase with one parent austenite grain, and will have one or two additional γ/α interphase boundaries which can either be semi-coherent or incoherent. In case of an incoherent γ/α interphase boundary, this can either lead to an interphase boundary that is smoothly curved or has a facetted nature with various length scales [134]. Therefore, a significant amount of curved or planar arrays of interphase precipitation can be expected for the incoherent side of the allotriomorphic ferrite grain, whereas its coherent side where a low energy OR is maintained will show no interphase precipitation.

For the semi-coherent faceted side of an allotriomorph where a low energy OR is obeyed, it is not fully understood why no interphase precipitation is observed. It has been suggested, the γ/α interface with a non-K-S OR has a higher interfacial energy than that of a K-S OR γ/α interface and hence that a non-K-S interface requires less energy for the formation of a critical nucleus. Additionally, solute atoms are known to segregate more readily to incoherent interfaces as the

diffusivity of solutes at incoherent interfaces is higher [90], increasing the driving force for interphase precipitation. Furthermore, it is unlikely that an allotriomorphic ferrite grain will exhibit dual orientation that will accommodate a low energy OR across the austenite grain boundary or grain boundaries in case of a triple point [18]. As a consequence, it is unlikely that interphase precipitation can be completely eliminated in case of allotriomorphic ferrite nucleation.

In contrast, Widmanstätten ferrite will only nucleate and grow from the side of the austenite grain boundary exhibiting a low-energy OR as an invariant line between austenite and ferrite cannot be sustained with large values of $\Delta\theta$ [193]. Therefore, as $\Delta\theta$ is always low, interphase precipitation is never expected to occur in Widmanstätten ferrite as the aforementioned factors favouring interphase precipitation for incoherent interfaces in case of allotriomorphic ferrite are not valid for the nucleation and growth of Widmanstätten ferrite.

It has been shown that in the case of idiomorphic ferrite precipitates, nucleating on incoherent inclusions in the matrix, do not hold any specific orientation relationship with that matrix [194]. As such, idiomorphic ferrite, which nucleates inside austenite grains and has a tendency to nucleate on non-metallic inclusions, is likely to have an orientation which substantially deviates from KS-OR. Hence, it is also expected that idiomorphic ferrite may exhibit interphase precipitation. Based on this, it is conceivable that the amount of interphase precipitation can be significantly enhanced through the optimization of incoherent particles in the steel matrix for effective nucleation of idiomorphic ferrite within austenite grains.

5.5. Conclusions

In this chapter, using *in-situ* characterization techniques, the influence of γ/α transformation upon the extent of interphase precipitation in a low-carbon vanadium-HSLA steel was investigated. EBSD analyses of the γ/α OR of samples subjected to continuous cooling of 2 and 10 °Cs^{-1} suggest that the proportion of ferrite likely to hold interphase precipitation varies little with cooling rate. In the present study, EBSD indicates that circa 32% and 34% of the ferrite microstructure will exhibit interphase precipitation with continuous cooling at 2 and 10 °Cs^{-1}, respectively, to room temperature. However, *a posteriori* TEM characterization does show that an increase in cooling rate from 5 to 10 °Cs^{-1} is coupled with a refinement of interphase precipitation in terms of carbide row spacing. At higher cooling rates, i.e., in excess of 20 °Cs^{-1}, interphase precipitation is increasingly suppressed due to the increasingly diffusional-displacive nature of the Widmanstätten γ/α transformation that is activated. It is suggested that interphase precipitation is not possible in a ferrite due to the lack of solute 'pile-up' ahead of the advancing γ/α interface. As a result, the critical concentration of solute at the interface required for carbide precipitation is not reached. This, in turn, implies that the extent and dimensions of interphase precipitation can be controlled through a controlled cooling.

6. Analytical Modelling: Interphase Precipitation – An Interfacial Segregation Model

This work was published in: Clark, S., Janik, V., Lan, Y. & Sridhar, S. Interphase Precipitation – An Interfacial Segregation Model. *ISIJ Int.* **57,** 524–532 (2017).

This chapter has successfully fulfilled the principle objective: *This work endeavours to derive a new microstructural model capable of explaining all the known phenomena regarding the evolution of inter-sheet spacing and transformation kinetics.*

This chapter has confirmed the following hypothesis: *It is hypothesized that the nucleation of interphase precipitates plays little role in the determination of ferrite growth ledge height and that interphase precipitates merely mark the prior growth ledge height in alloys where a strong carbide forming element is present.* This chapter has also confirmed the following hypothesis: *It is hypothesized that the observed refinements in inter-sheet spacing during the initial stages of the* $\gamma \rightarrow \alpha + MC$ *transformation can be explained by the transition in* α *growth mode from parequilibrium to negligible partitioning local equilibrium.*

6.1. Chapter Summary

The size and distribution of interphase precipitates in micro-alloyed steels is a crucial micro-structural feature to control for obtaining the necessary strength in low-cost automotive sheets. In order to optimize both alloy chemistry and thermal processing, an enhanced understanding of the interphase precipitation mechanism is required. It is proposed that the evolution of inter-sheet spacing of

MC carbides during the $\gamma \rightarrow \alpha$+*MC* transformation can be explained considering the interfacial segregation and the corresponding dissipation of Gibbs energy inside the moving interphase boundary. The inter-sheet spacing of interphase precipitates is controlled by a complex interplay between the interfacial energy and interfacial segregation, this is presented in the form of an analytical model. It is shown that the general trend of refining inter-sheet spacing with growing ferrite half-thickness can be well predicted by the proposed model.

6.2. Introduction

Recent experimental studies have elucidated the periodicity of interphase precipitates; Murakami *et al.*[72] found that the inter-sheet spacing decreases as the interface velocity reduces during an isothermal transformation at $675\ ^{\circ}\mathrm{C}$. Gray and Yeo [75] also showed that the inter-sheet spacing decreases with the proceeding of austenite to ferrite transformation during continuous cooling. This decreasing inter-sheet spacing, however, is the combined effect of ferrite growth and transformation temperature. Sakuma and Honeycomb [51] reported that the inter-sheet spacing was increased when Mn was added to a Nb micro-alloyed steel to slow down the austenite to ferrite transformation. Previous models such as Lagneborg and Zajac [121] have been found to be unable to predict the phenomenon (the decreasing inter-sheet spacing with decreasing ferrite interface velocity) where the inter-sheet spacing is predicted to increase with the root of the distance from the ferrite grain centre.

It is hypothesised that the observed refinements in inter-sheet spacing during the initial stages of the $\gamma \rightarrow \alpha$+*MC* transformation can be explained by the transition from parequilibrium to negligible partitioning local equilibrium. It is further hypothesized that the nucleation of interphase precipitates plays little role in the determination of ferrite super-ledge height and the interphase precipitates merely mark the super-ledge height in alloys where a strong carbide forming element is present. The inter-sheet spacing is thought to be strongly

related to the factors of interfacial energy and interfacial segregation. The latter of which can be predicted according to approaches such as that outlined by Purdy and Bréchet [195]. It is proposed that interfacial segregation has a particularly marked effect on the inter-sheet spacing. Finally, it is hypothesized that the precipitation of carbides will consume sufficient carbon to accelerate the ferrite formation as stated in Section 3.2. The purpose of this study is to develop a new model for the prediction of the evolution of inter-sheet-spacing of interphase carbides in multi-component alloys as stated in Section 3.1.1.

6.3. Materials and Methods

Accurate characterisation of the initial condition, in terms of the prior austenite grain structure, is vital for the development of the present model. The prior austenitic grain structure which has an important effect on soft impingement of forming ferrite grains has been characterised *in-situ* using HT-EBSD. Furthermore, in order to test the validity of the interphase precipitation model experimental data must be collected to test its predictions. In this work, the phase transformation model shall be tested against the $\gamma \rightarrow \alpha$ transformation kinetics measured using dilatometry and the precipitation model against the inter-sheet spacing of interphase carbides, measured *a posteriori* using TEM.

Table 6.3-1 Chemical composition of the micro-alloyed steels in weight percent $[wt\%]$.

Element	**Alloy 1** $\boldsymbol{wt\%}$	**Alloy 2** $\boldsymbol{wt\%}$
Mn	1.60	1.60
Si	0.18	0.20
V	0.20	~
C	0.047	0.038
N	0.0046	0.0060

The experimental materials were provided by Tata Steel in the form of forged blocks with the composition according to *Table 6.3-1*. Samples were machined into rods of $4\ mm$ diameter, $10\ mm$ length for dilatometry and further analysis by *in-situ* High-Temperature Electron Backscatter Diffraction (HT-EBSD) and Transmission Electron Microscopy (TEM). Bähr-Thermoanalyse DIL 805A/D/T quenching dilatometer was used to perform all dilatometry experiments operated in a vacuum and utilizing a He assisted quench. An initial heat treatment was followed for all samples which consisted of heating $1150\ ℃$ at $5\ ℃s^{-1}$ and isothermal holding for $120\ s$ to dissolve all pre-existing precipitates. The samples were then cooled at a rate in excess of $100\ ℃s^{-1}$ to room temperature.

6.4. Experiments and Results

For dilatometric analysis, the samples quenched from $1150\ ℃$ were reheated to $900\ ℃$ at a rate of $5\ ℃s^{-1}$ and isothermally held for $120\ s$, followed by cooling at a rate in excess of $100\ ℃s^{-1}$ to an isothermal transformation temperature of $700\ ℃$ where the samples were held for $300\ s$. Figure 6.4-1 a-b) show the raw dilatometry traces for Alloys 1 and 2, respectively. The dilation due to the isothermal $\gamma \rightarrow \alpha$ transformation at a temperature of $700\ ℃$ is evident from the vertical sections of the isothermal transformation cycles shown in Figure 6.4-1 (a-b). Figure 6.4-1 (c-d) gives the thermal cycles from the spot-welded thermocouple during the dilatometer cycles. The orange highlighted segment from Figure 6.4-1 (c) shows the portion of the quench thermal cycle from which the expansion coefficient for the austenite phase was extracted. The red highlighted segment from Figure 6.4-1 (d) shows the portion of the quench thermal cycle from which the expansion coefficient for the ferrite phase was extracted. The fraction of ferrite transformed was extracted using the lever rule from an extrapolated value for the austenite phase and an interpolated value for the ferritic phase according to the lines of best fit shown in Table 6.4-1.

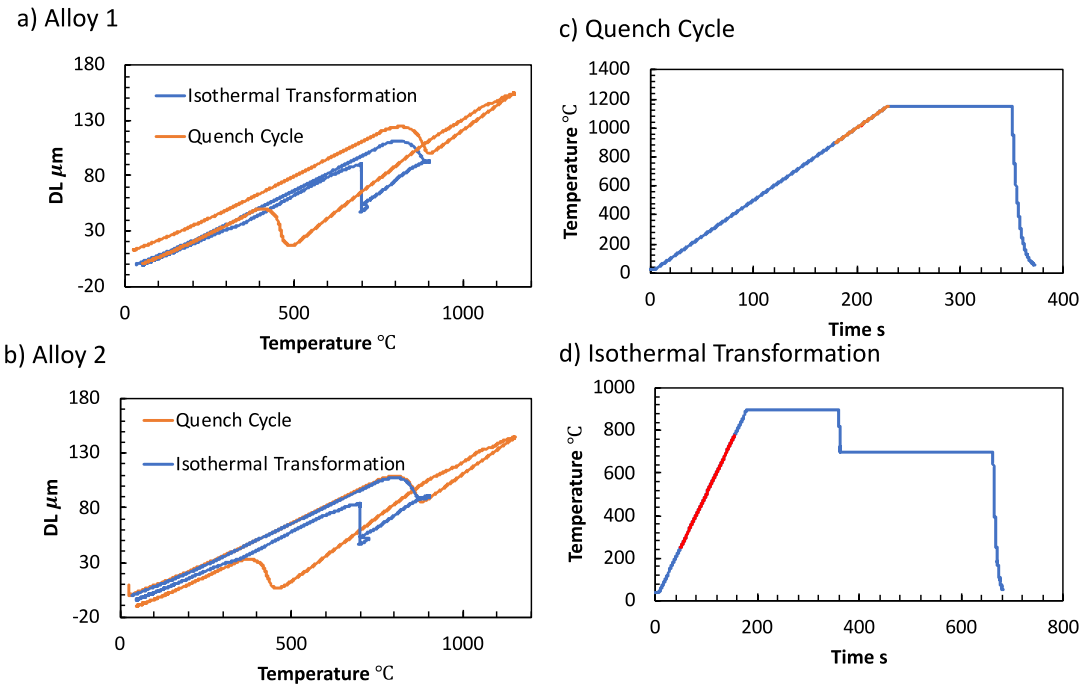

Figure 6.4-1 (a-b) Dilatometry traces of the $\gamma \rightarrow \alpha$ transformation at a temperature of 700 ℃ *for Alloys 1 and 2. (c-d) Thermal cycles outputted by the spot-welded thermocouple.*

Table 6.4-1 Extracted expansion coefficients and least square fitting coefficients for alloys 1 and 2.

	$dL(\alpha,T)\ \mu m$	R^2	$dL(\gamma,T)\ \mu m$	R^2
Alloy 1	$dL(\alpha,T) = 1.56337E-01T - 1.09636E+01$	$9.99955E-01$	$dL(\gamma,T) = 2.28017E-01T - 1.03272E+02$	$9.99989E-01$
Alloy 2	$dL(\alpha,T) = 1.52264E-01T - 1.06396E+01$	$9.99941E-01$	$dL(\gamma,T) = 2.23239E-01T - 1.12259E+02$	$9.99982E-01$

Figure 6.4-2 shows the results of dilatometric analysis of the $\gamma \rightarrow \alpha$ transformation at a temperature of 700 ℃ of Alloys 1 and 2. The phase fractions during the isothermal transformation were determined using linear expansion coefficients extracted from segments of the thermal cycle, the dilation from MC precipitates was assumed to be negligible and only a single matrix phase to be

present. It can be seen that within the isothermal holding period of $300\ s$ both the final ferritic fraction was greater and the transformation kinetics faster in the case of the alloy where V was present. It is proposed that the most plausible explanation of this effect is the consumption of carbon in the form of MC precipitates which would otherwise have been rejected into the residual austenite. This supports the stated hypothesis that carbide precipitation accelerates the ferrite formation. However, this evidence is not conclusive as the slower transformation kinetics could be explained by other factors such as a lager prior austenitic grain size.

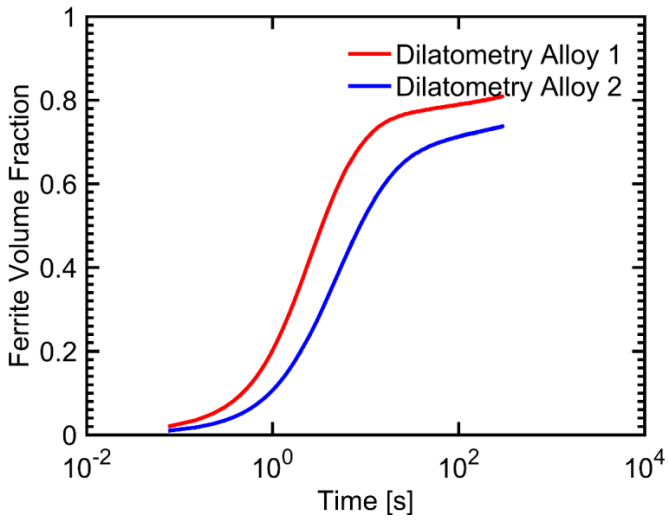

Figure 6.4-2 Dilatometric analysis of the $\gamma \rightarrow \alpha$ transformation at a temperature of $700\ ℃$ for Alloys 1 and 2.

The average prior austenitic grain size was measured by *in-situ* HT-EBSD performed using a Gatan Murano hot stage Model 525 attached to Secondary Electron Microscope (SEM) Carl Zeiss Gemini with ESBD camera Nordlys by Oxford Instruments. Samples were sectioned from dilatometry rods which had undergone the quench cycle indicated in Figure 6.4-1 (c) and were polished using standard metallography techniques. The samples were subsequently heated in the SEM at a continuous rate of $5\ ℃s^{-1}$ yielding an austenitic grain structure which was characterised at $900\ ℃$. *A posteriori* optical microscopy was

performed on sectioned samples from the dilatometry samples using standard metallography techniques.

Figure 6.4-3 a) shows an image of in-situ HT-EBSD of the austenitic microstructure of Alloy 1 taken at the temperature of $900\,℃$ after $300\,\mathrm{s}$ isothermal hold showing a heterogeneous distribution of prior austenite grain sizes with average prior austenite grain size of approximately $12.4 \pm 6.5\ \mu m$.

Figure 6.4-3 c) shows a corresponding histogram of the grain size distribution where all grains smaller than 3 μm have been removed. It should be noted this distribution and mean austenite grain size is based upon a limited sample of just 59 observations. The number of observations was limited by the size of the EBSD scan which could be acquired in the $120\ s$ isothermal hold at $900\ ℃$.

Figure 6.4-3 b) shows optical microscopy of the final microstructure obtained after isothermal hold at $900\ ℃$ for $300\ \mathrm{s}$ taken after the dilatometric test with a resultant microstructure consisting of roughly 80% of fine quasi-polygonal ferrite and 20% of untransformed austenite (dark phases) transforming to bainite during quenching after the isothermal hold. The above optical microscopy result shows a strong correspondence with the final ferrite fraction measured using dilatometry in Figure 6.4-2.

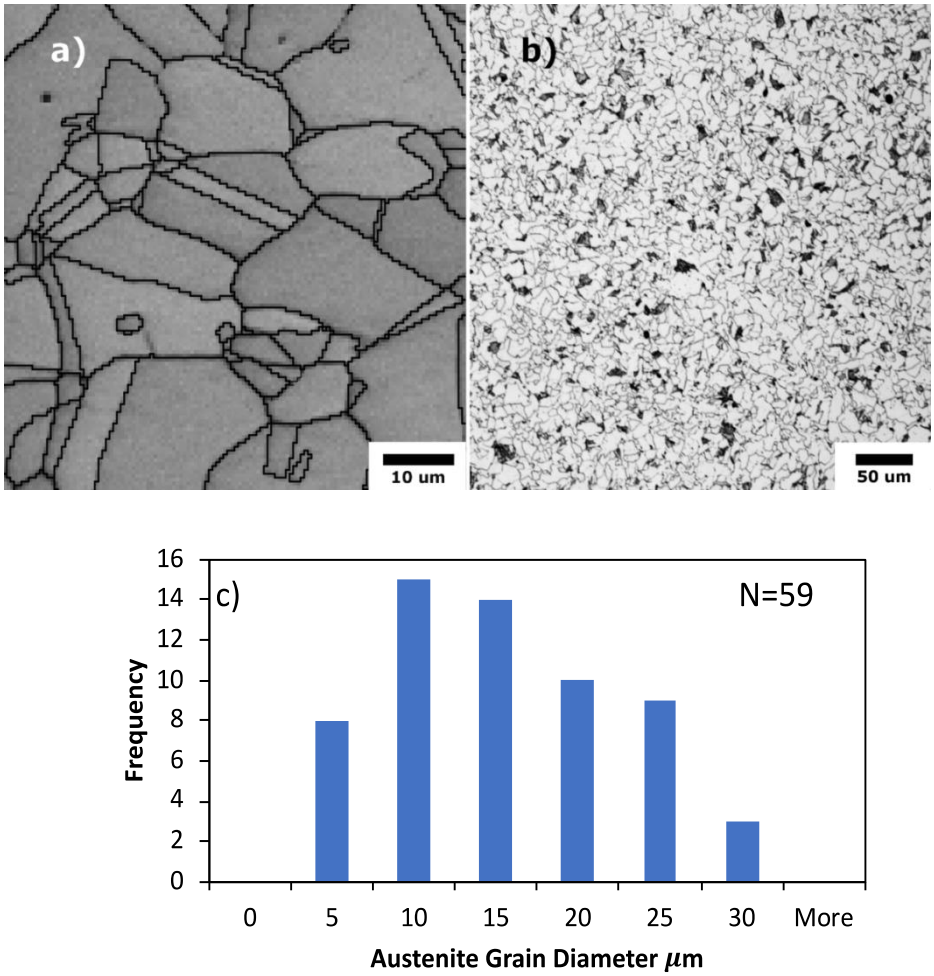

Figure 6.4-3 a) an in-situ HT-EBSD image of the austenitic microstructure of Alloy 1 taken at the temperature of $900\,℃$ *after* $300\,s$ *isothermal hold showing heterogeneous distribution of prior austenite grain size; average prior austenite grain* $12.4 \pm 6.5\,\mu m$*. b) Optical microscopy of the final microstructure obtained after isothermal hold at* $700\,℃$ *for* $300\,s$ *followed by quenching,* $80\,\%$ *of fine quasi-polygonal ferrite and* $20\,\%$ *of untransformed austenite (dark phases) transforming to bainite during quenching after the isothermal hold. c) Austenite grain size distribution measured from a total of 59 austenite grains.*

For *a posteriori* TEM analysis, five discs per alloy were cut from the samples after the dilatometric tests, thinned to $0.1\,mm$ and then punched and polished down to $50\,\mu m$ followed by a twin-jet electro-polishing in a Struers TenuPol-5 using a solution of $10\,vol\%$ $HClO_4$ mix with $90\,vol\%$ CH_3COOH (acetic acid) at

approximately -15 ℃. TEM observations were performed using a JEOL 2000FX TEM microscope and JEOL 2100 TEM with Energy Dispersive Spectroscopy (EDS) detector operating at $200\ kV$.

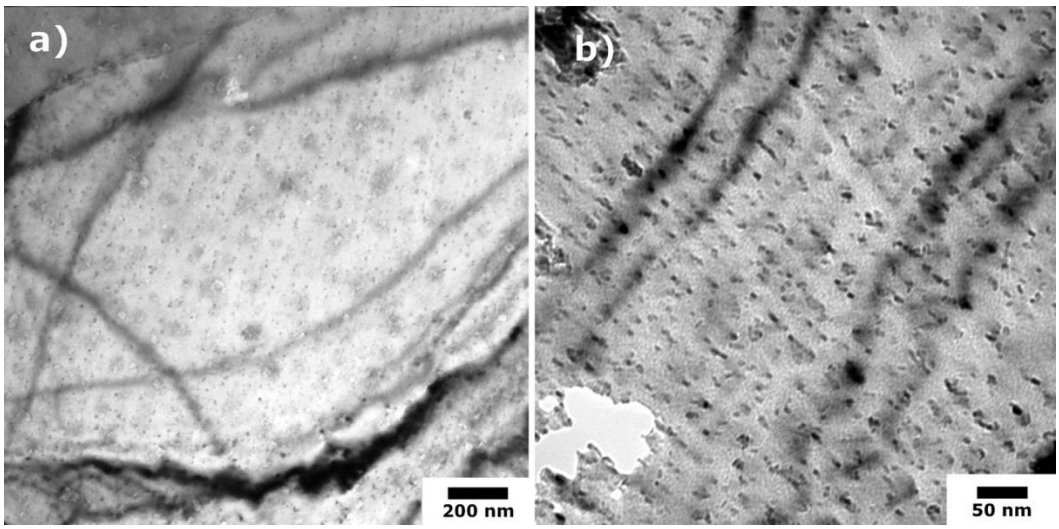

Figure 6.4-4 TEM Bright field images of Alloy 1 after isothermal holding at 700 ℃ *for* $300\ s$*; a) lower magnification TEM image showing characteristic rows of interphase precipitates (dark spots), b) detailed TEM image showing a region of stable in a separate ferritic grain where the distribution of the inter-sheet spacing with average inter-sheet spacing is* $19 \pm 2\ nm$*.*

Figure 6.4-4 shows TEM Bright field images of Alloy 1 after isothermal holding at 700 ℃ for $300\ s$; Figure 6.4-4 a) is a lower magnification TEM image showing characteristic rows of interphase precipitates. Figure 6.4-4 shows a detailed TEM image demonstrating a region where a relatively stable distribution of the interphase precipitates with average inter-sheet spacing $19 \pm 2\ nm$ is observed.

6.5. The Proposed Model

6.5.1. Inter-sheet spacing

For the purposes of this study it will be assumed that all the γ/α interphase boundaries regardless of crystallographic orientation relationships exhibit growth ledges and they agglomerate to form mobile super-ledges of a critical

height such as those described by Aaronson *et al.* [101]. Cahn stated that 'the mechanism of the motion of an interface in a crystalline material depends on the driving force rather than on the crystallographic nature of the interface. At sufficiently large driving forces, the interface can move uniformly'. However, at 'sharp interfaces the necessary driving force is so large that it may be difficult to achieve' [135]. More recently the incoherency view has received renewed attention, Massalski *et al.* [134] reviewed the experimental and theoretical nature of interphase boundaries concluding that an incoherent boundary may be facetted on various length scales. In particular in context to the pearlite transformation in steels Hackney and Shifflet [196] observed facets, misfit accommodating dislocations and most importantly mobile ledges on the interfaces of both growing phases on interfaces with the parent γ with no rational orientation relationship.

Bhadeshia [107] proposed Equation (6.5-1) which states that the critical height for the successful nucleation of a super-ledge at an γ/α interphase boundary, h^* which is assumed to be equal to the inter-sheet spacing λ, is controlled by the interfacial energy of the facet plane of the ledged interphase boundary, σ, the driving force for the transformation, $\Delta G_m^{\gamma\rightarrow\alpha}$.

$$h^* = \lambda = \frac{\sigma V_m}{\Delta G_m^{\gamma\rightarrow\alpha}}$$

(6.5-1)

Where, V_m is the molar volume. Bhadeshia argued that $\Delta G_m^{\gamma\rightarrow\alpha}$ has approximately constant maximum value for a given temperature as carbon is not enriched in the austenite, γ, the *MC* carbides consume the vast majority of the carbon rejected from the growing ferrite; $\Delta G_m^{\gamma\rightarrow\alpha}$ can be therefore calculated assuming parequilibrium conditions (PE). It was assumed that σ in (6.5-1) was a fixed constant and takes the frequently value of $0.2\ Jm^{-2}$ [197] for an interphase boundary obeying a low energy orientation relationship. It is assumed that the

lower bound for the inter-sheet spacing of interphase precipitates is equal to the critical step height since Bhadeshia stated that the inter-sheet spacing could not possibly take a value of significantly larger than the value of h^* as a larger super-ledge would degenerate into several smaller super-ledges each of height h^*.

Although this approach [107] was found to be able to predict the trend of refining inter-sheet spacing with reducing temperature excellently there was still a separation between the expected and predicted curves. It is suggested that all of the experimental and modelled trends can be fitted if the σ of the facet plane is allowed to vary within an order of magnitude. A model shall be proposed as part of this work with Equation (6.5-1) as basis, however, $\Delta G_m^{\gamma\to\alpha}$ and interfacial energy of the interphase boundary σ shall be carefully re-evaluated.

As indented in Section (2.2.5) a more general form of Equation (6.5-1) can be proposed. It was suggested that interphase precipitation attributable to either the ledge, bowing mechanisms and presumably the intermediate quasi-ledge mechanism all can be determined by the following equation:

$$\lambda = a_{crit} = \frac{C_3 \sigma V_m}{\Delta G_m^{\gamma\to\alpha}}$$

(6.5-2)

which states that the minimum spacing between rows of interphase precipitates is controlled by the interfacial energy of the facet plane of the ledged interphase boundary, σ, and the driving force for the transformation, $\Delta G_m^{\gamma\to\alpha}$. C_3 is a constant that can be varied according to the geometry of the mechanism When the constant C_3 is equal to 1 Equation (6.5-2) is analogous to the theory of diffusional super ledges proposed by Bhadeshia [107]. When C_3 is equal to 2 Equation (6.5-2) is analogous to the model for the bowing mechanism proposed by Ricks and Howell [65]. Similarly when C_3 is equal to 2 Equation (6.5-2)is also analogous to the pillbox model proposed by Lange III [115]. In this work chapter

the constant C_3 is set to be equal to 1 Equation (6.5-2) and is therefore analogous to the theory of diffusional super ledges proposed by Bhadeshia [107].

6.5.2. Interfacial energy

The interfacial energy or interfacial free energy is defined as the energy associated with the interaction atoms constituting the two phases interact with one another across the new interphase boundary. The interfacial energy is influenced by both a structural, i.e. misfit and coherency, and concentration gradients across the boundary [24]. Song and Hoyte [198], using molecular dynamics modelling of the γ/α interphase boundary in pure iron, calculated that the interfacial energy in an interphase boundary with a Kurdjumov-Sachs (K-S) orientation relationship had an interfacial energy of $0.37 \pm 0.05\, Jm^{-2}$ and an incoherent random interphase boundary had an interfacial energy of $1.40 \pm 0.2\, Jm^{-2}$. These results were comparable to the work of Nagano and Enomoto [199]. The interfacial energy of an interphase boundary is known to vary with bulk alloying content and under equilibrium conditions can be predicted based on the Gibbs-Duham equation [200]. Gjostien *et al.* [201] proposed and experimentally fitted a semi-empirical approach. It was shown how the interfacial energy drops significantly with increasing bulk C concentration: whilst an acceptable match was found at low concentrations of C, the modified isotherm failed at high C concentration. At equilibrium in coherent interphase boundaries Dregia and Wynblatt [202] modelled segregation and interfacial energy in a multicomponent system, this approach, however, is of considerable complexity and again is not applicable beyond the context of systems in equilibrium. The interfacial energy under a dynamic equilibrium incorporating the formation of sharp concentration spikes at the interface is likely to be of considerable additional complexity and as to the best of the authors knowledge has not been explored. The dynamic interfacial energy will be considered as a fitting parameter in this analysis within the following bounds, $(0.1 \leq \sigma \leq 2.5)\, Jm^{-2}$ [203].

6.5.3. Prediction of the dissipation of Gibbs energy balance at the γ/α interphase boundary

A recently proposed method for determining the required chemical driving force throughout the austenite to ferrite transformation, $\Delta G_m^{\gamma\to\alpha}$, is that of the Gibbs Energy Balance (GEB) approach [204,205] which built upon the paper by Purdy and Bréchet [195]. In this approach the driving force is equal to the energy dissipation in the interphase boundary, which is equal to the combination of a diffusional dissipation of substitutional solutes in the interface and an interphase boundary friction term related to the intrinsic interphase boundary mobility, (Eqn. (6.5-3)).

$$\Delta G_m^{\gamma\to\alpha} = \Delta G_m^{diff} + \Delta G_m^{frict} \qquad (6.5\text{-}3)$$

Such an approach allows a gradual transition between transformation modes traditionally thought quite distinct. At a relatively high interfacial velocity, there is little interfacial segregation, consistent with a transformation under preequilibrium (quasi-PE) like conditions, whereas, there is significant segregation when the interphase boundary is moving much slower, consistent with a transformation under negligible partitioning local equilibrium (N-PLE) like, (quasi-N-PLE) conditions.

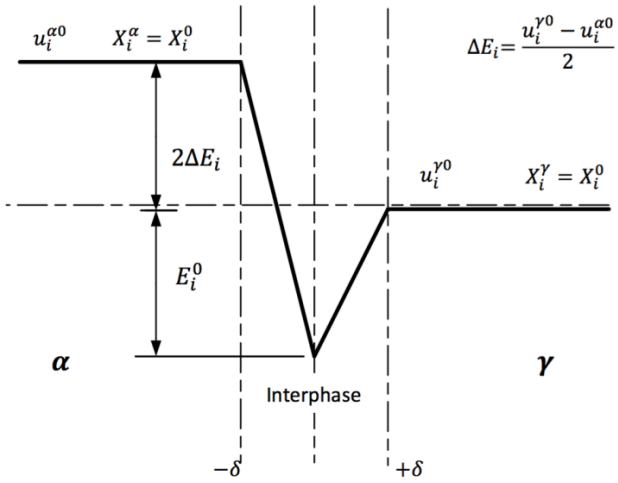

Figure 6.5-1 Schematic of a Purdy-Bréchet interphase boundary potential well for a general austenite stabilizing component.

It has been proposed that the segregation in an interphase boundary can be described by a triangular potential well [195], as shown in Figure 6.5-1, where δ is half the interphase boundary thickness and taken in this study to be equal to $0.25\ nm$, X is the solute concentration, x is the distance from the center of the interphase boundary, E_i^0 is the binding energy of the solute element, D_i is the interfacial diffusivity of the solute element i and v is the velocity of the interphase boundary. The magnitude of $\Delta E_i = \frac{u_i^{\gamma 0} - u_i^{\alpha 0}}{2}$, where $u_i^{\gamma 0}$and $u_i^{\alpha 0}$ are the chemical potential of component i in austenite and ferrite respectively, and can be calculated for each respective component using thermodynamic software, in this case, Matcalc. The dissipation of Gibbs free energy due to the diffusion of alloying elements inside the interphase boundary can be determined using Cahn's equation, (Equation (6.5-4))[206], where, P is the solute drag force. Hillert and Sundman suggested an alternative equation [207], Hillert later reviewed both equations [208] concluding both were fundamentally the same although applicable in subtly different conditions.

$$\Delta G_m^{diff} = PV_m = \int_{-\delta}^{\delta} (X_i - X_i^0)\left(\frac{dE_i}{dx}\right) dx$$

(6.5-4)

The concentration profile, X_i, of segregating elements within a moving interphase boundary can be described by the governing equation, Equation (6.5-5).

$$\frac{\partial}{\partial x}\left[D_i \frac{\partial X_i}{\partial x} + \frac{D_i X_i}{RT}\frac{\partial E_i}{\partial x} + vX_i\right] = 0$$

(6.5-5)

The interfacial diffusivity remains a source of significant uncertainty, for this analysis a similar geometric mean methodology as Chen *et al.* [204,205] is adopted, $D_i = \sqrt[6]{D_i^{\alpha 2} D_i^{\alpha\alpha} D_i^{\gamma\gamma} D_i^{y\,2}}$, where, D_i^{α} , $D_i^{\alpha\alpha}$, $D_i^{\gamma\gamma}$, D_i^{y} are the diffusion coefficients of each component i in a ferrite matrix, at ferrite-ferrite grain boundary, austenite grain boundary, and within an austenite matrix respectively, each readily accessible within the computational package Matcalc using an appropriate mobility database. Additionally, the molar volume, V_m, can be predicted using Matcalc using an appropriate property database.

The binding energy E_i^0 has been calculated using first principles Density Functional Theory (DFT) calculations for ferrite $\Sigma 5$ tilt grain boundaries [129]. It will be assumed that similar values will hold true for the segregation energy in the interphase boundary. This would appear to be reasonable given the close correspondence of the values fitted in the work of Chen *et al.* [204,205]. The average binding listed in (Fig. 3 in Jin *et al.* [129]) the *ab-initio* study of Jin *et al.* [129] are adopted in this work and are shown in Table 6.5-1.

Table 6.5-1 Binding Energies Adopted for Segregation Calculations for elements relevant to this study.

Element i	$E_i^0\ kJ\ mol^{-1}$
Mn	10.6
V	7.7
Si	6.8

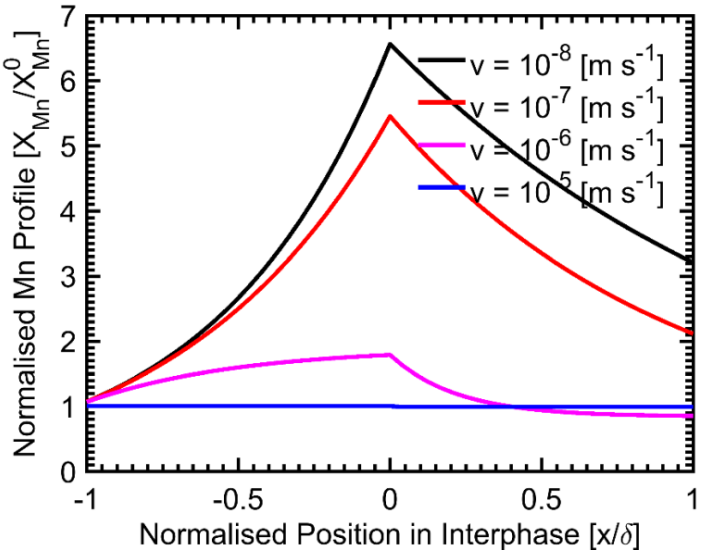

Figure 6.5-2 Extemporary Mn profiles of Alloy 1 with an interphase boundary moving at different velocities at a temperature of 700 ℃.

The dissipation of Gibbs free energy due to interphase boundary friction can be determined by Equation (6.5-6), where M_m^{int} is the intrinsic mobility of the interphase boundary. As of yet there is no fundamental evaluation of the intrinsic mobility of the γ/α interphase boundary in iron. Hillert assumed the upper bound of the pre-exponential of a α/α grain boundary was equal to the intrinsic mobility of the γ/α interphase boundary, which is calculated according to the following relationship: $M_m^{int} = 4800 \times exp\left(\frac{-147\times10^3}{RT}\right)\ mol\ s\ kg^{-1}\ m^{-1}$[209] when an average molar volume of $7.3\ \times 10^{-6}\ m^3\ mol^{-1}$ is considered. This relationship was determined assuming that the γ/α interphase boundary has an intrinsic mobility to the evaluation of

the intrinsic mobility of α/α grain boundaries by Speich and Szirmae [210]. A high mobility yields extremely low dissipation under quasi-parequilibrium conditions unless the interphase boundary is moving at exceptionally high velocities. Hillert later reviewed the topic concluding that the mobility of the interphase boundary was much lower especially within the temperature range considered in this study [211]. Therefore, the lower bound of the lower apparent mobility of Gamsjäger *et al.* [212] shall be adopted in this work using the following Arrhenius relationship $M_m^{int} = (6 \leq M_0 \leq 15) \times exp\left(\frac{-140\times10^3}{RT}\right) mol\ s\ kg^{-1}\ m^{-1}$.

$$G_m^{frict} = \frac{v}{M_m^{int}}$$

(6.5-6)

Combining Equations (6.5-3), (6.5-5) and (6.5-6) and assuming that the total dissipation of n substitutional alloying component can be predicted by summing together their individual contributions, i.e. assuming there are no interactions between each respective element.

$$\Delta G_m^{diff} + \Delta G_m^{frict} = \frac{v}{M_m^{int}} - \sum_{i=0}^{n} \int_{-\delta}^{\delta} (X_i - X_i^0)\left(\frac{dE_i}{dx}\right) dx$$

(6.5-7)

6.5.4. Prediction of the Chemical Driving Force

The chemical driving force can be predicted as proposed by Chen *et al.*[204,205] by the following equation:

$$\Delta G_m^{\gamma\to\alpha} = \sum_{i=0}^{n} X_i^0 \left(u_i^{\gamma\alpha} X_i^{\gamma\alpha} - u_i^{\alpha\gamma} X_i^{\alpha\gamma}\right)$$

(6.5-8)

where $u_i^{\gamma\alpha}$ and $u_i^{\alpha\gamma}$ are chemical potentials of element i at austenite and ferrite sides of the interface. In a similar manner to that of Chen [204,205], $X_i^{\alpha\gamma}$ and $X_i^{\gamma\alpha}$ for substitutional alloying elements are set to the be equal to the nominal concentration X_i^0, consistent with negligible partitioning of substitutional solute elements between the two matrix phases. This is apart from that of the carbide forming substitutional alloying element $X_M^{\alpha\gamma}$, which is consumed during the formation of interphase precipitates. This is consistent with the 3D atom probe tomography study of Nöhrer *et al.* [157] which mapped the concentration spikes in the γ/α interphase boundary, finding by far the largest substitutional element spike was that of Mn with relativity smaller spikes for that of Si and V. Furthermore, Nöhrer *et al.* [157] found no enrichment of N at the interphase boundary, which may in part explain why it is commonly found that interphase precipitates are predominantly carbides. It is assumed that $X_M^{\gamma\alpha}$ locally takes the value corresponding to the equilibrium solubility of M (K_{MC}) with respect to an austenitic matrix i.e.:

$$X_M^{\gamma\alpha} = \frac{\left(\frac{A_{Fe}}{100}\right)^{(1+y)} K_{MC}}{A_M {A_C}^y X_C^{0\,y}}$$

(6.5-9)

Where, y, is the interstitial to substitutional ratio in the precipitate, A_{Fe}, A_M, A_c are the atomic masses of the respective elements and X_M^0, X_C^0 are the bulk mole fractions. In this work, prior Small Angle Neutron Scattering studies on Alloy 1 suggested that the composition of the interphase precipitates was consistent with the precipitates being considerably sub-stoichiometric (Section 4.5.1) which is consistent with the findings from another V micro-alloyed steel [166]. The

austenite solubility product $\log\left(K_{V_4C_3}\right) = 7.06 - \left(\frac{10800}{T}\right)$ could, therefore, be used from Gladman [17]. More generally, and implemented in this work, the solubility of M in austenite for a given alloy composition can be determined using thermodynamic software with the appropriate thermodynamic database.

Two transformation modes are derived as part of this study. The $\gamma \rightarrow \alpha$ transformation with no consumption of carbon from carbide precipitates at the interphase boundary where, $X_C^{\alpha\gamma}$ is the equilibrium carbon concentration on the ferrite side of the interphase boundary, $X_C^{\alpha\gamma}$.

$$X = X_C^{\alpha\gamma}$$

(6.5-10)

For the $\gamma \rightarrow \alpha + MC$ with consumption of carbon from carbide precipitates, the consumed carbon consists of two parts: Carbon in the ferrite $X_C^{\alpha\gamma}$ and the carbon in the forming carbides $y\left(X_M^0 - X_M^{\gamma\alpha}\right)$.

$$X = \left(X_C^{\alpha\gamma} + y\left(X_M^0 - X_M^{\gamma\alpha}\right)\right)$$

(6.5-11)

It is assumed that the progression of a ledged interphase can be approximated by that of a macroscopically smooth interphase boundary. Chen and Zwaag [213] describe the $\gamma \rightarrow \alpha$ phase transformation, they assumed a 1-dimensional simplification of two ferrite grains growing towards each other from the either side of a parent austenite grain. The same approach is adopted in this work. The interface velocity under non-soft impinging conditions can be calculated by the following equation where,

$$v = \frac{(n-1)D_C^{\gamma}\left(X_C^{\gamma\alpha} - X_C^0\right)}{L\left(X_C^{\gamma\alpha} - X\right)}$$

(6.5-12)

$X_C^{\gamma\alpha}$ is the carbon mole fraction on the austenite side of the interphase boundary. The parameter n determines whether a linear $(n = 2)$ or quadratic diffusion field $(n = 3)$ is considered, D_C^{γ} is the diffusivity of carbon in austenite. L is the diffusion length, which can be calculated in turn by Equation (6.5-13) [213].

$$L = \frac{nS(X_C^0 - X)}{\left(X_C^{\gamma\alpha} - X_C^0\right)}$$

(6.5-13)

where, S, is the half thickness of the growing ferrite allotriomorph. Substituting Equation (6.5-13) into (6.5-12) and rearranging yields,

$$X_C^{\gamma\alpha} = \frac{(X_C^0 - X)\sqrt{nSv}\sqrt{4nD_C^{\gamma} - 4D_C^{\gamma} + nSv} - 2D_C^{\gamma}X_C^0 + 2nSX_C^0 - 2nSvX}{2(n-1)D_C^{\gamma}}$$

(6.5-14)

Similarly under conditions where soft impingement is triggered i.e. $L > L_0 - S$ where L_0 is half the original austenite grain size a similar set of equations can be derived [213].

$$v = \frac{(n-1)D_C^{\gamma}\left(X_C^{\gamma\alpha} - X_C^m\right)}{(L_0 - S)\left(X_C^{\gamma\alpha} - X\right)}$$

(6.5-15)

$$X_C^m = \frac{1}{(n-1)}\left(\frac{nS(X_C^0 - X)}{L_0 - S} + nX_C^0 - X_C^{\gamma\alpha}\right)$$

(6.5-16)

Where X_C^m is the mole fraction of carbon at the centre of the austenite grain. Substituting Equation (6.5-16) into (6.5-15) and rearranging yields,

$$X_C^{\gamma\alpha} = \frac{nSD_C^{\gamma}X - nL_0D_C^{\gamma}X_C^0 + {L_0}^2vX - 2L_0SvX + S^2vX}{(L_0 - S)\left(L_0v - nD_C^{\gamma} - Sv\right)}$$

(6.5-17)

Through combining equations (4.3-8), (6.5-14) and (6.5-16) and the use of an appropriate computational thermodynamics package the chemical driving force, $\Delta G_m^{\gamma\to\alpha}$, can be calculated. Finally, through post-processing the computed data, finding the intersect between the $\Delta G_m^{\gamma\to\alpha}$ and $\Delta G_{Diss}^{Total} = \Delta G_m^{diff} + \Delta G_m^{frict}$curves, as shown in Figure 6.5-3, the inter-sheet spacing (using Equation 6.5-18) and the transformation kinetics in terms of interface velocity, ferrite thickness can be calculated. Simple processing allows the volume fraction of ferrite and the transformation time to be calculated.

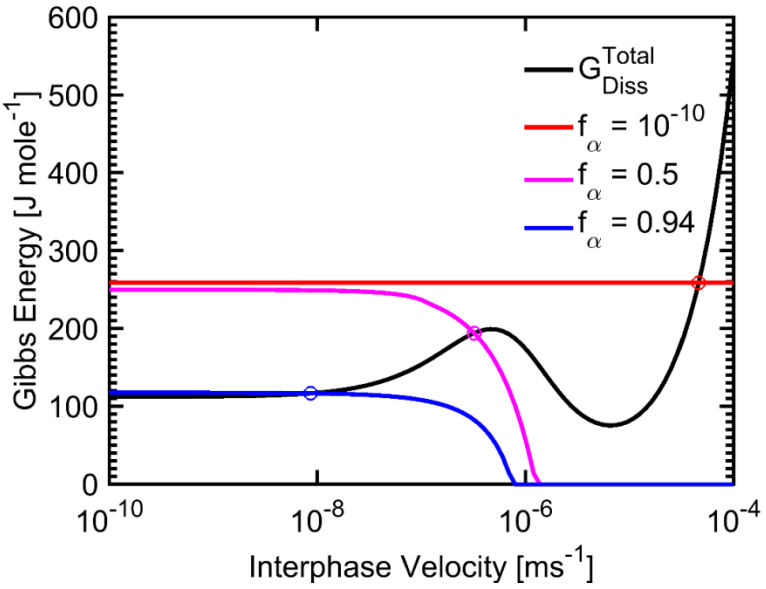

Figure 6.5-3 Extemporary dissipation and driving force curves for Alloy 1 at a temperature of 700 ℃.

6.6. Discussion

The kinetics of the $\gamma \rightarrow \alpha + MC$ transformation in Alloy 1 are calculated using the carbon consumption model. Figure 6.6-1 shows the correlation between the modelled volume fraction and dilatometric analysis of Alloy 1 during isothermal holding at 700 ℃ for different values of initial half austenite grain size, L_0. The initial mismatch between the predicted and experimental transformation rates could be attributed to a combination of numerous factors, namely: a) an overestimation of the intrinsic interphase boundary mobility; b) a spherical growth mode rather than the planar mode assumed in this analysis; c) the effect of a transient nucleation rate of quasi-polygonal ferrite and d) the effect of the heterogeneity of the prior austenite grain-size. The mismatch between the modelled and experimental final ferrite phase fraction is similarly attributable to many of the aforementioned reasons. Although, the uncertainty in the boundary diffusivities of substitutional alloying elements will significantly dominate over intrinsic interphase boundary mobility in a slow-moving interphase boundary. Additionally, inherent inaccuracies and subjective interpretation in the

assessments used for the creation of the multicomponent thermodynamic database used may be influential. Furthermore, as explained by the atom probe study of Mukherjee *et al.* [84,86] the formation of interphase precipitates becomes more significant as the interphase boundary slows. Therefore, a pinning force exerted by the precipitates upon the interphase boundary may become increasingly significant in the latter stages of the transformation. Finally, as nano-clusters are by far richer in metallic elements rather than interstitial elements the carbon consumption at the interphase boundary is likely to have been significantly overestimated. As such, more carbon would, in reality, have been rejected into the residual austenite hastening the soft impingement of the interphase boundary. As the onset of soft impingement cannot be accurately predicted an accurate correlation of inter-sheet spacing and $\gamma \rightarrow \alpha$ transformation kinetics under soft impingement conditions remains elusive.

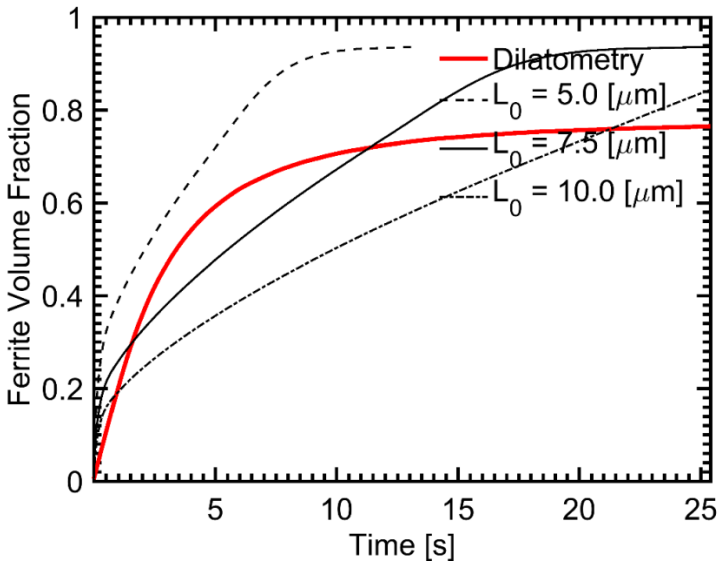

Figure 6.6-1 Correlation between the modelled volume fraction and dilatometric analysis of Alloy 1 during isothermal holding at 700 ℃.

As shown in Figure 6.6-2 a reasonable qualitative correlation between the experimental results in Figure 6.4-4 and the modelled prediction can be achieved

after the transformation mode transitions from quasi-PE to quasi-N-PLE with a fitted γ/α interfacial energy of $\sigma = 0.55\ Jm^{-2}$.

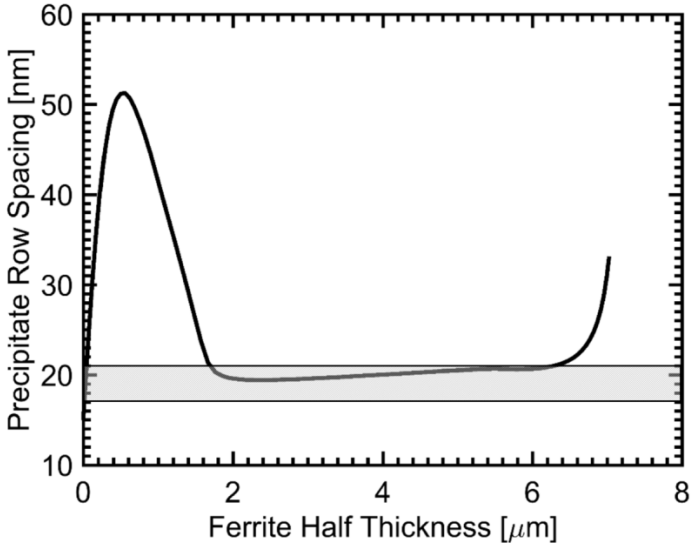

Figure 6.6-2 Modelled evolution of inter-sheet spacing for Alloy 1 during isothermal holding at 700 ℃ *for an half austenite grain size of* $L_0 = 7.5\ \mu m$ *with fitted* $\sigma = 0.55\ Jm^{-2}$ *using the Inter-sheet spacing in the stable region* $(19 \pm 2\ nm)$ *in Figure 6.4-4 b) as an error band.*

Further analysis of the performance of the proposed model has been performed using literature data. In particular, the model has been tested using the experimental finding that inter-sheet spacing initially refines. This finding is contradictory to the results of many models previously proposed [121].

Figure 6.6-3 shows the correlation between the proposed model and the experimental results of Murakami *et al.* [72], it is shown how the model is capable of predicting the experimentally observed refinement of inter-sheet spacing. The interfacial energy was found to best match the experimental results when $\sigma = 0.17\ Jm^{-2}$, however, the model under-predicts the majority of the measurements close to the ferrite centre. An interfacial energy of $\sigma \approx 0.20\ Jm^{-2}$ produces a good fit of the results near the ferrite centre and over-predicts measurements further into the ferritic grain, where an interfacial energy

of $\sigma \approx 0.14\,Jm^{-2}$ yields a good fit. This mismatch is to be expected as the interfacial energy is known to be reduced with increasing segregation to the interphase boundary. It is clear that the ability to predict the interfacial energy during a dynamic phase transformation would further improve the predictive capability of the model. The discrepancy between the large interfacial energy $\sigma = 0.55\,Jm^{-2}$ required to fit the results for Alloy one and the $\sigma \approx 0.17\,Jm^{-2}$ for the experimental data from Murakami *et al.* [72] is most likely explained by the interface in the latter case having an orientation relationship closer than the former case to an ideal low energy orientation relationship. Figure 6.6-4 shows the correlation between the predicted ferrite growth rate and the experimentally measured ferrite half thickness, a slightly improved match from the model proposed Murakami *et al.* [72].

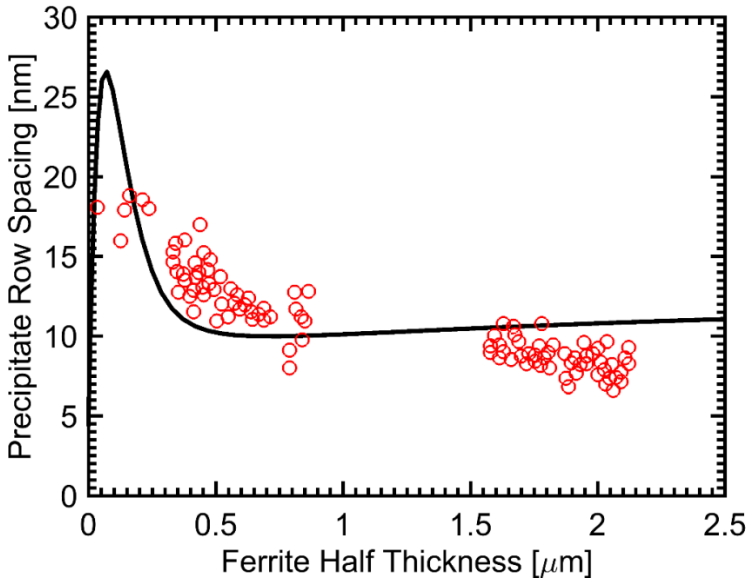

Figure 6.6-3 Correlation between this model and measured inter-sheet spacing for an Fe-0.75Mn-0.43C-0.25Si-0.29V alloy transformed at 675 °C *[72] with fitted* $\sigma = 0.17\,Jm^{-2}$.

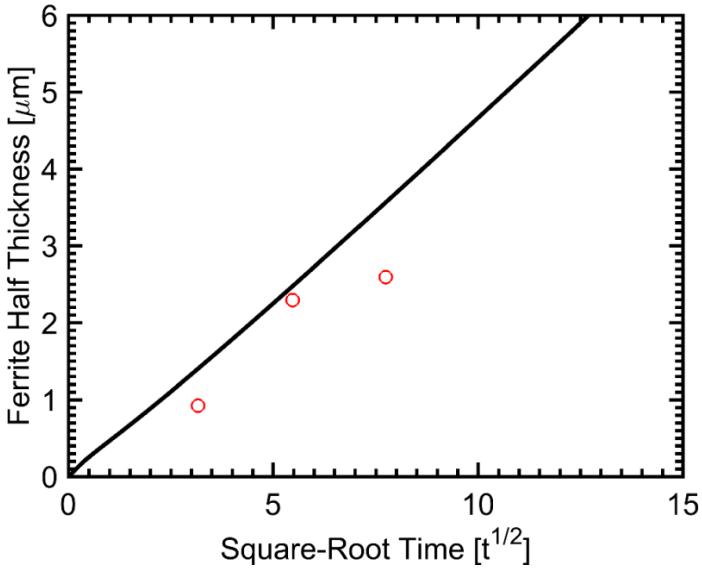

Figure 6.6-4 *Correlation between this model and measured half ferrite thickness for an Fe-0.75Mn-0.43C-0.25Si alloy transformed at* 675 ℃ [72].

The significantly larger interfacial energy required in Alloy 1 $(0.55\,Jm^{-2})$ compared to that $(0.17\,Jm^{-2})$ when fitting the literature experimental results of Murakami *et al.*[72] as reducing the bulk C alloying in an alloy is well known to increase the interfacial energy of the incoherent interphase boundary [201].

Manganese is an austenite stabilizing element intrinsically reducing the driving force, $\Delta G^{\gamma\rightarrow\alpha}$, for ferrite growth at a given transformation temperature. As the driving force is reduced through Equation (6.5-2) the inter-sheet spacing of interphase carbide precipitates would be expected to increase if the interfacial energy, σ, is assumed to vary little. It is suggested that this mechanism could explain the results reported by Sakuma and Honeycombe.[51] The effect of precipitate pinning could also be important which would be affected by the increased solubility of niobium carbide with increasing manganese alloying [51].

6.7. Further discussion – On the effect of carbon consumption at the γ/α interphase boundary

It is noted that the quantity of carbon consumed at the γ/α interphase boundary is not known to any degree of certainty. It is therefore, at this opportunity, expedient to explore the role this parameter has upon the $\gamma \rightarrow \alpha$ transformation kinetics and inter-sheet spacing of interphase precipitates. Further, modelling has been undertaken.

Through considering a threshold velocity at which the γ/α interphase boundary can be said to have become impinged and the transformation completed of $v = 1 \times 10^{-10}\, ms^{-1} = 0.1\, nms^{-1}$ an analogue of Figure 6.5-3 can be calculated. Through computing Equations (4.3-8), (6.5-14) and (6.5-16) with the fixed threshold velocity over the range $S = 0 \rightarrow \frac{L_0}{2}$ (i.e. over the range of ferrite fraction $0 \rightarrow 1$) $\Delta G_m^{\gamma \rightarrow \alpha}$ can be calculated. As before, through post-processing the computed data, an intersect between the intersect between the $\Delta G_m^{\gamma \rightarrow \alpha}$ against S curve and ΔG_{Diss}^{Total} against S curve can be found as shown in Figure 6.7-1. The intersect corresponds to the distance from the prior austenite boundary at which the interphase boundary becomes impinged. The process is repeated considering varying degrees of carbon consumption at the interphase boundary according to the normalised parameter $\frac{X_C^{\alpha\gamma} + X_C^{MC}}{X_C^0}$ in the range of no carbon consumption by interphase precipitates to the entire bulk nominal carbon concentration, X_C^0, being accounted for in the forming ferrite and interphase precipitates, i.e. $\frac{X_C^{\alpha\gamma} + X_C^{MC}}{X_C^0} = \frac{X_C^{\alpha\gamma}}{X_C^0} \rightarrow 1$.

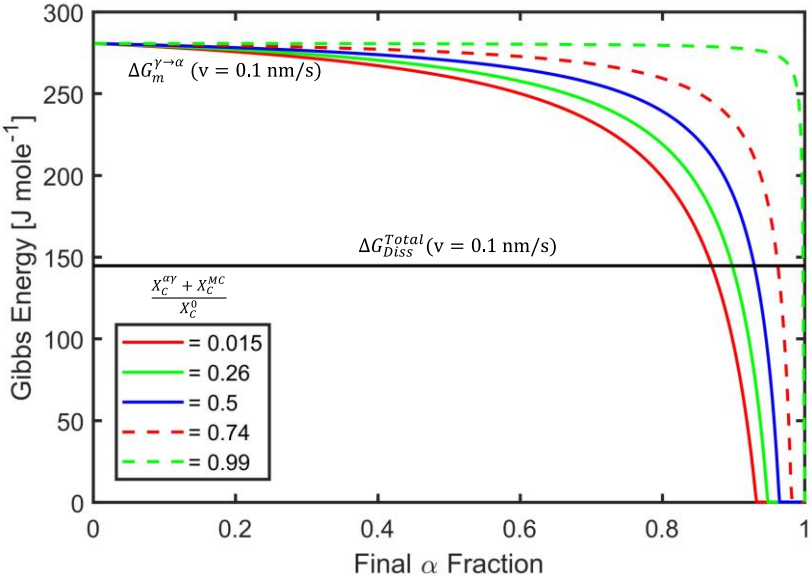

Figure 6.7-1 Extemporary dissipation and driving force curves determining the final ferrite fraction for Alloy 1 at a temperature of 700 ℃ *for with varying degree of carbon consumption.*

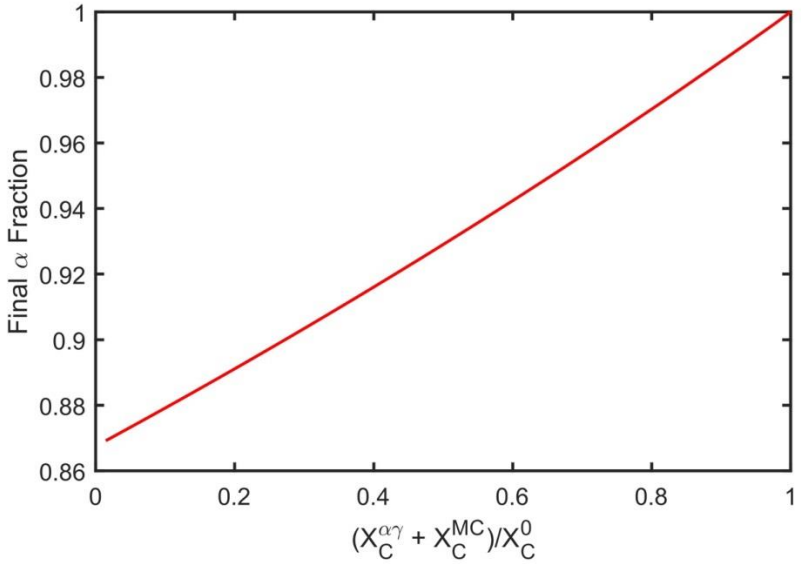

Figure 6.7-2 Final ferrite fraction for Alloy 1 at a temperature of 700 ℃ *for with varying degree of carbon consumption.*

Figure 6.7-2 shows that the final α fraction is directly proportional to the degree of carbon consumption at the γ/α interphase boundary by interphase carbide

precipitates. Now that the role of carbon consumption by interphase carbide precipitates at the interphase boundary has been established the role of this parameter on the $\gamma \rightarrow \alpha$ should be established. This is accomplished through sequentially computing the model as cast in Section 6.5 with variable carbon consumption at the interphase boundary according to the normalised parameter $\frac{X_C^{\alpha\gamma}+X_C^{MC}}{X_C^0}$ in the range of no carbon consumption by interphase precipitates to the entire bulk nominal carbon concentration, X_C^0, being accounted for in the forming ferrite and interphase precipitates, i.e. $\frac{X_C^{\alpha\gamma}+X_C^{MC}}{X_C^0} = \frac{X_C^{\alpha\gamma}}{X_C^0} \rightarrow 1$.

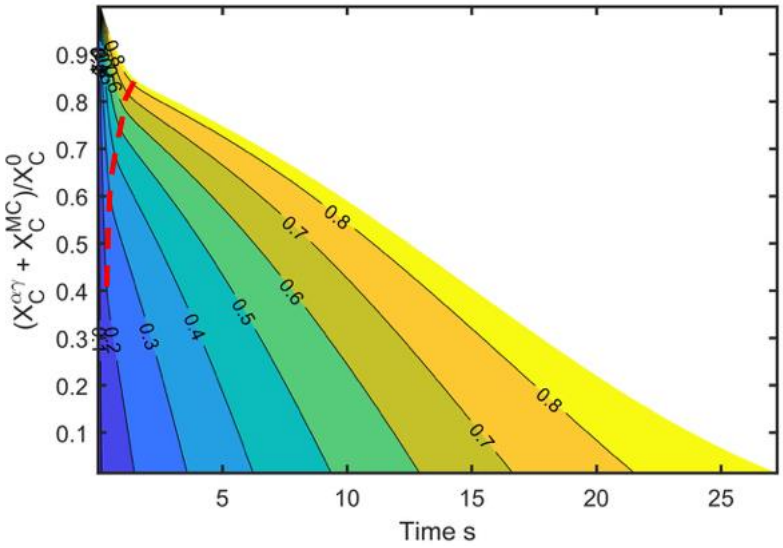

Figure 6.7-3 Contour plot showing the effect of consumption at the γ/α interphase boundary by interphase carbide precipitates upon the $\gamma \rightarrow \alpha$ transformation kinetics for for Alloy 1 at a temperature of 700 ℃.

Figure 6.7-3 shows a contour plot elucidating the effect of consumption at the γ/α interphase boundary by interphase carbide precipitates upon the $\gamma \rightarrow \alpha$ transformation kinetics for Alloy 1 at a temperature of 700 ℃. It is evident that increasing the degree of carbon consumption not only increases the final fraction at which the γ/α interphase boundary becomes impinged but also accelerates the $\gamma \rightarrow \alpha$ transformation. Closer inspection of the α fraction contour lines reveals a characteristic 'kink' that is located at a later time and larger α fraction

with increasing $\frac{X_C^{\alpha\gamma}+X_C^{MC}}{X_C^0}$, the location of the 'kink' is marked on Figure 6.7-3 by the red dashed line. This 'kink' is also evident in the transformation curves shown in Figure 6.6-1 and corresponds to the transition between quasi-parequilibrium where, the dissipation of Gibbs energy is dominated by ΔG_m^{fricct} and quasi-negligible partitioning local equilibrium where, the dissipation of Gibbs energy is dominated by ΔG_m^{diff}.

Finally, the role of carbon consumption at the γ/α interphase boundary on the inter-sheet spacing (using Equation 6.7-1) can be revealed considering an γ/α interfacial energy of $\sigma = 0.55\, Jm^{-2}$. Figure 6.7-4 shows a contour plot elucidating the effect of consumption at the γ/α interphase boundary by interphase carbide precipitates upon the inter-sheet spacing of interphase precipitates in *nm* for Alloy 1 at a temperature of $700\,℃$. A characteristic 'boomerang' in the inter-sheet spacing can be seen in the results. Generally, at a given $\frac{X_C^{\alpha\gamma}+X_C^{MC}}{X_C^0}$ the inter-sheet spacing initially increases with ferrite half thickness to a peak value then falls down to a roughly constant value as shown in Figure 6.6-2 and Figure 6.6-3. However, the ferrite half thickness distances at which these transitions occur are increasingly delayed with increasing carbon consumption by interphase carbide precipitates, $\frac{X_C^{\alpha\gamma}+X_C^{MC}}{X_C^0}$.

Figure 6.7-4 shows that as $\frac{X_C^{\alpha\gamma}+X_C^{MC}}{X_C^0} \to 1$ the inter-sheet spacing goes to a constant small value. $\frac{X_C^{\alpha\gamma}+X_C^{MC}}{X_C^0} \to 1$ corresponds to a partitionless massive transformation where the velocity of the interphase boundary moves at a constant and large velocity until the $\gamma \to \alpha$ transformation is fully completed. Although, this uniform fine array of interphase carbide precipitates would yield the optimised exploitation of the interphase precipitation mechanism at a given

transformation temperature for a given temperature, it remains to be revealed if interphase precipitation can occur during a rapid massive transformation.

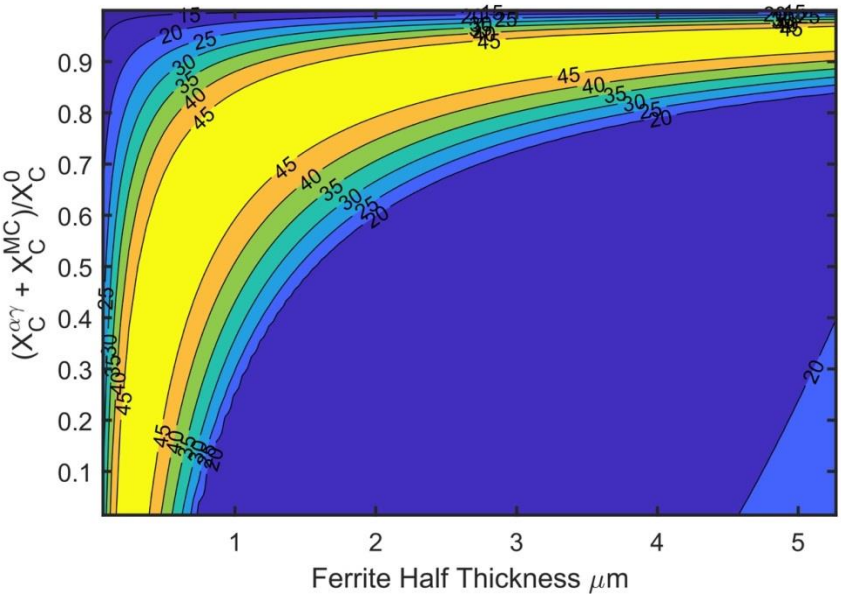

Figure 6.7-4 Contour plot showing the effect of consumption at the γ/α interphase boundary by interphase carbide precipitates upon the inter-sheet spacing of interphase precipitates in nm for Alloy 1 at a temperature of 700 ℃.

In order to develop this study further an improved understanding of the following is prerequisite:

- An accurate means of determination and prediction of the interfacial energy of the γ/α interphase boundary is required.
- Further theoretical work is required towards understanding the formation of nano-clusters and their composition.
- Additional experimental studies are required where both the crystallography and transformation kinetics are extracted simultaneously coupled with site-specific *a posteriori* and site-specific TEM analysis, using Focused Ion Beam lift-out and 3D Atom Probe Tomography in order to directly relate interphase boundary and interphase precipitation parameters.

6.8. Novelty of this Model

The model presented in this chapter uses the solute drag model of Purdy and Bréchet, the GEB concept, and the theory of the diffusional formation of super-ledges by Bhadeshia. In this chapter, the phenomenon of interphase precipitation and how the inter-sheet spacing of interphase precipitates relates to the dissipation of Gibbs energy inside the moving, ledged interphase boundary was elucidated. The particular strength of this model in comparison to previous models described in the literature is modelling of a continuous transition between $\gamma \rightarrow \alpha$ transformation modes and its effect upon the inter-sheet spacing of interphase precipitates. It was shown that the contradictory observations of refining and relatively constant inter-sheet spacing as $\gamma \rightarrow \alpha$ transformation progresses (evidenced in Section 2.2.2) can be explained. It is felt the relationship between $\gamma \rightarrow \alpha$ transformation kinetics and inter-sheet spacing elucidated in this work offer a timely and relevant insight into the phenomenon of interphase precipitation. A further strength of this model in comparison to previous models is that it can easily and readily be applied to complex, industrial, multi-component alloys.

6.9. Conclusions

A model is presented using the solute drag model of Purdy and Bréchet, the GEB concept, and the theory of the diffusional formation of super-ledges by Bhadeshia. Unlike the majority of previous models, the actual nucleation of interphase precipitates is considered to play little role in the determination of super-ledge height rather the inter-sheet spacing is controlled by a complex interplay between the factors of interfacial energy and interfacial segregation. It is shown that the general trend of refining inter-sheet spacing with the distance to ferrite grain centre can be well predicted by the proposed model.

To take the observed accelerated kinetics of $\gamma \rightarrow \alpha$ transformation in the vanadium micro-alloyed steel into consideration, the consumption of carbon at γ/α interface due to the formation of interphase carbides has been incorporated into the $\gamma \rightarrow \alpha$ transformation model. Increasing carbon consumption at the γ/α interphase boundary is found to; increase the final fraction of ferrite; increase the rate transformation and has a strong influence on the inter-sheet spacing through increasingly delaying the progression through $\gamma \rightarrow \alpha$ transformation modes. The developed model has been used to elucidate the mechanism for interphase precipitation of vanadium carbides in a vanadium micro-alloyed low carbon steel subjected to an isothermal phase transformation at $700\,℃$. Furthermore, the model has also been tested on simulating the interphase precipitation in a medium carbon steel transformed at $675\,℃$ using the experimental data found in [72]. The conclusions are as follows:

1) The sheet spacing of interphase precipitation in the vanadium micro-alloyed low carbon steel isothermally transformed at $700\,℃$ is simulated to be about $20\,nm$ in the distance 2 to $6.6\,\mu m$ to the centre of ferrite grains. This is similar to the value $(19 \pm 2\,nm)$ measured using TEM.
2) The inter-sheet spacing of interphase precipitation formed at $675\,℃$ in the medium carbon steel is simulated to decrease with the distance to ferrite grain centre (from $25\,nm$ to $10\,nm$ from ferrite grain centre to a distance $1\,\mu m$). This is consistent with the measured values in [72] (from $18\,nm$ to $8\,nm$ from ferrite centre to a distance $1\,\mu m$).
3) At a transformed distance above $1\,\mu m$ from ferrite grain centre, the inter-sheet spacing is simulated to be stable, i.e., a constant of $10\,nm$. This is because a constant chemical driving force is maintained at the γ/α interface in this distance due to the segregation of substitutional alloying elements Mn, Si and V (Figure 6.5-3). The above simulated stable inter-sheet spacing is observed in [72].

4) The ferrite fraction transformed at $700\ ℃$ in the vanadium micro-alloyed low carbon steel is simulated to increase from 0 to about $90\ \%$ within $25\ s$, which is in general agreement with the measured values (80%). Although the calculated final ferrite fraction is slightly higher than the measured one. The above results indicate that the velocity of γ/α interface used in the model of interphase precipitation is correct at least in terms of magnitude.

7. Phase-Field Model Investigations of the Role of Elastic Strain Energy During the Growth Interphase Precipitates

This work was published in: Rahnama, A., Clark, S., Janik, V. & Sridhar, S. A phase-field model investigating the role of elastic strain energy during the growth of closely spaced neighbouring interphase precipitates. *Comput. Mater. Sci.* **142,** 437–443 (2018).

This chapter has confirmed the following hypothesis: *The elastic strain associated with interphase precipitate growth and the minimisation of interfacial energy is hypothesised to play a critical role in the growth of individual interphase precipitates and the interactions between neighbouring interphase precipitates, explaining the complex, compound* morphologies, particularly necking behaviour of interphase carbide precipitates

7.1. Chapter Summary

A multi-phase field method is developed to investigate the effects of transformation strain on the transformation kinetics, thermodynamic stability and pairing of interphase precipitates in micro-alloyed steels. The model conserves homogeneity of stress in the diffuse interface between elastically inhomogeneous phases and provides an explanation of the mechanism resulting

in the pairing of two adjacent interphase precipitates. Several scenarios of inhomogeneous elastic conditions have been considered. The simulations for a situation where only the interfacial energy is considered to contribute to the transformation show that this energy can lead to the establishment of a neck between two neighbouring precipitates. However, if sufficient time is given, one of the precipitates will completely dissolve into its neighbouring particle. On the other hand, when both strain and interfacial energies act on the system, the bridge between the particles becomes stabilised leading to the pairing of the particles. This is a result of the tendency for particles to minimise the strain energy due to the excessive strain field generated by the neck between the two particles.

7.2. Introduction

Interphase precipitates are found in allotriomorphic α ferrite which itself is considered to grow on either side of a prior γ austenite grain boundary, with at least one interphase boundary adopting a low energy, semi-coherent, orientation relationships [102], such as the Kurdjumov-Sachs (KS) [103], or the Nishiyama-Wasserman (NW) [80,81] orientation relationships (OR). A growth ledge on a semi-coherent γ/α interphase boundary consists of a disordered, mobile riser and a comparatively coherent and immobile tread [97]. Typically, it is thought that the nucleation of interphase precipitates occurs on ledged γ/α interphase boundaries [60]. Although the high-energy interphase boundary of the riser would be favourable for the nucleation of precipitates through the formation of abutted spherical cap nuclei [214], and further eased by the segregation of substitutional solutes through the solute drag effect [215], interphase precipitates are however observed to have nucleated on the comparatively low energy γ/α tread [54]. This is thought to be because there would be an insufficient time for successful, stable nuclei to form on the mobile riser. Further, implications of nucleation on the low energy tread are as follows:

- As the interfacial energy of the ledged interphase boundary tread is low, therefore a precipitate nuclei would subsequently be expected to be nearly spherical [214].
- The segregation of substitutional alloying elements does not aid the nucleation of interphase precipitates as they are not thought to be able to readily segregate to the immobile, low energy tread of the semi-coherent γ/α interphase boundary [216].

It was stated in section 2.2.8, that it has been observed using TEM that in some circumstances disc-shaped interphase precipitates can join at the tips and form pairs of connected precipitates [52, 149]. To the best of the author's knowledge, the mechanisms for this interaction between neighbouring interphase precipitates has yet to be elucidated. Significantly more experimental

observations are required to reveal if precipitate-precipitate interactions on the densely populated planes of interphase precipitates occur or are in fact commonplace. In the absence of a body of experimental results this Chapter shall explore the plausibility of the pairing of precipitates through a modelling approach.

The elastic transformation strain associated with precipitation is known to have a potent influence upon the morphology of said precipitates. A coherent hard precipitate (nuclei) in an isotropic matrix would be expected to adopt the morphology of a sphere [217] to minimise the elastic strain energy whereas a soft, coherent precipitate would result in an oblate spheroid. In contrast, Nabarro [218], mathematically explored the role of strain upon the morphology of incoherent precipitates within an isotropic matrix. The elastic strain associated with interphase precipitates is hypothesised to play an important role in the growth of individual precipitates and the interactions between neighbouring precipitates, explaining the complex, compound morphologies, and particularly the necking behaviour of interphase carbide precipitates.

To fill this gap in the knowledge, and in order to capture the nature of the interphase precipitation a fundamentally different modelling approach was required, a phase field model (PFM), which has yet to have been applied to the interphase precipitation reaction was considered. The scope of the model developed was to predict; interphase precipitate composition, morphology and size as a function of temperature and time.

The use, basic principles and potential of PFM's for exploring a wide range of microstructural evolution and related phenomena have been reviewed in detail by Chen [219] and Militzer [220]. A particular strength of the PFM approach is that complex models exploring morphologically complex features can be readily

simulated [220] such as the precipitation of κ-carbide in low-density steels developed in our research group [221].

7.3. Phase Field Model

The model considers the growth and interaction between precipitates in-terms of transformation strain upon low energy γ/α ledged interphase boundary treads. In 3D space, for the problem with total strain ϵ^{ij} in the two directions i, j in terms of the phase strain ϵ_{α}^{ij} in each individual phase (α), yields:

$$\epsilon^{ij} = \sum_{\alpha} \phi_{\alpha} h_{\alpha}(\epsilon_{\alpha}^{ij})$$

(7.3-1)

h_{α} is dependant on the elastic properties of each individual phase and ϕ_{α} is the field variable for phase α. Equation (7.3-1) calculates the total strain as a linear summation of the strains of the individual phases α weighted by the phase densities ϕ_{α}. In other words, this equation is a direct extension of original multi-phase function for diffusive phase transformations [219]. To correlate the strain fields in the different phases equal elastic stresses in the interface are assumed.

7.3.1. The mechanical multi-phase model

The free energy can be defined as an integral of the density functional over the domain Ω. The density functional consists of the grain boundary energy density f^{gb}, the chemical free energy density f^{ch}, and the elastic energy density f^{el}:

$$F = \int_{\Omega} f^{gb} + f^{ch} + f^{el}$$

(7.3-2)

where,

$$f^{gb} = \sum_{\alpha,\beta=1}^{N} \frac{4\alpha_{\alpha\beta}}{\gamma_{\alpha\beta}} \left\{ \frac{\gamma_{\alpha\beta}^2}{\pi^2} |\nabla\phi_\alpha . \nabla\phi_\beta| + w_{\alpha\beta} \right\}$$

(7.3-3)

where $\alpha_{\alpha\beta}$ refers to the grain boundary energy between different phases. Subscript α and β refer to the relevant pair from ferrite, austenite or precipitate. $\gamma_{\alpha\beta}$ refers to the interface width and $w_{\alpha\beta}$ is the dimensionless repulsive potential function that keeps the interface upright [222]. $w_{\alpha\beta} = \phi_\alpha \phi_\beta$ when $0 < \phi_{\alpha/\beta} < 1$ and ∞ elsewhere. This specific form of Equation (7.3-3) follows the scaling invariance of the total interface energy as an integral over f^{gb} with respect to the interface width $\gamma_{\alpha\beta}$.

f^{ch} is expressed as:

$$f^{ch} = \sum_{\alpha=1}^{N} \phi_\alpha f_\alpha(\vec{c}_\alpha) + \vec{\mu}\left(\vec{c} - \sum_{\alpha=1}^{N} \phi_\alpha \vec{c}_\alpha\right)$$

(7.3-4)

$f_\alpha(\vec{c}_\alpha)$ is the bulk free energy of each individual phase, which depends on the phase concentrations $\vec{c}_\alpha$. $\vec{\mu}$ refers to the chemical potential vector. This vector is defined as a Lagrange multiplier to account for the mass balance between the neighbouring phases. This was achieved by defining the mixture concentration $\vec{c}$, which is continuous over the interface as $\vec{c} = \sum_\alpha \phi_\alpha \vec{c}_\alpha$.

Similarly, f^{el} is defined as:

$$f^{el} = \frac{1}{2}\left\{ \sum_{\alpha=1}^{N} \phi_\alpha (\epsilon_\alpha^{ij} - \epsilon_\alpha^{*ij}) C_\alpha^{ijkl} (\epsilon_\alpha^{kl} - \epsilon_\alpha^{*kl}) \right\}$$

(7.3-5)

where ϵ_α^{ij} is the total strain in individual phases, ϵ_α^{*ij} is the eigenstrain and C_α^{ijkl} is the Hook's matrix (Young's modulus). It is noted that ϵ_α^{*ij} and C_α^{ijkl} are

concentration and temperature dependant, however in the present work, it is assumed that these quantities are constant with both concentration and temperature but vary from phase to phase. To correlate the strain fields in the different phases, it is required to define an additional condition. Since $\vec{\mu} = \frac{\partial f^{ch}}{\partial \vec{c}}$, by analogy, the elastic stresses as $\sigma_{\alpha}^{ij} = \frac{1}{\phi_{\alpha}} \frac{f^{el}}{\partial \epsilon_{\alpha}^{ij}}$. To define the additional condition, mechanical equilibrium is assumed between phases in the strong form, i.e. to solve the equations of elasticity it is required to define a domain for finding an equilibrium configuration of a deformable elastic body which is in the present case is the precipitates' body. It is also assumed that a continuity of all stress components σ_{α}^{ij} exists in the interface. Thus, in the mathematical form for all α and β:

$$\sigma_{\alpha}^{ij} = \sigma_{\beta}^{ij} = \sigma^{ij}$$

(7.3-6)

Therefore:

$$(\epsilon_{\alpha}^{ij} - \epsilon_{\alpha}^{*ij}) C_{\alpha}^{ijkl} = (\epsilon_{\beta}^{ij} - \epsilon_{\beta}^{*ij}) C_{\beta}^{ijkl} = (\epsilon^{ij} - \epsilon^{*ij}) C^{ijkl}$$

(7.3-7)

and

$$\epsilon^{ij} - \epsilon^{*ij} = \sigma^{kl} [C^{ijkl}]^{-1}$$

(7.3-8)

$\epsilon^{ij} - \epsilon^{*ij}$, ϵ^{*ij} and C^{ijkl} are the effective strain, the effective eigenstrain and the effective elasticity matrix, respectively. Effective strain and effective compliance matrix $\left[C^{ijkl}\right]^{-1}$ can be defined by a linear mixture model:

$$\epsilon^{ij} - \epsilon^{*ij} = \sum_{\alpha=1}^{N} \phi_{\alpha} (\epsilon^{ij} - \epsilon^{*ij})$$

(7.3-9)

and

$$[C^{ijkl}]^{-1} = \sum_{\alpha=1}^{N} \phi_\alpha [C^{ijkl}]_\alpha^{-1}$$

(7.3-10)

Thus, the effective elasticity matrix can be expressed as:

$$C^{ijkl} = \left[\sum_{\alpha=1}^{N} \phi_\alpha [C_\alpha^{ijkl}]^{-1} \right]^{-1}$$

(7.3-11)

This expression of effective elasticity matrix is known as the Reuss limit for the elastic behaviour of a compound [223,224]. The elastic energy (Equation (7.3-5)) can be expressed in a reduced form as:

$$f^{el} = \frac{1}{2}(\epsilon^{ij} - \epsilon^{*ij}) C^{ijkl} (\epsilon^{kl} - \epsilon^{*kl})$$

(7.3-12)

The quantities ϵ^{*ij} and C^{ijkl} vary continuously from phase to phase according to the respective properties of the phases. Noting that Equation (7.3-12) is not a linear function of ϕ_α because of the additional constraint of mechanical equilibrium applied to Equation (7.3-5).

7.3.2. Kinetic equations

Kinetic equations can be defined according to the field variables $\phi_\alpha(x, y, z, t)$, $\vec{c}(x, y, z, t)$ and $\epsilon^{ij}(x, y, z, t)$:

$$\dot{\phi}_\alpha = -\sum_{\beta=1}^{N} \frac{\mu_{\alpha\beta}}{N} \left(\frac{\delta F}{\delta \phi_\alpha} - \frac{\delta F}{\delta \phi_\beta} \right)$$

(7.3-13)

$$\dot{\vec{c}} = \nabla\left(\sum_{\alpha=1}^{N} \vec{\vec{M}} \nabla \frac{\delta F}{\delta \vec{c}}\right)$$

(7.3-14)

$$\epsilon^{ij} = \nabla^j \sigma^{ij} = \nabla^j \frac{\delta F}{\delta \epsilon^{ij}}$$

(7.3-15)

$\mu_{\alpha\beta}$ and $\vec{\vec{M}}$ are the chemical mobility and the interface mobility matrix, respectively. Considering a double obstacle potential [219], the multi-phase field equation can be expressed as:

$$\dot{\phi}_\alpha = \sum_{\beta=1}^{N} \frac{\mu_{\alpha\beta}}{N} \left\{ \sum_{\gamma=1}^{N} [\sigma_{\beta\gamma} I_{\beta\gamma} - \sigma_{\alpha\gamma} I_{\alpha\gamma}] + \Delta G_{\alpha\beta} \right\}$$

(7.3-16)

where,

$$I_{\alpha\gamma} = \frac{8}{\gamma_{\alpha\gamma}} \left[\delta_\alpha \frac{\gamma_{\alpha\gamma}^2}{\pi^2} \nabla^2 \phi_\gamma + \delta_\alpha \phi_\gamma \right]$$

(7.3-17)

$I_{\alpha\gamma}$ denotes the generalised curvature terms and $\delta = 0$ if $\phi_\alpha = 0$ and $\delta = 1$ elsewhere. In Equation (7.3-16), $\Delta G_{\alpha\beta}$ is the local deviation from thermodynamic equilibrium and consists of the chemical and the elastic components because only these two components are assumed to be at equilibrium at the interface:

$$\Delta G_{\alpha\beta} = \Delta G^{ch}_{\alpha\beta} + \Delta G^{el}_{\alpha\beta}$$

(7.3-18)

For the chemical non-equilibrium contribution $\Delta G^{ch}_{\alpha\beta}$:

$$\Delta G^{ch}_{\alpha\beta} = -\left(\frac{\partial}{\partial\phi_\alpha} - \frac{\partial}{\partial\phi_\beta}\right) f^{ch} = -f_\alpha(\vec{c}_\alpha) + f_\beta(\vec{c}_\beta) + \vec{\mu}(\vec{c}_\alpha - \vec{c}_\beta)$$

(7.3-19)

Similarly, $\Delta G^{el}_{\alpha\beta}$ can be expressed as follows:

$$\Delta G^{el}_{\alpha\beta} = -\left(\frac{\partial}{\partial\phi_\alpha} - \frac{\partial}{\partial\phi_\beta}\right) f^{el} = (\epsilon^{ij} - \epsilon^{*ij}) C^{ijkl} \times \left\{ (\epsilon^{*ij}_\alpha - \epsilon^{*ij}_\beta) - \frac{1}{2}\left([C^{ijkl}_\alpha]^{-1} - [C^{ijkl}_\beta]^{-1} \right) C^{mnop} (\epsilon^{op} - \epsilon^{*op}) \right\}$$

(7.3-20)

$\epsilon^{*ij}_\alpha - \epsilon^{*ij}_\beta$ in Equation (7.3-20) takes into account the difference in Eigenstrain between the phases involved in transformation. $\left([C^{ijkl}_\alpha]^{-1} - [C^{ijkl}_\beta]^{-1} \right)$ determines the difference in elasticity. $(\epsilon^{ij} - \epsilon^{*ij}) C^{ijkl}$ is the linear-dependency on the local elastic stress state, i.e. based on the sign of the local stress this term determines if a phase transformation with expansion or contraction will be favoured or hindered. Equation (7.3-14) can be rewritten in terms of diffusion matrices as:

$$\dot{\vec{c}} = \nabla\left(\sum_{\alpha=1}^{N} \phi_\alpha \vec{\vec{M}}_\alpha \nabla \frac{\partial f_\alpha}{\partial \vec{c}_\alpha} \right) = \nabla\left(\sum_{\alpha=1}^{N} \phi_\alpha \vec{\vec{D}}_\alpha \nabla \vec{c}_\alpha \right)$$

(7.3-21)

where $\vec{\vec{M}}$ is chemical mobility matrices defined as $\vec{\vec{M}} = \sum_{\alpha=1}^{N} \phi \vec{\vec{M}}_\alpha$. $\vec{\vec{D}}$ is diffusion matrices defined as $\vec{\vec{D}} = \vec{\vec{M}}_\alpha \left(\frac{\partial^2 f_\alpha}{\partial \vec{c}_\alpha \partial \vec{c}_\beta} \right)$. From the parallel tangent rule $\frac{\partial f_\alpha}{\partial \vec{c}_\alpha} = \frac{\partial f_\beta}{\partial \vec{c}_\beta} = \vec{\mu}$, the quasi-equilibrium concentrations $\overrightarrow{c^0}_{\alpha\beta}$ (function in space and time) can be

determined for a pair of phases α and β and for a given mixture concentration $\vec{c}$. Thus, the phase concentrations can be formulated according to these concentrations [225,226]:

$$\Delta\vec{c}_{\alpha} = \vec{c}_{\alpha} - \vec{c}^{0}_{\alpha\beta}$$

(7.3-22)

Substituting the relationship obtained from tangent rule into Equation (7.3-22):

$$\Delta\vec{c}_{\alpha} = \Delta\vec{c}_{\beta}\frac{\partial\vec{c}_{\alpha}}{\partial\vec{c}_{\beta}} = \Delta\vec{c}_{\beta}\frac{\partial f_c^{\beta}}{\partial f_c^{\alpha}}\frac{\partial\vec{c}_{\alpha}}{\partial\vec{c}_{\beta}} = \Delta\vec{c}_{\beta}\frac{f_{cc}^{\beta}}{f_{cc}^{\alpha}} = \Delta\vec{c}_{\beta}\vec{\vec{k}}_{\alpha\beta}$$

(7.3-23)

Here the abbreviation $f_c^{\alpha} = \frac{\partial f_{\alpha}}{\partial\vec{c}_{\alpha}}$ is introduced and a generalized partitioning coefficient is $\vec{\vec{k}}_{\alpha\beta}$ used. Using $\vec{c} = \sum_{\alpha}\phi_{\alpha}\vec{c}_{\alpha}$, Equation (7.3-22) and Equation (7.3-23) the phase concentrations can be eliminated and Equation (7.3-14) can be rewritten as:

$$\dot{\vec{c}} = \nabla\left(\sum_{\alpha=1}^{N}\phi_{\alpha}\vec{\vec{D}}_{\alpha}\nabla\frac{\left(\vec{c} - \sum_{\beta=1}^{N}\phi_{\beta}\left(\vec{c}^{0}_{\beta\alpha}\vec{\vec{k}}_{\beta\alpha}\vec{c}^{0}_{\alpha\beta}\right)\right)}{\sum_{\beta=1}^{N}\phi_{\beta}\vec{\vec{k}}_{\beta\alpha}}\right)$$

(7.3-24)

The derivation for $\dot{\vec{c}}$ in Equation (7.3-24) is similar to the one expressed in [227] with a different expression for the diffusion matrix. This is done to eliminate the unknown $\vec{c}_{\alpha}$ using the local linearisation, thereby enabling the efficient numerical solution.

7.3.3. Solution procedure, case study and experimental validation

The composition of the micro-alloyed steel considered in this work is, Fe-1.962C-0.748Mn-0.312V (all in at.%) [72,166]. The generalized chemical potential $\vec{\mu}$ in the chemical non-equilibrium contribution (Equation (7.3-19)) is computed iteratively for a given average concentration $\vec{c}$ and a given set of phase field ϕ_α by the minimization of the total free energy described by the free energy functions $f_\alpha(\vec{c}_\alpha)$.

The displacements are calculated using the principle of relaxation to mechanical equilibrium (Equation (7.3-15)), i.e. this equation is numerically solved for the displacement vector u^i using $\epsilon^{ij} = \frac{1}{2}\left(\frac{\partial}{\partial u^i}u^i + \frac{\partial}{\partial u^j}u^j\right)$ in the weak formulation by linear finite elements. C_{11} and C_{12} are considered to be $280\,GPa$ and $120\,GPa$, respectively. The dimensionless elastic constants for the individual phases α (matrix) were defined as $C_{11}^{\alpha} = \frac{1-\nu}{1-2\nu} \times C_{44}^{\alpha}$ and $C_{11}^{\alpha} = \frac{\nu}{1-2\nu} \times C_{44}^{\alpha}$. The eigenstrain $\epsilon^*$is 1% and σ_0 $1980\,MPa$. The parameter $h = \frac{C_{44}^{\beta}}{C_{44}^{\alpha}}$ is defined in order to compare the strength of the precipitates with that of the matrix. In addition, a scaled strain parameter is defined as $\bar{\eta} = \eta\sqrt{\frac{E}{\rho_0 k_B T(T-\nu)}}\left(\frac{2}{C^{\beta}-C^{\alpha}}\right)^2$ where ϵ is the strain parameter that strongly depends on the composition of the material, $\eta = 0.126$ [228] is adopted in this study. η determines the dilatational strain due to the compositional change according to Vegard's law, $\eta = \frac{\boldsymbol{\epsilon}}{c-c_0}$ [229] where c_0 is the stress-free composition. ρ_0 is density, k_B Boltzmann constant, T temperature, and ν Poisson ratio. All displacements are placed at the corners of a square grid and the physical properties are assumed to be constant over the control volume. The stiffness tensor of any intermediate phase (IP) formed during the particle interactions was assumed to take an intermediate value. The boundary conditions used for the current calculations are free volume expansions/contractions while keeping the rectangular shape of the calculation grid.

The chemical Gibbs energies, mobilities and diffusion coefficients are taken from Ref.[230]. The interfacial energy is taken as isotropic, $\sigma = 5 \times 10^{-5}\, Jcm^{-2}$ for the interface between ferrite and austenite [231]. The interface between precipitates and austenite γ and ferrite α is assumed to be semi-coherent with similar interfacial energies of $\sigma = 2 \times 10^{-5}\, Jcm^{-2}$ and $\sigma = 2.5 \times 10^{-5}\, Jcm^{-2}$, respectively. The interfacial energies are selected within the range of interfacial energies proposed by Howe [203] for semi-coherent interphase boundaries. Due to the similar values of the precipitate/matrix interfacial energies, the modelled results of the interphase boundary precipitates, considered in this work would be similar to the case where precipitates were placed fully within either matrix phase. At the nucleation stage, two particles are placed at the γ/α interphase boundary assuming a radius of $1\ nm$. The following terms are defined:

- *Necking* - as a metastable stage where ϕ in the bridge between the neighbouring precipitates has an intermediate value.
- *Pairing* - as a stage of the transformation encountered where ϕ in the bridge between the neighbouring precipitates has a value equal to that of precipitates.

The domain size was $300 \times 300 \times 300$ cells with a discretization of $\Delta x = 0.25\, nm$. The interface width is considered to be $\gamma = 6$ cells. The time discretization is set as 10^{-2}. Instantaneous relation to mechanical equilibrium is considered for every time step.

Multi-Component PFM microstructural simulations produce a spatially and time-resolved distribution of alloying elements. This lends the results of such simulations to be validated against elemental distribution mapping techniques such as STEM-EDS which offer a sufficient resolution on nano-scale. For the purposes of qualitative validation of the model, Figure 7.3-1 is presented showing STEM-EDS map (V-K_α) of VC interphase precipitates, representative of a broader microstructure of an industrial HSLA steel obtained after typical thermo-

mechanical processing finished with controlled coiling at $630\,℃$. The alloy in question has a similar V composition to that of the modelled alloy providing a suitable means of qualitatively validating the PFM model in this work. A FEG-TEM FEI microscope model Talos F200X, operating at 200 kV with four integrated Super-X SDD EDS detectors at a detection angle of $0.9\,rad$ was used for elemental mapping of vanadium. Samples were prepared from industrial coil using a focused ion beam (FIB) lift-out method, foils were thinned down to approximately $120\,nm$ in thickness, using a final gentle low voltage cleaning step. In Figure 7.3-1 specific cases highlighting specific conditions of interphase precipitates have been identified: 1) a neck has faintly formed joining two spaced precipitates (black box), 2) a neck has formed between two precipitates (magenta box), and 3) a case where several precipitates have paired together (orange box). It should be noted that the EDS maps presented in Figure 7.3-1 suffer from the same issue as the micrograph presented by Chamisa [149] as it was impossible to tilt the FIB lamella such as to reveal individual precipitates on an IP sheet plane therefore, a critical appraisal would suggest that even in this case the 'paired' precipitates may actually be spaced though the thickness of the TEM sample.

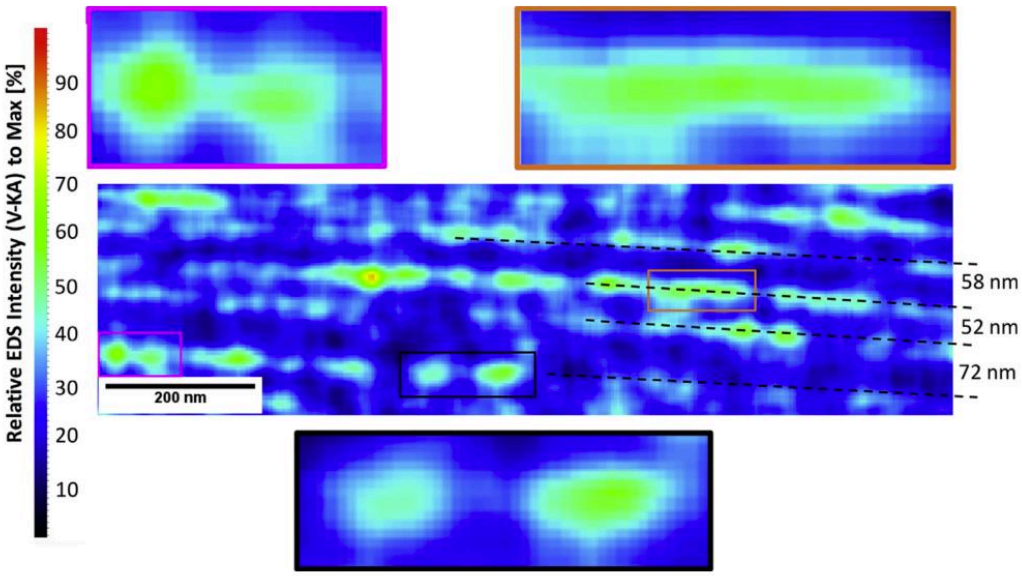

Figure 7.3-1 STEM-EDS mapping (V-K_α) of an industrial HSLA steel showing rows of interphase precipitates; expanded sections illustrate selected cases exhibiting specific conditions of interphase precipitates: a neck begins to form (black box), a neck between two precipitates has become established (magenta box), and a case where several precipitates have paired together (orange box).

7.4. Results and Discussion

Figure 7.4-1 shows the interaction between two neighbouring precipitates with almost equal radii $(\bar{r})$ which is a dimensionless quantity. Two growth mechanisms for the precipitates presented in Figure 7.4-1 are considered: interfacial energy assumed to be the only contributing energy (Figure 7.4-1 a1-a3), and both strain and interfacial energy considered to contribute to the growth of the precipitates. The spacing between the adjacent precipitates is assumed to be $\bar{d} = \frac{\bar{r}}{3}$ ($\bar{d}$ is a dimensionless quantity). Throughout the course of the interaction, the precipitates develop necking without any contribution from the strain energy because $\bar{\eta} = 0$. The diffusion distance between the particles was small so that surface tensions rapidly activated precipitation that bridged the two particles. The pronounced curvature gradients then occurred because of

the establishment of a bridge between the two particles. The curvature gradients then, in turn, lead to the formation of a single precipitate with uniform curvature at the interface. In the second scenario Figure 7.4-1b1-b3, forced necking occurred and the strain energy and the resultant stresses drive atoms to the region with minimal distance between the adjacent particles. The two precipitates thus coalesced and paired with each other.

As is evident from these simulations, both interfacial and elastic energy result in the establishment of a bridge between the adjacent particles, however, it is the strain energy that leads to a stable pairing of the particles, provided that enough time is given to the precipitates to grow. With sufficient elapsed time the interfacial energy causes the dissolution of the particle into its adjacent neighbour, while in the second scenario, strain energy became the dominating contributory energy that leads to the decrease of the excessive tension between the two particles.

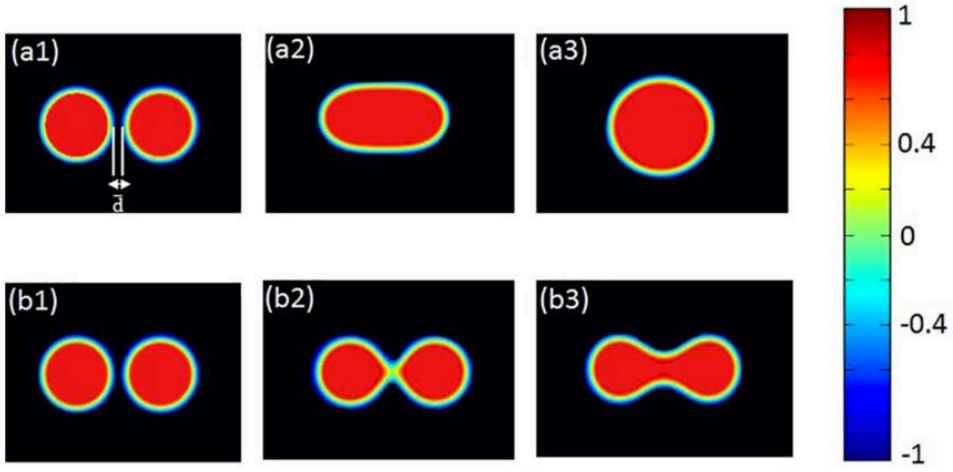

Figure 7.4-1 Interaction of two neighbouring precipitates; $\bar{d}$ is the initial distance between the precipitates ($\bar{d} = \frac{\bar{r}}{3}$). Note that $\bar{r}$ (the initial radii) of precipitates is dimensionless. (a) Necking mechanism of neighbouring precipitates without strain effects. (b) Necking of precipitates with the effects of strain energy. The

colours do not represent strain distribution in a1-a3 as the contribution of strain energy is ignored. The legend thus only refers to Figure 7.4-1b1-b3.

The effects of strain energy on the necking time between two adjacent particles were studied further. Figure 7.4-2 shows the necking time for closely spaced particles versus the initial distance between them for various values of $\bar{\eta}$ for particle radii of $\bar{r} = 12$. The necking time decreased with increasing $\bar{\eta}$. In other words, increasing the strain field due to the compositional change between the two particles led to an accelerated pairing of the precipitates. When $\eta = 0$ the threshold particle spacing was identified between $\bar{d} = 18$ and $\bar{d} = 19$. Figure 7.4-3 shows a similar graph to that of Figure 7.4-2 but for particles with a radius of $\bar{r} = 21$. as is evident from Figure 7.4-3, the effects of strain parameter was more pronounced in the case of larger particles, i.e. for $\bar{\eta} = 0.03$ with $\bar{d} = 9$ for particles with a radii of 12 the necking time occurred after $\bar{t} = 8.9 \times 10^4$, while for the similar conditions but for particles with a radii of 21 the necking time only took place after $\bar{t} = 3.2 \times 10^4$. This is because of an increase in the curvature in the case of larger particles and thus a larger tension between the two precipitates which in turn increased the strain energy and resulted in an accelerated necking.

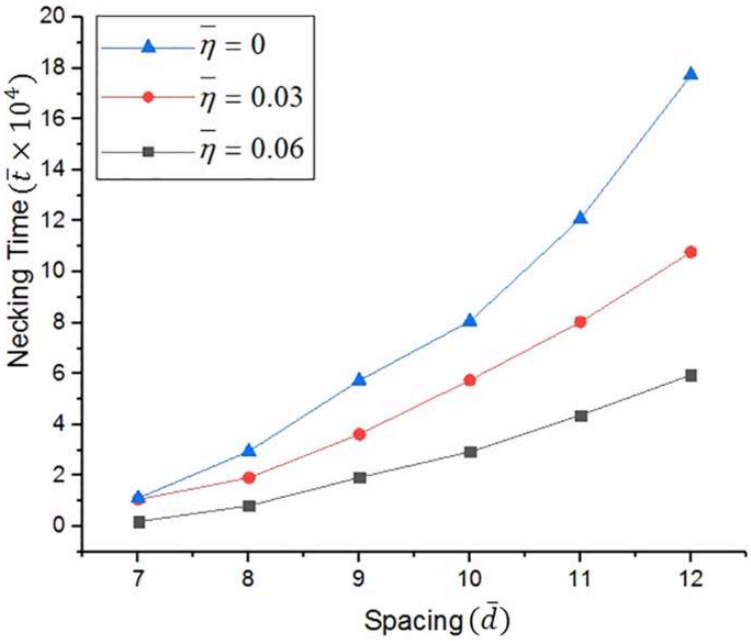

Figure 7.4-2 The necking time as a function of initial distance between two neighbouring precipitates ($\bar{r} = 12$) for different values of the strain parameter. $\bar{t}$ is dimensionless.

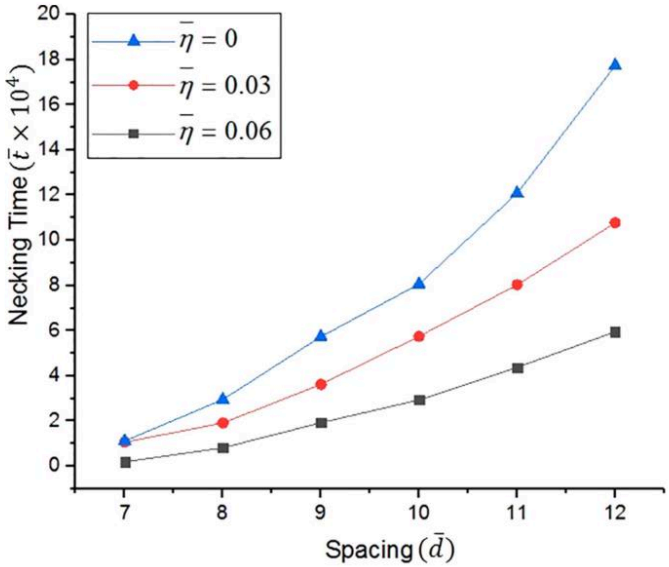

Figure 7.4-3 The necking time as a function of initial distance between two neighbouring precipitates ($\bar{r} = 21$) for different values of the strain parameter.

We performed three controlled simulations for homogeneous elasticity $h = 1$, inhomogeneous elasticity with soft particles $h = 0.5$, and hard inhomogeneous elasticity with hard particles $h = 1.5$ to examine the effect of the relative hardness/softness of particles on the pairing time. In all three cases, $\bar{\eta}$ assumed to be 0.03 and particles radii considered to be 12. The results are shown in Figure 7.4-4. Figure 7.4-4 exhibits that the necking between two adjacent particles was much more prolonged when the particles were hard compared to when they were soft, i.e. for the case where $\bar{d} = 12$, necking time was calculated to be $\bar{t} = 17.8 \times 10^4$ when $h = 1.5$ while necking only took $\bar{t} = 5.9 \times 10^4$ to occur when $h = 0.5$. This is because the hard particles show higher resistance to deformation resulted from the tension between the particles.

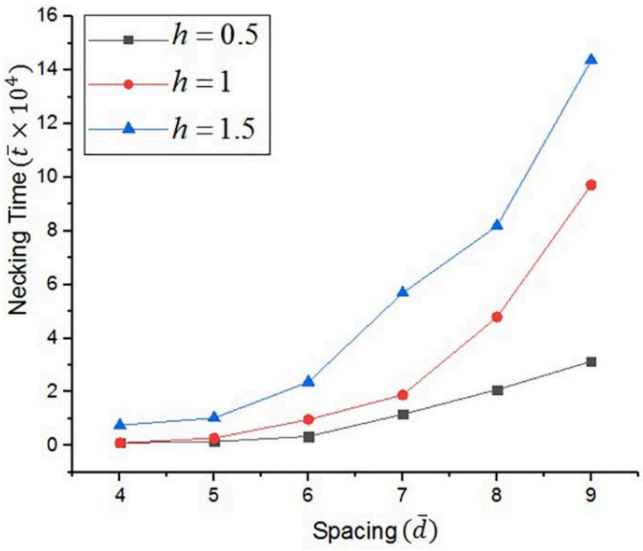

Figure 7.4-4 The necking time versus the initial spacing between two neighbouring precipitates for various values of h, with $\bar{\eta} = 0.03$ *and* $\bar{r} = 12$.

Figure 7.4-5 a-c shows the simulation of V-composition contours during the formation of a pair in a two-particle system. The simulation results showed the formation of an intermediate phase β. The β phase grew from the matrix and the precipitates and formed a thin β-phase containing crust between the precipitates. The growth of this phase affected the overall precipitating

behaviour and decreased the effective spacing. Therefore, the growth of β-phase enhanced the necking process and thus pairing. The thickness of this phase depends on the chemical energy and the compositional strain parameter $\bar{\eta}$. After precipitates growth for a certain amount of time ($\bar{t} = 8 \times 10^4$) the β -phase disappeared causing the formation of the paired precipitates, similar to that imaged in Figure 7.3-1 (orange box). Our simulation results in Figure 7.4-5b-c of necking precipitates show a qualitative agreement with the STEM-EDS analysis in Figure 7.3-1 (black and magenta boxes). In both cases, the relative EDS intensity of V in the necking region is shown to be reduced in comparison to the two initial nuclei but significantly enriched in comparison to the bulk V concentration. The different stages of necking are imagined in the same region of the sample since the distance between the initial neighbouring nuclei is considerably non-uniform.

Figure 7.4-5 d-f shows the development of stresses within one of the neighbouring particles at a similar time step as that shown in Figure 7.4-5 c for different effective spacing $\bar{d}$. When the two particles were closely spaced ($\bar{d} = 5$) the stress distribution was at its maximum at the tip of the particle. For larger spacing $\bar{d} = 7$, the value of the stress was at a maximum at the tip, on the top and at the side of the particle. However, the stresses at the tip of a particle not only had a maximum magnitude but, also the area bearing the maximum stresses was larger at the tip compared to that on either the top or the side of the particle. Thus, the most probable location for the pairing of the particle was again at its tip. Moreover, the development of such stresses causes the final shape of the particle to be an oblate sphere (or disc-like shape). For largely spaced particles, the location of the maximum stresses was only at the tip and the area that tolerated this stress was relatively small compared to the two other cases.

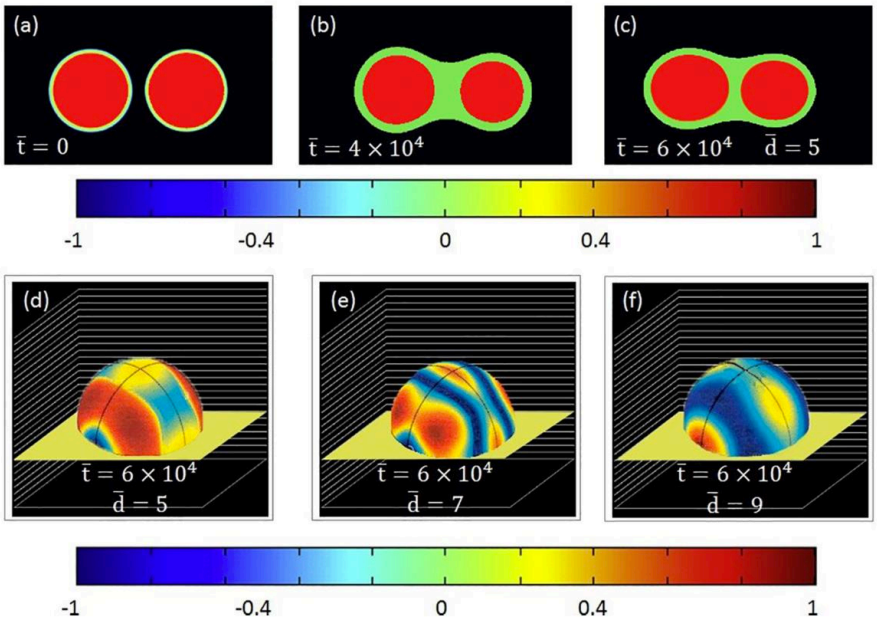

Figure 7.4-5 (a-c) Simulation results showing the distribution of V throughout the transition (The legend shows V composition contour.). The location of maximum stress of one of the neighbouring particle at the time step equal to that of shown in Figure 7.4-5 c ($\bar{t} = 6 \times 10^4$) when spacing (d) $\bar{d} = 5$, (e) $\bar{d} = 7$, and (f) $\bar{d} = 9$ (The legend shows stress contours). The yellow plane marks the location of the planar interface between α and γ.

7.5. Conclusions

A phase-field simulation was performed to study the mechanisms leading to the pairing of neighbouring precipitates in micro-alloyed steels. The results showed that when interfacial energy was considered to be the only contributing energy, the pairing of precipitates does not occur, and the dissolution of one of the particles into its neighbour was the dominating mechanism. However, when both interfacial and strain energy were included in the computation, the pairing took place because the adjacent particles tend to minimise the strain energy. The effects of strain parameter (η) and spacing between the particles on the necking time were also studied. It was understood that the necking time decreased with increasing the strain parameter. This effect was pronounced for particles with a

larger radius. Three controlled simulations to examine the effect of relative hardness of precipitates on the necking time were performed. The results showed that necking is delayed significantly when the neighbouring particles are hard. The V-composition contour throughout the precipitation was simulated and the formation of an intermediate β phase that facilitates necking and pairing between the two adjacent particles was observed. The location of maximum stress for different spacing was investigated and it was confirmed that the most probable location for the pairing of the particles is at their tips. This work is considered as an incremental step towards the coupled prediction of microstructural evolution and mechanical properties.

8. Overarching Discussion

8.1. General Overarching Discussion

In Chapter 4 small angle neutron scattering (SANS) was employed to characterise the precipitates and their size distributions in an Fe-0.047C-0.2V-1.6Mn (in wt.%) alloy isothermally transformed at $700\,°C$ up to $600\,min$. The analysis of the precipitate volume fraction showed that it had increased from 0.009 after $3\,min$ of isothermal transformation to 0.022 after $600\,min$. An equilibrium volume fraction of 0.030 was calculated using Thermo-Calc and the TCFE7 database. Referring to the dilatometry performed in Chapter 6 for similar thermal cycles to those of the salt-bath cycles in Chapter 4 it shows that the γ→α transformation reaches 90% of the final measured fraction of $\approx 80\%$ after just $12.5\,s$. After $180\,s$ $(3\,min)$ the dilatometry reveals that the $\gamma \rightarrow \alpha$ transformation reaches 99% of the final measured fraction of $\approx 80\%$. It is suggested that the SANS measurements after $3\,min$ of isothermal transformation are associated with the nature of the VC precipitates formed shortly after the $\gamma \rightarrow \alpha$ effectively stagnates, presumably due to soft impingement. It is thus suggested that the SANS characterisation of the precipitates is a reasonably reliable characterisation of the precipitates as formed at the γ/α interphase boundary in the case of interphase precipitates.

The implicit assumptions of the aforementioned interpretation are that the growth of the precipitates once engulfed in the α matrix phase is sluggish in comparison to the initial rapid growth of precipitates at the γ/α interphase boundary due to the significantly enhanced diffusion coefficient. It is assumed that the heterogeneous nucleation of VC precipitates within supersaturated ferrite is also similarly sluggish in comparison to the formation of interphase precipitates and the SANS signal is dominated by the signal associated with interphase precipitation. It can, therefore, be suggested that the initial

interphase precipitation in this alloy and with this thermal cycle results in the precipitation of in the order of 30% of the equilibrium volume fraction of the VC precipitate phase (i.e. 0.009 volume fraction after 3 minutes compared to 0.03 equilibrium predicted).

In chapter 5 *in-situ* Electron Dispersive Backscatter Diffraction (EBSD) and High-Temperature Laser Confocal Microscopy (HT-CSLM) were applied to elucidate the influence of $\gamma \rightarrow \alpha$ transformation upon the extent of interphase precipitation in an Fe-0.047C-0.2V-1.6Mn (in wt.%) alloy. EBSD analyses of the γ/α OR of samples subjected to continuous cooling of 2 and 10 $℃s^{-1}$ suggest that the proportion of ferrite likely to hold interphase precipitation varies little with cooling rate. In the present study, EBSD indicates that circa 32% and 34% of the ferrite microstructure has the preferred orientation to exhibit interphase precipitation with continuous cooling at 2 and 10 $℃s^{-1}$, respectively, to room temperature.

Although the thermal cycles are fundamentally different with the transformations in Chapter 4 being associated with isothermal transformations at $700\ °C$ rather than continuous cooling from $900\ °C$ in the case of Chapter 5, there appears to be a correlation between EBSD results and the SANS results. The correlation between EBSD results and the SANS results is in the form of an agreement in ~30% non-OR grains (likely to be associated with interphase precipitation) and as stated above, 30% of thermodynamically predicted volume fraction of precipitates was measured using SANS at a stage in the transformation where the SANS signal was likely to be dominated by interphase precipitation. The direct corollary of this proposition is that locally in the grains where the interphase precipitation mechanism results in the precipitation of the near equilibrium fraction of the carbide phase.

Referring to the analytical modelling in Chapter 6 the effect of carbon consumption at the γ/α interphase boundary by the precipitation of interphase carbide precipitates was explored. In this alloy where the atomic ratio of the bulk alloying of C and V is ≈ 1, the consumption of carbon at γ/α interphase boundaries conducive to the formation of interphase precipitates would suggest that the majority of carbon being consumed at these specific γ/α interphase boundaries. However, the exact quantity of carbon consumed at the interphase boundary would depend upon the stoichiometry of vanadium and carbon in the formed precipitates. In Chapter 4 the stoichiometry of the precipitates was approximated from the nuclear contrast factor, $R(q)$, as $VC_{0.90}$ after $300\ mins$ and near stoichiometric VC after $600\ mins$. Although, only based upon two measurements, extrapolating backwards these results would suggest at the point of nucleation these precipitates would be significantly sub-stoichiometric regarding C although the exact degree of sub-stoichiometry is yet to elucidated. An educated guess would be to take the lower bound of the measurements by Ishiguro and Sato [180], who used electron energy loss spectroscopy (EELS) to identify non-stoichiometric MC_x in ultra-low carbon micro-alloyed steels with x in the range 0.82 to 0.91.

In Chapter 6 it was revealed that increasing carbon consumption at the γ/α interphase boundary; increases the final fraction of ferrite; increases the rate of transformation and has a strong influence on the inter-sheet spacing through increasingly delaying the progression through $\gamma \rightarrow \alpha$ transformation modes. However, it should be noted that the predictions from this model were associated with the assumption that the global microstructure behaved uniformly and therefore the transformation could be approximated by a simple 1D model of 2 infinitely long flat γ/α interphase boundaries growing towards each other. The combined results of Chapters 4 and 5 as discussed above would contradict the validity of this assumption, instead, suggesting that a proportion of γ/α interphase boundaries could be migrating significantly quicker than the

remaining γ/α interphase boundaries resulting in a microstructure with approximately 30% of grains containing interphase precipitation. Variable carbon consumption could be partially accounted for in the model proposed in Chapter 6 by the appropriately weighted averaging of computing the model with different values of carbon consumption at the interphase boundary. However, it is argued that a different modelling approach, capable of simulating the broader evolution of the global microstructure, should be developed. The multi-phase-field model proposed in Chapter 7 which was developed to investigate the effects of transformation strain on the transformation kinetics, thermodynamic stability and pairing of interphase precipitates in micro-alloyed steels as they grow on the stationary tread of the γ/α interphase boundary is intended as a first building block towards the development of such a model.

8.2. 'layman's' recommendations for the optimisation of interphase precipitation in a given alloy

Drawing together the findings discussed in this thesis a series of 'layman's' recommendations can be proposed for the optimisation of interphase precipitation in a given alloy. In the following section, a series of steps will be outlined for the 'layman' to quickly optimise the exploitation of interphase precipitation in a given alloy. The recommendations are intended to be simple such that they can be readily applied to into a broader alloy development program.

Firstly, the thermo-mechanical controlled processes (TMCP) in strip steel production should be introduced. Figure 8.2-1 shows a schematic representation of typical thermo-mechanical controlled processes (TMCP) in strip steel production (after Lagneborg et al. [232]). In traditional production from continuously cast steel, the slabs are reheated before rolling, however, in the

latest thin slab processes the solidified strand is directly hot charged into the equilibrating tunnel furnace this offers the potential of a considerable saving in energy [233]. The steel then passes through a series of tandem rolls. As well as to meet the desired dimensional requirements, the rolling process aims to maximise the area of austenite grain boundary per unit volume, i.e. refine the austenite grain size. This is achieved in two steps, rolling above the recrystallisation temperature principally refines the austenite grain size, rolling below the recrystallisation temperature pancakes the austenite grains further increasing the austenite grain boundary area and storing considerable residual strain. Upon accelerated controlled cooling to a predetermined coiling temperature the steel transforms from austenite to ferrite — generally, the finer the parent austenite, the finer the child ferrite. In order to achieve the best mechanical properties, each of these processing steps must be optimised.

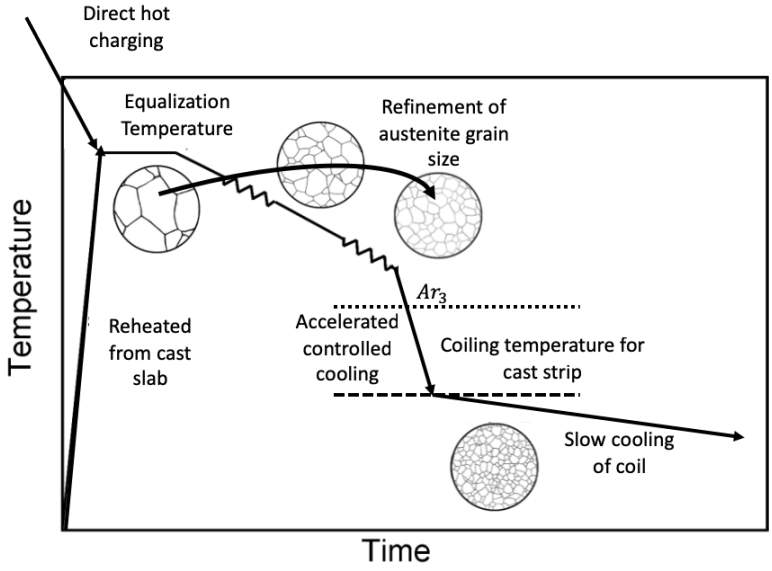

Figure 8.2-1 Schematic representation of the thermo-mechanical controlled processes (TMCP) in strip steel production (after Lagneborg et al. [232]*).*

The 'layman' should generate and refer to the well-known time-temperature-transformation, TTT, and continuous cooling transformation, CCT representations. These diagrams provide a good starting point for the

examination of hardenability and transformation kinetics in alloys [1]. Deformation CCT curves would be most appropriate as the role of residual strain and austenite grain pancaking upon the transformation kinetics would be accounted for. However, an initial approximation can be based upon standard CCT curves, as described below. These diagrams can be generated experimentally, although with some considerable effort. Alternatively, there are commercially and freely available software packages available that allow them to be predicted. In this work, the freely available MAP_STEEL_MUCG83 [140] program is utilised. MAP_STEEL_MUCG83 [140] is a powerful suite of software for modelling of the thermodynamics and kinetics of solid-state transformations in steels. The package principally calculates the incubation time (i.e. the start time) as a function of temperature and alloy composition for both the diffusional and displacive shear transformation products that form upon the decomposition of austenite [234]. It is able to calculate the characteristic Widmanstätten, W_S, Bainite, B_S, and Martensite, M_S, start temperatures. The CCT representation can then be generated from the TTT representation using Scheil's additive reaction rule, in this work the freely available MAP_TTTtoCCTlinear package [235] has been utilised.

Figure 8.2-2 shows the predicated TTT C-curves for diffusional and displacive shear transformations for the alloy Fe-0.047C-0.2V-0.18Si-1.6Mn (in wt.%) using Program MAP_STEEL_MUCG83 [140]. The Widmanstätten start temperature range, W_S, bainite start temperature, B_s, and the martensite start temperature M_s are also plotted. Figure 8.2-3 shows the corresponding CCT curve calculated by applying Scheil's additive reaction rule to the TTT curve for diffusional and displacive shear transformations for the alloy Fe-0.047C-0.2V-0.18Si-1.6Mn (in wt.%) using Program MAP_STEEL_MUCG83 [140]. Figure 8.2-4 shows the minimum inter-sheet spacing for the alloy Fe-0.047C-0.2V-0.18Si-1.6Mn (in wt.%) calculated using the maximal driving force outputted by the Program

MAP_STEEL_MUCG83 and Equation 8.2-1 adopting an interfacial energy of $0.55\ \mathrm{J/m^2}$ as was fitted in Chapter 6.

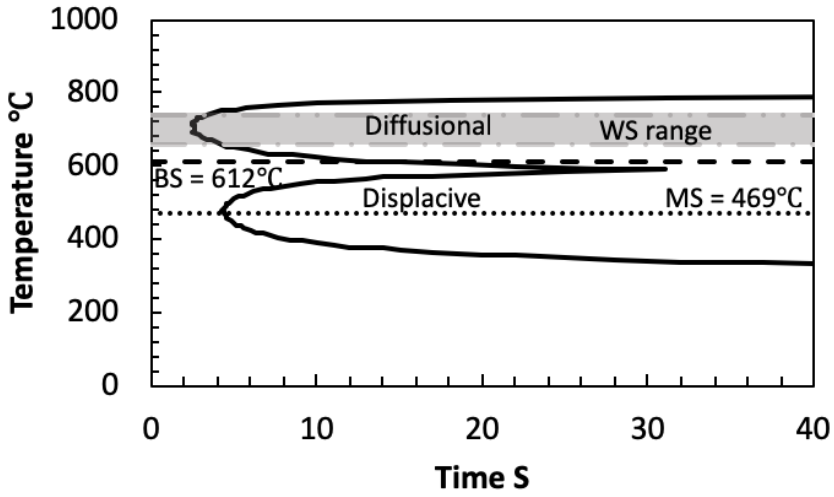

Figure 8.2-2 Predicted TTT C-curves for diffusional and displacive shear transformations for the alloy Fe-0.047C-0.2V-0.18Si-1.6Mn (in wt.%) using Program MAP_STEEL_MUCG83 [140]. The Widmanstätten start temperature range, W_S, bainite start temperature, B_S, and the martensite start temperature M_S are also plotted.

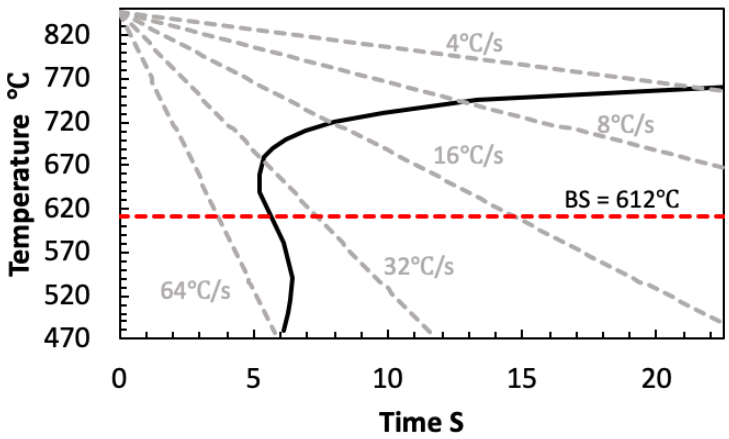

Figure 8.2-3 Predicted CCT curve calculated by applying Scheil's additive reaction rule, to the TTT curve for diffusional and displacive shear transformations for the

alloy Fe-0.047C-0.2V-0.18Si-1.6Mn (in wt.%) using Program MAP_STEEL_MUCG83 [140]. The bainite start temperature, B_s, is also plotted.

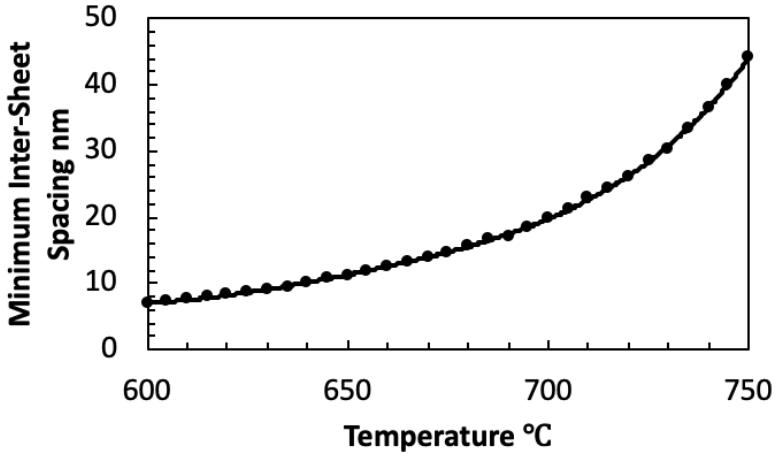

Figure 8.2-4 Minimum inter-sheet spacing for the alloy Fe-0.047C-0.2V-0.18Si-1.6Mn (in wt.%) calculated using the maximal driving force outputted by the Program MAP_STEEL_MUCG83 [140] and an interfacial energy of $0.55\ J/m^2$.

Interphase precipitation is associated with the diffusional formation of allotriomorphic ferrite (Reference Section 2.2) and is well known to refine with decreasing transformation temperature (Reference Section 2.2.2) and as shown for this alloy in Figure 8.2-4. Therefore, the activation of the displace shear transformation mechanism represents the practical limit at which interphase precipitation can be achieved. In this alloy, this would correspond to the bainite start temperature, $B_s = 612$℃. However, we also know from prior studies (reviewed in Section 2.2.2) and the agreement between the findings of Chapter 4 and 5 discussed in Section 8.1 that interphase precipitation is not associated with Widmanstätten ferrite. In this alloy, the Widmanstätten ferrite start temperature is predicted to be in the range of $W_s = 660 \rightarrow 740$℃. This Widmanstätten ferrite start temperature range would suggest that transforming the steel at a temperature approaching the bainite start temperature the resultant

microstructure may be sub-optimal and a significant proportion of Widmanstätten ferrite may form. However, the importance of a fine austenite grain size in minimising the formation of the Widmanstätten structure is known. Bodnar and Hansen [190] showed that with a sufficiently fine prior austenite grain size (e.g., $\sim < 30\,\mu m$), Widmanstätten ferrite can be largely avoided. Therefore, it can at this point be concluded that in order to access the lowest possible transformation temperatures the austenite grain size, conditioned by prior rolling and recrystallisation must be optimised in order to yield an austenite grain size which is as fine as practicably possible.

Another factor must also be considered, in order to access the lowest possible $\gamma \rightarrow \alpha$ transformation temperatures the steel must be cooled sufficiently quickly such that α does not form at high temperature during this initial cooling. For determining this critical cooling rate, the CCT diagram presented in Figure 8.2-3 is critical. In Chapter 5 it was reported that at higher cooling rates, i.e., in excess of $20\,℃s^{-1}$, interphase precipitation is increasingly suppressed due to the increasingly diffusional-displacive nature of the Widmanstätten γ/α transformation that is activated. Figure 8.2-3 reveals that an accelerated cooling rate of in excess of $42\,℃s^{-1}$ would be necessary in order to access a $\gamma \rightarrow \alpha$ transformation temperature above but approaching the bainite start temperature of $B_s = 612℃$. Referring back to Figure 8.2-1 it is apparent that the coil gradually cools, typically over many hours, hence the $\gamma \rightarrow \alpha$ transformation, occurs during a continuous cooling process rather than as an isothermal transformation. It is, therefore, necessary that this continuous cooling is taken into account when determining the optimal coiling temperature as the $\gamma \rightarrow \alpha$ transformation should be completed before the bainitic transformation mode is activated.

Considering a case study of an Fe-0.047C-0.2V-0.18Si-1.6Mn (in wt.%) alloy and the analysis of Figure 8.2-2 and Figure 8.2-3 using the knowledge derived in this thesis a series of recommendations can be made which are presented in a

hierarchy of influence (these recommendations are also shown schematically in Figure 8.2-5):

- The austenite should be TMCP conditioned such that its grain size is as fine as practicably possible. A fine austenitic grain size is required in order to minimise the formation of Widmanstätten ferrite.
- This steel should be processed utilising accelerated controlled cooling at a rate in excess of $42\ ℃/s$.
- This steel should be coiled at as low coiling temperature as possible without activating the bainitic transformation. It is recommended that the optimal range for coiling temperature is in the range of $620 \rightarrow 640℃$.

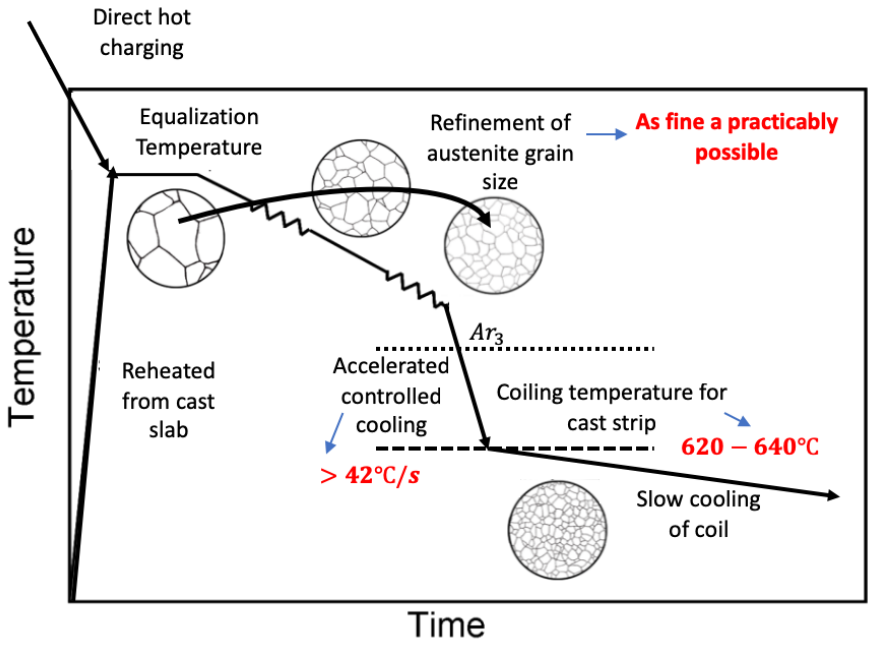

Figure 8.2-5 Schematic representation of the thermo-mechanical controlled processes (TMCP) in strip steel production (after Lagneborg et al. [232]*) annotated with the recommended processing parameters for an Fe-0.047C-0.2V-0.18Si-1.6Mn (in wt.%) alloy.*

9. Conclusions

9.1. General Conclusions

The principal purpose of this study was to further develop the fundamental understanding required for bridging the gap for development of a cost-effective novel hot-rolled high-strength steels. This study investigated high-strength yet formable steels, known as nano-steels exploiting the formation of nano-sized carbide precipitates in regular arrays through the mechanism of interphase precipitation. The phenomena of interphase precipitation have been systematically investigated both experimentally and computationally. The main conclusions of this are summarized as follows:

1) Small angle neutron scattering (SANS) was employed to characterize the precipitates and their size distributions in an Fe-0.047C-0.2V-1.6Mn (in wt.%) alloy isothermally transformed at $700\,°C$ up to $600\,min$. Model-independent analysis of the nuclear SANS signal and model fitting calculations, using oblate spheroid and disc-shapes suggested the major axis diameter increased from $18\,nm$ after $3\,min$ to $35\,nm$ after $600\,min$. Precipitate volume fraction correspondingly increased from 0.009 to 0.022 over the same period and number density fell from 2×10^{21} to $5 \times 10^{20}\,m^{-3}$. This explored the hypothesis *"The precipitation of carbides will consume sufficient carbon at the γ/α interphase boundary, therefore, the amount of carbon redistributed into the remaining γ is reduced. It is hypothesised that this will significantly accelerate the growth kinetics of"* It was found in a low carbon HSLA steel that that after $3\,mins$ of isothermal transformation the phase fraction of VC interphase precipitates was 0.009 which is well below the value of 0.030 determined by the CALPHAD method. It was also shown that the precipitates were significantly sub-stoichiometric in terms of C. Taken in

combination these two findings indicate that in the case of the low carbon HSLA transformed at $700\,℃$ a relatively small quantity of C is consumed by precipitation at the interphase boundary which is in contradiction to the aforementioned hypothesis.

2) *In-situ* characterization techniques were applied to elucidate the influence of $\gamma \rightarrow \alpha$ transformation upon the extent of interphase precipitation in the same low-carbon, vanadium-HSLA steel. Electron Back-scattered diffraction analyses of the γ/α orientation relationship with continuous cooling at 2 and $10\,℃s^{-1}$ suggest that the proportion of ferrite likely to hold interphase precipitation varies little with cooling rate. However, TEM analyses show that the interphase precipitation refines with increasing cooling rate in this cooling range. With cooling rates in excess of $20\,℃s^{-1}$, interphase precipitation is increasingly suppressed due to the increasingly diffusional-displacive nature of the Widmanstätten $\gamma \rightarrow \alpha$ transformation that is activated.
3) Although the thermal cycles are fundamentally different with the transformations in Chapter 4 being associated with isothermal transformations at $700\,°C$ rather than continuous cooling from $900\,°C$ in the case of Chapter 5, there appears to be a correlation between EBSD results and the SANS results. The correlation between the EBSD results and the SANS results is in the form of an agreement that $\approx 30\%$ non-OR grains (likely to be associated with interphase precipitation) and 30% of thermodynamically predicted volume fraction of precipitates was measured using SANS at a stage in the transformation where the SANS signal is dominated by interphase precipitation. The direct corollary of this proposition is that locally the interphase precipitation mechanism results in the complete precipitation of the carbide phase.
4) A new analytical model is presented which suggests the inter-sheet spacing of interphase precipitates is controlled by a complex interplay between the interfacial energy and interfacial segregation. It is shown

that the general trend of refining inter-sheet spacing with growing ferrite half-thickness can be well predicted by the proposed model. This model supports the following hypothesis: *It is hypothesized that the nucleation of interphase precipitates plays little role in the determination of ferrite growth ledge height and that interphase precipitates merely mark the prior growth ledge height in alloys where a strong carbide forming element is present.* This chapter has provided a mechanistic explanation in the form of a model for the following hypothesis: *It is hypothesized that the observed refinements in inter-sheet spacing during the initial stages of the* $\gamma \rightarrow \alpha + MC$ *transformation can be explained by the transition in* α *growth mode from parequilibrium to negligible partitioning local equilibrium.*

5) Through utilising a multi-phase field method, the effects of transformation strain on the transformation kinetics, thermodynamic stability and pairing of interphase precipitates in micro-alloyed steels was investigated. Where only the interfacial energy is considered to contribute to the transformation show that this energy can lead to the establishment of a neck between two neighbouring precipitates. However, if sufficient time is given, one of the precipitates will completely dissolve into its neighbouring particle. When both strain and interfacial energies act on the system, the bridge between the particles becomes stabilized leading to the pairing of the particles. This is a result of the tendency for particles to minimise the strain energy due to the excessive strain field generated by the neck between the two particles. This model supported the following hypothesis: *The elastic strain associated with interphase precipitate growth and the minimisation of interfacial energy is hypothesised to play a critical role in the growth of individual interphase precipitates and the interactions between neighbouring interphase precipitates, explaining the complex, compound*

morphologies, particularly necking behaviour of interphase carbide precipitates.

6) A procedure for the 'layman' is recommended for how to optimise interphase precipitation in any given alloy. For the Fe-0.047C-0.2V-0.18Si-1.6Mn (in wt.%) alloy considered in this study the hierarchical order (valid generally) of importance and specific recommendations of processing parameters are as follows:

- The austenite should be TMCP conditioned such that its grain size is as fine as practicably possible. A fine austenitic grain size is required in order to minimise the formation of Widmanstätten ferrite.
- This steel should be processed utilising accelerated controlled cooling at a rate in excess of $42\ ℃/s$.
- This steel should be coiled at as low coiling temperature as possible without activating the bainitic transformation. It is recommended that the optimal range for coiling temperature is in the range of $620 \rightarrow 640℃$.

9.2. Suggestions for future work

An innovative experimental approach is required in order to decouple the intrinsically linked phenomena of the matrix phase transformation and interphase carbide precipitation. An extension of the work performed in Chapter 5 is proposed. In Chapter 5 although it was found that the orientation relationship between the austenite and ferrite could be determined using in-situ HT-EBSD, the only way that high-quality TEM foils could be produced was using electropolishing. This approach meant that it was impossible to relate the precipitation observed in the TEM directly to the grains characterised with EBSD. Using a high-end Focussed Ion Beam milling system (FIB-SEM) and a means of cleaning and removing damage from the FIB lamellae, such as the Gatan PIPSII precision ion polishing system it is envisaged that a site-specific sampling

strategy could be employed. Targeted TEM lamellae could be lifted out following HT-EBSD from non-OR/OR grains.

In a new model alloy where the $\gamma \rightarrow \alpha$ phase transformation is considerably slower than that of the micro-alloyed steels studied in this Thesis, it is possible that High-Temperature EBSD scans could be acquired at such a rate that the kinetics of an isothermal $\gamma \rightarrow \alpha$ phase transformation could be tracked. Coupling this with the targeted site-specific FIB lift-out would allow the assembly of a spatially and temporally resolved data set where: the transformation kinetics, i.e. γ/α interphase boundary velocity; γ/α orientation relationship; and finally, how both of these parameters influence interphase precipitation. Such a dataset is critical if models such as that outlined in Chapter 6 and Chapter 7 are to be developed further.

An alternate experimental approach would be to use controlled decarburization experiments such as those performed by Hutchinson and co-workers [236,237] (Figure 9.2-1) have successfully decoupled the kinetics of phase transformation and solute drag. In the studies as mentioned above, the researchers were careful to perform their experiments on Fe-C-Mo and Fe-C-Cr alloys at elevated temperatures at which carbides would not be expected to precipitate.

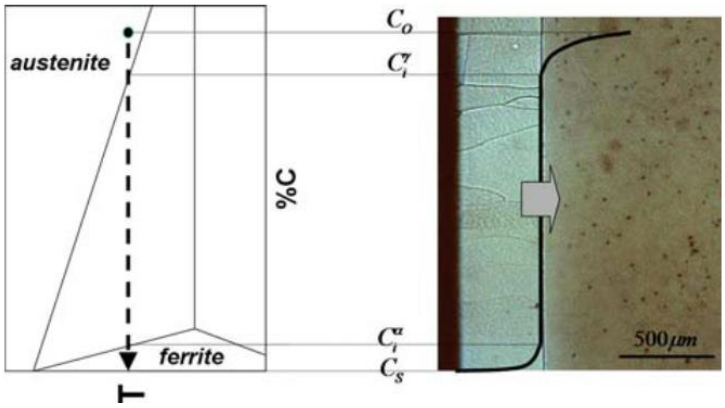

Figure 9.2-1 Schematic illustration of the diffusion profile during the decarburization of a binary Fe-C alloy. A very uniform ferrite layer is formed due to carbon removal at the surface (taken from [237]*).*

It is proposed that similar studies were undertaken at temperatures where carbide precipitates would be expected to form. Samples rich in carbon should be annealed a protective argon atmosphere in the single-phase austenite region such that a large austenite grain size ($\approx 400\ \mu m$) is achieved. The samples should then be cooled to an isothermal transformation temperature upon which an active decarburising atmosphere containing hydrogen saturated in water is introduced. After a period of isothermal transformation, the samples shall be quenched in iced brine and multi-modally characterised.

It is known the austenite/ferrite orientation relationship is an influential factor in determining the prevalence of interphase precipitation and interphase precipitation consumes C locally at the interphase boundary. It is hypothesised that the regions of austenite/ferrite boundary where the orientation relationship is conducive for precipitation will advance more rapidly than those where the kinetics of the interphase boundary is controlled by decarburization alone.

The information gathered from the above procedure would be used to interrogate interphase precipitation and solute drag as a function of interphase boundary crystallography and boundary kinetics. The interpretation of this data

and the extraction of interfacial energy required for the development of an advanced microstructural model of interphase precipitation.

10. Supplementary Information

10.1. Supplementary Note 1 – Selection of austenitisation and transformation temperatures

The austenitisation temperature and time were selected to dissolve Fe_3C or vanadium carbonitride (VX) precipitates already present in the steel. Calculations performed using Thermo-Calc and the TCFe7 database indicate that in this steel VX becomes unstable above approximately $1050\,℃$. The isothermal treatment temperature of $700\,℃$ was chosen to obtain a ferritic microstructure with nanoscale interphase VX precipitates and to allow precipitate growth and coarsening to occur at the more extended holding times.

10.2. Supplementary Note 2 – Methodology of small angle neutron scattering experiments

The specimens for SANS were sectioned from the heat-treated materials using a precision saw and then mechanically polished using a 4 step standard metallographic preparation approach to $1.0\ \mu m$ diamond finish prior to the SANS measurements. The specimen dimensions were approximately $10\,mm \times 10\,mm \times \sim 1\,mm$ (thickness). The thicknesses at nine different positions on each specimen were accurately measured using micrometer and a mean value calculated. The neutron beam was 8 mm in diameter giving a scanned volume of approximately $50\ mm^3$ and containing over 10^5 grains. The data acquisition time was $60\ min$ for each specimen. Scattered neutrons were recorded by two arrays of position sensitive area detectors each $\sim 1\ m^2$, one located $2.38\ m$ behind the sample and the other $4\ m$ behind the sample. This configuration gives small angle scattering vector (q) values between 0.004 and $0.3\ \text{Å}^{-1}$, where $q = 4\pi \sin\left(\frac{\theta}{\lambda_N}\right)$ and the scattering angle is 2θ. This corresponds very approximately

to characteristic particle sizes, d, ranging from ~ $1.5\,nm$ to $80\,nm$ (assuming $d{\sim}2\pi/q$).

10.3. Supplementary Note 3 – Data used in SANS analysis

10.3.1. Magnetic scattering length densities

The magnetic scattering length density (SLD) of the ferrite matrix, ρ_{mag}^{m} is given by the equation

$$\rho_{mag}^{m} = \frac{\rho_0 u}{\nu}$$

where $\rho_0 = 2.7 \times 10^{-15}$ m is a constant, $u = 2.1869$ is the mean atomic magnetic moment of the matrix and ν = 11.7x10^{-30} m^3 is the mean volume per atom. The value obtained for ρ_{mag}^{m} is $5.04 \times 10^{14}\ m^{-2}$. In SANS, precipitate phases which are paramagnetic or diamagnetic are generally considered to have a zero magnetic SLD. This applies to common precipitates in steel such as Fe_3C and MX carbonitrides (where M =Ti, Mo, Nb, V and X=C, N). Thus the magnetic contrast factor $\Delta\rho_{mag}$ where $\Delta\rho_{mag} = \rho_{mag}^{p} - \rho_{mag}^{m}$ is taken to be $-5.04 \times 10^{14}\ m^{-2}$.

10.3.2. Nuclear scattering length densities

The nuclear scattering length density of a phase, i, is calculated from the equation

$$\rho_{nuc}^{i} = \frac{\sum x_i\, b_i}{v_i}$$

where x_i is the atom fraction of i in the phase, v_i is the atomic volume and b_i is the coherent nuclear scattering length density of element i. The nuclear contrast factor is $\Delta\rho_{nuc}$ where $\Delta\rho_{nuc} = \rho_{nuc}^{p} - \rho_{nuc}^{m}$. Table 10.3-1 lists the nuclear SLD and nuclear contrast factor for i=matrix and i=precipitates relevant to the

present study along with values of $R(q)$, the ratio of magnetic to nuclear scattering intensity

Table 10.3-1 Values of nuclear scattering length density, nuclear contrast factor and $R(q)$ phases potentially relevant to this study.

Phase	ρ_{nuc} ($10^{14}m^{-2}$)	ρ_{mag} ($10^{14}m^{-2}$)	$\Delta\rho_{nuc}$ ($10^{14}m^{-2}$)	$\Delta\rho_{mag}$ ($10^{14}m^{-2}$)	$R(q)=(\Delta\rho_{mag}/\Delta\rho_{nuc})^2$
Fe	7.93	5	0	0	-
Fe_3C	6.73	0	1.2	5	17.36
MnS	-0.249	0	8.179	5	0.37
VC	3.43	0	4.5	5	1.23
VN	5.07	0	2.86	5	3.05
TiN	3.04	0	4.89	5	1.04

It is clear that all potential precipitate phases will contribute strongly to the magnetic contrast but VC and any MnS that might form will dominate the nuclear contrast although the latter is likely to form micron size phase outside the range of detection of the SANS detectors. Fe_3C, on the other hand, has a relatively small contrast factor. It is also notable that VC has magnetic and nuclear contrast factors that are close, with a ratio ~ 1.2 whereas the ratio for V(C, N) is larger reaching ~ 3 for VN.

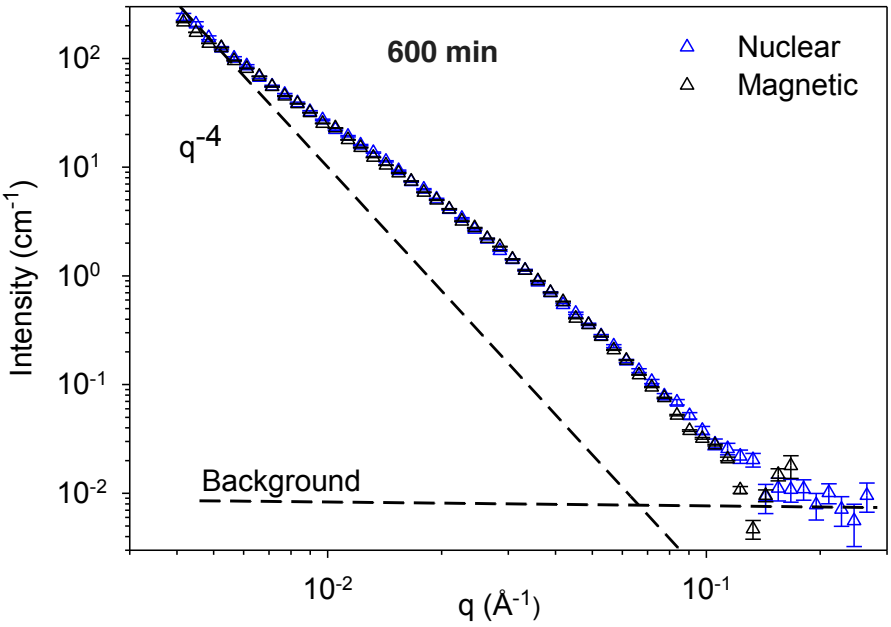

10.4. Supplementary Note 4 – comparison of SasView model fitting for a disc shape and an oblate spheroid shape (also termed oblate ellipsoid of revolution)

The fitting procedure is described in the main text and compared a disc shaped model with an oblate spheroid model. The calculated 1-D nuclear scattering profiles were fitted to the experimental 1-D scattering curves using, as fixed parameters, the precipitate volume fractions, obtained from equation 7, and the contrast between precipitates and ferrite matrix calculated from $R(q)$ (*Table 4.4-1*). Two different particle shapes were investigated namely a disc shape and an oblate spheroid shape. The starting estimates in the model for the disc mean radius (R) and half-thickness (T/2) (major, a, and minor, b, axes in the case of the oblate spheroid) were the radius and thickness values found from the Guinier model-independent analysis.

The goodness of fit between experimental and calculated 1-D scattering profiles was determined using the well known chi-squared quantity for all computations. The effect of altering the dispersion parameter in the range 0 to 0.6 for the major axis was explored; the polydispersity of the minor axis was set to zero as initial trials showed that varying this had a negligible effect on the fitting results. It was found that consistently better fitting was obtained with values of σ in the range 0.1 to 0.3 than for larger values of σ.

Representative graphs of experimental SANS nuclear scattering data plotted as *I versus q* from samples transformed for the time shown (symbols) along with model fitted data (solid lines) using either an oblate spheroid model or a disc model are shown in Figure 10.4-1 (a) and (b) (3 min transformation) and Figure 10.4-2 (a) and (b) (300 min transformation). It is clear from these figures that a polydispersity value (PD) of 0.2 fitted better than 0 or 0.5. However, there is very little difference in the fitting of oblate spheroid (frequently termed an oblate ellipsoid of revolution) or disc. Both appear to fit the experimental data well.

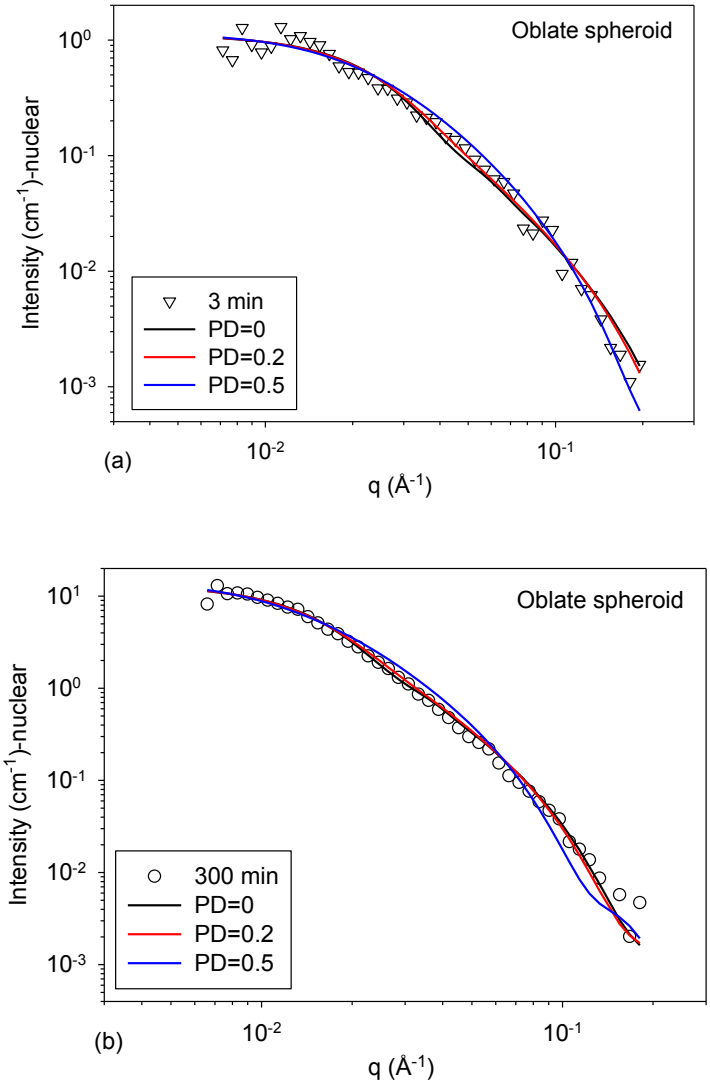

Figure 10.4-1 Experimental SANS nuclear scattering data plotted as I versus q from samples transformed for the time shown (symbols) along with model fitted data (solid lines) using an oblate spheroid model

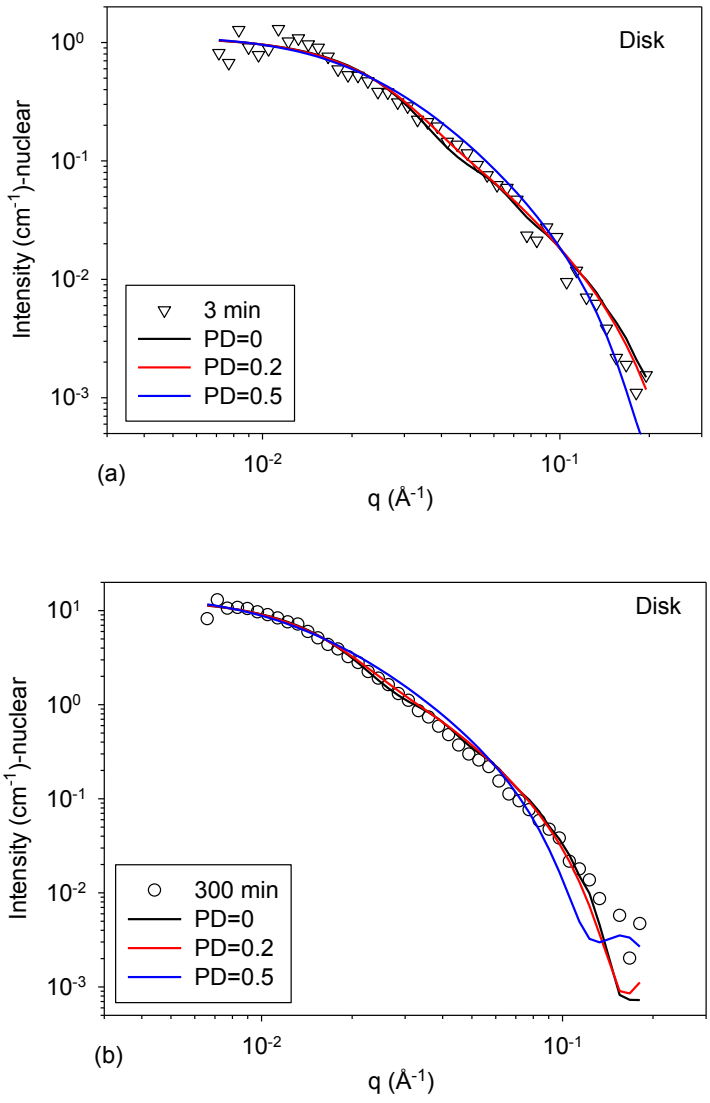

Figure 10.4-2 Experimental SANS nuclear scattering data plotted as I versus q from samples transformed for the time shown (symbols) along with model fitted data (solid lines) using a disc model

More detail of the fitting is given in the Tables below for the model calculations at representative ageing times and in these Tables the effect of polydispersity of the major axes on the fitting for both shapes is examined. The normalized chi-square value is computed by setting the value for the oblate spheroid calculation at $\sigma = 0.5$ equal to 1. Therefore, smaller normalized chi-square values equate to a better fit between model and experimental data.

Both the disc and oblate spheroid models give acceptable fitting results with very little difference between them for all ageing times but it is very clear that goodness of fit deteriorated significantly once the PD parameter exceeded 0.3. This provides justification for using a PD value of 0.2 in the representative calculations shown in the main text of the paper.

The error introduced into the estimation of equatorial radius by selecting a PD of 0.2 as opposed to 0.1 or 0.3 is of the order of $\pm 15\%$. The thickness error is less than this, it is $\sim \pm 10\%$.

AGEING TIME 3 MIN.

Dispersion parameter (PD)-equatorial radius	2 x polar radius/nm	Equatorial radius/nm	Normalised chi-square	Dispersion parameter (PD)-disc radius	Disc Thickness/nm	Disc Radius/nm	Normalised chi-square
0.1	2.5	10.2	0.909	0.1	2.1	9.1	0.908
0.2	2.7	9.1	0.921	0.2	2.3	8.1	0.920
0.3	3.0	7.5	0.947	0.3	2.5	6.7	0.947
0.4	3.3	5.9	0.982	0.4	2.8	5.2	0.982
0.5	3.7	4.4	1.000	0.5	3.2	3.9	1.000

AGEING TIME 5 MIN.

Dispersion parameter (PD)-equatorial radius	2 x polar radius/nm	Equatorial radius/nm	Normalised chi-square	Dispersion parameter (PD)-disc radius	Disc Thickness/nm	Disc Radius/nm	Normalised chi-square
0.1	2.7	11.6	0.749	0.1	2.3	10.3	0.741
0.2	2.8	10.4	0.714	0.2	2.4	9.3	0.698
0.3	3.0	11.5	0.754	0.3	2.6	7.8	0.739
0.4	3.3	14.8	0.881	0.4	2.8	6.2	0.874
0.5	3.6	17.5	1.000	0.5	3.1	4.8	1.000

AGEING TIME 60 MIN.

Dispersion parameter (PD)-equatorial radius	2 x polar radius/nm	Equatorial radius/nm	Normalised chi-square	Dispersion parameter (PD)-disc radius	Disc Thickness/nm	Disc Radius/nm	Normalised chi-square
0.1	3.2	12.9	0.799	0.1	2.7	11.5	0.797
0.2	3.3	11.5	0.829	0.2	2.8	10.2	0.827
0.3	3.7	9.5	0.887	0.3	3.1	8.5	0.886
0.4	4.1	7.4	0.960	0.4	3.5	6.5	0.960
0.5	4.7	5.5	1.000	0.5	4.0	4.9	1.000

AGEING TIME 300 MIN.

Dispersion parameter (PD)-equatorial radius	2 x polar radius/nm	Equatorial radius/nm	Normalised chi-square	Dispersion parameter (PD)-disc radius	Disc Thickness/nm	Disc Radius/nm	Normalised chi-square
0.1	4.6	16.4	0.768	0.1	3.9	14.5	0.763
0.2	4.8	14.8	0.797	0.2	4.1	13.1	0.791
0.3	5.2	12.6	0.857	0.3	4.4	11.1	0.853
0.4	5.6	10.0	0.938	0.4	4.8	8.9	0.936
0.5	6.2	7.6	1.000	0.5	5.3	6.7	1.000

AGEING TIME 600 MIN.

Dispersion parameter (PD)-equatorial radius	2 x polar radius/nm	Equatorial radius/nm	Normalised chi-square	Dispersion parameter (PD)-disc radius	Disc Thickness/nm	Disc Radius/nm	Normalised chi-square
0.1	5.9	19.4	0.665	0.1	5.0	17.2	0.659
0.2	6.2	17.5	0.714	0.2	5.3	15.5	0.708
0.3	6.7	14.8	0.805	0.3	5.7	13.1	0.801
0.4	7.3	11.8	0.918	0.4	6.2	10.4	0.917
0.5	8.1	9.0	1.000	0.5	6.9	7.9	1.000

10.5. Supplementary Note 5 – Precipitate size distributions

AGEING TIME 5 MIN

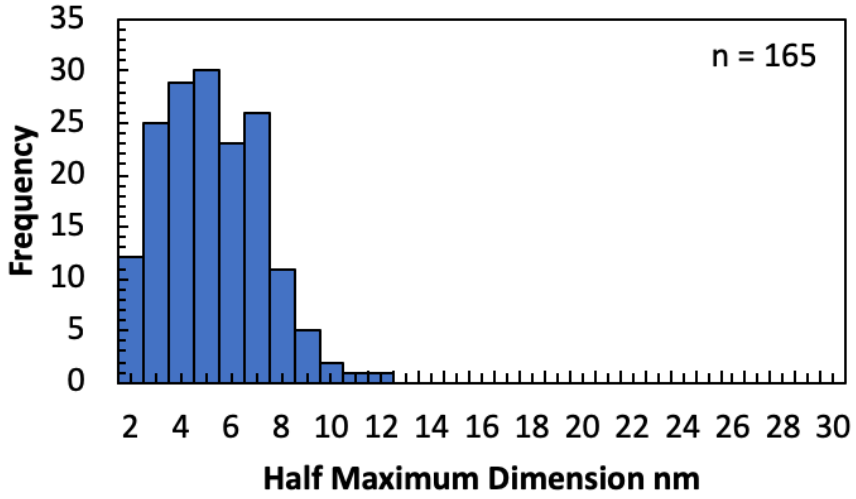

Figure 10.5-1 Precipitate size distribution after 5 *min of ageing at* 700 ℃

AGEING TIME 600 MIN

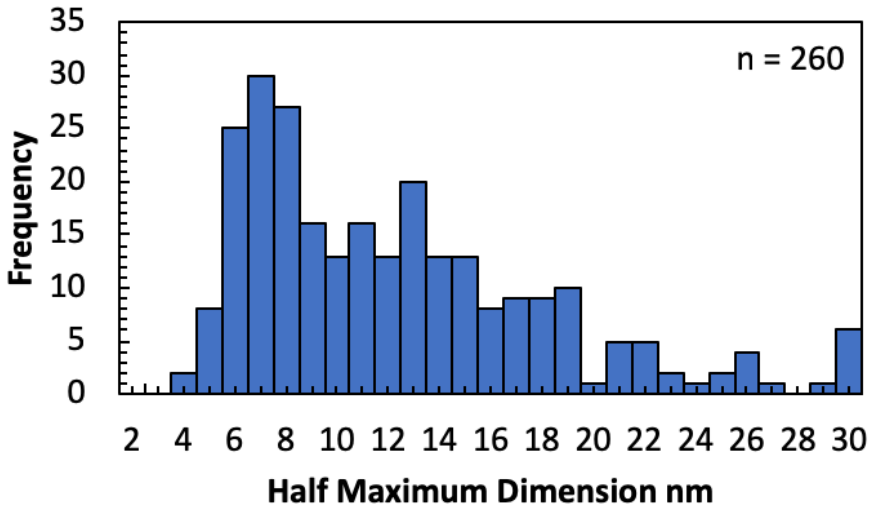

Figure 10.5-2 Precipitate size distribution after 600 *min of ageing at* 700 ℃

References

[1] H.K.D.H. Bhadeshia, R.W.K. Honeycombe, Steels Microstructure and Properties, Third Edit, Butterworth-Heinemann, Oxford, 2006.

[2] J.M. Allwood, J.M. Cullen, M.A. Carruth, D.R. Cooper, M. McBrien, R.L. Milford, et al., Sustainable materials: with both eyes open, UIT Cambridge, Cambridge, 2012.

[3] T.A. Swartzell, Lightweighting and Steel Technologies in the All-New 2016 Chevrolet Malibu and 2017 Buick LaCrosse, in: Gt. Des. STEEL Semin. May 16th 2016, Livonia, 2016.

[4] Worldsteel Association, Fact Sheet: Advanced steel applications, 2016.

[5] European Commission, Reducing CO2 emissions from passenger cars, (2015). http://ec.europa.eu (accessed February 19, 2015).

[6] R. Heuss, N. Müller, W. van Sintern, A. Starke, A. Tschiesner, Lightweight, heavy impact - How carbon fiber and other lightweight materials will develop across industries and specifically in automotive, 2012.

[7] ULSAB, Ultra Light Steel Auto Body; Electronic Report; 1.0, 1998.

[8] UltraLight Steel Auto Body Consortium, ULSAB-AVC - Advanced Vehicle Concepts Overview Report., 2002.

[9] EDAG, FutureSteelVehicle Phase 2 - Report, 2011.

[10] A.T. Mayyas, A. Qattawi, A.R. Mayyas, M.A. Omar, Life cycle assessment-based selection for a sustainable lightweight body-in-white design, Energy. 39 (2012) 412–425. doi:10.1016/j.energy.2011.12.033.

[11] M. Slesser, Dictionary of energy, 2nd ed., Mamillan Press LTD, London, 1988. doi:10.1007/978-1-349-19476-6.

[12] H.C. Kim, T.J. Wallington, Life-cycle energy and greenhouse gas emission benefits of lightweighting in automobiles: Review and harmonization, Environ. Sci. Technol. 47 (2013) 6089–6097. doi:10.1021/es3042115.

[13] S. Keeler, M. Kimchi, P. J. Mooney, Advanced High-Strength Steels Apllication Guidelines Version 6.0, Brussels, 2017.

[14] Y. Funakawa, T. Shiozaki, K. Tomita, T. Saito, H. Nakata, M. Suwa, et al., High Tensile Hot Rolled Steel Sheet And Method For Production Therof, 01980929.2, 2002.

[15] C.M. Sonsino, Light-weight design chances using high-strength steels, Materwiss. Werksttech. 38 (2007) 9–22. doi:10.1002/mawe.200600090.

[16] R.A. Rijkenberg, A. Blowey, P. Bellina, C. Wooffindin, Advanced High Stretch-Flange Formability Steels for Chassis & Suspension Applications 3 . Product concept : tensile properties and microstructure, 4th Int. Conf. Steels Cars Truck. June 15-19, Braunschweig, Ger. (2014) 426–433.

[17] T. Gladman, The Physical Metallurgy of Microalloyed Steels, 2nd Editio, Institute of Materials, London, 2002.

[18] F.B. Pickering, Physical metallurgy and the design of steels, Applied Science Publishers, London, 1978.

[19] E.O. Hall, The Deformation and Ageing of Mild Steel: III Discussion of Results, Proc. Phys. Soc. Sect. B. 64 (1951) 747–753. doi:10.1088/0370-1301/64/9/303.

[20] N.J. Petch, The Cleavage Strengh of Polycrystals, J. Iron Steel Inst. 174 (1953) 25–28.

[21] D.J. Dingley, D. McLean, Components of the flow stress of iron, Acta Metall. 15 (1967) 885–901.

[22] J.E. Bailey, P.B. Hirsch, The dislocation distribution, flow stress, and stored energy in cold-worked polycrystalline silver, Philos. Mag. 5 (1960) 485–497. doi:10.1080/14786436008238300.

[23] A.S. Keh, Work hardening and deformation sub-structure in iron single crystals deformed in tension at 298k, Philos. Mag. 12 (1965) 9–30. doi:10.1080/14786436508224942.

[24] E. Kozeschnik, Modelling Solid-State Precipitation, Momentum Press, New York, 2013. doi:10.5643/9781606500644.

[25] S. Ukai, H. Okada, M. Inoue, T. Nishida, M. Fujiwara, S. Nomura, et al., Alloying design of oxide dispersion for long life FBRs core materials

strengthened ferritic steel, J. Nucl. Mater. 204 (1993) 5–73. doi:10.1016/0022-3115(93)90200-I.

[26] M. Charleux, W.J.W. Poole, M. Militzer, A. Deschamps, Precipitation behavior and its effect on strengthening of an HSLA-Nb/Ti steel, … Mater. Trans. A. 32 (2001) 1635–1647. doi:10.1007/s11661-001-0142-6.

[27] F.G. Wei, T. Hara, K. Tsuzaki, High-resolution transmission electron microscopy study of crystallography and morphology of TiC precipitates in tempered steel, Philos. Mag. 84 (2004) 1735–1751. doi:10.1080/14786430310001638762.

[28] H.-W. Yen, C.-Y. Chen, T.-Y. Wang, C.-Y. Huang, J.-R. Yang, Orientation relationship transition of nanometre sized interphase precipitated TiC carbides in Ti bearing steel, Mater. Sci. Technol. 26 (2010) 421–430. doi:10.1179/026708309x12512744154207.

[29] H.-W. Yen, P.-Y. Chen, C.-Y. Huang, J.-R. Yang, Interphase precipitation of nanometer-sized carbides in a titanium–molybdenum-bearing low-carbon steel, Acta Mater. 59 (2011) 6264–6274. doi:10.1016/j.actamat.2011.06.037.

[30] E. Orowan, Discussion on internal stresses, in: Symp. Intern. Stress. Met. Alloy., London, 1948: pp. 451–453.

[31] U.F. Kocks, A statistical theory of flow stress and work-hardening, Philos. Mag. 13 (1966) 541–566. doi:10.1080/14786436608212647.

[32] A.J.E. Foreman, M.J. Makin, Dislocation ensemble movement through random arrays of obstacles, Philos. Mag. 14 (1966) 911–924. doi:10.1080/14786436608244762.

[33] M. Ashby, Results and consequences of a recalculation of the frank-read and the orowan stress, Acta Metall. 14 (1966) 679–681.

[34] S.A. Kim, W.L. Johnson, Elastic constants and internal friction of martensitic steel, ferritic-pearlitic steel, and α-iron, Mater. Sci. Eng. A. 452–453 (2007) 633–639. doi:10.1016/j.msea.2006.11.147.

[35] A.J.J. Ardell, Precipitation hardening, Metall. Trans. A. 16 (1985) 2131–

2165. doi:10.1007/BF02670416.

[36] T. Gladman, Precipitation hardening in metals, Mater. Sci. Technol. 15 (1999) 30–36. doi:10.1179/026708399773002782.

[37] T. Yokota, A. Kobayahi, K. Seto, Y. Hosoya, T. Heller, B. Hammer, et al., A High Strength Steel Excelent in Uniform Elongation Properties and Method of Manufacturing the Same, 2006.

[38] K. Seto, Y. Funakawa, S. Kaneko, Hot Rolled High Strength Steels for Suspension and Chassis Parts "NANOHITEN" and "BHT® Steel," JFE Tech Rep. 10 (2007) 19–25.

[39] R.A. Rijkenberg, A high-strength hot-rolled steel strip or sheet with excelent formability and fatigue performance and a method of manufacturing said steel strip or sheet, WO2014EP52334 20140206, 2014.

[40] Y. Huang, A. Zhao, X. Wang, X. Wang, J. Yang, J. Han, et al., A High-Strength High-Ductility Ti- and Mo-Bearing Ferritic Steel, Metall. Mater. Trans. A Phys. Metall. Mater. Sci. 47 (2015) 450–460. doi:10.1007/s11661-015-3232-6.

[41] J.-B. Seol, S.-H. Na, B. Gault, J.-E. Kim, J.-C. Han, C.-G. Park, et al., Core-shell nanoparticle arrays double the strength of steel, Sci. Rep. 7 (2017) 42547. doi:10.1038/srep42547.

[42] Y. Funakawa, T. Shiozaki, K. Tomita, T. Yamamoto, E. Maeda, Development of High Strength Hot-rolled Sheet Steel Consisting of Ferrite and Nanometer-sized Carbides, ISIJ Int. 44 (2004) 1945–1951. doi:10.2355/isijinternational.44.1945.

[43] A.J.E. Foreman, M.J. Makin, Dislocation movement through random arrays of obstacles, Canad. J. Phys. 45 (1967) 511–517. doi:10.1080/14786436608244762.

[44] N. Kamikawa, Y. Abe, G. Miyamoto, Y. Funakawa, T. Furuhara, Tensile Behavior of Ti,Mo-added Low Carbon Steels with Interphase Precipitation, ISIJ Int. 54 (2014) 212–221. doi:10.2355/isijinternational.54.212.

[45] M.-Y. Chen, M. Gouné, M. Verdier, Y. Bréchet, J.-R. Yang, Interphase

precipitation in vanadium-alloyed steels: Strengthening contribution and morphological variability with austenite to ferrite transformation, Acta Mater. 64 (2014) 78–92. doi:10.1016/j.actamat.2013.11.025.

[46] N. Kamikawa, K. Sato, G. Miyamoto, M. Murayama, N. Sekido, K. Tsuzaki, et al., Stress-strain behavior of ferrite and bainite with nano-precipitation in low carbon steels, Acta Mater. 83 (2015) 383–396. doi:10.1016/j.actamat.2014.10.010.

[47] M. Mannerkoski, On the decompositio of austenite in a 13 per cent chromium steels, ACTA Polytech. Scand. Incl. Metall. Ser. (1964) 7.

[48] K. Relander, AUSTENITZERFALL EINES 0, 18 PERCENT C-2 PERCENT MO-STAHLES IM TEMPERATURBEREICH DER PERLITSTUFE, ACTA Polytech. Scand. Incl. Metall. Ser. (1964) 7.

[49] A.T. Davenport, F.G. Berry, R.W.K. Honeycombe, Interphase Precipitation in Iron Alloys, Met. Sci. 2 (1968) 104–106. doi:10.1179/030634568790443341.

[50] F.G. Berry, R.W.K. Honeycombe, The isothermal decomposition of austenite in Fe-Mo-C alloys, Metall. Trans. 1 (1970) 3279–3286. doi:10.1007/BF03037854.

[51] T. Sakuma, R.W.K. Honeycombe, Effect of manganese on microstructure of an isothermally transformed Fe–Nb–C alloy, Mater. Sci. Technol. 1 (1985) 351–356. doi:10.1179/026708385790124747.

[52] A.T. Davenport, R.W.K. Honeycombe, Precipitation of carbides at y-a boundaries in alloy steels, Proc. R. Soc. London A. 322 (1971) 191–205.

[53] A.D. Batte, R.W.K. Honeycombe, Strengthening of Ferrite by Vanadium Carbide Precipitation, Met. Sci. 7 (1973) 160–168. doi:10.1179/030634573790445370.

[54] K. Campbell, R.W.K. Honeycombe, The Isothermal Decomposition of Austenite in Simple Chromium Steels, Met. Sci. 8 (1974) 197–203.

[55] A. Barbacki, R. Honeycombe, Transitions in carbide morphology in molybdenum and vanadium steels, Metallography. (1976) 277–291.

[56] S. Freeman, R.W.K. Honeycombe, Strengthening of titanium steels by carbide precipitation, Met Sci. 11 (1977) 59–64. doi:10.1179/msc.1977.11.2.59.

[57] N.K. Balliger, R.W.K. Honeycombe, The effect of nitrogen on precipitation and transformation kinetics in vanadium steels, Metall. Trans. A. 11 (1980) 421–429. doi:10.1007/BF02654566.

[58] P.R. Howell, R.A. Ricks, J. V Bee, R.W.K. Honeycombe, Precipitate orientations in isothermally transformed iron-base alloys, Philos. Mag. A. 41 (1980) 165–175. doi:10.1080/01418618008236132.

[59] T. Sakuma, R.W.K. Honeycombe, Microstructures of Isothermally Transformed Fe-Nb-C Alloys, Met. Sci. 18 (1984) 449–454.

[60] R.W.K. Honeycombe, Transformation from austenite in alloy steels, Metall. Trans. A. 7 (1976) 915–936. doi:10.1007/BF02644057.

[61] R. Honeycombe, 29th HATFIELD MEMORIAL LECTURE: Ferrite, Met. Sci. 14 (1980) 201–214. doi:10.1179/030634580790426481.

[62] T. Obara, G.J. Shiflet, H.I. Aaronson, Influence of Interfacial Structure upon Carbide Precipitation at Austenite : Ferrite Boundaries in an Fe-C-Mo Alloy, Metall. Trans. A. 14 (1983) 1159–1167. doi:10.1007/BF02659863.

[63] P. Li, J.A. Todd, Application of a new model to the interphase precipitation reaction in vanadium steels, Metall. Trans. A. 19 (1988) 2139–2151. doi:10.1007/BF02645039.

[64] R.M. Smith, D.P. Dunne, Structural aspects of alloy carbonitride precipitation in microalloyed steels, Mater. Sci. Forum. 11 (1988) 166–181.

[65] R.A. Ricks, P.R. Howell, Bowing Mechanism for Interphase Boundary Migration in Alloy-Steels, Met. Sci. 16 (1982) 317–321. doi:10.1179/030634582790427389.

[66] R.A. Ricks, P.R. Howell, The formation of discrete precipitate dispersions on mobile interphase boundaries in iron-base alloys, Acta Metall. 31 (1983) 853–861. doi:10.1016/0001-6160(83)90113-X.

[67] G.L. Dunlop, C.J. Carlsson, G. Frimodig, Precipitation of VC in ferrite and

pearlite during direct transformation of a medium carbon microalloyed steel, Metall. Trans. A. 9 (1978) 261–266. doi:10.1007/BF02646709.

[68] A. Itman, K.R. Cardoso, H.-J. Kestenbach, Quantitative study of carbonitride precipitation in niobium and titanium microalloyed hot strip steel, Mater. Sci. Technol. 13 (1997) 49–55. doi:10.1179/mst.1997.13.1.49.

[69] G. Miyamoto, R. Hori, B. Poorganji, T. Furuhara, Interphase precipitation of VC and resultant hardening in V-added medium carbon steels, ISIJ Int. 51 (2011) 1733–1739. doi:10.2355/isijinternational.51.1733.

[70] M.R. Ahmadi, B. Sonderegger, E. Povoden-Karadeniz, A. Falahati, E. Kozeschnik, Precipitate strengthening of non-spherical precipitates extended in <100> or {100} direction in fcc crystals, Mater. Sci. Eng. A. 590 (2014) 262–266. doi:10.1016/j.msea.2013.10.043.

[71] R. Okamoto, A. Borgenstam, J. Ågren, Interphase precipitation in niobium-microalloyed steels, Acta Mater. 58 (2010) 4783–4790. doi:10.1016/j.actamat.2010.05.014.

[72] T. Murakami, H. Hatano, G. Miyamoto, T. Furuhara, Effects of Ferrite Growth Rate on Interphase Boundary Precipitation in V Microalloyed Steels, ISIJ Int. 52 (2012) 616–625. doi:10.2355/isijinternational.52.616.

[73] C.Y. Chen, C.C. Chen, J.R. Yang, Microstructure characterization of nanometer carbides heterogeneous precipitation in Ti-Nb and Ti-Nb-Mo steel, Mater. Charact. 88 (2014) 69–79. doi:10.1016/j.matchar.2013.11.016.

[74] Y. Zhang, G. Miyamoto, K. Shinbo, T. Furuhara, T. Ohmura, T. Suzuki, et al., Effects of transformation temperature on VC interphase precipitation and resultant hardness in low-carbon steels, Acta Mater. 84 (2015) 375–384. doi:10.1016/j.actamat.2014.10.049.

[75] J.M. Gray, R.B.G. Yeo, Columbium carbonitride precipitation in low-alloy steels with particular emphasis on precipitate- row formation, ASM Trans. Quart. 61 (1968) 255–269.

[76] R.G. Baker, J. Nutting, ISI Report No 64, (1969).

[77] T.N. Baker, Processes, microstructure and properties of vanadium microalloyed steels, Mater. Sci. Technol. 25 (2009) 1083–1107.

[78] H.-W. Yen, C. Chen, J.-R. Yang, Heat treatment induced orientation change of nanometer-sized interphase precipitated TiC in a Ti-bearing Steel, Semin. Taiwan Met. Heat Treat. Soc. (2006).

[79] N.G. Chechenin, P.M. Bronsveld, A. Chezan, C.B. Craus, D.O. Boerma, TEM Study of Ti-N and Cr-N Precipitate Formation in Iron Alloys, 117 (2000) 117–126.

[80] Z. Nishiyama, X-ray investigation on the mechanism of the transformation from facecentered cubic lattice to body-centered cubic lattice, Sci. Reports Res. Institutes, Tohoku Univ. 23 (1934) 637–664.

[81] G. Wasserman, Einfluß der α-γ-Umwandlung eines irreversiblen Nickelstahls auf Kristallorientierung und Zugfestigkeit, Eisenhuettenwes. 16 (1933) 647.

[82] M. Tanino, Crystal Structure and Precipitation Characteristics of Carbides in Steel, Bull. Japan Inst. Met. 11 (1972) 202–220.

[83] D. V Edmonds, R.W.K. Honeycombe, Precipitation processes in solids, in: K.C. Russell (Ed.), Precip. Process. Solids Proc. a Symp. Spons. by TMS-AIME Heat Treat. Comm. 1976 TMS Fall Meet. Niagara Falls, Metallurgical Society of AIME, New York, 1978: p. 121.

[84] S. Mukherjee, I.B. Timokhina, C. Zhu, S.P. Ringer, P.D. Hodgson, Three-dimensional atom probe microscopy study of interphase precipitation and nanoclusters in thermomechanically treated titanium-molybdenum steels, Acta Mater. 61 (2013) 2521–2530. doi:10.1016/j.actamat.2013.01.028.

[85] I. Timokhina, M.K. Miller, J. Wang, H. Beladi, P. Cizek, P.D. Hodgson, On the Ti-Mo-Fe-C atomic clustering during interphase precipitation in the Ti-Mo steel studied by advanced microscopic techniques, Mater. Des. 111 (2016) 222–229. doi:10.1016/j.matdes.2016.08.086.

[86] S. Mukherjee, I.B. Timokhina, C. Zhu, S.P. Ringer, P.D. Hodgson, Clustering

and precipitation processes in a ferritic titanium-molybdenum microalloyed steel, J. Alloys Compd. 690 (2017) 621–632. doi:10.1016/j.jallcom.2016.08.146.

[87] C. Smith, Grains, phases, and interphases: an interpretation of microstructure, Trans. Met. Soc. AIME, Vol. 175, p. 15-51 (1948). 20 (1948).

[88] C.-Y. Chen, J.-R. Yang, C.-C. Chen, S.-F. Chen, Microstructural characterization and strengthening behavior of nanometer sized carbides in Ti–Mo microalloyed steels during continuous cooling process, Mater. Charact. 114 (2016) 18–29. doi:10.1016/j.matchar.2016.01.023.

[89] G. Miyamoto, R. Hori, B. Poorganji, T. Furuhara, Crystallographic Analysis of Proeutectoid Ferrite/Austenite Interface and Interphase Precipitation of Vanadium Carbide in Medium-Carbon Steel, Metall. Mater. Trans. A. 44 (2013) 3436–3443. doi:10.1007/s11661-013-1702-2.

[90] Y.-J. Zhang, G. Miyamoto, K. Shinbo, T. Furuhara, Effects of α/γ orientation relationship on VC interphase precipitation in low-carbon steels, Scr. Mater. 69 (2013) 17–20. doi:10.1016/j.scriptamat.2013.03.020.

[91] C. Chih-Yuan, C. Chien-Chon, Y. Jer-Ren, Dualism of precipitation morphology in high strength low alloy steel, Mater. Sci. Eng. A. 626 (2015) 74–79. doi:10.1016/j.msea.2014.12.029.

[92] Y.-J.J. Zhang, G. Miyamoto, K. Shinbo, T. Furuhara, Quantitative measurements of phase equilibria at migrating α/γ interface and dispersion of VC interphase precipitates: Evaluation of driving force for interphase precipitation, Acta Mater. 128 (2017) 166–175. doi:10.1016/j.actamat.2017.02.020.

[93] H.-W. Yen, C.-Y. Huang, J.-R. Yang, Characterization of interphase-precipitated nanometer-sized carbides in a Ti-Mo-bearing steel, Scr. Mater. 61 (2009) 616–619. doi:10.1016/j.scriptamat.2009.05.036.

[94] J.H. Jang, C.-H. Lee, Y.-U. Heo, D.-W. Suh, Stability of (Ti,M)C (M=Nb, V, Mo and W) carbide in steels using first-principles calculations, Acta Mater. 60

(2012) 208–217. doi:10.1016/j.actamat.2011.09.051.

[95] H.I. Aaronson, Decomposition of austenite by diffusional processes: proceedings of a symposium held in Philadelphia, Pennsylvania, October 19, 1960 under the sponsorship of the Ferrous Metallurgy Committee of the Institute of Metals Division, the Metallurgical Society, in: V.F. Zackay, H.I. Aaronson (Eds.), Decompos. Austenite by Diffus. Process. Proc. a Symp. Held Philadelphia, Pennsylvania, Oct. 19, 1960 under Spons. Ferr. Metall. Comm. Inst. Met. Div. Metall. Soc., Interscience Publishers, New York, 1962.

[96] M. Onink, F.D. Tichelaar, C.M. Brakman, E.J. Mittemeijer, S. van der Zwaag, An in situ hot stage TEM study of the decomposition of Fe-C austenites.pdf, J. Mater. Sci. 30 (1995) 6223–6234. doi:10.1007/BF00369670.

[97] H.I. Aaronson, Observations on interphase boundary structure, J. Microsc. 102 (1974) 275–300. doi:10.1111/j.1365-2818.1974.tb04640.x.

[98] H. Aaronson, Atomic mechanisms of diffusional nucleation and growth and comparisons with their counterparts in shear transformations, Metall. Mater. Trans. A. 24 (1993) 241–276. doi:10.1007/BF02657313.

[99] G.J. Shiflet, M. a Mangan, W.G. Meng, Growth by Ledges, Interface Sci. 6 (1998) 133–154.

[100] H.I. Aaronson, W.T. Reynolds, G.R. Purdy, Coupled-solute drag effects on ferrite formation in Fe-C-X systems, Metall. Mater. Trans. A. 35 (2004) 1187–1210. doi:10.1007/s11661-004-0294-2.

[101] H.I. Aaronson, T. Furuhara, M.G. Hall, J.P. Hirth, J.F. Nie, G.R. Purdy, et al., On the mechanism of formation of diffusional plate-shaped transformation products, Acta Mater. 54 (2006) 1227–1232. doi:10.1016/j.actamat.2005.10.049.

[102] C.S. Smith, Microstructure: 1952 Campbell, Edward, Demille Memorial Lecture, Trans. Am. Soc. Met. 45 (1953) 533–575.

[103] G. Kurdjumov, G. Sachs, On the mechanisms of steel hardening, Z. Phys. 64

(1930) 325–343.

[104] H.I. Aaronson, M.R. Plichta, G.W. Franti, K.C. Russell, Precipitation at interphase boundaries, Metall. Trans. A. 9 (1978) 363–371. doi:10.1007/BF02646386.

[105] K.R. Kinsman, E. Eichen, H.I. Aaronson, Thickening kinetics of proeutectoid ferrite plates in Fe-C alloys, Metall. Trans. A. 6 (1975) 303–317. doi:10.1007/BF02667284.

[106] H. Aaronson, M. Enomoto, J. Lee, Mechanism of Diffusional Phase Transformations in Metals and Alloys, CRC Press, London, 2010. doi:10.1007/s13398-014-0173-7.2.

[107] H.K.D.H. Bhadeshia, Diffusional Transformations: A theory for the formation of superledges, Phys. Status Solidi a-Applied Res. 69 (1982) 745–750.

[108] C. Laird, H.I. Aaronson, The growth of γ plates in an Al-15% Ag alloy, Acta Metall. 17 (1969) 505–519. doi:10.1016/0001-6160(69)90032-7.

[109] J.W. Christian, Crystallographic theories, interface structures, and transformation mechanisms, Metall. Mater. Trans. A. 25 (1994) 1821–1839. doi:10.1007/BF02649031.

[110] J.A. Todd, P. Li, S.M. Copley, A new model for precipitation at moving interphase boundaries, Metall. Trans. A. 19 (1988) 2133–2138. doi:10.1007/BF02645038.

[111] J.A. Todd, Y.J. Su, A mass transport theory for interphase precipitation with application to vanadium steels, Metall. Trans. A. 20 (1989) 1647–1655. doi:10.1007/BF02663198.

[112] C. Zener, Theory of growth of spherical precipitates from solid solution, J. Appl. Phys. 20 (1949) 950–953. doi:10.1063/1.1698258.

[113] W.J. Liu, Computer simulation of VC Precipitation at Moving γ/α Interfaces, Metall. Trans. A. 24 (1993) 2195–2207. doi:10.1007/BF02648594.

[114] V.K. Heikkinen, Formation of Two-Dimensional Granular Colonies in V-

Treated Fine-Grain Steels, Scand. J. Metall. 2 (1973) 109–112.

[115] W.F. Lange, M. Enomoto, H.I. Aaronson, The kinetics of ferrite nucleation at austenite grain boundaries in Fe-C alloys, Metall. Trans. A. 19 (1988) 427–440. doi:10.1007/BF02649256.

[116] M.-Y. Chen, M. Gouné, M. Militzer, Y. Bréchet, J.-R. Yang, Superledge Model for Interphase Precipitation During Austenite-to-Ferrite Transformation, Metall. Mater. Trans. A. 45 (2014) 5351–5361. doi:10.1007/s11661-014-2486-8.

[117] C. Zener, Private communication to CS Smith, Priv. Commun. to CS Smith Trans. AIME. 175 (1949).

[118] T. Gladman, On the Theory of the Effect of Precipitate Particles on Grain Growth in Metals, Proc. R. Soc. A Math. Phys. Eng. Sci. 294 (1966) 298–309. doi:10.1098/rspa.1966.0208.

[119] M.F. Ashby, The influence of particles on boundary mobility, in: N. Hansen, A.R. Jones, T. Leffers (Eds.), Recryst. Grain Growth Multi-Phase Part. Contain. Mater. Proc. 1st Risø Int. Symp. Metall. Mater. Sci., Danmarks Tekniske Universitet, Risø Nationallaboratoriet for Bæredygtig Energi, 1980: p. 325.

[120] W. Roberts, Internal Report IM-1333, Stockholm, 1978.

[121] R. Lagneborg, S. Zajac, A model for interphase precipitation in V-microalloyed structural steels, Metall. Mater. Trans. A. 31 (2001) 1–12.

[122] J.W. Cahn, The kinetics of cellular segregation reactions, Acta Metall. 7 (1959) 18–28. doi:10.1016/0001-6160(59)90164-6.

[123] R. Okamoto, J. Ågren, A model for interphase precipitation based on finite interface solute drag theory, Acta Mater. 58 (2010) 4791–4803. doi:10.1016/j.actamat.2010.05.016.

[124] J. Odqvist, M. Hillert, J. Ågren, Effect of alloying elements on the γ to α transformation in steel. I, Acta Mater. 50 (2002) 3213–3227. doi:10.1016/S1359-6454(02)00143-X.

[125] J. Odqvist, B. Sundman, J. Ågren, A general method for calculating

deviation from local equilibrium at phase interfaces, Acta Mater. 51 (2003) 1035–1043. doi:10.1016/S1359-6454(02)00507-4.

[126] P.R. Rios, Morphology of interphase precipitation in microalloyed steels, J. Mater. Sci. Lett. 10 (1991) 981–983. doi:10.1007/BF00722153.

[127] P.R. Rios, A model for interphase precipitation in stoichiometrically balanced vanadium steels, J. Mater. Sci. 30 (1995) 1872–1878. doi:10.1007/BF00351624.

[128] D. V Edmonds, OCCURRENCE OF FIBROUS VC DURING TRANSFORMATION OF AN FE-V-C STEEL, J. Iron Steel Inst. 210 (1972) 363–365.

[129] H. Jin, I. Elfimov, M. Militzer, Study of the interaction of solutes with Σ5 (013) tilt grain boundaries in iron using density-functional theory, J. Appl. Phys. 115 (2014). doi:10.1063/1.4867400.

[130] M. Mannerkoski, The Mechanism of Formation of a Periodic Eutectoid Structure at Low Temperatures in Plain Chromium Steel, Met. Sci. J. 3 (1969) 54–55. doi:10.1179/msc.1969.3.1.54.

[131] F.A. Khalid, D. V. Edmonds, Interphase precipitation in microalloyed engineering steels and model alloy, Mater. Sci. Technol. 9 (1993) 384–396. doi:10.1179/026708393790350468.

[132] D. V Edmonds, R.W.K. Honeycombe, Photoemission electron microscopy of growth of grain boundary ferrite allotriomorphs in chromium steel, Met. Sci. 12 (1978) 399–405. doi:10.1179/030634578790434016.

[133] C. Yanar, J.M.K. Wiezorek, W.A. Soffa, V. Radmilovic, Massive transformation and the formation of the ferromagnetic L10 phase in manganese-aluminum-based alloys, Metall. Mater. Trans. A. 33 (2002) 2413–2423. doi:10.1007/s11661-002-0363-3.

[134] T.B. Massalski, D.E. Laughlin, W.A. Soffa, The nature and role of incoherent interphase interfaces in diffusional solid-solid phase transformations, Metall. Mater. Trans. A. 37 (2006) 825–831. doi:10.1007/s11661-006-0055-5.

[135] J.W. Cahn, Theory of crystal growth and interface motion in crystalline

materials, Acta Metall. 8 (1960) 554–562. doi:http://dx.doi.org/10.1016/0001-6160(60)90110-3.

[136] T. Furuhara, H.I. Aaronson, On the mechanisms of interphase boundary carbide precipitation, Scr. Metall. 22 (1988) 1635–1637. doi:10.1016/S0036-9748(88)80256-4.

[137] T. Furuhara, A.M. Dalley, H.I. Aaronson, INTERFACIAL STRUCTURE OF GRAIN BOUNDARY alpha ALLOTRIOMORPHS IN A HYPOEUTECTIOD Ti-Cr ALLOY, Scr. Metall. 22 (1988) 1509–1514.

[138] T. Furuhara, H.I. Aaronson, Crystallography and interfacial structure of proeutectoid alpha grain boundary allotriomorphs in a hypoeutectoid TiCr alloy, Acta Metall. Mater. 39 (1991) 2887–2899. doi:10.1016/0956-7151(91)90105-A.

[139] T. Furuhara, T. Maki, Interfacial structure of grain boundary precipitate in a Ni-45 mass% Cr alloy, Mater. Trans. JIM. 33 (1992) 734–739.

[140] M. Peet, H.K.D.H. Bhadeshia, Program MAP_STEEL_MUCG83, Mater. Algorithms Proj. Progr. Libr. (2006). http://www.msm.cam.ac.uk/map/ (accessed February 2, 2015).

[141] D. V Edmonds, The strengthening of an fe-vc low-alloy steel by carbide precipitation during continuous cooling from the austenitic condition, Metall. Trans. 4 (1973) 2527–2533.

[142] C.Y. Chen, H.W. Yen, F.H. Kao, W.C. Li, C.Y. Huang, J.R. Yang, et al., Precipitation hardening of high-strength low-alloy steels by nanometer-sized carbides, Mater. Sci. Eng. A. 499 (2009) 162–166. doi:10.1016/j.msea.2007.11.110.

[143] F.Z. Bu, X.M. Wang, L. Chen, S.W. Yang, C.J. Shang, R.D.K. Misra, Influence of cooling rate on the precipitation behavior in Ti–Nb–Mo microalloyed steels during continuous cooling and relationship to strength, Mater. Charact. 102 (2015) 146–155. doi:10.1016/j.matchar.2015.03.005.

[144] F.Z. Bu, X.M. Wang, S.W. Yang, C.J. Shang, R.D.K. Misra, Contribution of interphase precipitation on yield strength in thermomechanically

simulated Ti–Nb and Ti–Nb–Mo microalloyed steels, Mater. Sci. Eng. A. 620 (2015) 22–29. doi:10.1016/j.msea.2014.09.111.

[145] G.L. Dunlop, R.W.K. Honeycombe, The role of dislocations in the coarsening of carbide particles dispersed in ferrite, Philos. Mag. 32 (1975) 61–72. doi:10.1080/14786437508222805.

[146] Y. Funakawa, K. Seto, Stabilization in Strength of Hot-rolled Sheet Steel Strengthened by Nanometer-sized Carbides, Tetsu-to-Hagane. 93 (2007) 49–56. doi:10.2355/tetsutohagane.93.49.

[147] J.H. Jang, Y.-U. Heo, C.-H. Lee, H.K.D.H. Bhadeshia, D.-W. Suh, Interphase precipitation in Ti–Nb and Ti–Nb–Mo bearing steel, Mater. Sci. Technol. 29 (2013) 309–313. doi:10.1179/1743284712Y.0000000131.

[148] J.H. Jang, C.-H. Lee, H.N. Han, H.K.D.H. Bhadeshia, D.-W. Suh, Modelling coarsening behaviour of TiC precipitates in high strength, low alloy steels, Mater. Sci. Technol. 29 (2013) 1074–1079. doi:10.1179/1743284713Y.0000000254.

[149] A. Chamisa, Development of Ultra High Strength Steels for Reduced Carbon Emissions in Automotive Vehicles, University of Sheffield, 2014.

[150] R. Wagner, R. Kampmann, P.W. Voorhees, Homogeneous Second-Phase Precipitation, in: G. Kostorz (Ed.), Phase Transform. Mater., Wiley-VCH Verlag GmbH & Co. KGaA, Weinheim, FRG, 2005: pp. 309–407.

[151] P. Fratzl, Small-angle scattering in materials science - A short review of applications in alloys, ceramics and composite materials, J. Appl. Crystallogr. 36 (2003) 397–404. doi:10.1107/S0021889803000335.

[152] H. Yasuhara, K. Sato, Y. Toji, M. Ohnuma, J. Suzuki, Y. Tomota, Size Analysis of Nanometer Titanium Carbide in Steel by Using Small-Angle Neutron Scattering, Tetsu-to-Hagane. 96 (2010) 545–549.

[153] T. Dorin, K. Wood, A. Taylor, P. Hodgson, N. Stanford, Effect of coiling treatment on microstructural development and precipitate strengthening of a strip cast steel, Acta Mater. 115 (2016) 167–177. doi:10.1016/j.actamat.2016.05.043.

[154] S. Dhara, R.K.W. Marceau, K. Wood, T. Dorin, I.B. Timokhina, P.D. Hodgson, Precipitation and clustering in a Ti-Mo steel investigated using atom probe tomography and small-angle neutron scattering, Mater. Sci. Eng. A. 718 (2018) 74–86. doi:10.1016/j.msea.2018.01.070.

[155] Y. Oba, S. Koppoju, M. Ohnuma, T. Murakami, H. Hatano, K. Sasakawa, et al., Quantitative Analysis of Precipitate in Vanadium-microalloyed Medium Carbon Steels Using Small-angle X-ray and Neutron Scattering Methods, ISIJ Int. 51 (2011) 1852–1858. doi:10.2355/isijinternational.51.1852.

[156] J.B. Wiskel, D.G. Ivey, H. Henein, The effects of finish rolling temperature and cooling interrupt conditions on precipitation in microalloyed steels using small Angle neutron scattering, Metall. Mater. Trans. B Process Metall. Mater. Process. Sci. 39 (2008) 116–124. doi:10.1007/s11663-007-9104-8.

[157] M. Nöhrer, S. Zamberger, S. Primig, H. Leitner, Atom probe study of vanadium interphase precipitates and randomly distributed vanadium precipitates in ferrite, Micron. 54–55 (2013) 57–64. doi:10.1016/j.micron.2013.08.008.

[158] T. Dorin, A. Taylor, K. Wood, J. Wang, P.D. Hodgson, N. Stanford, Complex precipitation phenomena in strip cast steels with high sulfur and copper contents, J. Appl. Crystallogr. 49 (2016) 1777–1785. doi:10.1107/S1600576716013054.

[159] T. Dorin, K. Wood, A. Taylor, P. Hodgson, N. Stanford, Quantitative examination of carbide and sulphide precipitates in chemically complex steels processed by direct strip casting, Mater. Charact. 112 (2016) 259–268. doi:10.1016/j.matchar.2015.12.028.

[160] G. Albertini, F. Carsughi, R. Coppola, F. Fiori, F. Rustichelli, M. Stefanon, Small-angle neutron scattering microstructural investigation of MANET steel, J. Nucl. Mater. 233–237 (1996) 253–257. doi:10.1016/S0022-3115(96)00131-6.

[161] P. Staron, B. Jamnig, H. Leitner, R. Ebner, Small-angle neutron scattering

analysis of the, (2003) 415–419.

[162] B.S. Seong, E. Shin, S.H. Choi, Y. Choi, Y.S. Han, K.H. Lee, et al., Quantitative analysis of fine nano-sized precipitates in low-carbon steels by small angle neutron scattering, Appl. Phys. A Mater. Sci. Process. 99 (2010) 613–620. doi:10.1007/s00339-010-5630-3.

[163] F. Perrard, A. Deschamps, F. Bley, P. Donnadieu, P. Maugis, A small-angle neutron scattering study of fine-scale NbC precipitation kinetics in the α-Fe-Nb-C system, J. Appl. Crystallogr. 39 (2006) 473–482. doi:10.1107/S002188980601301X.

[164] A. Deschamps, F. Danoix, F. De Geuser, T. Epicier, H. Leitner, M. Perez, Low temperature precipitation kinetics of niobium nitride platelets in Fe, Mater. Lett. 65 (2011) 2265–2268. doi:10.1016/j.matlet.2011.03.110.

[165] N.H. Van Dijk, S.E. Offerman, W.G. Bouwman, M.T. Rekveldt, J. Sietsma, S. Van Der Zwaag, et al., High temperature SANS experiments on Nb(C, N) and MnS precipitates in HSLA steel, Metall. Mater. Trans. A Phys. Metall. Mater. Sci. 33 (2002) 1883–1891. doi:10.1007/s11661-002-0021-9.

[166] Y. Oba, S. Koppoju, M. Ohnuma, T. Murakami, H. Hatano, K. Sasakawa, et al., Quantitative Analysis of Precipitate in Vanadium-microalloyed Medium Carbon Steels Using Small-angle X-ray and Neutron Scattering Methods, ISIJ Int. 51 (2011) 1852–1858. doi:10.2355/isijinternational.51.1852.

[167] J. Scott, F.T. Docherty, M. MacKenzie, W. Smith, B. Miller, C.L. Collins, et al., Sample preparation for nanoanalytical electron microscopy using the FIB lift-out method and low energy ion milling, J. Phys. Conf. Ser. 26 (2006) 1742–6588. doi:10.1088/1742-6596/26/053.

[168] C.A. Schneider, W.S. Rasband, K.W. Eliceiri, NIH Image to ImageJ: 25 years of image analysis, Nat. Methods. 9 (2012) 671–675. doi:10.1038/nmeth.2089.

[169] R.K. Heenan, S.E. Rogers, D. Turner, A.E. Terry, J. Treadgold, S.M. King, Small angle neutron scattering using sans2d, Neutron News. 22 (2011) 19–21. doi:10.1080/10448632.2011.569531.

[170] W. Woo, V. Em, E. Shin, P. Mikula, V. Ryukhtin, Influence of multiple small-angle neutron scattering on diffraction peak broadening in ferritic steel, J. Appl. Crystallogr. 48 (2015) 350–356. doi:10.1107/S1600576715000813.

[171] A. Michels, J. Weissmüller, Magnetic-field-dependent small-angle neutron scattering on random anisotropy ferromagnets, Reports Prog. Phys. 71 (2008) 066501. doi:10.1088/0034-4885/71/6/066501.

[172] F. De Geuser, A. Deschamps, Precipitate characterisation in metallic systems by small-angle X-ray or neutron scattering, Comptes Rendus Phys. 13 (2012) 246–256. doi:10.1016/j.crhy.2011.12.008.

[173] G.D. Wignall, F.S. Bates, Absolute Calibration of Small-Angle Neutron Scattering Data*, J. Appl. Crystallogr. 20 (1987) 28–40. doi:10.1107/S0021889887087181.

[174] A. Deschamps, F. De Geuser, On the validity of simple precipitate size measurements by small-angle scattering in metallic systems, J. Appl. Crystallogr. 44 (2011) 343–352. doi:10.1107/S0021889811003049.

[175] O. Glatter, O. Kratky, Small angle X-ray scattering, Academic press, 1982.

[176] T. Imae, T. Kanaya, M. Furusaka, N. Torikai, Neutrons in soft matter, John Wiley & Sons, 2011.

[177] A. Deschamps, F. De Geuser, Quantitative characterization of precipitate microstructures in metallic alloys using small-angle scattering, Metall. Mater. Trans. A Phys. Metall. Mater. Sci. 44 (2013) 77–86. doi:10.1007/s11661-012-1435-7.

[178] P. Butler, G. Alina, R.C. Hernandez, M. Doucet, A. Jackson, P. Kienzle, et al., SASView for Small Angle Scattering Analysis, (2013).

[179] F. Cousin, Small angle neutron scattering, EPJ Web Conf. 104 (2015) 01004. doi:10.1051/epjconf/201510401004.

[180] Y. Ishiguro, K. Sato, Determination of non-stoichiometric composition of complex carbon-nitrides in steel by measuring plasmon energy, Mater. Trans. Jim. 37 (1996) 643–649.

[181] J.M. Howe, H.I. Aaronson, J.P. Hirth, Aspects of interphase boundary

structure in diffusional phase transformations, Acta Mater. 48 (2000) 3977–3984. doi:10.1016/S1359-6454(00)00183-X.

[182] K. Verbeken, L. Barbé, D. Raabe, Evaluation of the Crystallographic Orientation Relationships between FCC and BCC Phases in TRIP Steels, ISIJ Int. 49 (2009) 1601–1609. doi:10.2355/isijinternational.49.1601.

[183] H. Kitahara, R. Ueji, N. Tsuji, Y. Minamino, Crystallographic features of lath martensite in low-carbon steel, Acta Mater. 54 (2006) 1279–1288. doi:10.1016/j.actamat.2005.11.001.

[184] H. Kitahara, R. Ueji, M. Ueda, N. Tsuji, Y. Minamino, Crystallographic analysis of plate martensite in Fe-28.5 at.% Ni by FE-SEM/EBSD, Mater. Charact. 54 (2005) 378–386. doi:10.1016/j.matchar.2004.12.015.

[185] A. Morawiec, Orientations and Rotations, Springer Berlin Heidelberg, Berlin, 2004. doi:10.1007/978-3-662-09156-2.

[186] D. Phelan, R. Dippenaar, Widmanstätten ferrite plate formation in low-carbon steels, Metall. Mater. Trans. A. 35 (2004) 3701–3706. doi:10.1007/s11661-004-0276-4.

[187] D. Phelan, N. Stanford, R. Dippenaar, In situ observations of Widmanstätten ferrite formation in a low-carbon steel, Mater. Sci. Eng. A. 407 (2005) 127–134. doi:10.1016/j.msea.2005.07.015.

[188] X.L. Wan, R. Wei, L. Cheng, M. Enomoto, Y. Adachi, Lengthening kinetics of ferrite plates in high-strength low-carbon low alloy steel, J. Mater. Sci. 48 (2013) 4345–4355. doi:10.1007/s10853-013-7250-8.

[189] J. Pak, D. Suh, H. Bhadeshia, Displacive Phase Transformation and Surface Effects Associated with Confocal Laser Scanning Microscopy, Metall. Mater. Trans. A. 43 (2012) 4520–4525.

[190] R.L. Bodnar, S.S. Hansen, Effects of austenite grain size and cooling rate on Widmanstatten ferrite formation in low-alloy steels, Metall. Mater. Trans. A. 25 (1994) 665–675. doi:10.1007/BF02665443.

[191] M. Enomoto, T. Sonoyama, H. Yada, Kinetics of austenite to ferrite transformation in 3 mass% Mn low carbon steels, Mater. Trans. JIM. 39

(1998) 189–195.

[192] H.K.D.H. Bhadeshia, Phase transformations contributing to the properties of modern steels, Bull. Polish Acad. Sci. Tech. Sci. 58 (2010) 255–265. doi:10.2478/v10175-010-0024-4.

[193] D.W. Kim, R.S. Qin, H.K.D.H. Bhadeshia, Transformation texture of allotriomorphic ferrite in steel, Mater. Sci. Technol. 25 (2009) 892–895. doi:10.1179/174328408X365793.

[194] T. Furuhara, T. Maki, Variant selection in heterogeneous nucleation on defects in diffusional phase transformation and precipitation, Mater. Sci. Eng. A. 312 (2001) 145–154. doi:10.1016/S0921-5093(00)01904-3.

[195] G.R. Purdy, Y.J.M. Bréchet, A solute drag treatment of the effects of alloying elements on the rate of the proeutectoid ferrite transformation in steels, Acta Metall. Mater. 43 (1995) 3763–3774. doi:10.1016/0956-7151(95)90160-4.

[196] S.A. Hackney, G.J. Shiflet, The pearlite-austenite growth interface in an Fe-0.8 C-12 Mn alloy, Acta Metall. 35 (1987) 1007–1017. doi:10.1016/0001-6160(87)90048-4.

[197] H.I. Aaronson, M. Enomoto, J.K. Lee, Mechanisms of Diffusional Phase Transformations in Metals and Alloys, CRC Press, London, 2010. doi:10.1007/s13398-014-0173-7.2.

[198] H. Song, J.J. Hoyt, A molecular dynamics study of heterogeneous nucleation at grain boundaries during solid-state phase transformations, Comput. Mater. Sci. 117 (2016) 151–163. doi:10.1016/j.commatsci.2016.01.027.

[199] T. Nagano, M. Enomoto, Calculation of the interfacial energies between α and γ iron and equilibrium particle shape, Metall. Mater. Trans. A. 37 (2006) 929–937. doi:10.1007/s11661-006-0066-2.

[200] J.W. Cahn, Thermodynamics of Solid and Fluid Surfaces, Pap. Present. a Semin. Am. Soc. Met. Oct. 22 23, 1977, Chicago, USA. (1979) 3–23.

[201] N.A. Gjostein, H.A. Domian, H.I. Aaronson, E. Eichen, Relative interfacial

energies in Fe-C alloys, Acta Metall. 14 (1966) 1637–1644. doi:10.1016/0001-6160(66)90016-2.

[202] S.A. Dregia, P. Wynblatt, Equilibrium segregation and interfacial energy in multicomponent systems, Acta Metall. Mater. 39 (1991) 771–778. doi:10.1016/0956-7151(91)90277-8.

[203] J.M. Howe, Interfaces in materials: atomic structure, thermodynamics and kinetics of solid-vapor, solid-liquid and solid-solid interfaces, John Wiley & Sons, New York, 1997.

[204] H. Chen, K. Zhu, L. Zhao, S. van der Zwaag, Analysis of transformation stasis during the isothermal bainitic ferrite formation in Fe–C–Mn and Fe–C–Mn–Si alloys, Acta Mater. 61 (2013) 5458–5468. doi:10.1016/j.actamat.2013.05.034.

[205] H. Chen, S. van der Zwaag, A general mixed-mode model for the austenite-to-ferrite transformation kinetics in Fe–C–M alloys, Acta Mater. 72 (2014) 1–12. doi:10.1016/j.actamat.2014.03.034.

[206] J.W. Cahn, The impurity-drag effect in grain boundary motion, Acta Metall. 10 (1962) 789–798. doi:10.1016/0001-6160(62)90092-5.

[207] M. Hillert, B. Sundman, A treatment of the solute drag on moving grain boundaries and phase interfaces in binary alloys, Acta Metall. 24 (1976) 731–743. doi:10.1016/0001-6160(76)90108-5.

[208] M. Hillert, Solute drag, solute trapping and diffusional dissipation of Gibbs energy, Acta Mater. 47 (1999) 4481–4505. doi:10.1016/S1359-6454(99)00336-5.

[209] M. Hillert, Diffusion and interface control of reactions in alloys, Metall. Trans. A. 6 (1975) 5–19. doi:10.1007/BF02673664.

[210] G.R. Speich, A. Szirmae, Formation of Austenite From Ferrite and Ferrite-Carbide Aggregates, Trans. Met. Soc. AIME. 245 (1969) 1063–1074.

[211] M. Hillert, L. Höglund, Mobility of α/γ phase interfaces in Fe alloys, Scr. Mater. 54 (2006) 1259–1263. doi:10.1016/j.scriptamat.2005.12.023.

[212] E. Gamsjäger, M. Militzer, F. Fazeli, J. Svoboda, F.D. Fischer, Interface

mobility in case of the austenite-to-ferrite phase transformation, Comput. Mater. Sci. 37 (2006) 94–100. doi:10.1016/j.commatsci.2005.12.011.

[213] H. Chen, S. Van Der Zwaag, Modeling of soft impingement effect during solid-state partitioning phase transformations in binary alloys, J. Mater. Sci. 46 (2011) 1328–1336. doi:10.1007/s10853-010-4922-5.

[214] P.J. Clemm, J.C. Fisher, The influence of grain boundaries on the nucleation of secondary phases, Acta Metall. 3 (1955) 70–73.

[215] H.K.D.H. Bhadeshia, Diffusional formation of ferrite in iron and its alloys, Prog. Mater. Sci. 29 (1985) 321–386. doi:10.1016/0079-6425(85)90004-0.

[216] H.I. Aaronson, S.K. Liu, W.T. Reynolds Jr, G.J. Shiflet, Discussion On the influence of a solute drag-like effect upon the growth of ferrite in F e - C - X alloys, J. Mater. Sci. 20 (1985) 4232–4238.

[217] D.A. Porter, K.E. Easterling, M.Y. Sherif, Phase Transformations in Metals and Alloys, Third Edit, CRC Press, Boca Raton, 2009.

[218] F.R.N. Nabarro, The Strains Produced by Precipitation in Alloys, Proc. R. Soc. A Math. Phys. Eng. Sci. 175 (1940) 519–538. doi:10.1098/rspa.1940.0072.

[219] L.-Q. Chen, Phase -Field Models for Microstructure Evolution, Annu. Rev. Mater. Res. 32 (2002) 113–140. doi:10.1146/annurev.matsci.32.112001.132041.

[220] M. Militzer, Phase field modeling of microstructure evolution in steels, Curr. Opin. Solid State Mater. Sci. 15 (2011) 106–115. doi:10.1016/j.cossms.2010.10.001.

[221] A. Rahnama, R. Dashwood, S. Sridhar, A phase-field method coupled with CALPHAD for the simulation of ordered ordered k-cabide precipitates in both disorered gamman and alpha phases in low density steel, Comput. Mater. Sci. 126 (2017) 152–159. doi:10.1016/j.commatsci.2016.09.015.

[222] I. Steinbach, F. Pezzolla, A generalized field method for muliphase transformations using interface fields, Phys. D. 134 (1999) 385–393.

[223] A. Reuss, Berechnung der Fließgrenze von Mischkristallen auf Grund der

Plastizitätsbedingung für Einkristalle ., ZAMM - Zeitschrift Für Angew. Math. Und Mech. 9 (1929) 49–58. doi:10.1002/zamm.19290090104.

[224] R. Hill, Elastic properties of reinforced solids: Some theoretical principles, J. Mech. Phys. Solids. 11 (1963) 357–372. doi:10.1016/0022-5096(63)90036-X.

[225] J. Tiaden, B. Nestler, H.J. Diepers, I. Steinbach, The multiphase-field model with an integrated concept for modelling solute diffusion, Phys. D Nonlinear Phenom. 115 (1998) 73–86. doi:10.1016/S0167-2789(97)00226-1.

[226] J. Tiaden, U. Grafe, I. Steinbach, The prospectives of phase field modelling for the investigation of phase transformations in steel, in: Cut. Edge Comput. Simul. Solidif. Cast., 1999: pp. 13–20.

[227] S.G. Kim, W.T. Kim, T. Suzuki, Phase-field model for binary alloys., Phys. Rev. E. Stat. Phys. Plasmas. Fluids. Relat. Interdiscip. Topics. 60 (1999) 7186–7197. doi:10.1103/PhysRevE.60.7186.

[228] F. Larche, J.W. Cahn, a Linear Theory of Thermochemical of Solids Under Stress, Acta Metall. 21 (1973) 1051. doi:10.1016/0001-6160(73)90021-7.

[229] A.R. Denton, N.W. Ashcroft, Vegard's law, Phys. Rev. A. 43 (1991) 3161–3164. doi:10.1103/PhysRevA.43.3161.

[230] A. Rahnama, S. Clark, V. Janik, S. Sridhar, A phase-field model for interphase precipitation in V-micro-alloyed structural steels, Comput. Mater. Sci. 137 (2017) 257–265. doi:10.1007/s11661-001-0249-9.

[231] M. Segawa, A. Yamanaka, S. Nomoto, Multi-phase-field simulation of cyclic phase transformation in Fe-C-Mn and Fe-C-Mn-Si alloys, Comput. Mater. Sci. 136 (2017) 67–75. doi:10.1016/j.commatsci.2017.04.014.

[232] R. Lagneborg, B. Hutchinson, T. Siwecki, S. Zajac, The Role of Vanadium in Microalloyed Steels, 2nd ed., Swerea KIMAB, Stockholm, 2014.

[233] T.N. Baker, Microalloyed steels, Ironmak. Steelmak. 43 (2016) 264–307. doi:10.1179/1743281215Y.0000000063.

[234] H.K.D.H. Bhadeshia, Thermodynamic analysis of isothermal transformation

diagrams, Met. Sci. 16 (1982) 159–166. doi:10.1179/030634582790427217.

[235] M. Peet, T. Okumara, Program MAP_TTTtoCCTlinear, Mater. Algorithms Proj. Progr. Libr. (1996).

[236] C.R. Hutchinson, H.S. Zurob, Y. Bréchet, The growth of ferrite in Fe-C-X alloys: The role of thermodynamics, diffusion, and interfacial conditions, Metall. Mater. Trans. A. 37 (2006) 1711–1720. doi:10.1007/s11661-006-0114-y.

[237] A. Béché, H.S. Zurob, C.R. Hutchinson, Quantifying the Solute Drag Effect of Cr on Ferrite Growth Using Controlled Decarburization Experiments, Metall. Mater. Trans. A Phys. Metall. Mater. Sci. 38 (2007) 2950–2955. doi:10.1007/s11661-012-1547-0.